The Dissertation Committee for Kent Billington Fischer Certifies that this is the approved version of the following Dissertation:

Corrosion of Stainless and Carbon Steel in Aqueous Amine for CO_2 Capture

Committee:

Gary T. Rochelle, Supervisor

Gyeong S. Hwang

Benjamin Keith Keitz

Harovel G. Wheat

Corrosion of Stainless and Carbon Steel in Aqueous Amine for CO_2 Capture

by

Kent Billington Fischer

Dissertation

Presented to the Faculty of the Graduate School of

The University of Texas at Austin

in Partial Fulfillment

of the Requirements

for the Degree of

Doctor of Philosophy

The University of Texas at Austin

May 2019

Dedication

To my parents, Anne and Duncan

Acknowledgements

I could not have asked for a better advisor than Dr. Rochelle. He is an exacting and brilliant scientist, but he never let that take priority over being kind and patient. “Re-treading” me from a chemist into a chemical engineer was not an easy task, and I will always be grateful that he took a chance on me. I would also like to thank Keith Keitz, Gyeong Hwang, and Harovel Wheat for serving on my supervising committee and for their feedback on this project.

I would also like to thank several key mentors in the Rochelle group who helped me with this work. Dr. Eric Chen trained me how to design, procure, and fabricate experimental equipment. He also trained me how to work responsibly and safely in an industrial environment at the Pickle Research Center. Omkar Namjoshi trained me in several experimental and analytical techniques, and was in general a kind and supportive friend. Paul Nielsen provided analytical training and support, and was also the source of many insights into the autocatalytic nature of amine degradation and corrosion. Matthew Beaudry blazed the trail for my pilot work with his significant, independent pilot work. Without his training, I would have been unable to complete the ambitious 2018 piperazine pilot campaign. Maeve Cooney has been a constant source of advice, wit, and fondly remembered conversations—thanks for your patience and help with writing. Thanks to Matthew Walters, Darshan Sachde, Yu-Jeng Lin, and Brent Sherman for teaching me about the subtleties of process modeling and optimization. Former group members that I also owe gratitude are: Yang Du, Nathan Fine, Peter Frailie, Steven Fulk, Lynn Li, and Di Song.

This work would not have been possible without the help of my undergraduate research assistants: Akshay Daga, Shyam Sharma, and Victor Chan Wai Han. I am

exceptionally proud of your dedication and accomplishments in the lab, and I am very lucky to know and have worked with you. Thanks to the other undergraduates who assisted me when we briefly crossed paths: Daniel Hatchell, Hanbi Liu, and Mark Tomasovic.

Thanks to my recently graduated cohort in the Rochelle group: Ye Yuan, Yue Zhang, and Joseph Selinger. I have really appreciated your help with this project and your friendship. Among the current cohort, I owe special thanks to Korede Akinpelumi and Ching-Ting Liu, both of whom helped me during the 2018 piperazine pilot campaign. Ching-Ting is continuing this corrosion work, and her help and insights have been invaluable. I also owe gratitude to Tianyu Gao, Athreya Suresh, and Yuying Wu.

Experiments at the pilot scale are very much a team effort. I would like to thank Tony Wu, John Carroll and all the engineers and operators at the National Carbon Capture Center who contributed to this work. Significant planning for the 2018 piperazine pilot campaign was done by Katherine Dombrowski, Andrew Sexton, and Karen Farmer. Thanks also to Eric Chen, Frank Seibert, and all the personnel and operators at the UT Separations Research Program who coordinated the 2017 piperazine pilot campaign.

I am also grateful for the assistance of Andrei Dolocan and Richard Piner with SEM and Vincent Lynch with X-ray diffraction. Shallaco McDonald provided frequent mechanical assistance, particularly with fabricating and welding the corrosion loop apparatus.

Thanks to my friends, with whom I remember especially fondly many excellent conversations over Saturday morning pancake breakfasts at Kerbey Lane Café.

Financial support for this project was provided by the Texas Carbon Management Program and the Cockrell Foundation.

Finally, thanks to my fiancée Carly Holcomb. Without your love and support, I wouldn't have been able to finish this project.

Abstract

Corrosion of Stainless and Carbon Steel in Amine Solutions for CO_2 Capture

Kent Billington Fischer, Ph.D.

The University of Texas at Austin, 2019

Supervisor: Gary T. Rochelle

Post-combustion carbon capture and storage with amine absorbents is a key technology needed to provide low-cost decarbonized electricity. Improving understanding of corrosion by amines may reveal a solvent system compatible with carbon steel, which would reduce plant capital costs.

Corrosion of stainless and carbon steel in aqueous monoethanolamine (MEA) and piperazine (PZ) has been measured. High temperature amine corrosion was measured in a bench-scale pressure vessel and iron solubility in amines was screened in stirred reactors. Corrosion was measured at two PZ pilot plants and one MEA pilot plant, using coupons and electrical resistance probes. Corrosion products were characterized by SEM and powder X-ray diffraction.

Carbon steel (C1010) often performs well in 5 molal PZ up to 150 °C due to the formation of a passivating $FeCO_3$ layer. This layer is promoted at high temperature, high CO_2 loading, low solution velocity, and in amines with low Fe^{2+} solubility. $FeCO_3$ formation is favorable at high temperature because Fe^{2+} solubility decreases and the kinetics of $FeCO_3$ formation are faster. This also means that $FeCO_3$ is not observed at low

temperature. Despite this, carbon steel performs well at low temperature due to slower kinetics of metal oxidation.

Depassivation and high corrosion of stainless steel (316L) can occur in amine solutions at high temperature (150 °C) when conditions are relatively anoxic and reducing. Performance of stainless at high temperature in PZ suggests that it can be pushed into and out of the passive state by small process changes, such as different flue gas O_2 concentrations. However, stainless performs well in both MEA and PZ in pilot plants at ≈120 °C.

Fe^{3+} corrosion products are generated in the absorber, then reduced to Fe^{2+} in the high temperature, anoxic conditions of the stripper. In this way, carried-over Fe^{3+} is responsible for oxidation of amine and corrosion at high temperature.

Certain highly corrosive amines also have high Fe^{2+} solubility. Ethylamines like MEA are likely the correct chain length to form stable complexes with Fe^{2+} in solution. Stable Fe^{2+}-amine complexes cause high Fe^{2+} solubility, which prevents $FeCO_3$ formation and leads to high corrosion.

Table of Contents

Dedication iv

Acknowledgements v

Table of Contents ix

List of Tables xvi

List of Figures xix

Chapter 1. Introduction 1

Chapter 2. Background 5

2.1. Argument for the implementation of carbon capture and storage 5

2.1.1. Atmospheric carbon dioxide and temperature 5

2.1.2. Impacts of rising global temperature 6

2.1.3. Sources of atmospheric carbon dioxide 7

2.1.4. Mitigating carbon dioxide emissions from electricity generation 8

2.1.5. Mitigating carbon dioxide emissions with carbon capture and storage 10

2.2. Post-combustion carbon capture with chemical absorption 11

2.2.1. Description of a typical amine absorption process 11

2.2.2. Developments in PCCC with chemical absorption 12

2.3. Corrosion in PCCC with chemical absorption 15

2.3.1. Motivation 15

2.3.2. Corrosion thermodynamics 17

2.3.3. Passive film formation 24

2.3.4. Corrosion experience in natural gas sweetening 26

2.3.5. Corrosion measurements at PCCC conditions 29
2.3.6. Corrosion measurement at PCCC conditions in pilot plants 32
Chapter 3. Experimental Methods 35
3.1. Techniques for Measurement of Corrosion 35
3.1.1. Electrical Resistance Corrosion Probes 35
3.1.2. Oxidation-Reduction Probes 38
3.1.3. Corrosion Coupons 39
3.1.4. Coupon Characterization 41
3.2. Equipment for Simulating Amine Corrosion at the Bench-Scale 44
3.2.1. Corrosion Loop Apparatus 44
3.2.2. Thermal Degradation Cylinders 47
3.2.3. Equilibrium Fe^{2+} Solubility Measurement 49
3.3. Amine Solution Characterization 50
3.3.1. Preparation of Amine Solutions 50
3.3.2. Anion Chromatography 51
3.3.3. Cation Chromatography 51
3.3.4. Inductively Coupled Plasma Optical Emission Spectroscopy 52
3.3.5. Total Inorganic Carbon Measurement 53
3.4. Miscellaneous Equipment and Equipment Part Numbers 54
3.4.1. Corrosion Coupon Mounting Hardware 54
3.4.2. Bench-Scale Data Logger 56
3.4.3. Equipment Part Numbers 58

Chapter 4. Bench-Scale Corrosion Measurement 59

4.1. Corrosion Loop Results: Piperazine 60

4.2. Corrosion Loop Results: Linear Amines 65

4.3. Limitations of Corrosion Loop results 67

4.4. Thermal Cylinder Results: Linear Amines 68

4.5. Conclusions 75

4.5.1. Corrosion in steel thermal degradation cylinders and corrosion by measurement of electrical resistance in a loop apparatus gave similar results for relative amine corrosivity. 75

4.5.2. Thermal cylinders are useful for predicting relative corrosivity of amines, but they underpredict carbon steel corrosion rates and overpredict stainless steel corrosion rates.. 75

4.5.3. Thermal cylinders suggest that each mol of formate generation is accompanied by 2.75 mol of steel corrosion. 76

4.5.4. Ethylamines, such as, MEA and EDA, are more corrosive than their propylamine counterparts, EDA and PDA. The ethyl- backbone amines likely form more stable coordination complexes with oxidized iron, increasing corrosion. 76

4.5.5. The corrosion loop with an electrical resistance probe yields realistic corrosion rates for C1010 in amines. 77

4.5.6. Stainless steel sometimes experiences attack in PZ at high temperature, anoxic conditions. 77

4.5.7. Carbon steel experiences low corrosion at high temperature in PZ solutions. 77

4.5.8. PZ degradation apparently accelerates corrosion of carbon and stainless steel. 78

Chapter 5. Fe^{2+} Solubility and Siderite Formation in Monoethanolamine and Piperazine 79

5.1. Introduction 80

5.2. Methods....81

5.3. Results....83

5.4. Conclusions....92

5.4.1. In loaded amine solutions, Fe^{2+} solubility is a strong negative function of temperature.....92

5.4.2. Fe^{2+} is significantly more soluble in MEA than clean PZ at rich loadings.....92

5.4.3. The effect of CO_2 loading on Fe^{2+} solubility is affected by amine type.....92

5.4.4. The presence of amine degradation products significantly increased Fe^{2+} solubility in PZ.....93

5.4.5. In low temperature, agitated solubility experiments, Fe^{2+} is frequently converted to Fe^{3+}, except in PZ at high CO_2 loadings.....93

5.4.6. Fe^{3+} has limited solubility in PZ solutions.....94

5.4.7. The strong effects of CO_2 loading and T on Fe^{2+} solubility suggest the equilibrium concentration of Fe^{2+} will change as the solvent moves through a real plant.....94

Chapter 6. Corrosion in Monoethanolamine and Piperazine during 2017 Pilot Campaigns....95

6.1. SRP 2017 PZ Campaign Measurement Locations....96

6.2. NCCC 2017 MEA Campaign Measurement Locations....99

6.3. SRP 2017 PZ campaign ER probe results....100

6.4. SRP 2017 PZ campaign corrosion coupon results....103

6.5. NCCC 2017 MEA campaign corrosion coupon results....109

6.6. Discussion....115

6.7. Conclusions....117

6.7.1. $FeCO_3$ formation at 150°C in 5 m PZ protects carbon steel, leading to low corrosion rates. 117

6.7.2. Equipment commissioning with water and steam appears more corrosive to carbon steel than PZ operation. 117

6.7.3. Absorber corrosion of carbon steel can be moderate, but this may be due to equipment commissioning rather than exposure to PZ operation. 117

6.7.4. Stainless steel performed well in 5 m PZ both in the absorber and in the hot, lean stream. This may be partially due to the high O_2 content at SRP. 118

6.7.5. Carbon steel performs well at 40-70 °C in 7 m MEA, but it is unacceptable at 120 °C. 118

6.7.6. Stainless steel performs well in 7 m MEA at both absorber and stripper conditions. 118

6.7.7. Corrosion products on carbon steel are largely Ferric (Fe^{3+}) in 7 m MEA service, suggesting more oxidizing conditions than PZ. Protective corrosion product layers were not observed. 118

Chapter 7. Corrosion in Piperazine during 2018 Pilot Campaign 120

7.1. Corrosion Measurement Locations 120

7.2. Coupon Batching Schedule 125

7.3. Corrosion Results 127

7.3.1. Effect of Temperature and Velocity 127

7.3.2. Summary of corrosion by location 132

7.3.3. Corrosion compared between batches 134

7.4. Corrosion by Location 137

7.4.1. Absorber Middle 137

7.4.2. Absorber Sump 139

7.4.3. Absorber Top 143

7.4.4. Cold Lean 144
7.4.5. Cold Rich Bypass 147
7.4.6. Warm Rich Bypass 150
7.4.7. Hot rich 154
7.4.8. Hot lean 158
7.4.9. AFS Sump 162
7.5. Powder X-ray diffraction of corrosion products. 166
7.6. ER Probe Corrosion Measurement 170
7.7. ER Probe Corrosion by location 175
7.7.1. Absorber middle and sump 176
7.7.2. Cold rich bypass 177
7.7.3. Warm rich bypass 179
7.7.4. Hot Rich 181
7.7.5. Hot Lean 182
7.8. Conclusions 184
7.8.1. Carbon steel performs well in 5 m PZ at lean and rich loadings, at 116 – 150 °C, when fluid velocities are low. This good performance is due to the formation of a protective $FeCO_3$ film. 184
7.8.2. At 150 – 155 °C, at lean and rich loadings, when fluid velocity is moderate or high (> 0.8 m/s), $FeCO_3$ films are sometimes not protective to carbon steel, leading to high corrosion in 5 m PZ. 184
7.8.3. Limited evidence suggests environmentally induced cracking of carbon steel can occur in 5 m PZ at 155 °C at high fluid velocity. ..185
7.8.4. At 50 °C, carbon steel performs well in 5 m PZ, despite not forming protective $FeCO_3$ layers. 185
7.8.5. At 150 – 155 °C, stainless steel sometimes experiences high corrosion in 5 m PZ 185

7.8.6. At 50 – 116 °C, stainless steel performs well in 5 m PZ. 186

7.8.7. Fe^{3+} products are observed at rich conditions, which are relatively oxidizing, but Fe^{2+} is observed at lean conditions, which are reducing. The cyclic oxidation and reduction of Fe^{3+} likely plays a role in high temperature oxidation of PZ. 186

7.8.8. Equipment commissioning with water and steam appears more corrosive to carbon steel than PZ operation. 187

Chapter 8. Conclusions 188

8.1. Carbon steel often performs well in 5 molal PZ due to the formation of a passivating $FeCO_3$ layer. This layer is promoted at high T, high CO_2 loading, low solution velocity, and in amines with low Fe^{2+} solubility. 188

8.2. Depassivation and high corrosion of stainless steel can occur in amine solutions at high temperature. Depassivation of stainless is promoted by higher T (150 °C) when conditions are relatively anoxic and reducing. 192

8.3. Ferric products are generated in the absorber, then reduced at high temperature, anoxic conditions. This reduction reaction increases the oxidation of steel and amine. 195

8.4. Certain amines and amine degradation products have high iron solubility. These amines likely complex iron and stabilize it in solution, accelerating corrosion. 197

APPENDICES 201

Appendix A. Operating Procedures 202

A.1. Corrosion Loop Procedure and Safety Analysis 202

A.2. ER Probe Insertion Procedure 204

Appendix B. ORP Measurement in Piperazine during Pilot Campaigns 209

References 215

Vita 224

List of Tables

Table 2-1: Standard Gibbs free energy of formation at 25°C for relevant species.....18

Table 2-2: Standard Gibbs free energy of reaction and Standard reaction potential (for the reaction as written) at 25°C.....19

Table 2-3: Corrosion rates of carbon steel (1020) at 80 °C in 3 M amines. DEA is diethanolamine (Veawab et al., 1999) 30

Table 2-4: Corrosion of carbon steel (UNS K02600) in 50 wt % MDEA at 120 °C, Heat Stable Salts (HSS) are 3002 ppm H_2SO_4, 2818 ppm CH_2O_2, 10000 ppm bicine, O_2 = 8 kPa (Xiang, Choi, et al., 2014) 31

Table 3-1: Nomenclature used in Equation 3-1 36

Table 3-2: Relative corrosion resistance (Fontana, 1986). 37

Table 3-3: Nomenclature used in Equations 3-2 and 3-3 38

Table 3-4: Nomenclature for Equation 3-5 41

Table 3-5: Density and composition of alloys investigated (Bauccio, 1993) 41

Table 3-6: Reference spectra used for powder X-ray diffraction identification.....44

Table 3-7: Nomenclature used for describing amine solutions 51

Table 3-8: Wavelengths analyzed for metals measurement by ICP-OES 53

Table 3-9: ER and ORP Instruments used in corrosion measurement.....58

Table 3-10: Coupon mounting hardware 58

Table 3-11: Coupon part numbers and surface finish.....58

Table 4-1: ER probe corrosion of C1010 and 316L in PZ solutions 64

Table 4-2: ER probe corrosion of C1010 and 316L in MEA, MPA, and EDA solutions 67

Table 4-3: Thermal cylinder corrosion of C1010 and SS 316 L in MEA, MPA, EDA, PDA solutions 73
Table 4-4: Oxidation of amines in low gas flow apparatus at 70°C , 98 kPa O_2, 2 kPa CO_2, 100 ml/min gas flow, 1400 rpm, approx. 250 hr (Liu et al., 2015; Liu et al., 2014; Sexton, 2008). 74
Table 5-1: Nomenclature for Fe^{2+} solubility 80
Table 5-2: Equilibrium Fe in 9 m MEA and 5 m clean PZ 91
Table 5-3: Equilibrium Fe in degraded Tarong and SRP PZ 91
Table 6-1: Gas conditions during SRP 2017 campaign (Zhang, 2018). 96
Table 6-2: Flue gas composition at NCCC (Zhang et al., 2017). 99
Table 6-3: Summary of SRP 2017 PZ campaign ER probe corrosion measurement 102
Table 6-4: Weight loss for SRP 2017 PZ campaign coupons 105
Table 6-5: Weight loss for NCCC 2017 MEA campaign coupons 110
Table 7-1: Flue gas composition at NCCC (Zhang et al., 2017). 121
Table 7-2: PZ 2018 campaign CO_2 loadings during steady state runs. 121
Table 7-3: Description of Absorber ER and WL locations 122
Table 7-4: Description of regeneration system ER and WL locations 124
Table 7-5: PZ 2018 campaign superficial fluid velocity during steady state runs and typical operating temperatures. 125
Table 7-6: Calendar illustration of coupon batches. The colored sections of each row represent the coupon batches insertion and removal dates. Green sections represent periods of piperazine operation, black sections represent periods when coupons were inserted but the plant was shut down, and the yellow section represents the period of simple stripper operation. 125

Table 7-7: Apparent activation energies for coupon corrosion rates. 130
Table 7-8: Coupon weight loss corrosion rates (μm/yr) of carbon steel (C1010) by batch and location 136
Table 7-9: Coupon weight loss corrosion rates (μm/yr) of stainless steel (316L and 304) by batch and location 137
Table 7-10: Summary of coupon weight loss for ER2 and WL2 (Absorber Middle locations) 138
Table 7-11: Summary of coupon weight loss for ER3 (Absorber Sump) 141
Table 7-12: Summary of coupon weight loss for WL4 (Absorber Top) 144
Table 7-13: Summary of coupon weight loss for WL12 (Cold lean) 145
Table 7-14: Summary of coupon weight loss for WL13 (Cold rich bypass) 148
Table 7-15: Summary of coupon weight loss for WL14 (Warm rich bypass) 152
Table 7-16: Summary of coupon weight loss for WL19 (Hot rich) 156
Table 7-17: Summary of coupon weight loss for WL21 (Hot lean) 160
Table 7-18: Summary of coupon weight loss for WL22 (AFS Sump) 164
Table 7-19: Coupon weight loss (WL) corrosion rates (μm/yr) compared to ER corrosion rates (μm/yr) of carbon steel (C1010) by batch and location 172
Table 7-20: Coupon weight loss (WL) corrosion rates (μm/yr) compared to ER corrosion rates (μm/yr) of stainless steel (316L and 304) by batch and location 173
Table 7-21: Comparison of ER and coupon corrosion rates. 174
Table 7-22: Summary Table of ER Probe corrosion rate regression parameters. 175

List of Figures

Figure 2-1: CO_2 emissions from fossil fuels by country in 2012 (Janssens-Maenhout et al., 2017) 7

Figure 2-2: CO_2 emissions from fossil fuels by sector in the United States in 2016 (EPA, 2018). 8

Figure 2-3: Simplified amine scrubbing flow sheet....12

Figure 2-4: Top left: Monoethanolamine (MEA), top right: piperazine (PZ), bottom left: methyldiethanolamine (MDEA), bottom right: aminomethyl propanol (AMP) 14

Figure 2-5: Pourbaix diagram for Fe-CO_2-H_2O system, T=120°C, C_{Fe2+}=10ppm, C_{Fe3+}=10ppm, P_{H2}=1 bar, P_{O2}=1 bar, Pc_{O2}=2.27 bar (Tanupabrungsun et al., 2012). 22

Figure 2-6: (left) Pourbaix diagram for Nickel-water at 100°C and $[Ni(aq)]_{total}=10^{-6}$ molal and (right) Pourbaix diagram for Chromium-water at 100°C and $[Cr(aq)]_{total}=10^{-6}$ molal (Beverskog et al., 1997a, 1997b). 24

Figure 2-7: (left) Potentiodynamic curve of carbon steel (A106) in 5 M MEA, no O_2, α =0.2. (right) Potentiodynamic curve of stainless steel (304) in 5 M MEA, no O_2, α =0.2 (Y. Sun et al., 2011)....26

Figure 2-8: Natural gas sweetening plant diagram, with recommendations for materials of construction (Kohl et al., 1997). 27

Figure 2-9: (left) SEM of carbon steel (A106) in 30 wt % PZ for 150 h (right) SEM micrograph of carbon steel (A106) in 30 wt % MEA, 183 h. In both cases α=0.43, 80°C (Zheng, Landon, Zou, et al., 2014) 30

Figure 3-1: Electrical resistance corrosion probe 35

Figure 3-2: Blank coupons, from left to right: C1010 strip coupon, 316L strip coupon, 304 strip coupon, C1010 disc coupon, 316L disc coupon, 304 disc coupon. 39
Figure 3-3: SEM micrographs of blank coupons: a) C1010 strip, b) C1010 disc, c) 316L strip, d) 316L disc, e) 304 strip, f) 304 disc. 43
Figure 3-4: Corrosion loop apparatus 45
Figure 3-5: Corrosion loop apparatus, ORP probe not shown. 46
Figure 3-6: a) Reactor used for Fe^{2+} solubility experiments. b) Sparged reactor used for Fe^{2+} solubility experiments. 50
Figure 3-7: Illustration of the WL probes used on the AFS skid (Metal Samples Company, 2019). Each probe holds two strip coupons. 54
Figure 3-8: WL probe used on legacy NCCC equipment. Each probe holds four disc coupons. 55
Figure 3-9: Coupon adapter for ER probes holding two strip coupons. 55
Figure 3-10: An ER probe and a coupon probe inserted into a vessel at a pilot plant. 56
Figure 3-11: Bench-Scale Data Logger 57
Figure 4-1: ER Probe corrosion of C1010 and 316L in PZ solutions in corrosion loop ...61
Figure 4-2: ER Probe corrosion of C1010 and 316L in piperazine solutions at loading of α = 0.23-0.24 in corrosion loop 63
Figure 4-3: ER Probe corrosion of C1010 in MEA and EDA solutions in corrosion loop 66
Figure 4-4: ER Probe corrosion of C1010 and 316L in MEA and MPA solutions in corrosion loop 66
Figure 4-5: Linear monoamine concentration and its effect on average corrosion rate in thermal cylinders at 287-333 hrs., 316L and C1010, 135 °C, α = 0.35 69

Figure 4-6: Linear monoamine loading and its effect on average corrosion rate in thermal cyinders at 287-333 hrs., 316L and C1010, 135 °C, 10 m 70
Figure 4-7: Formate production and average corrosion rate in thermal cylinders, 287-333 hrs., 316L and C1010, 135 °C, 10 m, α = 0.35. 71
Figure 4-8: Hypothetical Stable MEA carbamate metal catalytic center (left) and unstable MPA carbamate metal catalytic center (right).....75
Figure 5-1: Soluble Fe in 9 m MEA with the addition of 0.25 M $FeSO_4$ and Na_2CO_3. 84
Figure 5-2: Soluble Fe in 5 m clean PZ with the addition of 0.25 M $FeSO_4$ and Na_2CO_3.....85
Figure 5-3: a) Rich MEA soluble Fe as a function of temperature. b) Rich PZ soluble Fe as a function of temperature (Fytianos, 2016). 86
Figure 5-4: Soluble Fe in 5 m degraded SRP PZ with the addition of 0.25 M $FeSO_4$ and 0.25 M Na_2CO_3. 87
Figure 5-5: Soluble Fe in 3 m degraded Tarong PZ with the addition of 0.25 M $FeSO_4$ and Na_2CO_3. 88
Figure 5-6: Soluble Fe as a function of CO_2 loading for 9 m MEA and 5 m PZ.....89
Figure 5-7: Soluble Fe as a function of CO_2 loading for degraded PZ. 90
Figure 6-1: Simplified PFD for the SRP pilot plant highlighting location of ER probes ..98
Figure 6-2: Simplified PFD for the NCCC PSTU highlighting location of WL (coupon) probes 100
Figure 6-3: Corrosion of carbon steel (C1010) measured with ER probe in SRP stripper corrosion bypass line. Probe life values are averages for each steady state run. 101

Figure 6-4: Corrosion of stainless steel (316L) measured with ER probe in SRP stripper corrosion bypass line. Probe life values are averages for each steady state run. 101
Figure 6-5: Corrosion of carbon steel (C1010) measured with ER probe in SRP absorber sump. Readings are instantaneous values recorded with handheld ER reader. 102
Figure 6-6: Pilot- vs bench-scale SRP PZ, 150° C, 95% confidence intervals shown. 5 m PZ results are from SRP 2017 pilot plant campaign; 8 m PZ results are from a bench-scale experiment using a SRP 2011 pilot plant campaign sample. 103
Figure 6-7: Coupon removal timeline for SRP 2017 PZ campaign 104
Figure 6-8: 316L and C1010 coupons after removal from SRP stripper. Coupons experienced approximately 340 hours of water testing and 167 hours operating at temperature in PZ solution. Average $\alpha = 0.21$. T = 150 °C. 105
Figure 6-9: (a) SEM micrograph of red product on C1010 coupon after removal from SRP stripper. Identified with powder XRD as FeO(OH). (b) SEM micrograph of black product on C1010 coupon after removal from SRP stripper. Identified with powder XRD as Fe_3O_4. Probe experienced approximately 340 hours of water testing and 167 hours operating at temperature in PZ solution. 106
Figure 6-10: (a) 316L and C1010 coupons after removal from SRP stripper. (b) SEM micrograph of black product on C1010 coupon. Identified with powder XRD as $FeCO_3$. Probe experienced 152 hours operating at temperature in PZ solution. Average $\alpha = 0.21$. T = 150 °C 107

Figure 6-11: (a) 316L and C1010 coupons after removal from SRP absorber. (b) SEM micrograph of black product on C1010 coupon after removal from SRP absorber. Identified by powder XRD as Fe. EDS suggests crystal in SEM micrograph center could be $FeCO_3$. Probe experienced approximately 340 hours of water testing and 320 hours operating at temperature in PZ solution. Average $\alpha = 0.33$. 108
Figure 6-12: Powder X-ray diffraction products observed on C1010 coupons from the SRP PZ campaign. Reference diffraction patterns for Iron, Magnetite, Goethite and Siderite are shown. 109
Figure 6-13: (a) C1010 coupon after removal from NCCC absorber sump. (b) SEM micrograph of red product. Identified by powder XRD as $Fe(OH)_3$. (c) SEM micrograph of steel surface without product formation. Probe experienced 625 hours of operation in 7 m MEA. 111
Figure 6-14: (a) C1010 coupon after removal from NCCC stripper inlet separator (ER6) corrosion coupon. (b) SEM micrograph of steel surface. Product identified as a mixture of Fe_3O_4 and $FeCO_3$. Probe experienced 625 hours of operation in 7 m MEA. 112
Figure 6-15: (a) 316L coupon after removal from NCCC stripper sump. (b) SEM micrograph of white product. Identified by powder XRD as $MnCO_3$. Probe experienced 622 hours of operation in 7 m MEA. 113
Figure 6-16: (a) C1010 coupon after removal from NCCC stripper sump. (b) SEM micrograph of steel surface. EDS suggests the surface is bare Fe. Probe experienced 622 hours of operation in 7 m MEA. 114

Figure 6-17: Powder X-ray diffraction products observed on coupons from the NCCC MEA campaign. Reference diffraction patterns for Iron, Magnetite, Ferric Hydroxide, Rhodochrosite, and Siderite are shown. 115
Figure 7-1: Simplified PFD of NCCC absorber system, showing ER and WL locations. 122
Figure 7-2: Simplified PFD of NCCC regeneration system, showing ER, WL, and ORP locations. 123
Figure 7-3: Carbon steel corrosion rates from coupon weight loss during 2018 PZ campaign, excluding Batch 1 results. Blue points are low velocity locations (eg. Sumps, vessel sample points), and red points are high velocity locations (eg. Inside pipes). Points that are circles have a rich CO_2 loading, and points that are triangles have a lean CO_2 loading.....128
Figure 7-4: Stainless steel (304 and 316L) corrosion rates from coupon weight loss during 2018 PZ campaign. Blue points are low velocity locations (eg. Sumps, vessel sample points), and red points are high velocity locations (eg. Inside pipes). Points that are circles have a rich CO_2 loading, and points that are triangles have a lean CO_2 loading. 129
Figure 7-5: Carbon steel corrosion rates from coupon weight loss during 2018 PZ campaign, excluding Batch 1 results. Velocities represent median velocities at that location over all steady state runs throughout the entire campaign. Velocities are assumed to be zero in vessel sumps and midbed sample points. Points that are circles have a rich CO_2 loading, and points that are triangles have a lean CO_2 loading. 131

Figure 7-6: Stainless steel (304 and 316L) corrosion rates from coupon weight loss during 2018 PZ campaign. Velocities represent median velocities at that location over all steady state runs throughout the entire campaign. Velocities are assumed to be zero in vessel sumps and midbed sample points. Points that are circles have a rich CO_2 loading, and points that are triangles have a lean CO_2 loading. 132
Figure 7-7: Simplified equipment selection diagram, highlighting locations where stainless steel (SS) or carbon steel are appropriate. 134
Figure 7-8: (a) 316L and C1010 coupons from Batch 2 and 3 after removal from absorber middle (WL2). (b) SEM micrograph of 316L coupon. The small imperfections are not pits, but rather are small crystal deposits, which energy-dispersive X-ray spectroscopy suggests are a calcium compound, possibly $CaCO_3$. (c) SEM micrograph of C1010, coupon, showing small amounts of an unidentified corrosion product. 139
Figure 7-9: (a) 316L and C1010 coupons from Batch 4 after removal from absorber middle (ER2). (b) SEM micrograph of 316L coupon, showing largely pristine coupon surface. (c) SEM micrograph of C1010, coupon, showing largely pristine coupon surface.....139
Figure 7-10: (a) C1010 coupon from Batch 1 after removal from absorber sump. (b) SEM micrograph of C1010 coupon, showing black product identified by powder XRD as iron. 141
Figure 7-11: (a) 316L and C1010 coupons from Batch 2 after removal from absorber sump. (b) SEM micrograph of 316L coupon, showing largely pristine coupon surface. (c) SEM micrograph of C1010, coupon, showing largely pristine coupon surface. 142

Figure 7-12: (a) 304 and C1010 coupons from Batch 3 after removal from absorber sump. (b) SEM micrograph of 304 coupon, showing largely pristine coupon surface. (c) SEM micrograph of C1010, coupon, showing largely pristine coupon surface. 142
Figure 7-13: (a) 316L and C1010 coupons from Batch 4 after removal from absorber sump. (b) SEM micrograph of 316L coupon, showing largely pristine coupon surface. (c) SEM micrograph of C1010, coupon, showing largely pristine coupon surface. 143
Figure 7-14: (a) 316L and C1010 coupons from Batch 2 and 3 after removal from absorber top. (b) SEM micrograph of 316L coupon, showing largely pristine surface. (c) SEM micrograph of C1010, coupon, showing product identified by powder XRD as a mix of goethite and magnetite. ...144
Figure 7-15: (a) C1010 coupon from Batch 1 after removal from cold lean stream. (b) SEM micrograph of C1010, coupon, showing product identified by powder XRD as a mix of iron, siderite, and magnetite.....146
Figure 7-16: (a) 316L and C1010 coupons from Batch 2 and 3 after removal from cold lean stream. (b) SEM micrograph of 316L coupon, showing largely pristine surface. (c) SEM micrograph of C1010, coupon, showing a rough, porous layer identified by powder XRD as iron.....146
Figure 7-17: (a) 316L and C1010 coupons from Batch 4 after removal from cold lean stream. (b) SEM micrograph of 316L coupon, showing largely pristine surface. (c) SEM micrograph of C1010, coupon, showing a rough, porous layer identified by powder XRD as iron. Can we add the measured corrosion rate to all of the figures?.....147

Figure 7-18: (a) C1010 coupon from Batch 1 after removal from cold rich bypass. (b) SEM micrograph of C1010, coupon, showing patchy layer identified by powder XRD as a mix of iron, siderite, and magnetite.....149
Figure 7-19: (a) 316L and C1010 coupons from Batch 2 after removal from cold rich bypass. (b) SEM micrograph of 316L coupon, showing largely pristine surface. (c) SEM micrograph of C1010, coupon, showing a rough layer identified by powder XRD as iron. 149
Figure 7-20: (a) 304 and C1010 coupons from Batch 3 after removal from cold rich bypass. (b) SEM micrograph of 304 coupon, showing largely pristine surface. (c) SEM micrograph of C1010, coupon, showing a crystalline layer identified by powder XRD as a mix of iron and siderite. 150
Figure 7-21: (a) 316L and C1010 coupons from Batch 4 after removal from cold rich bypass. (b) SEM micrograph of 316L coupon, showing largely pristine surface. (c) SEM micrograph of C1010, coupon, showing a crystalline layer identified by powder XRD as a mix of siderite and iron. 150
Figure 7-22: (a) C1010 coupon from Batch 1 after removal from warm rich bypass. (b) SEM micrograph of C1010, coupon, showing crystalline layer identified by powder XRD as a mix of siderite and magnetite.....152
Figure 7-23: (a) 316L and C1010 coupons from Batch 2 after removal from warm rich bypass. (b) SEM micrograph of 316L coupon, showing slightly etched surface. (c) SEM micrograph of C1010, coupon, showing a layer identified by powder XRD as goethite.....153

Figure 7-24: (a) 304 and C1010 coupons from Batch 3 after removal from warm rich bypass. (b) SEM micrograph of 304 coupon, showing largely pristine surface. (c) SEM micrograph of C1010, coupon, showing a layer identified by powder XRD as siderite and goethite. 153
Figure 7-25: (a) 316L and C1010 coupons from Batch 4 after removal from warm rich bypass. (b) SEM micrograph of 316L coupon, showing largely pristine surface. (c) SEM micrograph of C1010, coupon, showing a layer identified by powder XRD as siderite. 154
Figure 7-26: (a) C1010 coupon from Batch 1 after removal from hot rich stream. (b) SEM micrograph of C1010, coupon, showing crystalline layer identified by powder XRD as a mix of siderite and magnetite. 156
Figure 7-27: (a) 316L and C1010 coupons from Batch 2 after removal from hot rich stream. (b) SEM micrograph of 316L coupon, showing etched surface. (c) SEM micrograph of C1010, coupon, showing black product identified by powder XRD as a mix of siderite and magnetite. 157
Figure 7-28: (a) 304 and C1010 coupons from Batch 3 after removal from hot rich stream. (b) SEM micrograph of 304 coupon, showing its etched surface. (c) SEM micrograph of C1010 coupon, showing black product identified by powder XRD as siderite and iron. 157
Figure 7-29: (a) 316L and C1010 coupons from Batch 4 after removal from hot rich stream. (b) SEM micrograph of 316L coupon, showing its largely pristine surface. (c) SEM micrograph of C1010 coupon, showing somewhat porous black product identified by powder XRD as siderite and iron. 158

Figure 7-30: (a) C1010 coupon from Batch 1 after removal from hot lean stream. (b) SEM micrograph of C1010, coupon, showing crystalline layer identified by powder XRD as siderite. 160
Figure 7-31: (a) 316L and C1010 coupons from Batch 2 after removal from hot lean stream. (b) SEM micrograph of 316L coupon, showing etched surface. (c) SEM micrograph of C1010 coupon, showing black product identified by powder XRD as siderite. 161
Figure 7-32: (a) 304 and C1010 coupons from Batch 3 after removal from hot lean stream. (b) SEM micrograph of 304 coupon, showing its relatively clean surface. (c) SEM micrograph of C1010 coupon, showing black product identified by XRD as siderite and iron. 161
Figure 7-33: (a) 316L and C1010 coupons from Batch 4 after removal from hot lean stream. (b) SEM micrograph of 316L coupon, showing its relatively clean surface. (c) SEM micrograph of C1010 coupon, showing black product identified by XRD as siderite and magnetite. 162
Figure 7-34: (a) C1010 coupon from Batch 1 after removal from AFS sump. (b) SEM micrograph of C1010, coupon, showing crystalline layer identified by powder XRD as siderite and magnetite. 164
Figure 7-35: (a) 316L and C1010 coupons from Batch 2 after removal from AFS sump. (b) SEM micrograph of 316L coupon, showing yellow product identified by powder XRD as siderite. (c) SEM micrograph of C1010 coupon, showing black product identified by powder XRD as siderite. 165

Figure 7-36: (a) 304 and C1010 coupons from Batch 3 after removal from AFS sump. (b) SEM micrograph of 304 coupon, showing its relatively clean surface. (c) SEM micrograph of C1010 coupon, showing black product identified by XRD as siderite and iron. 165
Figure 7-37:(a) 316L and C1010 coupons from Batch 4 after removal from AFS sump. (b) SEM micrograph of 316L coupon, showing slightly etched surface. (c) SEM micrograph of C1010 coupon, showing black product identified by powder XRD as a mix of iron and siderite. 166
Figure 7-38: Powder X-ray diffraction products observed on C1010 coupons from Batch 1. Reference diffraction patterns for Iron, Magnetite, Goethite and Siderite are shown. 167
Figure 7-39: Powder X-ray diffraction products observed on coupons from Batch 2. All coupons are C1010 except one from WL22. Reference diffraction patterns for Iron, Magnetite, Goethite and Siderite are shown. 168
Figure 7-40: Powder X-ray diffraction products observed on C1010 coupons from Batch 3. Coupons from WL12 and WL4 experienced corrosion during Batch 2 and Batch 3. Reference diffraction patterns for Iron, Magnetite, Goethite and Siderite are shown. 169
Figure 7-41: Powder X-ray diffraction products observed on C1010 coupons from Batch 4. Reference diffraction patterns for Iron, Magnetite, and Siderite are shown. 170
Figure 7-42: Corrosion of carbon steel (C1010) at absorber middle (ER2) ER Probe during Batch 4. 176
Figure 7-43: Corrosion of carbon steel (C1010) at absorber sump (ER3) ER Probe during Batch 3. 177

Figure 7-44: Corrosion of carbon steel (C1010) at absorber sump (ER3) ER Probe during Batch 4. 177
Figure 7-45: Corrosion of carbon steel (C1010) at cold rich bypass (40513) ER Probe during Batch 2. 178
Figure 7-46: Corrosion of carbon steel (C1010) at cold rich bypass (40513) ER Probe during Batch 3. 178
Figure 7-47: Corrosion of stainless steel (316L) at cold rich bypass (40513) ER Probe during Batch 4. 179
Figure 7-48: Corrosion of carbon steel (C1010) at warm rich bypass (40514) ER Probe during Batch 2. 180
Figure 7-49: Corrosion of stainless steel (304) at warm rich bypass (40514) ER Probe during Batch 3. 180
Figure 7-50: Corrosion of carbon steel (C1010) at warm rich bypass (40514) ER Probe during Batch 4. 181
Figure 7-51: Corrosion of stainless steel (316L) at hot rich stream (40519) ER Probe during Batch 3. 182
Figure 7-52: Corrosion of stainless steel (304) at hot rich stream (40519) ER Probe during Batch 4. 182
Figure 7-53: Corrosion of stainless steel (316L) at hot lean stream (40521) ER Probe during Batch 3. 183
Figure 7-54: Corrosion of carbon steel (C1010) at hot lean stream (40521) ER Probe during Batch 4. 184
Figure B-1: ORP measurement in hot lean stream during 2017 SRP PZ campaign. 210
Figure B-2: ORP measurement in cold rich bypass (AT40512) during Batch 2 of 2018 NCCC PZ campaign 211

Figure B-3: ORP measurement in hot lean stream (AT40522) during Batch 2 of 2018 NCCC PZ campaign 212
Figure B-4: ORP measurement in cold rich bypass (AT40512) during Batch 3 of 2018 NCCC PZ campaign 212
Figure B-5: ORP measurement in hot lean stream (AT40522) during Batch 3 of 2018 NCCC PZ campaign 213
Figure B-6: ORP measurement in cold rich bypass (AT40512) during Batch 4 of 2018 NCCC PZ campaign 213
Figure B-7: ORP measurement in hot lean stream (AT40522) during Batch 4 of 2018 NCCC PZ campaign 214

Chapter 1. Introduction

Post combustion carbon capture and storage (PCCC) with amine absorbents is a key technology needed to provide low-cost decarbonized electricity (Boot-Handford et al., 2014; Edenhofer et al., 2014; Pacala et al., 2004; Parson et al., 1998; G. T. Rochelle, 2009) in a timeframe quick enough to avert the worst consequences of rising atmospheric CO_2 concentration (Pachauri et al., 2015).

PCCC amine plants capture CO_2 from power plant flue gas into an aqueous solution, then high temperature is used to reverse the reaction and create a gas stream containing only CO_2. The pure CO_2 gas is compressed and pumped underground for permanent storage. Significant work has been done to improve the energy performance of amine absorbents (Frailie, 2014; Ramezan et al., 2007; G. T. Rochelle, 2009), such that future gains in energy performance will suffer from diminishing returns (Boot-Handford et al., 2014; Lin et al., 2016). Reducing plant capital costs will be a crucial way to reduce the cost of decarbonized electricity going forward. It is likely that the lowest-cost solvent system will be whichever of the current high energy-efficiency solvents has the lowest capital costs.

Most capital cost estimates for PCCC plants assume largely stainless steel construction. Plant capital costs are a strong function of materials choice, with stainless process equipment costing 2-3.5X that of carbon steel (Turton et al., 2008). Although stainless steel is required for first generation solvents (ethanolamine), several second generation solvents such as piperazine appear significantly less corrosive (K. L. S. Campbell et al., 2016; Gunasekaran et al., 2013; Zheng, Landon, Zou, et al., 2014). Improving understanding of corrosion in PCCC amine plants may reveal a solvent system compatible with carbon steel, which would reduce plant capital costs.

Corrosion of steel is well understood in aqueous solutions (Beverskog et al., 1996; Pourbaix, 1974) and in H_2O-CO_2 systems (Nešić & Lee, 2003; Nešić, Nordsveen, et al., 2003; Nordsveen et al., 2003; Tanupabrungsun et al., 2012). However, a lack of thermodynamic data in complex metal-amine-H_2O-CO_2 mixtures prevents accurate corrosion predictions in amine systems. Strong complexation of metal species by amines is one such complicating factor (Ibanez et al., 1987) that is poorly characterized. However corrosion behavior in simpler systems is used to explain phenomena observed in this work. Notably, depassivation of stainless steel can occur at reducing conditions in aqueous systems (Jones, 1996; Raja et al., 2006), and passivation of carbon steel by $FeCO_3$ formation depends on T, fluid velocity, and local Fe^{2+} and CO_3^{2-} activities in H_2O-CO_2 systems (Nešić & Lee, 2003).

Corrosion data is abundant in amine natural gas sweetening systems, which use the same process as PCCC plants except to remove H_2S and CO_2 from high pressure natural gas (DuPart et al., 1993; Kohl et al., 1997). Experience from natural gas sweetening is difficult to apply to PCCC systems because the conditions are substantially different and more corrosive. PCCC systems use higher amine concentrations, absorb O_2, and do not contain H_2S, all of which increase corrosion (DuPart et al., 1993; Xiang, Yan, et al., 2014). Despite these differences, experience with corrosion in natural gas sweetening supplies several common assumptions about corrosion in PCCC systems. For example, stainless performs well at all locations and higher CO_2 concentrations increase corrosion in ethanolamine natural gas sweetening units. Both of these assumptions are shown in this work to be sometimes incorrect in PCCC units because the solvent and process conditions are different.

Bench-scale work indicates that carbon steel is protected by $FeCO_3$ in many second generation amines, including piperazine, which is the reason these solvents are less

corrosive (K. L. S. Campbell et al., 2016; Gunasekaran et al., 2013; Zheng, Landon, Zou, et al., 2014). Bench-scale efforts have focused on the performance of carbon steel in second generation solvents. Notably missing is work on performance of stainless steel, particularly at high temperatures. This is likely because stainless steel is presumed passive at most conditions in amine service due to experience from natural gas sweetening.

Corrosion is seldom measured in amines other than ethanolamine at the pilot scale (Cousins et al., 2013; Flø et al., 2019; Hjelmaas et al., 2017; Khakharia et al., 2015; Kittel et al., 2009; Li et al., 2017). Corrosion measurements at the pilot scale are important to validate bench-scale measurements at fully representative conditions. Bench-scale measurements may not capture small subtleties that may impact corrosion in a real plant, like the role of solvent degradation, O_2 absorption, and flue gas impurities.

Finally, both bench and pilot corrosion data in PCCC systems are typically at or below 120 °C, which is the typical operating temperature for ethanolamine. Piperazine is typically operated at 150-160 °C, and data at that elevated temperature is lacking.

To briefly summarize: there is a need for low-cost PCCC amine plants to combat rising atmospheric CO_2 concentrations. Capital cost reduction in these plants can be achieved through proper materials choice, which requires understanding corrosion in these systems. Predicting corrosion behavior in these systems is difficult because thermodynamic data is incomplete in the H_2O-CO_2-amine system, and because analogous corrosion work in natural gas sweetening is at substantially different conditions. Despite recent interest in corrosion in PCCC systems, several crucial gaps in knowledge include: incomplete understanding of the relationship between amine structure and corrosivity, the lack of high T measurements, limited investigation of stainless behavior in second generation amines, and limited pilot work in second-generation amines. The practical goal of this dissertation is to contribute to closing these knowledge gaps, reduce uncertainty

about materials choices in piperazine systems, and thereby reduce capital costs in future PCCC plants. This goal is accomplished through four specific objectives:

1. Quantify the corrosion performance of stainless and carbon steel in several primary and secondary amine solutions to understand the effect of temperature, CO_2 loading, amine structure and amine degradation on corrosion.
2. Measure Fe^{2+} solubility in amine solutions to improve understanding of formation of protective $FeCO_3$ films as a function of amine type, CO_2 loading, amine structure and amine degradation.
3. Quantify the corrosion performance of stainless and carbon steel in piperazine and ethanolamine in PCCC pilot plants. Characterize corrosion products to understand the effect of temperature, loading, and fluid velocity on protective $FeCO_3$ films.
4. Identify any process conditions in piperazine that cause acute corrosion failure of an alloy and develop a strategy to mitigate corrosion. Make recommendations about what materials of construction are appropriate for each unit operation in a PCCC plant.

Chapter 2. Background

The context, need, and goals for the study of corrosion in amine solvents for CO_2 capture are discussed in this Chapter. Section 2.1 presents a brief argument for the use of CO_2 capture to stop rising atmospheric CO_2 concentration. Next, Section 2.2 introduces the amine scrubbing process and briefly highlights active areas of development. Section 2.3 discusses corrosion research relevant to amine scrubbing.

2.1. ARGUMENT FOR THE IMPLEMENTATION OF CARBON CAPTURE AND STORAGE

2.1.1. Atmospheric carbon dioxide and temperature

The concentration of CO_2 in the atmosphere has been rising steadily since 1750 AD, and current CO_2 levels are at the highest they've been in at least 800,000 years. Precise, direct measurement of atmospheric CO_2 began in 1958, when the annual average CO_2 concentration was 316.1 ppm. CO_2 concentration has steadily increased to 406.6 ppm since then (Keeling, 2017). Measurement of air trapped in Antarctic ice cores shows that pre-industrial (1750 AD) CO_2 concentration was approximately 277 ppm (Etheridge et al., 1996), and that over the last 800,000 years CO_2 has varied between 172-300 ppm (Lüthi et al., 2008). That CO_2 had exceeded these long-held bounds is somewhat concerning.

Atmospheric CO_2 concentration is very strongly related to the average global temperature. Average global temperature in the past can be estimated by measuring the ratio of ^{18}O to ^{16}O in Antarctic ice cores, then converting that ratio to precipitation rates and temperatures (Petit et al., 1999). These cores show that there is a strong positive correlation between past CO_2 concentration and temperature going back at least 800,000 years. Temperature variations caused by astronomical cycles increased CO_2 concentration, and higher CO_2 concentration further increased temperature in periodic cycles that only abated when radiative forcing significantly decreased. This periodic temperature

fluctuation is caused by astronomical cycles that affect incident solar radiation (Imbrie et al., 1992). The correlated CO_2 level oscillations were the product of temperature-dependent changes in precipitation and weathering of CO_2 containing minerals (Kump et al., 2000) and in oceanic capture of CO_2 (Wang et al., 2004). Since CO_2 absorbs infrared radiation (Tyndall, 1859), increasing atmospheric concentration of CO_2 exacerbates rising temperature (Arrhenius, 1896). The relationship between increasing CO_2 concentration and increasing global temperature is exceptionally strong, which has ominous implications for future temperature.

2.1.2. Impacts of rising global temperature

If atmospheric CO_2 concentration continues to increase, average global temperature will rise, which has serious negative consequences. If CO_2 concentration continues to increase at current rates, average global temperature is likely to be 2° C higher in 2100 AD than they were in 1850-1900 AD. Such a temperature increase would likely be accompanied by a decrease in oceanic pH by 0.2 to 0.32 points, changes in global precipitation, a decrease in Arctic and Antarctic ice volume, and a rise of sea levels by 0.45 to 0.82 m (Pachauri et al., 2015). A few of the likely consequences of these changes are (Field et al., 2014):

- Increased local and global extinction risk for terrestrial and freshwater species, which are unable to adjust their range quickly and relocate to suitable climates.
- Loss of marine-biodiversity and disruption of marine ecosystems, particularly reef-building corals, which are vulnerable to ocean acidification.
- Disruption of major crops (wheat, rice, maize) production in vulnerable regions and reduction of food security.
- Increased displacement of people from vulnerable regions.

- Reduction of renewable surface freshwater and groundwater resources and an increase in the frequency of drought in vulnerable regions.

These consequences are significant and broadly negative, so strategies to stop the increase of atmospheric CO_2 should be investigated.

2.1.3. Sources of atmospheric carbon dioxide

Understanding why atmospheric CO_2 is increasing is the first step to halting its increase. Rising atmospheric CO_2 levels are caused by CO_2 generated from fossil fuel combustion (Le Quéré et al., 2018; Pachauri et al., 2015). Emissions of CO_2 from fossil fuels by country are shown in Figure 2-1. China, the United States, and India are the countries with the highest CO_2 emissions in the world (Janssens-Maenhout et al., 2017). However, CO_2 emissions from the rest of the world are also significant, roughly equaling the emissions from the top three emitters. Slowing the increase of atmospheric CO_2 levels can be accomplished by a worldwide reduction in fossil fuel CO_2 emissions.

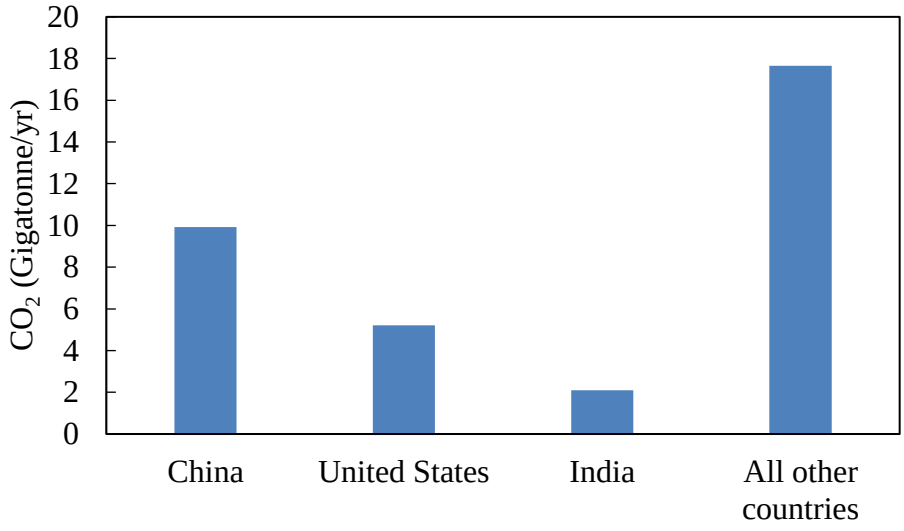

Figure 2-1: CO_2 emissions from fossil fuels by country in 2012 (Janssens-Maenhout et al., 2017)

In the United States, the largest sources of CO_2 emissions are electric power generation and transportation, and the magnitude of these emissions is shown in Figure 2-2 (EPA, 2018). Reducing CO_2 emissions from transportation can be achieved through reduction of CO_2 intensity of fuels (I.e. switching from oil-based to biofuels, electric, or hydrogen), but there has been lack of progress to date in slowing transport emissions in OECD countries (Edenhofer et al., 2014). Reducing emissions from electric power generation is particularly attractive because: these emissions come from relatively few, concentrated point-sources, and several viable technologies exist that allow decarbonization of electric power generation.

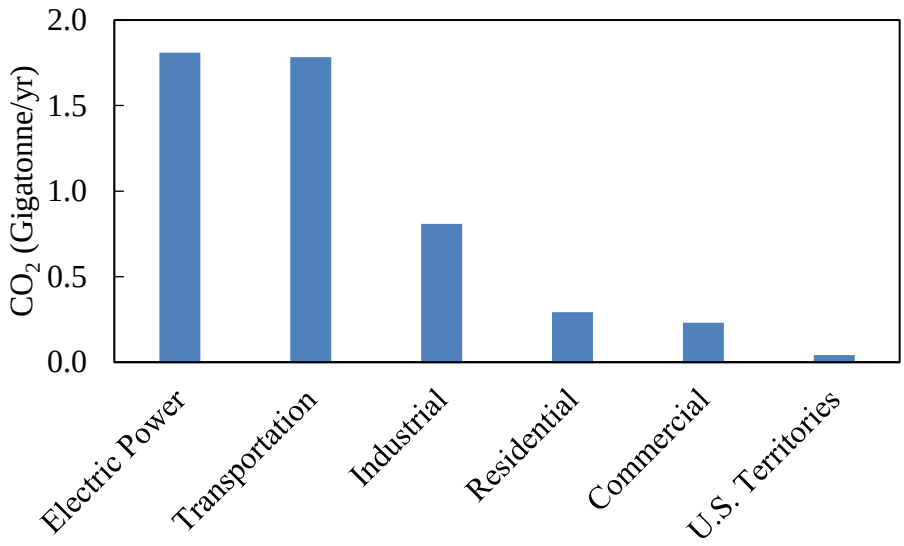

Figure 2-2: CO_2 emissions from fossil fuels by sector in the United States in 2016 (EPA, 2018).

2.1.4. Mitigating carbon dioxide emissions from electricity generation

Viable decarbonized electric power generation technologies include renewable energy sources (photovoltaics, wind, hydro), nuclear power, and carbon capture and

storage (CCS) (Edenhofer et al., 2014). Each of these technologies should be considered for implementation, although this work focuses on carbon capture and storage.

A renewable-only strategy is unlikely to be a cost effective strategy to mitigate CO_2 emissions because the intermittency problems of renewable energy have not yet been solved. Recent price reductions in renewable energy sources have led to quick growth, such that half of all new installed capacity in 2012 was renewable, bringing renewables share of global electricity generation to 21 % (Edenhofer et al., 2014). There is significant debate over whether electricity generation can be accomplished with a renewables-only strategy (Clack et al., 2017; Jacobson et al., 2015, 2017), but most researchers estimate that the most cost-effective strategy of decarbonization involves a mixture of renewables and other technologies, such as: energy efficiency, fuel switching, nuclear, and carbon capture and storage (Edenhofer et al., 2014; MacDonald et al., 2016; Pacala et al., 2004). Briefly, this is because at high penetration rates, the intermittency of renewables means that larger amounts of reserve renewable capacity are required and the efficiency of traditional power generation is negatively impacted due to increased cycling (Brouwer et al., 2014; Heuberger et al., 2017).

Nuclear energy is CO_2-free and clearly scalable; for example nuclear energy provided 20% of electricity in the USA and 72% in France in 2017 (IAEA, 2018). Unfortunately, expansion of nuclear power is blocked by political issues, including concern about operational risks and safety, unresolved waste management issues, concern about nuclear weapon proliferation, and adverse public opinion. The effect of these political issues is heightened regulation which increases plant costs and construction times (Lovering et al., 2016). Partially as a result of these issues, the nuclear share of worldwide electricity generation has declined from a high of 17 % in 1993 to 11 % in 2012 (Edenhofer et al., 2014). This decrease is because retirement of nuclear facilities exceeds their

replacement rate in the USA and because Japan and Germany have retired nuclear facilities in the wake of the Fukushima Daiichi nuclear accident (IAEA, 2018). Without resolution of its political issues, nuclear energy will likely struggle to achieve widespread deployment.

2.1.5. Mitigating carbon dioxide emissions with carbon capture and storage

CCS is the capture of CO_2 generated from combustion or industry and the sequestering of it away from the atmosphere indefinitely. Capture involves separating and concentrating the CO_2 from a dilute stream into a pure CO_2 stream, which is a technique widely employed in natural gas purification (Kohl et al., 1997). The CO_2 is then compressed and then transported by pipeline to a storage location. CO_2 can be permanently sequestered in underground deep saline formations, injected into unminable coal beds, or injected into oil fields for enhanced oil recovery (Metz et al., 2005). Sufficient storage sites exist in the US to allow storage of all CO_2 generated for the next 100 years (Szulczewski et al., 2012). Among the options for mitigation, CCS is particularly attractive because:

- It lacks the intermittency problems of renewables and the political problems of nuclear energy.
- A mix of CCS and other technologies (renewables, nuclear) is expected to minimize the cost of decarbonized electricity (Boot-Handford et al., 2014; Parson et al., 1998). This is partially because CCS plants can be operated flexibly to complement intermittent renewables (Bui et al., 2014; Wiley et al., 2011).
- CCS is a mature technology, in use at commercial-scale (Bui et al., 2018; M. Campbell, 2014; DOE, 2017; Singh et al., 2014), so it can be deployed quickly enough to achieve ambitious CO_2 emission reduction targets (Metz et al., 2005; Pacala et al., 2004; G. T. Rochelle, 2009).

- There are no obvious alternatives to CCS for decarbonizing the industrial sector (ie, steel cement, oil refining) (Bui et al., 2018).

There are risks associated with carbon capture and storage too, including: (Edenhofer et al., 2014)

- Potential lifecycle toxicity of some capture solvents.
- Safety and long-term integrity of CO_2 storage sites.
- Risks of transporting CO_2 by pipeline.

Nevertheless, the advantages of CCS suggest it should be considered for implementation. The remainder of this report focuses specifically on post-combustion carbon capture (PCCC). Although they are not considered here, two other forms of CCS are currently in development: coal gasification (pre-combustion capture) and oxy-fuel combustion. However, coal-gasification is expected to be more expensive than PCCC and oxy-fuel combustion is still in the early stages of development (Rubin et al., 2015).

2.2. POST-COMBUSTION CARBON CAPTURE WITH CHEMICAL ABSORPTION

2.2.1. Description of a typical amine absorption process

Currently, the most cost-effective PCCC systems use a chemical solvent, typically an aqueous amine solution, to capture CO_2 (Metz et al., 2005). Amines act as a base and react with CO_2, capturing the gas into the aqueous solution. Equation 2-1 summarizes this reaction, in which two moles of a secondary amine are consumed for each mole of CO_2 absorbed (Kohl et al., 1997; Shrier et al., 1969).

$$2\ R_1R_2NH\ (aq) + CO_2\ (g) \leftrightarrow\ R_1R_2NCO_2^-(aq) + R_1R_2NH_2^+(aq) \qquad (2\text{-}1)$$

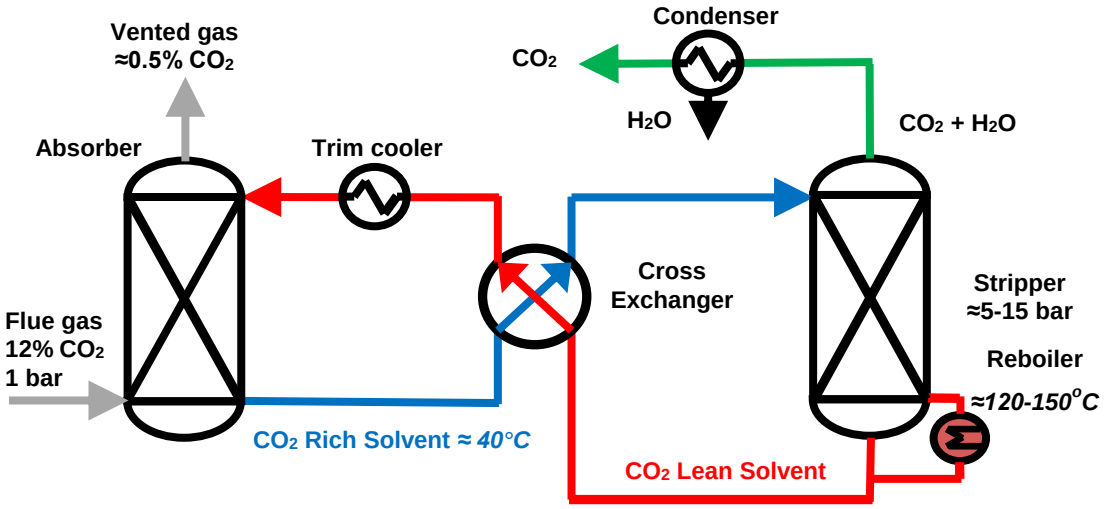

Figure 2-3: Simplified amine scrubbing flow sheet

Figure 2-3 shows a simplified PCCC plant flowsheet. Lean amine (low in CO_2 content) contacts flue gas in an absorber column, absorbing the CO_2 into solution. The scrubbed flue gas is then sent through a water wash and finally vented to the atmosphere. The amine solution, now rich in CO_2, is pumped through a cross exchanger and then to a stripper column with a steam-heated reboiler, where high temperature reverses the reaction and forces the CO_2 out of solution, creating a gas stream containing only CO_2 and H_2O. The gas stream goes through a condenser to remove H_2O, and then the pure CO_2 gas is compressed to 150 bar and pumped underground for permanent storage. The lean amine is then pumped through the cross exchanger and back to the absorber to repeat the cycle.

2.2.2. Developments in PCCC with chemical absorption

Amine absorbents were first used to capture acid gases almost 90 years ago (Bottoms, 1930), but they were only considered for flue gas capture more recently (Booras et al., 1991). Several review articles (Boot-Handford et al., 2014; Bui et al., 2018;

MacDowell et al., 2010) and a book (Kohl et al., 1997) cover the development history and challenges comprehensively. A few key developments will be highlighted here.

The main obstacle to widespread deployment of PCCC is cost. Both the plant capital cost and the cost of steam used in the stripper reboiler are significant. Early designs with MEA estimated the total cost of capture and compression to be 57-85 \$/MT CO_2 (Ramezan et al., 2007; G. T. Rochelle, 2009). Improved designs with new solvents estimate total cost to be 35.5 \$/MT CO_2 (Frailie, 2014).

Careful solvent selection and process optimization has improved the energy performance of amine plants. MEA has an expected energy performance of 3.6-4.0 GJ/MT CO_2 (Cousins et al., 2012), and PZ performance is as low as 2.1-2.5 GJ/MT CO_2 (E. Chen et al., 2017). Future advances in energy performance will not be dramatic because the overall process is already at about 53% thermodynamic efficiency (Lin et al., 2016).

Significant work has been done in solvent selection because the thermodynamic and kinetic properties of the solvent ultimately determine the process performance. Frequently, alkanolamines are used, as the hydroxyl group is necessary to increase water solubility and lower vapor pressure compared to organic amines. Amine scrubbing solvents can be broadly classified into three groups:

- Primary and secondary amines, such as monoethanolamine (MEA) and piperazine (PZ), shown in Figure 2-4. These amines are typically the most alkaline and thus have the highest absorption rates which proceed via the carbamate reaction shown in Equation 2-1(MacDowell et al., 2010).

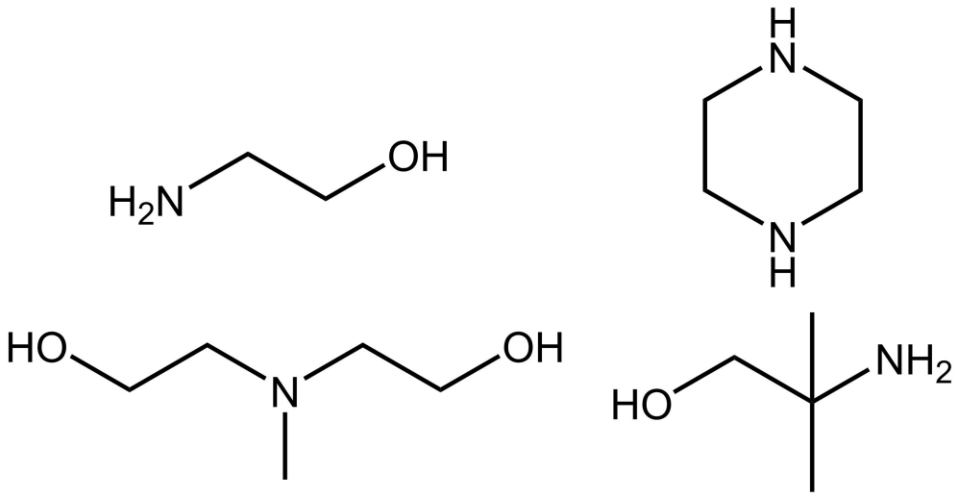

Figure 2-4: Top left: Monoethanolamine (MEA), top right: piperazine (PZ), bottom left: methyldiethanolamine (MDEA), bottom right: aminomethyl propanol (AMP)

- Tertiary amines, such as methyldiethanolamine (MDEA), typically have higher CO_2 capacity due to their reaction with CO_2, shown in Equation 2-2, which only consumes one mol of amine per mol of CO_2. Tertiary amines also have a lower rate of absorption. MDEA is important industrially because it is selective for H_2S in the presence of CO_2 (Kohl et al., 1997).

$$R_1R_2R_3N\ (aq) + CO_2\ (g) + H_2O\ (l) \leftrightarrow HCO_3^-\ (aq) + R_1R_2R_3NH^+(aq) \qquad (2\text{-}2)$$

- Sterically-hindered amines, such as aminomethyl propanol (AMP), form an unstable carbamate that rapidly converts to bicarbonate by the reaction shown in Equation 2-3. As a result, hindered amines have somewhat elevated rates associated with carbamate formation but also somewhat higher capacity associated with bicarbonate formation (Sartori et al., 1983).

$$R_1R_2NCO_2^-\ (aq) + H_2O\ (l) \leftrightarrow HCO_3^-\ (aq) + R_1R_2NH(aq) \qquad (2\text{-}3)$$

In general, amines used for PCCC must have high absorption rates to compensate for the low partial pressure of CO_2 in flue gas compared to natural gas streams, so primary and secondary amines are typically used.

Significant work has been conducted to ensure there are no negative environmental impacts associated with PCCC. Solvent degradation has been studied to reduce amine makeup cost and also to understand potentially toxic and carcinogenic degradation products. Thermal and oxidative degradation rates and products appear manageable (Namjoshi, 2015; Paul Thomas Nielsen, 2018). Nitrosamines form when NO_2 reacts with amines, but it can be controlled with pretreatment of gas or high temperature in the stripper (Fine, 2015). Amine aerosols sometimes form in the absorber, but these can be removed with a demister or gas pretreatment or passively controlled with careful process design (Beaudry, 2017; Zhang, 2018).

2.3. CORROSION IN PCCC WITH CHEMICAL ABSORPTION

2.3.1. Motivation

Future improvements in PCCC energy performance will suffer from diminishing returns because current solvents and plant designs have high thermodynamic efficiency and likely cannot improve dramatically (Lin et al., 2016). Future cost reductions will have to come from capital expenses, which contribute about half of the total cost of an amine plant (Capital Cost: 16 \$/MT CO_2; Energy cost: 19 \$/MT CO_2 (Frailie, 2014)). If PCCC plants are operated at low load factors to complement renewable generation (Bui et al., 2014; Wiley et al., 2011), capital costs will become even more significant (compared to energy costs, which decrease at lower load factors). It is likely that the lowest-cost solvent system will be whichever of the current high energy-efficiency solvents has the lowest capital costs.

Most capital cost estimates for PCCC plants assume largely stainless steel construction. Plant capital costs are a strong function of materials choice, with stainless process equipment costing 2-3.5X that of carbon steel (Turton et al., 2008). Although stainless steel is required for MEA, several second generation solvents such as PZ appear significantly less corrosive than MEA (Gunasekaran et al., 2013). Thorough investigations into carbon steel compatibility are needed for second generation PCCC solvents because a solvent that is largely compatible with carbon steel will have significantly lower capital costs.

In addition, the current use of stainless steel process equipment in PCCC is based on general good corrosion performance of this material in MEA in natural gas sweetening plants. Performance of stainless steel in second generation solvents could be substantially different than in MEA. Stainless steel needs to be thoroughly evaluated to ensure this material performs well and is safe at all conditions in second generation solvents.

Although there is past experience with corrosion in amine plants, prior work is difficult to adapt because critical corrosion parameters are different in PCCC plants. For example, natural gas sweetening typically has H_2S present, which can inhibit corrosion, and it lacks O_2, which exacerbates corrosion. This means there is significant uncertainty about whether prior corrosion results in acid-gas treating plants can be generalized to PCCC plants.

The potential benefit to capital costs and the lack of data about corrosion performance of second generation solvents at PCCC conditions motivated this work.

2.3.2. Corrosion thermodynamics

Corrosion is fundamentally a charge transfer reaction between a metal surface and its surroundings. In the case of carbon steel, iron is oxidized (Equation 2-4). Ferrous can be further oxidized to ferric, but this requires quite oxidizing conditions (Equation 2-5).

$$Fe \leftrightarrow Fe^{2+} + 2e^{-} \quad (2\text{-}4)$$

$$Fe^{2+} \leftrightarrow Fe^{3+} + e^{-} \quad (2\text{-}5)$$

This oxidation is always accompanied by a reduction. In oxygen containing, high pH aqueous solutions, the reduction is typically Equation 2-6. In anoxic, high pH aqueous solutions, this reduction is typically Equation 2-7 (Jones, 1996).

$$O_2 + 2H_2O + 4e^{-} \leftrightarrow 4\,OH^{-} \quad (2\text{-}6)$$

$$2H_2O + 2e^{-} \leftrightarrow H_2 + 2OH^{-} \quad (2\text{-}7)$$

Other electrochemical reductions may be relevant. Equation 2-8 is likely an important reduction in PCCC solutions (Veawab et al., 2002).

$$2HCO_3^{-} + 2e^{-} \leftrightarrow 2CO_3^{2-} + H_2 \quad (2\text{-}8)$$

Reduction of bicarbonate to formate is possible (Equation 2-9), but it seems unlikely and is usually only seen at very reducing electrode potentials or on catalysts (L. Chen et al., 2017; Sreekanth et al., 2014).

$$HCO_3^{-} + H_2O + 2e^{-} \leftrightarrow HCO_2^{-} + 2OH^{-} \quad (2\text{-}9)$$

Amines undergo oxidative degradation in PCCC systems. Although there are a variety of degradation pathways for MEA, ammonia and formaldehyde are important

products (Sexton, 2008). This is a multi-step reaction, but an overall representation of the amine oxidation is given in Equation 2-10.

$$NH_2CH_2CH_2OH + 2OH^- \leftrightarrow NH_3 + 2CH_2O + 2H_2O + 2e^- \quad (2\text{-}10)$$

Thermodynamics allows prediction of which oxidation and reduction reactions are favorable at different conditions. For example, the standard Gibbs free energy of formation ($\Delta_f G^0$) for different species can be combined to predict the ΔG^0_{rxn} for each of the corrosion reactions in the system. A negative ΔG^0_{rxn} indicates the reaction is spontaneous. The $\Delta_f G^0$ values for several relevant species in these corrosion reactions are listed in Table 2-1.

Table 2-1: Standard Gibbs free energy of formation at 25°C for relevant species

Species	Phase	$\Delta_f G^0$ (kJ/mol)	Citation
Fe	solid	0	(Beverskog et al., 1996)
Fe^{2+}	aqueous	-92	Ibid.
Fe^{3+}	aqueous	-18	Ibid.
$FeCO_3$	solid	-680	Ibid.
$Fe(OH)_3$	solid	-705	Ibid.
OH^-	aqueous	-157	(Tanupabrungsun et al., 2012)
H_2O	liquid	-237	Ibid.
Na^+	aqueous	-261	(Jones, 1996)
$NaCHO_2$	solid	-582	(DIPPR, 2019)
$NaHCO_3$	solid	-854	Ibid.
Na_2CO_3	solid	-1049	Ibid.
MEA	liquid	-126	Ibid.
NH_3	gas	-16	Ibid.
CH_2O	gas	-103	Ibid.

The ΔG^0_{rxn} for each of the oxidation and reduction half-cells presented in this section is given in Table 2-2. It is important to note that all of these reactions are at standard state (ie, P= 1 bar, liquids and solids in pure state, gases are ideal, aqueous species have

activity = 1) and at 25 °C. One of the drawbacks of this is that several of the reactions (ie. Equations 2-10, 2-6, 2-7, 2-9) are at pH = 14. This definition also implicitly relates half-cell spontaneity to the standard hydrogen electrode, which has a ΔG^0_{rxn} of zero. Despite these non-realistic conditions, these half-cell equations allow an approximate, first-pass prediction of reaction spontaneity. For example, combining the oxidation of iron and the reduction of oxygen is strongly spontaneous. Ignoring the very favorable reduction of oxygen, all of the reductions as written are not strongly favored. The reduction of NH_3 to MEA is spontaneous when paired with the oxidation of iron, but this again shows the limitation of comparing half-cell reactions, since this reaction is extremely unlikely to reverse in a real system due to its multi-step nature and the miniscule concentrations of ammonia and formaldehyde. The closest is the reduction of bicarbonate to carbonate, which still is not spontaneous when paired with the ferrous oxidation. If ferric is present, its reduction to ferrous is strongly favored, and it is able to oxidize iron (to ferrous) as well as bicarbonate (to carbonate).

Table 2-2: Standard Gibbs free energy of reaction and Standard reaction potential (for the reaction as written) at 25°C

Reaction Number	Reaction	ΔG^0_{rxn} (kJ/mol)	E^0_{rxn} (V vs SHE)
2-4	$Fe \leftrightarrow Fe^{2+} + 2e^-$	-92	0.476
2-5	$Fe^{2+} \leftrightarrow Fe^{3+} + e^-$	74	-0.770
2-10	$MEA + 2OH^- \leftrightarrow NH_3 + 2CH_2O + 2H_2O + 2e^-$	-18	0.093
2-6	$O_2 + 2H_2O + 4e^- \leftrightarrow 4\ OH^-$	-155	0.401
2-7	$2H_2O + 2e^- \leftrightarrow H_2 + 2OH^-$	160	-0.828
2-8	$HCO_3^- + e^- \leftrightarrow CO_3^{2-} + (1/2)H_2$	66	-0.686
2-9	$HCO_3^- + H_2O + 2e^- \leftrightarrow HCO_2^- + 2OH^-$	194	-1.005

Adjusting these ΔG_{rxn} values to make corrosion predictions at non-standard conditions is often performed. ΔG_{rxn} is a function of reactant and product activities. For

example, at pH = 7, the reduction of oxygen (Equation 1-6) becomes even more favorable (ΔG_{rxn}= -316 kJ/mol) and becomes able to oxidize the ferrous half-cell to ferric (Jones, 1996). The general form of the relationship between ΔG^0 and solution composition is given by Equation 2-11, where K is the equilibrium constant for the reaction, R is the universal gas constant, and T is temperature (Smith et al., 2005). Knowledge of solution activities at equilibrium (and thus K) allows the calculation of ΔG at non-standard conditions. In charge transfer reactions, it is often convenient to express ΔG as a solution potential, which more accurately represents the free energy change per unit charge transferred. Solution potential, E, is given in 2-12, where n is the number of electrons exchanged and F is Faraday's constant. These equations can be combined into the Nernst equation, given in Equation 2-13, where Q is the reaction quotient.

$$-\frac{\Delta G^0}{RT} = \ln(K) \tag{2-11}$$

$$\mathrm{E} = \Delta\mathrm{G}/(-\mathrm{nF}) \tag{2-12}$$

$$E = E^0 - \frac{RT}{\mathrm{n}F}\ln(Q) \tag{2-13}$$

ΔG_{rxn} is also a function of temperature. The relationship is given by Equation 2-14, where ΔH^0 is the standard enthalpy of reaction.

$$\frac{d\ln(K)}{d(T)} = \frac{\Delta H^0}{RT^2} \tag{2-14}$$

Knowing the thermodynamically favorable redox couple important for making corrosion predictions, but several additional non-charge transfer reactions are also important. Particularly insoluble corrosion products sometimes form and can act as a barrier that prevents further corrosion. Two such products are shown for iron in Equations

2-15 and 2-16. Typically, careful measurement of equilibrium solubilities for these species is used to determine a ΔG^0, which can be used with Equations 2-11 and 2-14 to determine if formation of these species is favorable at different solution compositions and temperature.

$$Fe^{2+} + CO_3^{2-} \leftrightarrow FeCO_3 \quad (2\text{-}15)$$

$$Fe^{3+} + 3OH^- \leftrightarrow Fe(OH)_3 \quad (2\text{-}16)$$

Knowing the effect of solution composition and T on ΔG_{rxn} for both redox and precipitation reactions allows the general prediction of corrosion. This is often plotted as a Pourbaix diagram. A Pourbaix diagram for an Fe-CO_2-H_2O system is shown in Figure 2-5. This technique shows what phase is thermodynamically stable as a function of pH and solution potential. These plots only represent the metal half-cell equations, and this can make interpreting the solution potential somewhat confusing. On the plot below, at pH=0, the oxidation of iron to ferrous is favorable as long as the reduction occurring in solution has an E_{rxn} greater than -0.625 volts. At more reducing conditions (lower E), iron will not be oxidized. The solution pH is plotted as the x-axis because many of the charge transfer reactions as well as the precipitation reactions are functions of pH. Note that this plot predicts regions of $FeCO_3$ and Fe_3O_4 stability at high pH and somewhat reducing conditions. Depending on the quality of the corrosion product layer, iron may be protected in these regions. Pourbaix diagrams have been made for Fe-H_2O (Beverskog et al., 1996), Fe-H_2O-CO_2 (Tanupabrungsun et al., 2012), and Fe-H_2O-MEA-CO_2 (Soosaiprakasam et al., 2008).

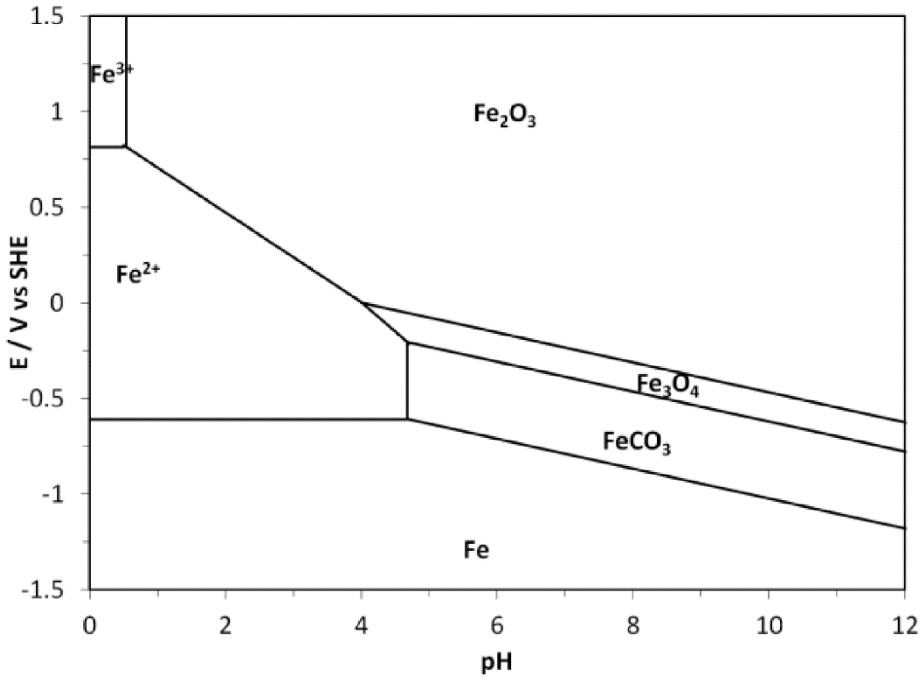

Figure 2-5: Pourbaix diagram for Fe-CO_2-H_2O system, T=120°C, C_{Fe2+}=10ppm, C_{Fe3+}=10ppm, P_{H2}=1 bar, P_{O2}=1 bar, Pc_{O2}=2.27 bar (Tanupabrungsun et al., 2012).

If amine solutions interact strongly in any of the charge transfer or precipitation reactions listed here, then ΔG_{rxn} values can be expected to change. For example, complexation of Fe^{3+} by triethanolamine or EDTA changes the E_{rxn} of the ferric to ferrous reduction dramatically (Ibanez et al., 1987). These interactions are probably significant in the concentrated, highly polar amine solutions, and this is one of the key limitations in thermodynamic predictions in these systems. Until ΔG_{rxn} values are adjusted for these amine-iron species interactions, thermodynamic predictions will need to be verified with experimental measurements of corrosion

While a layer of $FeCO_3$ or Fe_3O_4 may be favored in amine solutions, thermodynamics does not predict the quality of that layer. Experimental measurements of the protective qualities of these layers are needed.

Similar thermodynamic predictions can be made for stainless steel. The important reactions in stainless steel are the oxidation of nickel (Equation 2-17), the formation of its protective hydroxide product (Equation 2-18), the oxidation of chromium (Equation 2-19) and the formation of its protective oxide product (Equation2-20).

$$Ni \leftrightarrow Ni^{2+} + 2e^{-} \quad (2\text{-}17)$$

$$Ni^{2+} + 2OH^{-} \leftrightarrow Ni(OH)_2 \quad (2\text{-}18)$$

$$Cr \leftrightarrow Cr^{3+} + 3e^{-} \quad (2\text{-}19)$$

$$2Cr^{3+} + 6OH^{-} \leftrightarrow Cr_2O_3 + 3H_2O \quad (2\text{-}20)$$

Pourbaix diagrams for Nickel and Chromium are shown in Figure 2-6. These diagrams predict broad passivity due to $Ni(OH)_2$ and Cr_2O_3 protective layers at high pH regions relevant to amine scrubbing. However, sufficiently oxidizing conditions do convert these layers to non-protective species.

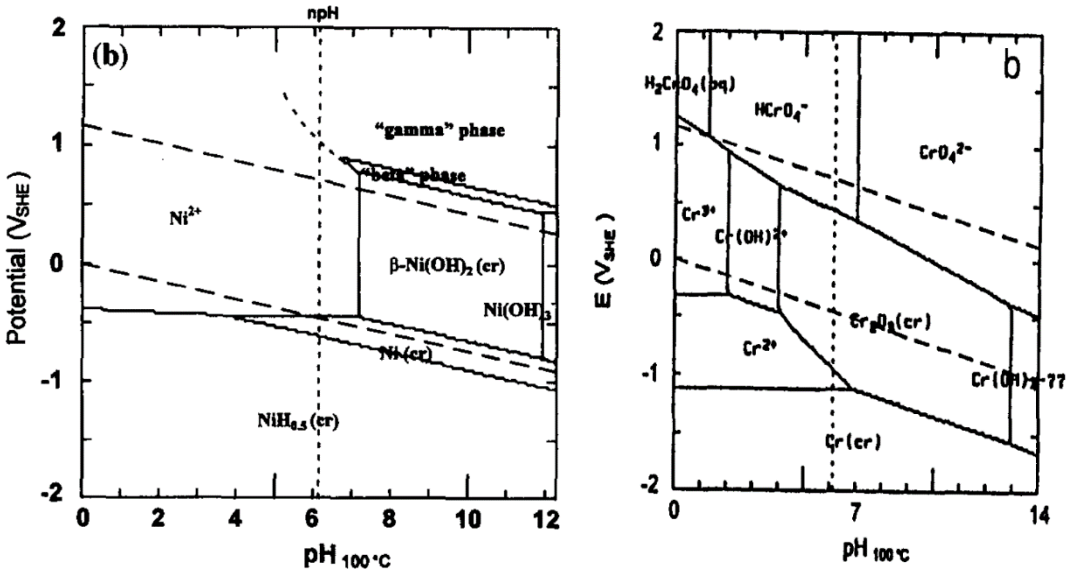

Figure 2-6: (left) Pourbaix diagram for Nickel-water at 100°C and $[Ni(aq)]_{total}=10^{-6}$ molal and (right) Pourbaix diagram for Chromium-water at 100°C and $[Cr(aq)]_{total}=10^{-6}$ molal (Beverskog et al., 1997a, 1997b).

2.3.3. Passive film formation

Although passive films are thermodynamically predicted at the high pH, reducing conditions expected in amine scrubbing, the rate of passive film formation controls whether that film is protective. This can lead to counterintuitive corrosion behavior at reducing conditions. For example, formation of $FeCO_3$ depends on the activity of CO_3^{2-}. Likewise, formation of Cr_2O_3 requires OH^-. At reducing conditions, the rate of formation of these product layers is unable to keep up with the rate of oxidation of the metal. This is because as oxidizer concentration decreases (ie, the solution potential is lower) the total rate of the reduction reactions in solution becomes smaller. Although the metal surface is still oxidizing, the lower rate of the reduction reactions in solution reduces the production of CO_3^{2-} and OH^-. This is known as the metals active state, where passive product formation

is thermodynamically favorable, but its formation is slower than the oxidation of the metal (Jones, 1996; Raja et al., 2006).

The passivation of metals requires slightly more oxidizing conditions than indicated by their Pourbaix diagrams to avoid this active state. This active to passive transition can be studied electrochemically through the use of potentiodynamic polarization. This technique applies a controlled voltage to a solution, then measures the resulting current through the electrode. High currents correspond to a high rate of oxidation of the steel and thus corrosion. Although solution potential is applied artificially, it can be understood as corresponding to the potential of the reduction half-cell of a corrosion reaction. Lower solution potentials represent a more reducing solution, and higher potentials represent a more oxidizing solution. Two such experiments are shown for carbon steel and stainless steel in 5 M MEA in Figure 2-7 (Y. Sun et al., 2011). At very low potentials (below 900 mV), the solution is so reducing that the metal is inert, and cannot be oxidized. Large currents below that potential reflect the reduction of water to hydrogen, not the oxidation of the metal. As potential increases, first current increases in the active region, then decreases in the passive region. In the passive region, formation of protective products is rapid enough to limit oxidation of the metal. At very oxidizing conditions, the formation of protective products is no longer rapid enough to keep up with the very quick oxidation of the metal, and corrosion resumes. Note that in MEA at these conditions, stainless steel has a very small active window. Presumably, the favorable oxidation of MEA has a high rate, which increases the rate of redox reactions in solution, leading to higher production of CO_3^{2-} and OH^-, even at reducing conditions. Also note that increasing T increases the current (and thus corrosion rate) in both the active and the passive region. One of the implications of this analysis is that a metal in the active state can experience a decrease in corrosion rate from a decrease in solution potential (ie, reduction and oxidation reactions

at the metal surface slow down) and an increase in solution potential which pushes the metal into the passive state (ie, oxidation reactions at the metal and in the solution become more rapid, the reduction rates in solution increase, and the increase in reduction product concentration causes precipitation of insoluble products).

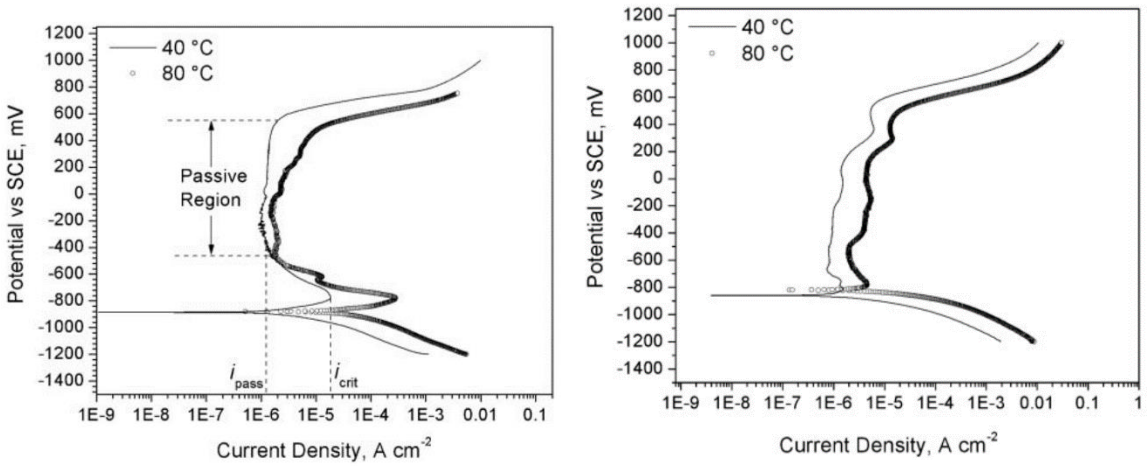

Figure 2-7: (left) Potentiodynamic curve of carbon steel (A106) in 5 M MEA, no O_2, α =0.2. (right) Potentiodynamic curve of stainless steel (304) in 5 M MEA, no O_2, α =0.2 (Y. Sun et al., 2011).

2.3.4. Corrosion experience in natural gas sweetening

A large amount of experience with corrosion in amine solutions has been gathered in natural gas sweetening plants. Typical recommendations for materials of choice for a natural gas sweetening plant are shown in Figure 2-8 (Kohl et al., 1997). Carbon steel is used in many locations, including the absorber and stripper columns. Stainless steel is recommended anywhere not wetted with amine, as the water-CO_2 environment is significantly different than the amine-water-CO_2 environment. In addition, stainless steel is recommended in the reboiler and the lean/rich exchanger.

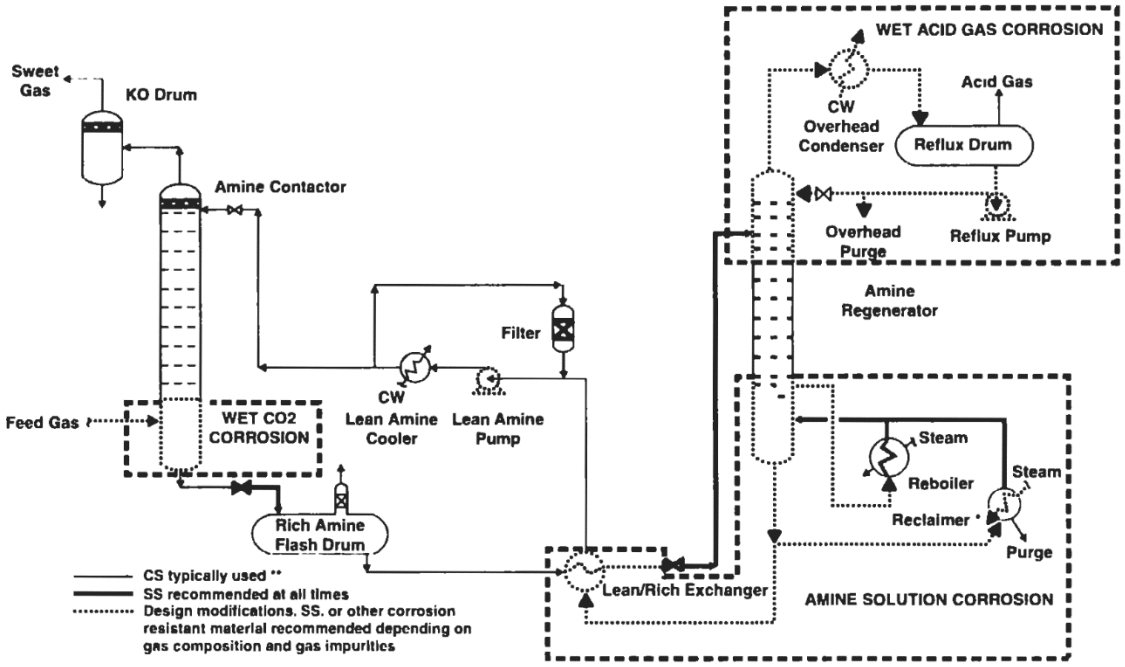

Figure 2-8: Natural gas sweetening plant diagram, with recommendations for materials of construction (Kohl et al., 1997).

As a general rule, most amines are non-corrosive in the absence of CO_2 and at very overstripped conditions (Kohl et al., 1997). Corrosion of carbon steel by MEA increases with temperature. In CO_2-only systems, carbon steel corrosion in 15% MEA is acceptable at low T (ie. 200 μm/yr at 60 °C), but unacceptable at high T (ie. 800 μm/yr at 116 °C) (DuPart et al., 1993). Corrosion of carbon steel also increases with CO_2 loading in MEA. At 80°C in an MEA solution, corrosion is 300 μm/yr at $\alpha = 0.35$ and 1300 μm/yr at $\alpha = 0.42$ (Kohl et al., 1997). Finally, different amines are significantly less corrosive to carbon steel. 30% MDEA corrodes carbon steel at 50 μm/yr at 99 °C and sat. CO_2 compared to 800 μm/yr in MEA (DuPart et al., 1993).

Stainless steel (316L) performs well (<25 μm/yr) in 20 wt % MEA at 116 °C sat. to CO_2 (Kohl et al., 1997). Although higher concentration of MEA (30 wt %) sees higher corrosion of 316L (≈130 μm/yr at 121 °C, CO_2 sat.) (DuPart et al., 1993).

Ultimately, corrosion of carbon steel in natural gas sweetening units is controlled by limiting MEA concentration to 20% and restricting rich loadings to a maximum of α= 0.35 (DuPart et al., 1993). Pipe velocities for carbon steel are limited to 0.9 M/s, whereas stainless steel is less sensitive and can be used at velocities up to 2.4 m/s (DuPart et al., 1993). MEA units are usually limited to operation at 120 °C because thermal degradation of the solvent becomes excessive at higher temperature (Davis, 2009). Stainless steel is used when needed because it performs well in 20 wt % MEA at all conditions.

Stress corrosion cracking of carbon steel is sometimes observed in natural gas sweetening plants. A large investigation into stress corrosion cracking in gas sweetening plants was undertaken after a vessel rupture in an MEA contactor in the 1980s caused 17 fatalities (McHenry et al., 1987). That particular incident was caused by hydrogen-induced cracking, which is associated with the presence of H_2S in gas sweetening plants. Stress corrosion cracking seems to occur in MEA solutions, but rarely in other amines like MDEA, when post-weld heat treatments are not used to relieve stress in carbon steel after welding (Richert et al., 1989). Stress corrosion cracking involves local disruption and attack of passive films at locations of high stress in the material. It typically occurs at solution potentials where the material should be passive, and it seems to require certain species such as OH^- or CO_3^{2-} (Sutcliffe et al., 1972). In amine units this can be avoided by proper heat treatment of carbon steel and by avoiding MEA (API, 2003).

Corrosion results from natural gas sweetening plants are difficult to adapt because critical corrosion parameters (amine concentration, presence of H_2S, presence of O_2) are

different in PCCC plants. However, experience from natural gas sweetening informs corrosion study in PCCC plants.

2.3.5. Corrosion measurements at PCCC conditions

There has been significant recent work at conditions relevant to PCCC plants. Efforts have largely focused on the conditions that are unique to PCCC work (ie, presence of O_2 and higher amine concentration). However other areas of interest have been intrinsic differences in corrosivities between amines, the performance of carbon steel when it is protected by $FeCO_3$, and the effect of degradation products on corrosion.

The addition of oxygen (6% O_2) was shown to increase the corrosion rate of carbon steel in 30 wt % MEA at absorber conditions (50°C, 12% O_2) from 50 μm/yr to 300 μm/yr (Xiang, Yan, et al., 2014).

Amines have been shown to have different intrinsic corrosivities (Table 2-3). It was proposed that amines with greater bicarbonate concentration, or with higher tendency to form bicarbonate (ie hindered amines like AMP) are expected to be more corrosive (Veawab et al., 1999). Higher bicarbonate concentration promotes the bicarbonate reduction to carbonate, which is a crucial reduction reaction coupled with oxidation of a metal surface. Carbon steel in MEA was noted to be in the active state at typical PCCC conditions, although at oxidizing conditions, it could be passivated by hematite (Fe_2O_3) (Soosaiprakasam et al., 2008). PZ was noted to have moderate corrosion of carbon steel at 80°C, 4 M, CO_2 sat, performing worse than MDEA but better than DEA (Gunasekaran et al., 2013).

Table 2-3: Corrosion rates of carbon steel (1020) at 80 °C in 3 M amines. DEA is diethanolamine (Veawab et al., 1999)

Amine	Lean ($\alpha = 0.2$) Corrosion Rate (μm/yr)	Rich (CO_2 sat.) Corrosion Rate (μm/yr)
MEA	508	3465
AMP	762	3198
DEA	483	2263
MDEA	-	1717

Carbon steel (A106) coupons exposed to PZ at 80 °C show a tight, coherent layer of $FeCO_3$, but coupons exposed to MEA show a porous, loose layer of Fe_3C. The Pourbaix diagrams constructed by the researchers predicted $FeCO_3$ for both cases (Zheng, Landon, Zou, et al., 2014).

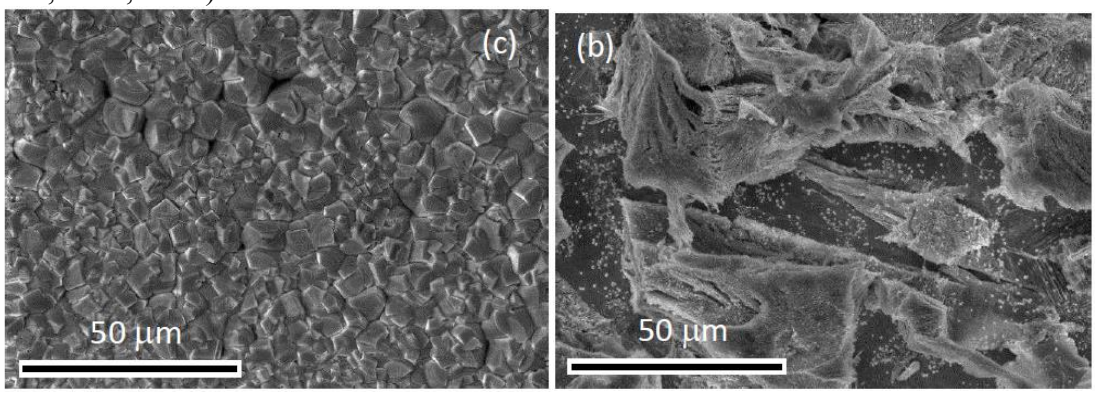

Figure 2-9: (left) SEM of carbon steel (A106) in 30 wt % PZ for 150 h (right) SEM micrograph of carbon steel (A106) in 30 wt % MEA, 183 h. In both cases α=0.43, 80°C (Zheng, Landon, Zou, et al., 2014)

Experiments show that 5 M MDEA and 5 M AMP also form protective $FeCO_3$ layers (80°C and 120°C), whereas 5 M MEA had no protective layer (K. L. S. Campbell et al., 2016; Yu et al., 2016). Protective films can be formed in comparable MEA solutions but only at very high CO_2 loading (L. Zheng, N. S. Matin, et al., 2016) or at controlled pH conditions (L. Zheng, J. Landon, et al., 2016).

Formation of protective $FeCO_3$ films can lead to very low corrosion rates (see Table 2-4). For example, MDEA corrosion of carbon steel is low (≤140 μm/yr) at lean and rich loadings at 120 °C. However, the addition of degradation products and oxygen lead to the breakdown of the protective film, which lead to high corrosion of 1840 μm/yr at lean conditions. Even with oxygen and degradation products, a $FeCO_3$ film was present at rich CO_2 loadings, but the high corrosion rate observed indicates it was not strongly protective. The effect of degradation product addition was attributed to a strong chelation effect between Fe^{2+} and bicine, which reduces the activity of Fe^{2+} and reduces $FeCO_3$ formation (Xiang, Choi, et al., 2014). Bicine and other degradation products were also found to increase the corrosion rate of stainless steel (316L) in 30 wt % MEA at 135 °C at anoxic conditions (Fytianos et al., 2016).

Table 2-4: Corrosion of carbon steel (UNS K02600) in 50 wt % MDEA at 120 °C, Heat Stable Salts (HSS) are 3002 ppm H_2SO_4, 2818 ppm CH_2O_2, 10000 ppm bicine, O_2 = 8 kPa (Xiang, Choi, et al., 2014)

Solution	Corrosion Rate (um/yr) α=0.05	Corrosion Rate (um/yr) α=0.3
MDEA	140	130
MDEA/HSS	-	320
MDEA/O_2/HSS	1840	750
MDEA/O_2	140	-

Intrinsic Fe^{2+} solubilities may differ greatly between amines, affecting the formation of $FeCO_3$ layers. Previous researchers showed that amines containing high Fe^{2+} concentration exhibited less $FeCO_3$ formation and higher carbon steel corrosion rates (Tsuda et al., 2010). Other researchers show that corrosive amines (MEA, EDA) had higher Fe^{2+} solubilities than less corrosive amines (PZ, MDEA) (Fytianos, 2016).

Recent work has yielded valuable data about corrosion performance in PCCC plants. Efforts have focused on the performance of carbon steel in second generation

solvents. Notably missing is work on performance of stainless steel, particularly at high temperature. This is likely because stainless steel is presumed passive at most conditions in amine service due to experience from natural gas sweetening.

2.3.6. Corrosion measurement at PCCC conditions in pilot plants

Corrosion in amine units for CO_2 capture has been measured at several pilot plants (Cousins et al., 2013; Hjelmaas et al., 2017; Khakharia et al., 2015; Kittel et al., 2009; Li et al., 2017). These studies all investigated MEA, and as a consequence are typically limited to operation at 120 °C. To date there is limited published data on pilot scale corrosion in second generation solvents, like PZ.

Corrosion of stainless steel (316L) and carbon steel (C1018) was measured in 30 wt % MEA at a pilot plant treating flue gas from a coal power station in Esbjerg, Denmark. Carbon steel performed acceptably in the absorber (<300 μm/yr), but poorly in the stripper sump (4500-8500 μm/yr). Stainless steel performed well (< 5 μm/yr) at all locations tested (Kittel et al., 2009).

Corrosion of stainless steel (316L), carbon steel (C1018), and galvanized carbon steel (C1018 GLV) was measured in 30 wt % MEA at a pilot plant treating flue gas from the Tarong coal power station in Australia. Stainless steel performed well at all locations tested (< 3 μm/yr). Galvanized coupons performed worse than corresponding carbon steel coupons at almost all locations. Carbon steel performance was moderate in the absorber (200-700 μm/yr), and unexpectedly poor (700 μm/yr) in the water wash. Carbon steel performance was acceptable in the column (≈50 μm/yr), but unacceptable (1000 μm/yr) in the sump. scale of Fe_2O_3 was observed in the sump (Cousins et al., 2013).

Corrosion of stainless steel (some 316L, some 304L) was measured in the hot lean stream (120 °C) of a 30 wt % MEA plant treating flue gas from a coal fired power plant in

Maasvlakte, the Netherlands. Corrosion varied from 4 – 130 μm/yr. The higher corrosion rate was attributed to a higher oxygen content in the flue gas (17 % by volume, instead of 7 % typically) used during one campaign to imitate natural gas conditions (Khakharia et al., 2015).

Extensive corrosion measurements of several alloys was made at the Technology Centre Mongstad in Norway. 30 wt % MEA was operated at 120 °C, capturing flue gas from a natural gas burner that was typically 4 % CO_2, 14 % O_2. Coupons were only evaluated at hot lean and hot rich locations. Carbon steel (S235) experienced high corrosion (>1400 μm/yr) in both the hot lean and hot rich locations. The corrosion rates for 304L, 316L, and 22 Cr duplex were << 100 μm/yr for all locations. Some pits were found on 316L coupons in the hot rich solvent with a pit depth of 0.15 mm/yr. No pitting was observed on 304L, Inconel 600, or 22 Cr Duplex. Inconel 600 was attacked in hot lean solvent (840 μm/yr), but performed well at rich conditions (<< 100 μm/yr) (Hjelmaas et al., 2017).

Corrosion of carbon steel (A106) and stainless steel (304) was evaluated at a pilot plant treating coal flue gas in Harrodsburg, Kentucky. The stripper operated up to 130 °C. One campaign evaluated 30 wt % MEA. Stainless steel performed well at all locations (< 100 μm/yr). Carbon steel performed well in the absorber and the cold lean location (< 100 μm/yr), but performed unacceptably in the hot rich location and in the stripper (3000-16000 μm/yr). Protective products were not observed on carbon steel coupons. A second campaign used a proprietary solvent that is a blend of primary amines with a corrosion inhibitor (1000 ppm 2-Mercaptobenzothiazole). Corrosion was only evaluated in the stripper and in the hot rich location in this campaign. Stainless steel performed well at all locations (< 100 μm/yr). Carbon steel performance was moderate at both locations (0-2000 μm/yr for the first 500 hours of the campaign. After that, the corrosion of carbon steel

increased (4000-7000 μm/yr), which was attributed to the eventual degradation of the inhibitor. FeCO3 was observed in the hot rich stream only at the end of the campaign (850 hours), but not on samples removed prior to that. $FeCO_3$ was not observed in the stripper (Li et al., 2018; Li et al., 2017).

Pilot experience with corrosion in PCCC systems is that MEA is more corrosive to carbon steel than at comparable natural gas sweetening conditions. Stainless typically performs very well in MEA at PCCC conditions. Although there is substantial interest in low corrosivity amines at the bench scale, only one pilot-scale study of a low-corrosion second generation amine has been published (Li et al., 2018).

Chapter 3. Experimental Methods

Experimental methods used throughout this work are grouped by their type in this chapter. Techniques used for the measurement of corrosion are presented in Section 3.1. Section 3.2 discusses equipment that was used to simulate corrosive conditions in amine solutions. Section 3.3 describes analytical techniques that are used to characterize amine solutions. Finally, Section 3.4 presents some miscellaneous equipment as well as several tables of equipment part numbers.

3.1. Techniques for Measurement of Corrosion

3.1.1. Electrical Resistance Corrosion Probes

Electrical resistance (ER) probes are used for online corrosion measurement at the bench-scale in Chapter 4, and in several pilot plant campaigns in Chapter 6 and Chapter 7. The ER probe exposes a thin carbon steel or stainless steel wire to the process fluid, allowing it to slowly corrode. The thin wire element of the corrosion probe is shown in Figure 3-1.

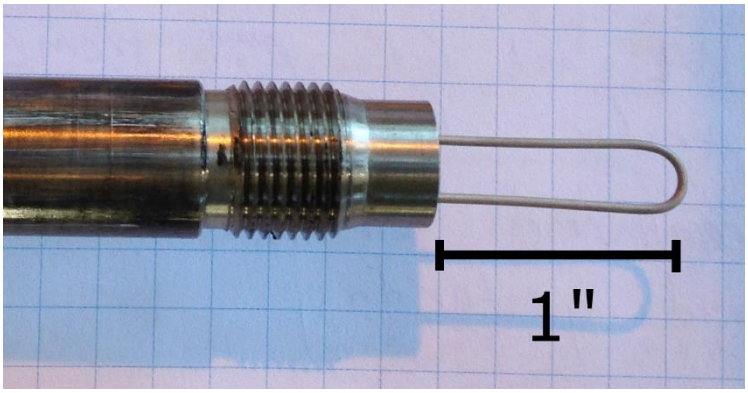

Figure 3-1: Electrical resistance corrosion probe

As the wire corrodes and loses metal to solution, the wire cross-sectional area decreases, thus increasing resistance in the wire. Resistance in a conductor is linearly proportional to the conductor cross sectional area (Equation 3-1). A transmitter connected to the ER probe constantly measures this resistance and outputs a signal that reflects the wire thickness remaining. Resistivity of metallic conductors generally increases with temperature, so the probe contains a reference element that is sealed within the probe body and shielded from the corrosive environment. Because the reference element and the exposed element are the same material and exposed to the same temperature, their resistivity is the same. The ER probe reports the ratio of the exposed element resistance and the reference element resistance, which eliminates the effect of temperature

$$R = \rho \frac{L}{A} \tag{3-1}$$

Table 3-1: Nomenclature used in Equation 3-1

R	Electrical Resistance (Ω)
ρ	Electrical resistivity (Ω·meters)
L	Length of conductor (meters)
A	Cross sectional area of conductor (meters^2)

Different methods were used for processing the data depending on the length of the experiment. Bench-scale experiments took one probe life reading per second, and this data was then directly regressed to determine a corrosion rate. For the SRP 2017 PZ campaign, one ER probe signal reading per minute was taken during operation. During each period of steady state operation (periods in this campaign were typically 1-3 hours long, after which conditions are changed), these measurements were averaged to give an average ER probe reading during that steady state period. Plotting the average ER probe readings chronologically showed that the probe life decreased over the course of the campaign. For

the NCCC 2018 PZ campaign, one ER probe signal reading per minute was taken during operation, and these data averaged to yield an average daily corrosion probe reading for each probe. Plotting the average probe life remaining for each day chronologically gives a corrosion rate over the entire exposure time for each probe. The corrosion rates were then determined using the method of least squares. For pilot scale work, ER probes were cleaned between batches using the same procedure described below for coupons (See Section 3.1.3). Table 3-9 lists the part numbers of ER used. In Chapter 6, bench-scale ER corrosion rates are compared to pilot-scale ER corrosion rates. In Chapter 6 and Chapter 7, simultaneous pilot ER corrosion rates and coupon corrosion rates are compared. Ultimately, the ER probe gave reliable corrosion rates at the bench-scale, but pilot-scale ER measurements were sometimes inconsistent.

Qualitative judgements about corrosion rates are given in Table 3-2 to give an idea about what an acceptable corrosion rate is. These judgements are appropriate for certain equipment with thick walls, like piping or vessels. However these corrosion rates may be too high for equipment with thin surfaces, like heat exchangers.

Table 3-2: Relative corrosion resistance (Fontana, 1986).

Qualitative Corrosion Resistance	μm/yr
Outstanding	<25
Excellent	25 to 100
Good	100 to 500
Fair	500 to 1000
Poor	1000 to 5000
Unacceptable	5000 +

3.1.2. Oxidation-Reduction Probes

Solution potential was measured in amine solutions at the bench-scale in Chapter 4. ORP measurements were made during the SRP 2017 PZ campaign (Chapter 6) and the NCCC 2018 PZ campaign (Chapter 7). Pilot ORP measurements at NCCC were slightly erratic because frequent retraction and recalibration of the ORP probes was not performed. These pilot ORP results are briefly discussed in Appendix B. The ORP probe measures the platinum electrode potential of solutions in the corrosion loop compared to a Ag/AgCl reference cell. Cell potential measures how thermodynamically favorable a redox reaction is. For example, Equation 3-2 shows the oxidation of iron at high pH and in the presence of O_2. If this reaction were separated into two half-cells, connected by a junction, the potential between the cells is given by Equation 3-3. Nomenclature for these equations is given in Table 3-3.

$$2\mathrm{Fe} + \mathrm{O_2} + 2\mathrm{H_2O} \leftrightarrow 2\mathrm{Fe^{2+}} + 4\ \mathrm{OH^-} \tag{3-2}$$

$$e = e^0 - \frac{RT}{4F}\ln\left(\frac{(Fe^{2+})^2(OH^-)^4}{(O_2)}\right) \tag{3-3}$$

Table 3-3: Nomenclature used in Equations 3-2 and 3-3

e	Cell potential (volts)
e^0	Standard cell potential (volts)
R	Universal gas constant
T	Temperature
F	Faraday's constant
(Fe^{2+}), (OH^-)…	Activity of a species

Unlike iron, platinum is inert to oxidation at most conditions. This means the reaction at the electrode is likely Equation 3-4. Thus in this system, the potential measured at a platinum electrode reflects the thermodynamic favorability of the reduction of O_2 to

OH^-. The redox reaction in an amine system may be more complicated than shown here. In particular, a different reduction reaction is likely relevant at anoxic conditions.

$$O_2 + 2H_2O + 4e^- \leftrightarrow 4\,OH^- \quad (3\text{-}4)$$

Table 3-9 lists the part numbers of the ORP equipment used.

3.1.3. Corrosion Coupons

Coupons were used to measure corrosion by weight loss and to characterize corrosion product layers at the pilot scale in Chapter 6 and Chapter 7. Two types of coupons were used: strip and disc, which are shown below in Figure 3-2. Strip coupon dimensions are 0.5 (width) x 3 (length) x 0.063 (thickness) inches. Disc coupon dimensions are: 1.25 (diameter) x 0.125 (thickness) inches. Coupon part numbers and a description of the coupon finish are given in Table 3-11.

Figure 3-2: Blank coupons, from left to right: C1010 strip coupon, 316L strip coupon, 304 strip coupon, C1010 disc coupon, 316L disc coupon, 304 disc coupon.

Once removed from pilot plants, coupons were immediately rinsed with deionized H_2O, air dried, photographed, wrapped with paper containing a volatile corrosion inhibitor, placed into plastic Ziploc bags, transported back to Austin, and finally placed into a glass desiccator until analysis was performed. Coupons were first mounted for scanning electron microscope imaging. Afterward, a small portion of corrosion product, if present, was gently scraped off and analyzed by powder X-Ray diffraction. Any residual corrosion product was removed using concentrated HCl inhibited with N,N'-Dibutylthiourea as recommended in literature (Kayafas, 1980; NACE, 2013), and the coupons were weighed for a final weight-loss measurement.

Coupons were cleaned and weighed by the following procedure. After all SEM and powder X-ray diffraction characterization, coupons were rinsed in acetone and then air dried. The coupons were then weighed in triplicate to measure the mass of the corroded coupon with its product layer. After this, each coupon was dipped in an inhibited HCl solution for 60 s with gentle stirring. Next, the coupon was immediately transferred to a saturated solution of $NaHCO_3$ in water, where it was gently stirred for 60 s. The coupon then was rinsed in water, then in acetone, then air dried. Finally the coupon was weighed in triplicate to measure the mass of the corroded coupon without its product layer. This final mass was used for all corrosion rates reported here. To prepare the inhibited HCl solution, 10 g/L of N,N'-Dibutylthiourea from Alfa Aesar was added to conc. HCl (37.5 wt. %) while stirring with a Teflon stir bar. The solid dissolved completely, leaving a clear "stock" solution. Immediately prior to use, this stock solution was diluted 50 % by volume with water.

One minor issue with this work is that stainless steel coupons were cleaned with concentrated HCl for final weight loss measurements. HCl is not recommended for use with stainless (ASTM, 2017) due to pitting (Jones, 1996). Future work should use a

different cleaning procedure for stainless steel. However, since coupons were evaluated by SEM for pitting before corrosion product removal, this error should not impact the accuracy of this work.

Corrosion by coupon weight loss is calculated by Equation 3-5 (Jones, 1996). The proportionality constant is a simple unit conversion. Densities and physical properties of alloys investigated in this report are given in Table 3-5.

$$C = 87600 \frac{W}{DAT} \tag{3-5}$$

Table 3-4: Nomenclature for Equation 3-5

C	corrosion rate (µm/yr)
W	coupon mass loss (mg)
D	density of metal (g/cm^3)
A	surface area of coupon (cm^2)
T	duration of experiment (hours)

Table 3-5: Density and composition of alloys investigated (Bauccio, 1993)

			Composition (wt %)								
Alloy	UNS #	Density (g/cm3)	C	Mn	Si	Cr	Ni	P	S	Mo	Fe
C1010	G10100	7.87	0.8-0.13	0.30-0.60	0	0	0	0	0	0	Bal.
316L	S31603	7.98	0.03	2.00	1.00	16.0-18.0	10.0-14.0	0.045	0.03	2.0-3.0	Bal.
304	S30400	8.00	0.08	2.00	1.00	18.0-20.0	8.0-10.5	0.045	0.03	0	Bal.

3.1.4. Coupon Characterization

Corrosion product films on coupons were imaged using either a FEI Quanta 650 scanning electron microscope or a FEI Quanta 600 FEG scanning electron microscope.

Accelerating voltage was typically 20 kV and magnification was typically 1000x-5000x. Details are included in each SEM micrograph. Corrosion product films were gently scraped off and the resulting powder product was analyzed by powder X-ray diffraction using a Rigaku R-Axis Spider instrument with a Cu Kα radiation source at 40 kV and 40 mA. Reference spectra are given in Table 3-6. Powder X-ray diffraction was also used to characterize the solid phase present in Fe^{2+} solubility experiments (Chapter 5). SEM micrographs of blank coupons are shown in Figure 3-3. Blank coupon micrographs show the significant difference between the finish on disc coupons (120 grit) and on strip coupons (glass bead). In general the blank coupons are unremarkable and free of features or corrosion products.

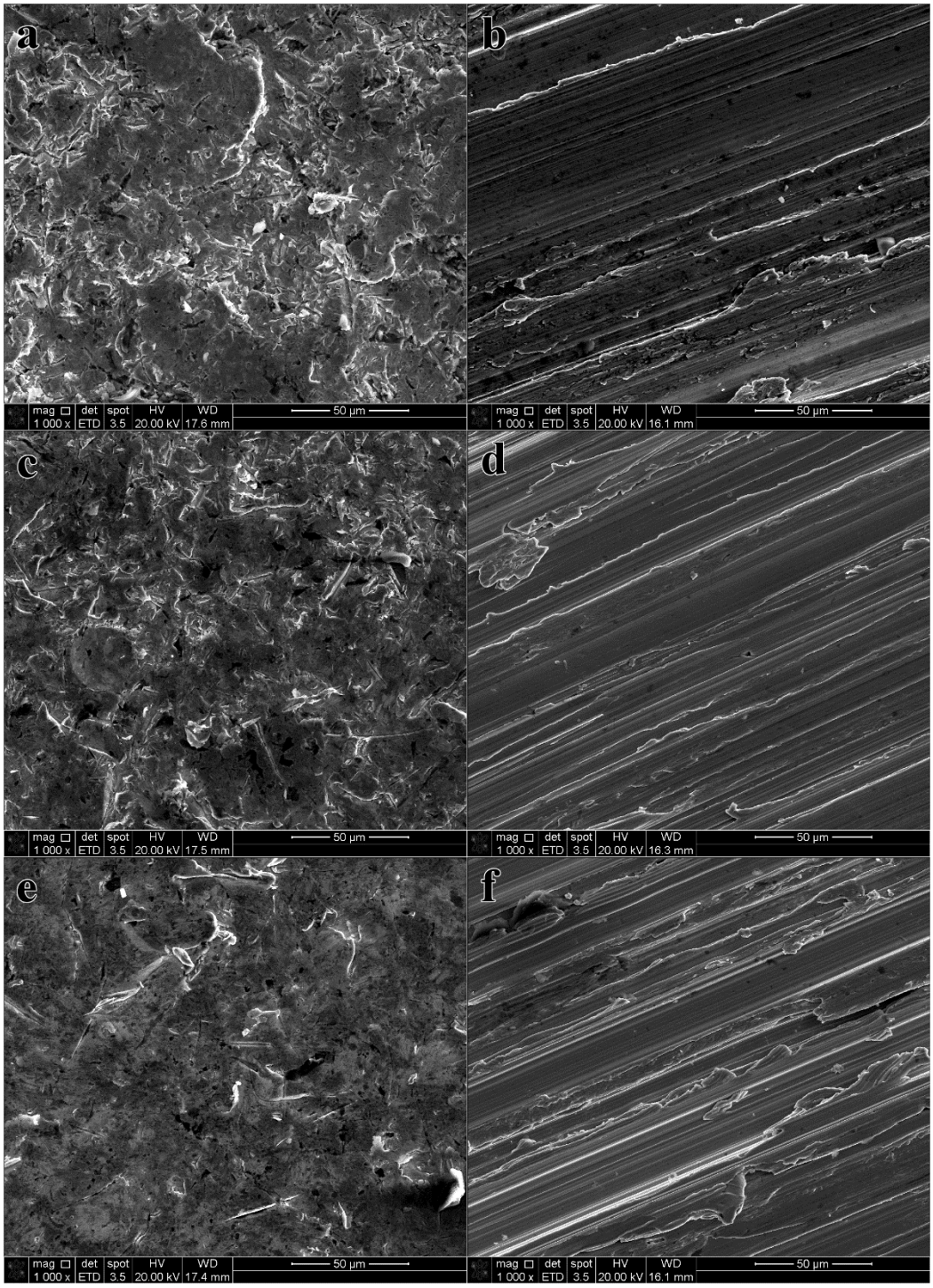

Figure 3-3: SEM micrographs of blank coupons: a) C1010 strip, b) C1010 disc, c) 316L strip, d) 316L disc, e) 304 strip, f) 304 disc.

Energy dispersive X-ray spectroscopy (EDS) was performed on many of the coupons analyzed in this report. Detailed EDS data is not presented because powder XRD product determinations were more conclusive.

Table 3-6: Reference spectra used for powder X-ray diffraction identification

Compound Name	Chemical Formula	Powder Diffraction File (PDF) #	Citation
Siderite	$FeCO_3$	00-029-0696	(NBS, 1978)
Iron	Fe	00-006-0696	(NBS, 1955)
Magnetite	Fe_3O_4	00-019-0629	(NBS, 1967)
Goethite	FeO(OH)	00-029-0713	(Harrison, 1975)
Ferric Hydroxide	$Fe(OH)_3$	00-038-0032	(Au-Yeung et al., 1984)
Rhodochrosite	$MnCO_3$	00-044-1472	(ICDD, 2018)

3.2. EQUIPMENT FOR SIMULATING AMINE CORROSION AT THE BENCH-SCALE

3.2.1. Corrosion Loop Apparatus

A pressure vessel was constructed and used in Chapter 4. This apparatus was built to study amine corrosion at high temperature and pressure (Figure 3-4 and Figure 3-5). The pressure vessel was a 1 inch diameter pipe loop with a 1-½" diameter pipe headspace. The volume of the 1-inch diameter pipe loop was 1100 mL, which does not include the 1-½" headspace. The pipe headspace has a pressure gauge and a pressure-relief disc to prevent over pressurization. Temperature was controlled using a PID controller connected to a J-type thermocouple on the hot side of the loop. The controller manipulated power to heat tape wrapped around the right side of the loop. This created a slow flow through the pipe due to natural convection. A temperature measurement was also taken on the cold side of the loop, and the resulting ΔT between the hot and cold sides of the loop varied between experiments from 70 to 97 °C, depending on the hot side temperature and the viscosity of the solution. Probes to measure corrosion and oxidation-reduction potential were exposed

to the process fluid inside the pressure vessel. The loop was filled with 1100 mL of a CO_2-loaded amine solution, sealed, and then heated to the target temperature. Once at temperature, the corrosion rate and electrode potential behavior were measured for 12 hours to 150 hours. Measuring very low corrosion rates required longer experiments, whereas high corrosion rates can be measured much more quickly.

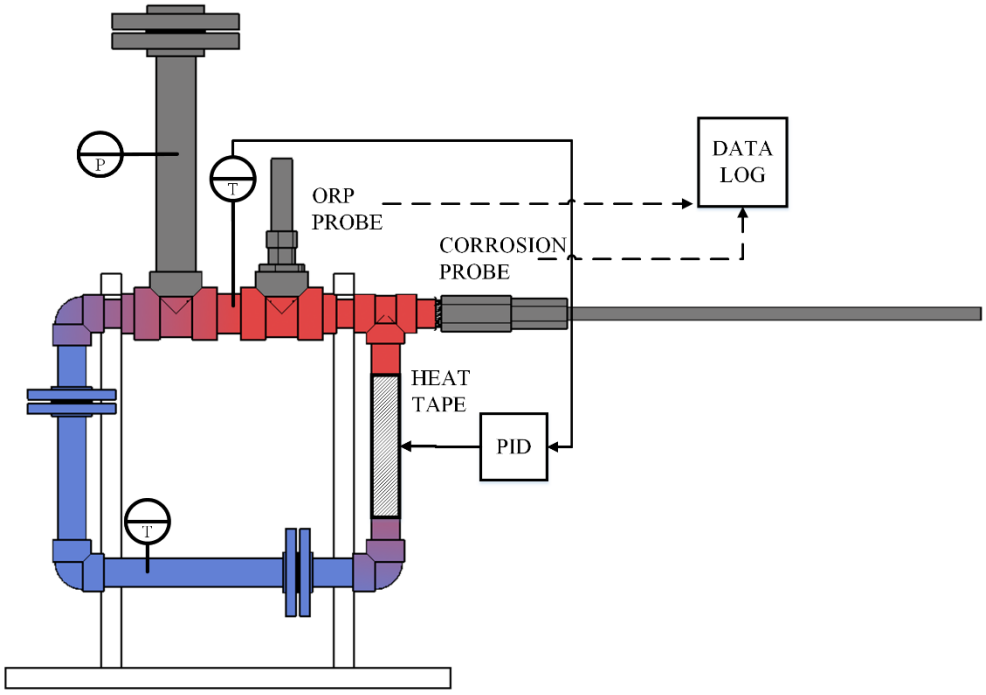

Figure 3-4: Corrosion loop apparatus

Figure 3-5: Corrosion loop apparatus, ORP probe not shown.

The pipe for the corrosion loop was schedule 40 stainless steel (304L) from Ferguson Enterprises, Inc. All construction was welded. All fittings were either 304 or 316L stainless steel. Flanges were slip-on 150# for the loop, and or slip-on 300# for the

headspace. Gaskets were 1/16" gylon from GHX Industrial, LLC. Pipe fittings and ball valves are typically rated for 150# and sourced from Ferguson Enterprises, Inc. Several tube adapters are from Swagelok® Company. The frame supporting the equipment was built with 1" x 1" aluminum T-slotted frame (Part No. 1010) and adapters from 80/20® Inc. The pressure burst disc was a 1-½" RA8 series stainless (316) metal burst disc specified to burst at 176 psig at 160°C (or 200 psig at 20 °C) and was manufactured by Zook Enterprises, LLC. The loop was insulated with 1" fiberglass insulation from W.W. Grainger, Inc. Two 400 Watt heating tapes (Glas-Col® Part No. 103B-SCC4) supplied heat and were controlled by a PID controller (AutomationDirect.com Part No. SL4896-RRE) with a J-type thermocouple (AutomationDirect.com Part No. THMJ-T06L06-01). The loop pressure was measured with a 0 – 300 psig analog gauge (AutomationDirect.com Part No. G25-SD300-4LS). A procedure for operating the corrosion loop and an analysis of its potential hazards is given in Appendix A.

3.2.2. Thermal Degradation Cylinders

Thermal cylinders were used to measure amine corrosion in Chapter 4. Swagelok® stainless steel cylinders have been extensively used for the measurement of thermal degradation of amines (Freeman, 2011; Namjoshi, 2015). Measuring the dissolved metal content in these thermal cylinders provides a way to estimate the corrosion rate of amines. This method has been used by other researchers to investigate the effect of degradation products on corrosion of 316L in MEA (Fytianos et al., 2014; Fytianos et al., 2016). That work showed comparably high corrosion of 316L in MEA. Two alloys were tested using this method: 316L stainless steel and 1010 carbon steel. These cylinders consist of a 10 cm long steel tube with an outer diameter of 0.95 cm and inner diameter of 0.77 cm. The inner surface area of steel used for the corrosion calculation was 25.67 cm^2. On both ends, the

cylinder has a Swagelok® ferrule fitting and cap that allows it to be sealed. The cylinders have a volume of 4.5 mL and a pressure rating above 130 barg. Amine solutions were prepared, and 4 mL added to each cylinder. This left headspace in the cylinder to prevent cylinder failure due to liquid expansion. The cylinders were sealed and placed into a Lab-Line Imperial V convection oven with a Eurotherm 2100-series digital temperature control. After a specified period of time, the cylinders were removed from the oven, weighed to ensure they had not leaked, quenched in water, opened, and emptied into clean glass vials. The vial contents were later analyzed for dissolved metals (by inductively coupled plasma optical emission spectroscopy), which were converted to corrosion rates.

Corrosion rates from the cylinders are calculated using the same equation used for coupon weight loss (Equation 3-5), except W is defined as the total metal mass in solution determined by ICP (mg), and A is defined as the inner surface area of the steel cylinder (cm_2). Several time series were conducted, and these show that the corrosion rate slowly decreases in the cylinders. When a time series is taken like this, it allows a curve to be fit so that the instantaneous corrosion rate at time = 0 can be estimated. However, to quickly screen a large number of amines and conditions, detailed time series were not done for each amine. Most amines and conditions have one time point taken at 333 hours. This allows only an average corrosion rate to be reported. These average corrosion rates probably underestimate the instantaneous corrosion rate. However, because all average corrosion rates are taken at the same time, they provide a good indicator of the relative corrosivity of different amines and process conditions.

3.2.3. Equilibrium Fe^{2+} Solubility Measurement

Iron solubility in amines was measured in small, low temperature stirred reactors in Chapter 5. Amine solutions were added to a jacketed, 1 L, glass reactor containing a Teflon stir bar. This reactor is shown in Figure 3-6A. Typically an excess (0.25 M) of $FeSO_4$ and Na_2CO_3 were added as solids to the reactor. The reactors were sealed using large rubber stoppers and stirred for 200–400 hours. In addition, several experiments were conducted in a gas-sparged reactor, shown in Figure 3-6B. In these experiments, a gas sparger was used to continuously bubble 100 mL/min of a mixture of 10% CO_2 and 90% air into the solution. The gas passed through a water saturator before entering the amine solution to prevent water loss. Gas flowrates were controlled by Brooks Instrument 5850E mass flow controllers. Liquid samples were taken periodically and immediately filtered with Corning® 0.20μm polyethersulfone membrane filters to remove suspended solids. When opened for sampling, the reactors were very briefly exposed to air.

For certain selected experiments, solid samples were collected and characterized. After the experiments reached equilibrium, solid samples were taken from the bottom of the reactors. The samples were vacuum-filtered and rinsed with deionized H_2O. The extracted solids were then placed in a desiccator to be dried. Finally, the solids were analyzed by powder X-ray diffraction.

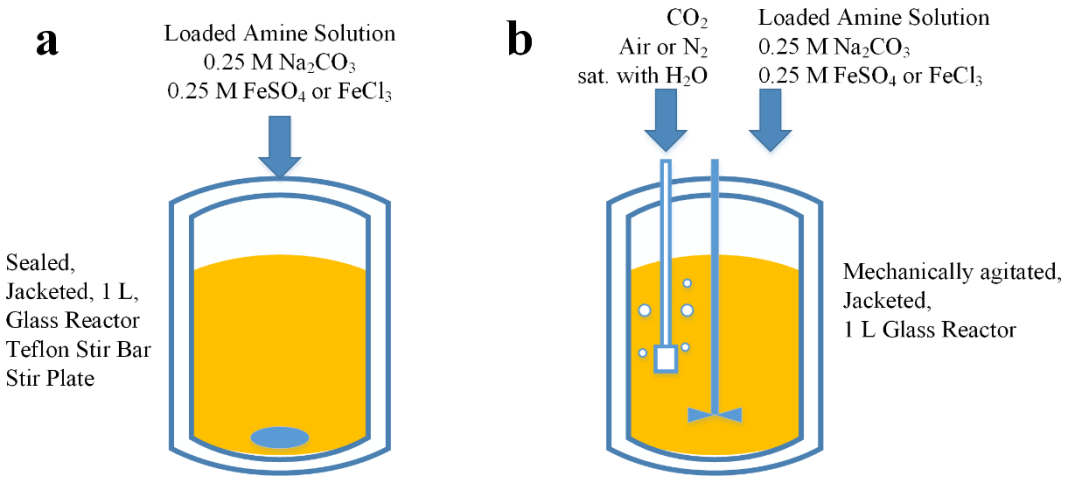

Figure 3-6: a) Reactor used for Fe^{2+} solubility experiments. b) Sparged reactor used for Fe^{2+} solubility experiments.

3.3. AMINE SOLUTION CHARACTERIZATION

3.3.1. Preparation of Amine Solutions

Amine solutions are prepared by diluting commercially purchased amines to target concentration with deionized water. All water used was purified to 18.2MΩ·cm by deionization beds followed by a Millipore Direct-Q® membrane unit. All amine preparation was performed gravimetrically, so concentration units are reported in molality, which is defined in Table 3-7. CO_2 is added to amine solutions by transferring the solution to a gas washing bottle, which allows CO_2 gas to be slowly bubbled through the solution. This gas washing bottle is placed onto a scale (± 0.1 g) during the bubbling procedure, so that the amount of gas added to the solution can be determined. CO_2 content in an amine solution is reported as CO_2 loading: "α", which is defined in Table 3-7. CO_2 loading captures the molar ratio of CO_2 in a solution to the amine alkalinity, or the moles of amine nitrogen groups available to complex CO_2. As a brief example, a solution of 5 m MEA prepared using 1 kg of H_2O has 5 mol of MEA, and 5 mol of alkalinity. A solution of 5 m

PZ prepared using 1 kg of H_2O has 5 mol of PZ, but 10 mol of alkalinity because PZ is a diamine. Adding 2.5 mol of CO_2 to each solution brings the MEA solution to $\alpha = 0.5$ and the PZ solution to $\alpha = 0.25$.

Table 3-7: Nomenclature used for describing amine solutions

m	Amine molality (mol amine/kg H_2O)
α	CO_2 loading (mol CO_2/mol alkalinity)

3.3.2. Anion Chromatography

The concentrations of anion degradation products (eg. formate) are determined by anion chromatography on a Dionex ICS3000. Small samples are taken and mixed with an equal volumetric portion of 5 N sodium hydroxide and allowed to react for 24 hours. This converts any amides present to the corresponding parent amine and formate. Samples are diluted to 100X and then eluted with a KOH/water mixture and separated over an IonPac AS15 analytical column. The column is filled with ethylvinylbenzene cross-linked with 55% divinylbenzene resin and a quaternary ammonium functional group. An anion suppressor reduces solution conductivity after the separation step. Analytes are quantified in a conductivity cell. The eluent followed a gradient starting at 2 mM and ending at 45 mM. Formate peaks typically elute at 20.2 minutes. This method is fully documented by Freeman (Freeman, 2011).

3.3.3. Cation Chromatography

The concentrations of parent amines are determined using cation chromatography on a Dionex ICS2100 instrument. The solution was diluted to 10,000X and then eluted with methanesulfonic acid mixed with water. The eluent followed a gradient starting at 5.5

mM and ending at 38.5 mM methanesulfonic acid. The samples were eluted over an IonPac GC 17 guard column followed by an IonPac CS 17 analytical column. These columns contain ethylvinylbenzene cross-linked with 55% divinylbenzene resin. A cation suppressor reduces solution conductivity after the separation step. Analytes are quantified in a conductivity cell. This method is fully documented by Namjoshi (Namjoshi, 2015).

3.3.4. Inductively Coupled Plasma Optical Emission Spectroscopy

Metals dissolved in amine solutions were measured to estimate corrosion in thermal cylinders (Chapter 4) and to determine equilibrium Fe^{2+} solubility in amines (Chapter 5). All metals analysis was done by inductively coupled plasma optical emission spectroscopy using a Varian 710-ES instrument run in axial configuration. Samples are diluted 25X-30X with 2 wt % HNO_3 prepared from 70 wt % trace metal grade HNO_3 and doubly deionized H_2O. Metal standards are prepared by diluting 1000 ppm Atomic Emission Spectroscopy standards obtained from Fisher Scientific® and Ricca Chemical Company®. The solution is nebulized through a small nozzle and injected into a plasma flame at 7000 K. Metal ions are excited, then relax, emitting energy at a characteristic wavelength. Wavelengths analyzed are given in Table 3-8. Results for each wavelength were averaged with other wavelengths for the same ion. When corrosion rates were estimated, dissolved metals were converted to an estimated corrosion rate using the surface area of the thermal cylinder and the density of the alloy.

Table 3-8: Wavelengths analyzed for metals measurement by ICP-OES

Characteristic Emission Wavelengths (nm)				
Cr	Fe	Mn	Mo	Ni
205.56	234.35	257.61	201.512	216.555
206.158	238.204	259.372	202.032	221.648
206.55	239.563	260.568	203.846	230.299
267.716	259.94	294.921	204.598	231.604

3.3.5. Total Inorganic Carbon Measurement

Total Inorganic Carbon (TIC) was occasionally used to determine the CO_2 loading in pilot plant solutions. All experiments using freshly prepared amine solutions report gravimetric loadings, but all experiments using pilot plant solutions report loadings calculated from TIC and the measured parent amine concentration (cation).

The concentration of CO_2 in amine solutions can be measured by acidifying the amine solution, then measuring the released CO_2 gas concentration. A TIC apparatus was built previously (Freeman, 2011) that allows this reaction and measurement to be performed quickly on small aliquots of amine solution. The apparatus uses a 6" long, ½" diameter glass tube with a glass frit at its midpoint. Just above the frit is a small injection port sealed with a rubber septum. Nitrogen, controlled with a rotameter, is blown upward through the tube as a carrier gas. 1 to 1.5 mL of 30 wt % phosphoric acid is injected with a needle through the injection port. The acid is suspended, bubbling, on the frit by the carrier gas. A small portion of a loaded amine solution is injected with a needle directly into the phosphoric acid. The CO_2 is liberated and is carried by the nitrogen out of the reaction tube. The gas is dried by passing over dessicant ($MgClO_4$) and then enters a infrared CO_2 gas analyzer (Horiba, Ltd. Part No VIA-510). The analyzer sees a quick spike, then decrease in CO_2 concentration. This peak is integrated and a total mass of CO_2 liberated is determined. The instrument is calibrated by measuring instrument response

after injection of standards prepared from a 1000 ppm Inorganic Carbon standard solution (Ricca Chemical Company®).

3.4. MISCELLANEOUS EQUIPMENT AND EQUIPMENT PART NUMBERS

3.4.1. Corrosion Coupon Mounting Hardware

Several types of coupon mounting hardware were used at the pilot scale. WL probes on the AFS skid (NCCC 2018 PZ campaign) use a retractable probe that holds two strip coupons. This WL probe is illustrated in Figure 3-7, which also shows the compression fitting that allows the probe to be inserted and retracted.

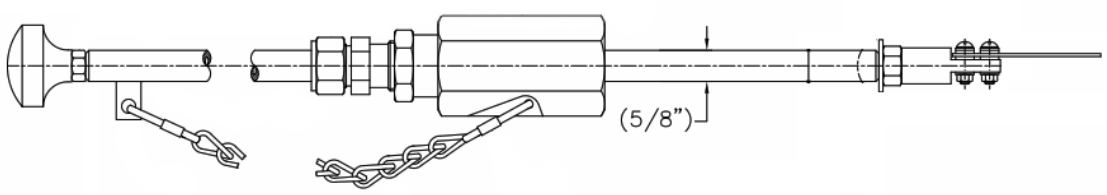

Figure 3-7: Illustration of the WL probes used on the AFS skid (Metal Samples Company, 2019). Each probe holds two strip coupons.

During the NCCC 2018 PZ campaign, coupons were inserted at several locations using a retractable probe that holds four disc coupons. This hardware was used in the cold lean stream and several locations in the absorber. The probe body is similar to Figure 3-7, but the coupon adapter holds disc coupons, as shown in Figure 3-8.

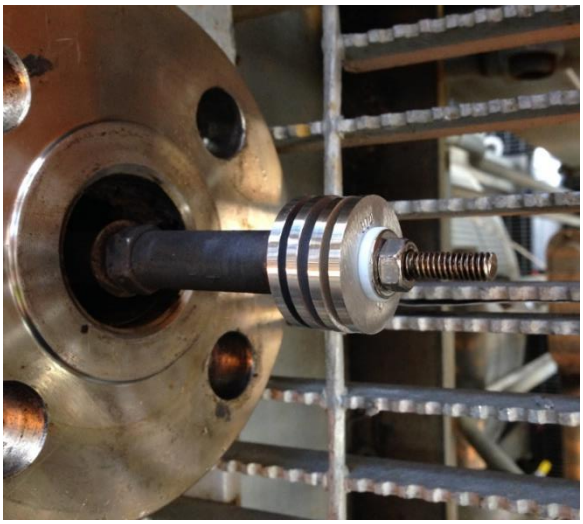

Figure 3-8: WL probe used on legacy NCCC equipment. Each probe holds four disc coupons.

During several campaigns (SRP 2017 PZ, NCCC 2017 MEA, some locations in the absorber during NCCC 2018 PZ), coupons were mounted at ER probe locations. This is accomplished using a simple adapter that allows strip coupons to be attached to the end of ER probes. The coupon adapter is shown in Figure 3-9.

Figure 3-9: Coupon adapter for ER probes holding two strip coupons.

An ER probe and a coupon probe inserted into a process vessel at a pilot plant are shown in Figure 3-10. Both pieces of equipment can be retracted, isolated, and removed during plant operation. This is accomplished by retracting the probe through a compression fitting, then closing a process isolation valve, then depressurizing and draining the probe mounting hardware, and finally removing the probe. The procedure for installing a probe, pressure testing it, and inserting it during operation is given in Appendix A.

Figure 3-10: An ER probe and a coupon probe inserted into a vessel at a pilot plant.

3.4.2. Bench-Scale Data Logger

The ER probe transmitter and the ORP probe transmitter both output a 4 – 20 mA signal, 24 V DC signal. At the pilot scale, transmitters are connected directly into plant instrumentation input/output controllers, and data recording is managed by plant equipment control software (ie. DeltaVTM). At the bench-scale, data was recorded by a

NIDAQ Data Acquisition module (National Instruments Corporation, Part No NI-USB-6009) connected to a Windows 7 PC running SignalExpress software. The NIDAQ measured voltage drop across a 10 Ω resistor, which allows calculation of the circuit current. The ER probe transmitter required a 24 V DC current to be supplied through the signal wire, since it does not have an internal power supply. This was supplied by a switching power supply (AutomationDirect.com Part No PSL-24-010). The power supply and NIDAQ enclosure is shown Figure 3-11.

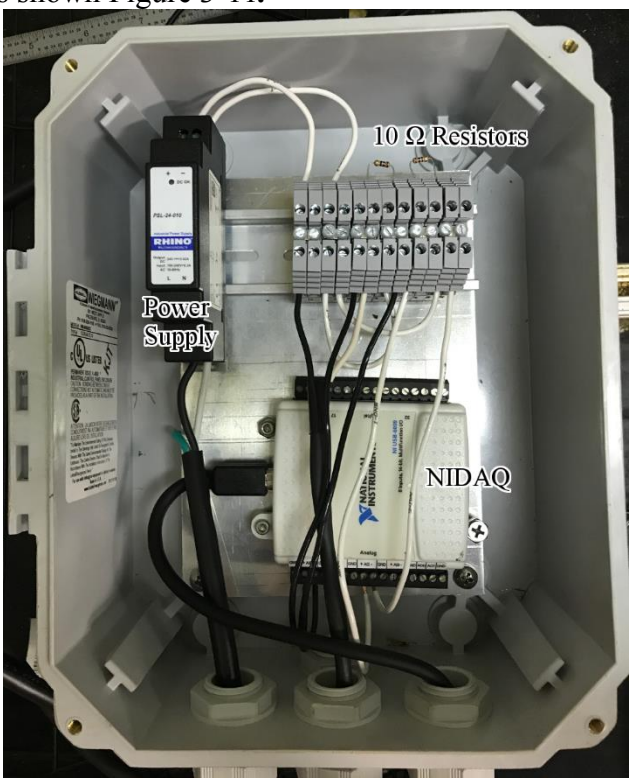

Figure 3-11: Bench-Scale Data Logger

3.4.3. Equipment Part Numbers

Table 3-9: ER and ORP Instruments used in corrosion measurement

Instrument Description	Part Number
ER Probe, 4 mil life, carbon steel element (C1010), length 24”	ER45223012437501 (Metal Samples Co.)
ER Probe, 4 mil life, carbon steel element (C1010), length 30”	ER45223013037501 (Metal Samples Co.)
ER Probe, 4 mil life, stainless steel element (316L), length 24”	ER45223012415901 (Metal Samples Co.)
ER Probe, 10 mil life, stainless steel element (304), length 24”	ER45220022414101 (Metal Samples Co.)
ER Probe Transmitter	IN2500E (Metal Samples Co.)
Oxidation Reduction Probe	3300HT-12-30 (Rosemount)
ORP Transmitter	1056-03-21-31-AN (Rosemount)

Table 3-10: Coupon mounting hardware

Instrument Type	Part Number (all from Metals Samples Co.)
Strip coupon holders used in the AFS (NCCC 2018 PZ)	RT4522030241
Disc coupon holders (NCCC 2018 PZ)	RT4522060421
ER Probe coupon adapters (SRP 2017 PZ, NCCC 2017 MEA, some locations NCCC 2018 PZ)	PR5659158 and CA611158

Table 3-11: Coupon part numbers and surface finish

Description	Part Number	Coupon Finish
C1010 strip coupon	CO1183750104110 (Metal Samples Co.)	Glass bead finish
316L strip coupon	CO1181590104110 (Metal Samples Co.)	Glass bead finish
304 strip coupon	CO1181410104110 (Metal Samples Co.)	Glass bead finish
C1010 disc coupon	CO2203750304110 (Metal Samples Co.)	Sanded, 120 grit
316L disc coupon	CO2201590304110 (Metal Samples Co.)	Sanded, 120 grit
304 disc coupon	CO2201410304100 (Metal Samples Co.)	Sanded, 120 grit

Chapter 4. Bench-Scale Corrosion Measurement

The work in this chapter was published as a paper in the proceedings of the 13th international conference on Greenhouse Gas Control Technologies (Fischer et al., 2017). Some early work on corrosion in thermal cylinders was performed by Daniel Hatchell, an undergraduate researcher (Hatchell et al., 2015; Hatchell et al., 2014). The experimental work with thermal cylinders and several of the experiments in the corrosion loop in this chapter was performed by Akshay Daga, another undergraduate researcher.

Two methods were developed to measure the corrosion of carbon steel (C1010) and stainless steel (316L) in solutions of ethanolamine, piperazine, and several other linear amines at high temperature and pressure. The effect of amine concentration, CO_2 loading, and temperature were measured. The first method uses Swagelok® steel cylinders heated in ovens to accelerate corrosion of the metal surface, which is then estimated by measuring dissolved metal. Although the steel cylinder method gave reasonable corrosion rates for 316L, it significantly under predicted the corrosion rate of C1010. This is likely due to the weakly adhering passive film that was protective only at the stagnant conditions in the non-agitated cylinders. The second method uses an electrical resistance probe to measure corrosion in a bench-scale thermosiphon apparatus, which was constructed to simulate more realistic flow conditions. Both methods were used to examine a series of linear amines and their results were compared. Corrosion of the electrical resistance probe by a variety of degraded piperazine solutions from pilot plants was measured. Loading was found to be the dominant factor in piperazine corrosion. Unexpectedly, corrosion rates of stainless steel decrease at high CO_2 loadings. Degraded piperazine was only slightly more corrosive than clean piperazine at most conditions. Over a wide variety of conditions, 1010 carbon steel showed lower corrosion rates in piperazine solutions than 316L stainless steel.

4.1. CORROSION LOOP RESULTS: PIPERAZINE

A large variety of piperazine (PZ) solutions were screened using ER corrosion probes in the corrosion loop apparatus. A summary of all PZ experiments conducted with the corrosion loop is given in Table 4-1. Concentration varied from 3 m to 8 m, loading from 0.20 to 0.32, temperature from 100°C to 160 °C, and both C1010 and 316L were evaluated using two separate ER probes. Amine loading here is defined as mol CO_2 per mol alkalinity. In addition to clean PZ, a variety of amines previously used in pilot plant campaigns were tested to evaluate the effect of amine degradation on corrosion. One of the pilot plant solutions was used in the CSIRO pilot plant (2013) at the coal-fired Tarong power station in Queensland, Australia. Degradation products in Tarong PZ have been characterized by Cousins (Cousins et al., 2015). The Tarong PZ was diluted during transport to a concentration of 3 m. PZ from the 2011 pilot plant campaign of the Separations Research Program (SRP) of the University of Texas was also used. The SRP campaign used a synthetic flue gas consisting of CO_2 mixed with air, and the PZ contains an oxidation inhibitor referred to here as inhibitor A (Paul T. Nielsen et al., 2013).

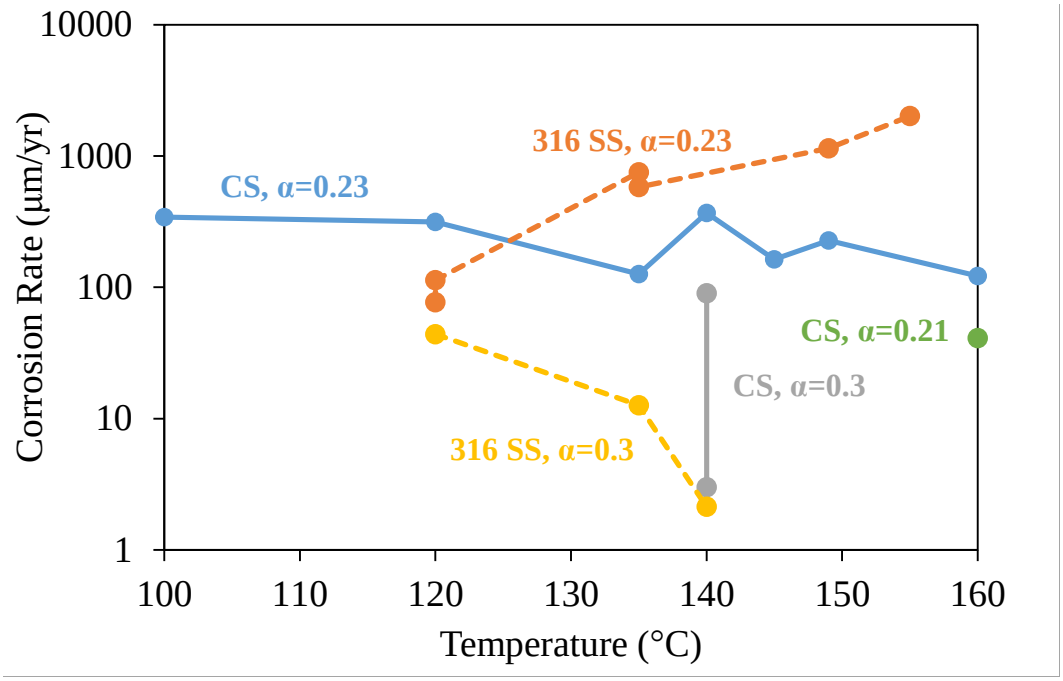

Figure 4-1: ER Probe corrosion of C1010 and 316L in PZ solutions in corrosion loop

The effect of loading and temperature on PZ corrosion is shown in Figure 4-1. This figure combines PZ solutions of varying concentrations and impurity levels, showing that temperature and loading trends are far more dominant than the effect of concentration, impurities, or degradation. Loading was varied over a small range, but had a dramatic effect on PZ corrosion. At loadings of $\alpha = 0.23$, stainless steel experienced corrosion with a strong temperature effect, with fair performance at 135 °C, but poor performance at 149 °C and higher. At similar loadings of $\alpha = 0.23$, carbon steel performance was good, and showed no temperature effect. The lack of a temperature effect suggests carbon steel corrosion has a different mechanism than stainless steel corrosion. At higher loadings of $\alpha = 0.3$, both carbon steel and stainless steel showed excellent corrosion performance. This contradicts conventional wisdom that higher CO_2 loading is always more corrosive (DuPart et al., 1993). Higher loading passivates carbon steel by the formation of a protective $FeCO_3$ layer,

as other researchers have observed (Zheng, Landon, Matin, et al., 2014). The reason for improved stainless performance at higher CO2 loadings is not immediately apparent.

PZ degradation apparently increased corrosion, although its effect was not as significant as either CO_2 loading or temperature. The effect of PZ degradation and temperature on corrosion with loading held constant at α = 0.23-0.24 is shown in Figure 4-2. PZ heavily degraded in the High Temperature Oxidation Reactor (HTOR) developed by Voice (Voice, 2013) was compared to several other solutions to see if a heavily degraded solution caused rapid corrosion. The HTOR PZ was compared to the Tarong PZ (slightly degraded) and the SRP PZ (clean with Inhibitor A). Stainless steel corrosion varied strongly with temperature from good at 120 °C to poor at 149 °C. The slightly degraded Tarong PZ experienced more severe corrosion than the clean SRP PZ, especially at high temperature. At 155 °C, the Tarong PZ caused 316L corrosion at a rate of 2010 μm/yr, 70% faster than the clean SRP PZ at 1140 μm/yr and 149 °C. Both of these corrosion rates are poor, but the difference is significant and shows that stainless steel corrosion is impacted by degradation products at intermediate loadings. However, at higher loading of α = 0.30, the Tarong PZ becomes non-corrosive to stainless steel (13 μm/yr at 135 °C). Carbon steel showed low corrosion for all three solutions tested, and apparently temperature did not affect corrosion. Both the clean SRP PZ and the slightly degraded Tarong PZ showed good performance, even at high temperature. The heavily degraded HTOR PZ had a slightly higher corrosion rate, although its performance was still good.

ORP did not show a clear relationship with corrosivity. In addition ORP values of the same solution were occasionally different between experiments. This might be a hysteresis effect on the platinum electrode between experiments. However, we expect the electrode potential to be relatively reducing in these experiments, because any dissolved oxygen in solution should rapidly be consumed by reaction with the amine (Voice, 2013).

Degraded amine solutions frequently had relatively reducing ORP values (less than -400 mV vs Ag/AgCl), whereas clean PZ solutions frequently had relatively oxidizing ORP values (greater than -200 mV). This suggests that degradation products have a strong effect on electrode potential.

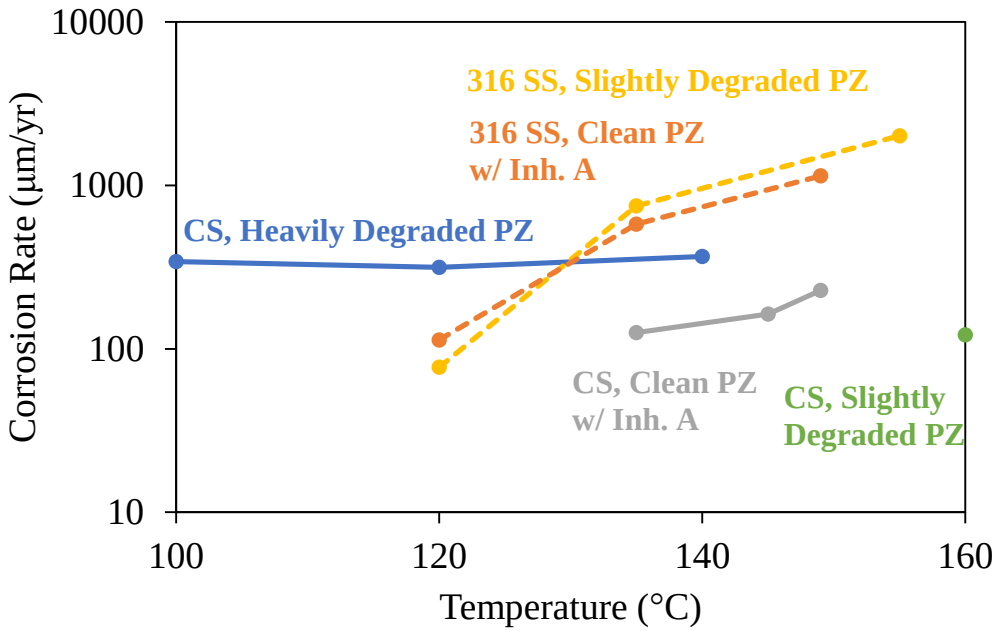

Figure 4-2: ER Probe corrosion of C1010 and 316L in piperazine solutions at loading of α = 0.23-0.24 in corrosion loop

Table 4-1: ER probe corrosion of C1010 and 316L in PZ solutions

Amine	T (°C)	α	C (μm/yr)	Alloy	P (psig)	Time (hr)	Avg. ORP (mV vs Ag/AgCl)	Notes
8 m PZ	160	0.21	-69 ± 1	C1010	140	57	NA	
8 m PZ	140	0.3	90 ± 35	C1010	130	8	NA	90 mmol/kg EDA
5 m PZ	140	0.31	3 ± 3	C1010	120	72	-584 ± 33	130 mmol/kg formate, other HSS
8 m PZ	160	0.20	41 ± 2	C1010	105	41	NA	90 mmol/kg EDA
3 m Tarong PZ	160	0.230	122 ± 1	C1010	145	63	NA	Degraded
4 m HTOR PZ	100	0.239	342 ± 13	C1010	6	23	-560 ± 25	Inh A, Very Degraded
4 m HTOR PZ	120	0.239	315 ± 19	C1010	38	23	-562 ± 34	Inh A, Very Degraded
4 m HTOR PZ	140	0.239	368 ± 2	C1010	95	89	-555 ± 36	Inh A, Very Degraded
8 m SRP PZ	149	0.238	228 ± 11	C1010	150	23	-451 ± 25	Inh A
8 m SRP PZ	145	0.238	163 ± 15	C1010	133	18	-391 ± 36	Inh A
8 m SRP PZ	135	0.238	126 ± 2	C1010	85	91	-471 ± 25	Inh A
3 m Tarong PZ	155	0.230	2012 ± 9	316L	150	26	-562 ± 22	Degraded
3 m Tarong PZ	135	0.230	749 ± 7	316L	65	32	-132 ± 165	Degraded
3 m Tarong PZ	120	0.230	77 ± 16	316L	25	17	-571 ± 23	Degraded
8 m SRP PZ	149	0.238	1143 ± 31	316L	155	11	-232 ± 92	Inh A
8 m SRP PZ	135	0.238	579 ± 4	316L	82	43	-167 ± 34	Inh A
8 m SRP PZ	120	0.238	113 ± 11	316L	35	20	-244 ± 37	Inh A
5 m PZ	135	0.32	-97 ± 5	316L	105	46	-146 ± 32	
5 m PZ	140	0.32	2 ± 2	316L	130	119	-168 ± 30	
5 m PZ	140	0.32	-6 ± 1	316L	130	162	NA	Inh A
3 m Tarong PZ	120	0.30	44 ± 14	316L	63	37	NA	Degraded
3 m Tarong PZ	135	0.30	13 ± 6	316L	130	45	NA	Degraded

4.2. CORROSION LOOP RESULTS: LINEAR AMINES

Several linear amine solutions were screened using ER corrosion probes in the corrosion loop apparatus. Table 4-2 summarizes all linear amine experiments conducted in the corrosion loop. The amines tested were ethanolamine (MEA), 3-amino-1-propanol (MPA), and ethylenediamine (EDA). Temperature was varied from 80 to 120 °C over moderate loadings (α = 0.37 to 0.46) to study the relationship between amine structure and corrosion. Figure 4-3 shows that amines can have dramatically different intrinsic corrosion rates. At 120 °C and α = 0.42, EDA, although structurally similar to MEA corrodes carbon steel at 42300 μm/yr compared to an MEA (α = 0.44) corrosion rate of 14000 μm/yr. Both rates are unacceptable, and even at 80 °C MEA corrosion of carbon steel is close to unacceptable. However, with MEA at very lean conditions of α = 0.2, carbon steel has outstanding corrosion performance of 19 μm/yr.

316L stainless steel exhibits good corrosion resistance to MEA at α = 0.42, with an apparently strong effect of temperature. MPA is intrinsically less corrosive to both carbon steel and stainless steel, as shown in Figure 4-4. At loadings of α = 0.37, carbon steel showed good corrosion resistance, while 316 SS had outstanding resistance. Despite the structural similarities of MEA and MPA, they display remarkably different intrinsic corrosivities. This may be because MPA is longer and more labile than MEA, which prevents it from forming stable amine-metal complexes and keeps iron from being stabilized in solution. Interestingly, the corrosion of carbon steel in MPA shows a decrease at higher temperature.

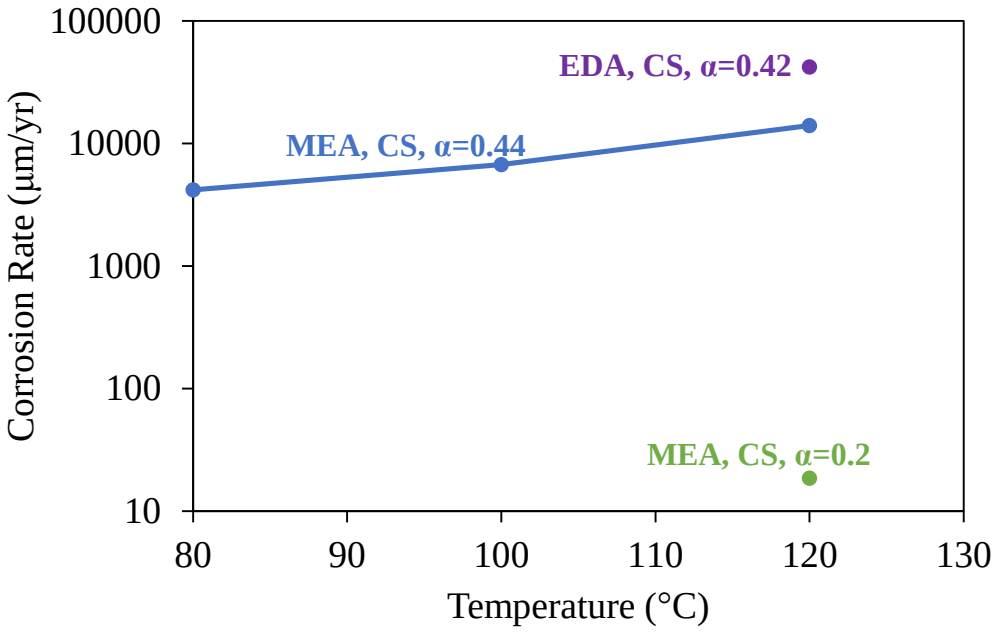

Figure 4-3: ER Probe corrosion of C1010 in MEA and EDA solutions in corrosion loop

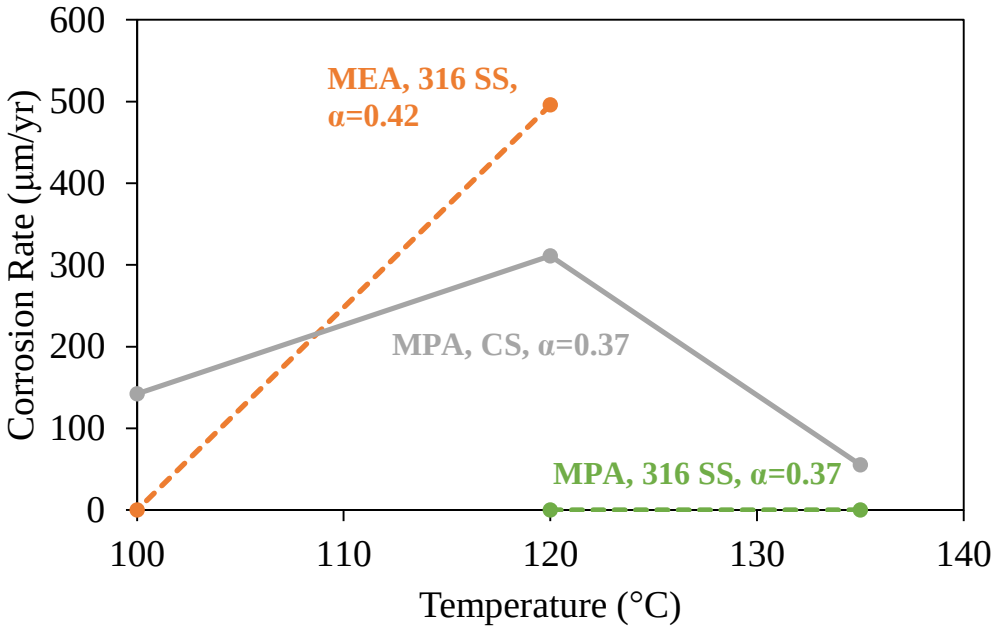

Figure 4-4: ER Probe corrosion of C1010 and 316L in MEA and MPA solutions in corrosion loop

Table 4-2: ER probe corrosion of C1010 and 316L in MEA, MPA, and EDA solutions

Amine	T (°C)	α	C (μm/yr)	Alloy	P (psig)	Time (hr)	Avg. ORP (mV vs Ag/AgCl)
9 m MEA	120	0.20	19 ± 1	C1010	12	43	NA
9 m MEA	120	0.19	-2 ± 1	C1010	10	133	NA
9 m MEA	80	0.46	4192 ± 56	C1010	150	3	NA
9 m MEA	100	0.44	6754 ± 111	C1010	45	2	NA
9 m MEA	120	0.44	14006 ± 66	C1010	82	4	NA
12 m EDA	120	0.42	42254 ± 161	C1010	89	5	NA
10 m MPA	100	0.37	142 ± 4	C1010	5	45	-406 ± 58
10 m MPA	120	0.37	311 ± 12	C1010	25	21	-560 ± 59
10 m MPA	135	0.37	55 ± 11	C1010	65	23	-253 ± 37
9 m MEA	120	0.42	496 ± 23	316L	65	19	-494 ± 50
9 m MEA	100	0.42	-155 ± 1	316L	20	35	-360 ± 29
10 m MPA	120	0.37	-79 ± 4	316L	25	51	-262 ± 36
10 m MPA	135	0.37	-1 ± 1	316L	65	164	-239 ± 77

4.3. LIMITATIONS OF CORROSION LOOP RESULTS

Clearly the formation of protective products is an important factor in the corrosion of C1010 in PZ solutions. One limitation of this work is that the protective products formed on the ER probe element were not cleaned between experiments. Although the probe elements were washed with water, the literature-recommended acid cleaning procedure (ASTM, 2017) was not performed to ensure products had been removed. Apparently, the effect of this was not significant. For example, frequently a temperature series was generated by running one experiment after another, using the same solution, without shutting down. Despite the lack of cleaning and the similar conditions in these time series, significantly different corrosion rates were determined for the different temperatures. This suggests that corrosion product films rapidly equilibrate with surrounding amine solutions when conditions change. Film formation on carbon steel in H_2O-CO_2 occurs rapidly (5

hours) at 80°C, although it is far slower at 55 °C (>25 hours) (Nešić & Lee, 2003). Presumably at high temperatures, the $FeCO_3$ film dissolution is relatively rapid at solutions where $FeCO_3$ film formation is not favored. However, it cannot be ruled out that the hysteresis of the ER probe affected corrosion measurements. In later work at pilot plants, ER probes were carefully cleaned at the beginning of experiments.

ER probe corrosion rates in this chapter were not confirmed by simultaneous weight loss coupon immersion. Given significant disagreement between ER probes and corrosion coupons at a later date in the pilot scale, a series of coupon experiments should be performed at the bench-scale to determine if the bench-scale ER measurements are reliable. It is not clear why ER probes give apparently reliable measurements at bench-scale, but are less reliable at pilot scale.

The corrosion loop flow rate is not controlled or measured. It is certainly slower than common fluid velocities used in amine scrubbing units. Some films that are protective at the low velocities present in the corrosion loop may not be protective at realistic velocities.

4.4. THERMAL CYLINDER RESULTS: LINEAR AMINES

A series of thermal cylinder experiments was conducted to estimate the corrosion rates of both 316L and C1010 when exposed to a variety of linear amines. The results from all thermal cylinder experiments are summarized in Table 4-3. Some thermal degradation results from these experiments were presented previously by Hatchell (Hatchell et al., 2015). In addition to the amines previously screened, 1,3-diaminopropane (PDA), a longer analog of EDA, was evaluated. It did not have a dramatically different corrosivity than EDA. Figure 4-5 shows the effect of concentration on linear monoamines. There are two effects that are notable here other than the relationship between concentration and

corrosion rate. First, once again MEA is significantly more corrosive than its longer analog MPA. Second, carbon steel sometimes out-performed stainless steel. These two effects are discussed separately.

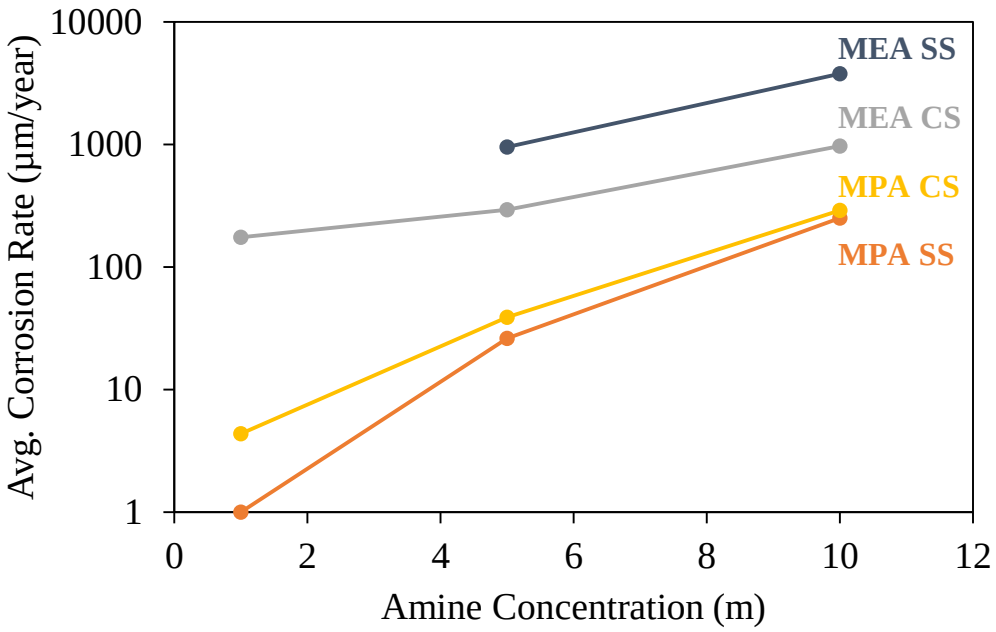

Figure 4-5: Linear monoamine concentration and its effect on average corrosion rate in thermal cylinders at 287-333 hrs., 316L and C1010, 135 °C, $\alpha = 0.35$

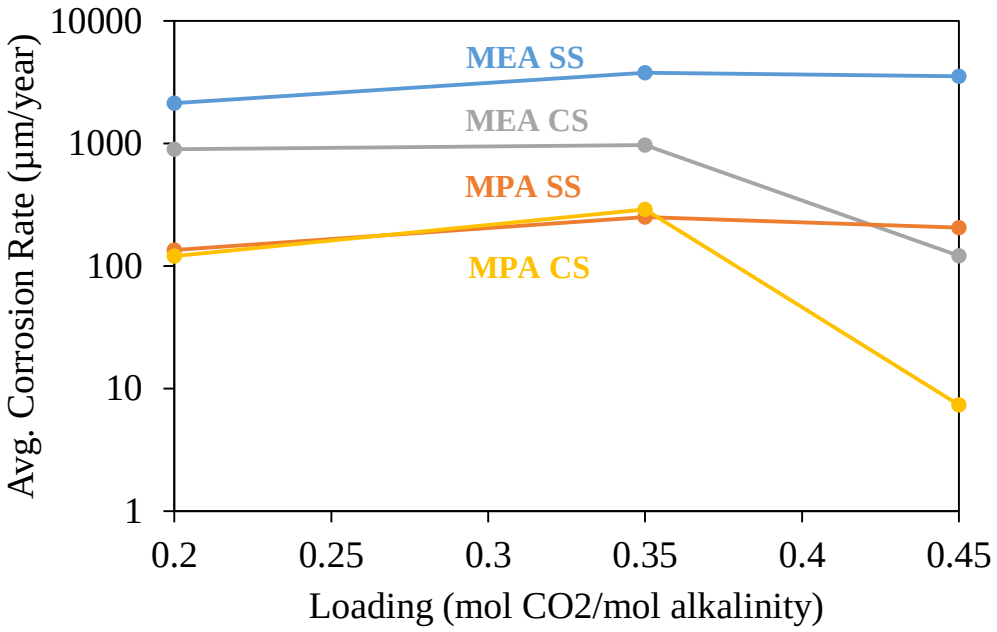

Figure 4-6: Linear monoamine loading and its effect on average corrosion rate in thermal cyinders at 287-333 hrs., 316L and C1010, 135 °C, 10 m

Increasing monoamine loading always increased corrosion for stainless steel (Figure 4-6). However, with carbon steel, increasing loading only increased corrosion up to a point, after which corrosion started decreasing. This can be attributed to increased precipitation of $FeCO_3$, forming a protective film at high loading.

Carbon steel seemed to outperform stainless steel in these experiments, despite significant industrial experience that suggests MEA corrodes stainless steel much less quickly than carbon steel. This is most evident in Figure 4-6, where carbon steel corroded less than stainless steel for MEA. During the experiments, scale was found on the inner surface of carbon steel cylinders, but was not found on the inner surface of stainless steel cylinders. Although corrosion products were not identified in this thermal cylinder work, the scale was likely $FeCO_3$ in some cases. This film did not adhere tightly in all cases, so it was probably sometimes only protective because the corrosion cylinders are stagnant and

not agitated. These experiments report low values for carbon steel corrosion, but the values are only valid for similar, stagnant conditions.

There appears to be a correlation between the rate of corrosion and the rate of formate production. These correlations are examined for several process conditions. Figure 4-7 give this correlation for 10 m amines at $\alpha = 0.35$. The least squares for the data suggests that for each mmol of formate that accumulated in solution, 2.75 mmol of metal had corroded from the cylinder wall. If formate were produced as part of the corrosion reaction, we would expect a constant relationship between formate and corrosion production. This ratio is not exactly constant, which suggests that there may be more than one mechanism producing formate. However, the correlation is strong enough to have some predictive value, and suggests that formate may participate in the corrosion reaction.

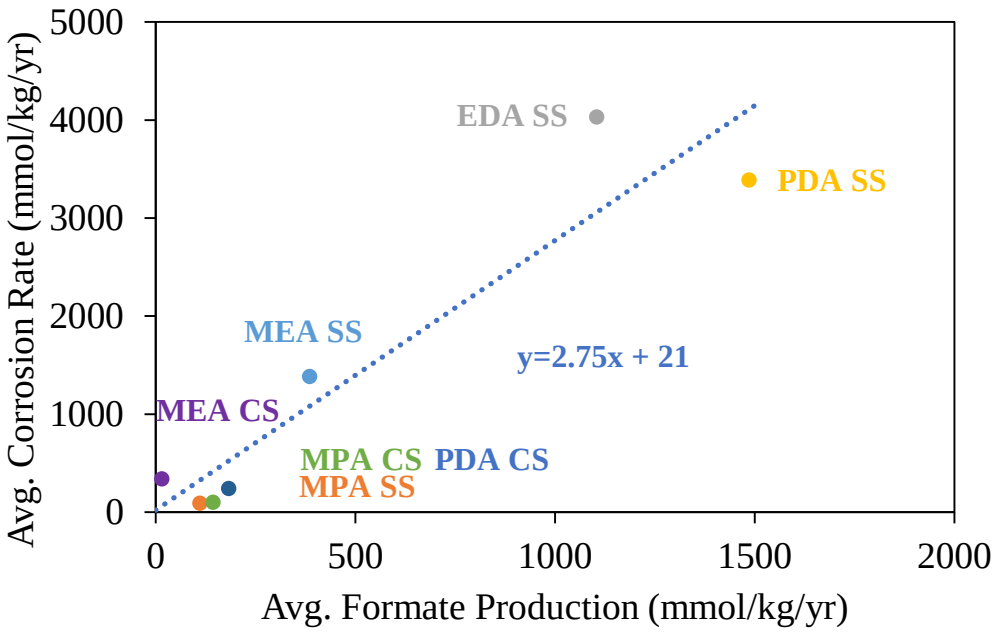

Figure 4-7: Formate production and average corrosion rate in thermal cylinders, 287-333 hrs., 316L and C1010, 135 °C, 10 m, $\alpha = 0.35$.

The thermal cylinder method yields useful qualitative data—for instance, showing the differences in intrinsic corrosivity between MEA, MPA, and EDA. However, this method significantly under predicted the corrosion of carbon steel by MEA. Thermal cylinders suggested a carbon steel corrosion rate of 121 μm/yr for a 10 m MEA solution (α = 0.45, 120 °C), whereas the ER corrosion probe gave a corrosion rate of 14000 μm/yr for a similar solution (9 m, α = 0.44, 120 °C). The thermal cylinder data for stainless steel actually over predicted corrosion relative to the ER corrosion probe, although it was much closer. We attribute these discrepancies to the stagnant conditions present in the thermal cylinders, which promotes formation of passivating films that are not representative of actual flow conditions.

Table 4-3: Thermal cylinder corrosion of C1010 and SS 316 L in MEA, MPA, EDA, PDA solutions

Conc. (m)	Amine	T (°C)	α	C (µm/yr)	C (mmol/kg/yr)	Alloy	Time (hr)	formate rate (mmol/kg/yr)
1	EDA	135	0.35	849	306	C1010	333	0
10	MEA	135	0.35	948	341	C1010	333	15
10	MEA	135	0.35	851	306	C1010	333	16
10	MEA	135	0.35	971	350	C1010	333	146
10	MEA	135	0.2	901	324	C1010	333	58
10	MEA	135	0.45	121	42	C1010	333	194
5	MEA	135	0.35	293	104	C1010	333	41
1	MEA	135	0.35	176	61	C1010	333	52
10	MPA	135	0.35	290	103	C1010	333	144
10	MPA	135	0.2	121	41	C1010	333	78
10	MPA	135	0.45	7	3	C1010	333	210
5	MPA	135	0.35	39	11	C1010	333	73
1	MPA	135	0.35	4	0	C1010	333	18
10	PDA	135	0.35	674	241	C1010	333	183
10	PDA	135	0.2	568	204	C1010	333	107
5	PDA	135	0.35	203	71	C1010	333	153
1	PDA	135	0.35	5	0	C1010	333	0
10	EDA	135	0.35	11038	4032	316L	333	1105
10	EDA	135	0.45	9422	3446	316L	333	1329
5	EDA	135	0.35	7251	2619	316L	333	2612
1	EDA	135	0.35	1152	404	316L	333	389
10	MEA	150	0.35	4254	1531	316L	333	2768
10	MEA	135	0.35	3781	1384	316L	288	386
10	MEA	120	0.35	1393	510	316L	333	186
10	MEA	135	0.2	2132	780	316L	333	162
10	MEA	135	0.45	3540	1292	316L	333	1100
5	MEA	135	0.35	956	344	316L	333	287
10	MPA	150	0.35	202	73	316L	333	292
10	MPA	135	0.35	252	92	316L	287	111
10	MPA	120	0.35	141	52	316L	333	69
10	MPA	135	0.2	135	50	316L	333	36
10	MPA	135	0.45	206	76	316L	333	57
5	MPA	135	0.35	26	9	316L	333	45
1	MPA	135	0.35	0	0	316L	333	0
10	PDA	135	0.35	9276	3387	316L	333	1486
10	PDA	135	0.2	10942	4002	316L	333	757

There is also a marked difference in oxidative degradation rates between the two-carbon backboned species, MEA and EDA, and the three-carbon backboned species, MPA and PDA. The more corrosive amines also show much greater rates of oxidative degradation, despite their structural similarity.

Table 4-4: Oxidation of amines in low gas flow apparatus at 70°C , 98 kPa O_2, 2 kPa CO_2, 100 ml/min gas flow, 1400 rpm, approx. 250 hr (Liu et al., 2015; Liu et al., 2014; Sexton, 2008).

	Concentration	Catalyst	Amine Loss (mM/hr)
EDA	5 m	0.4 mM Fe, 0.2 mM Mn, 0.05 mM Cr	9.788
PDA	5 m	0.4 mM Fe, 0.2 mM Mn, 0.05 mM Cr	negligible (<1)
MEA	7 m	0.6 mM Cr, 0.1 mM Ni	8
MPA	10 m	0.4 mM Fe 0.2 mM Mn, 0.05 mM Cr	negligible (<1)

One hypothesis for the different behavior of the linear amines is that the propylamines are too long and labile to form a stable metal center. This reduces the favorability of steel oxidation, and the absence of these metal catalytic complexes reduces amine oxidation. Figure 4-8 illustrates this effect with a stable MEA carbamate complex with iron, contrasted with an unstable MPA carbamate metal complex. The two-carbon backbone of MEA allows it to form a very stable octahedral complex with iron. The same complex cannot be formed with the three-carbon backbone of MPA, as it is too long and labile to easily form an octahedral complex. In corrosion, these metal centers serve as catalysts for the reduction of bicarbonate to formate, which is accompanied by rapid oxidation and corrosion of the metal.

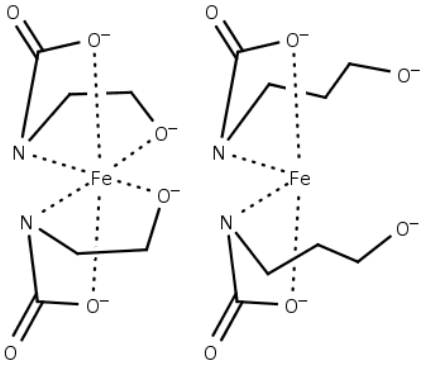

Figure 4-8: Hypothetical Stable MEA carbamate metal catalytic center (left) and unstable MPA carbamate metal catalytic center (right)

4.5. CONCLUSIONS

4.5.1. Corrosion in steel thermal degradation cylinders and corrosion by measurement of electrical resistance in a loop apparatus gave similar results for relative amine corrosivity.

These methods were developed for quick screening of the performance of C1010 and 316L in different amines. Qualitatively, the methods gave similar predictions for the relative intrinsic corrosivity of different linear amines. These methods were applied at temperature and reducing conditions most representative of stripper bottoms. One limitation of both methods is that they may be more reducing than in a plant with flue gas (and O_2) cycling

4.5.2. Thermal cylinders are useful for predicting relative corrosivity of amines, but they underpredict carbon steel corrosion rates and overpredict stainless steel corrosion rates..

Thermal cylinders are useful for quick, qualitative predictions about the intrinsic corrosivity of different amines. However, the method significantly under-predicted carbon steel corrosion rates. Most notably, corrosion of C1010 in MEA is an order of magnitude lower than C1010 corrosion at comparable pilot conditions. This is probably due to the

non-agitated, stagnant conditions in the thermal cylinders, which promote formation of passivating films that may not be protective at representative flow conditions. Stainless steel (316L) corrosion measurements in MEA appear significantly higher than in comparable pilot plants. This is likely because the anoxic, reducing environment of corrosion cylinders is particularly challenging for 316L.

4.5.3. Thermal cylinders suggest that each mol of formate generation is accompanied by 2.75 mol of steel corrosion.

Formate generation in C1010 and 316L thermal cylinders containing MEA, MPA, EDA, PDA was compared to corrosion rates. There is a correlation between formate generation and corrosion. This suggests that the reduction of bicarbonate to formate could be a dominant reduction accompanying corrosion in anoxic conditions.

4.5.4. Ethylamines, such as, MEA and EDA, are more corrosive than their propylamine counterparts, EDA and PDA. The ethyl- backbone amines likely form more stable coordination complexes with oxidized iron, increasing corrosion.

The amines evaluated were: ethanolamine (MEA), 3-amino-1-propanol (MPA), ethylenediamine (EDA), and 1,3-diaminopropane (PDA). MEA was significantly more corrosive to C1010 and 316L than MPA in both thermal cylinders and the corrosion loop. EDA. The results are less complete for EDA/PDA, but PDA appears to be less corrosive than EDA to 316L in thermal cylinders. One hypothesis is that ethylamine carbamates form very stable octahedral complexes with iron. The same complex cannot be formed with the longer propylamine carbamates as it is too long and labile to easily form an octahedral complex

4.5.5. The corrosion loop with an electrical resistance probe yields realistic corrosion rates for C1010 in amines.

Unlike thermal cylinders, which gave unrealistic C1010 corrosion rates due to its stagnant conditions, the corrosion loop appears to accurately represent conditions of amine corrosion. The ER probe gave apparently realistic corrosion rates during short bench-scale experiments, unlike later experiments at the pilot scale.

The corrosion rates for 316L in MEA seem to be higher than in representative pilot plants. This is likely because the reducing environment of the corrosion loop is particularly challenging for 316L.

4.5.6. Stainless steel sometimes experiences attack in PZ at high temperature, anoxic conditions.

In several solutions of slightly degraded PZ, at lean loadings ($\alpha \approx 0.23$), 316L experienced corrosion with a strong temperature effect, with good performance at 120 °C (<150 μm/yr), but poor performance (>1000 μm/yr) at 149 °C and higher. Notably, attack of stainless was not observed in completely clean PZ at similar conditions. Counterintuitively, at higher loading of $\alpha = 0.3$, both carbon steel and stainless steel showed excellent corrosion performance (<100 μm/yr). It is not clear why stainless steel performed well at higher CO_2 loadings. These stainless corrosion rates may be higher than in a real plant, because the reducing environment of the corrosion loop is particularly challenging for 316L.

4.5.7. Carbon steel experiences low corrosion at high temperature in PZ solutions.

From 100°C to 160°C, at lean loadings ($\alpha \approx 0.23$), even in very degraded solutions of PZ, C1010 performance was good to moderate (< 400 μm/yr), and showed no strong increase with temperature. Counterintuitively, at higher loading of $\alpha = 0.3$, both carbon

steel and stainless steel showed excellent corrosion performance (<100 μm/yr). Higher loading probably passivates carbon steel by promoting the formation of a $FeCO_3$ layer.

4.5.8. PZ degradation apparently accelerates corrosion of carbon and stainless steel.

PZ degradation apparently increased corrosion of both C1010 and 316L. Completely fresh PZ solutions were often non-corrosive to both C1010 and 316L. Pilot plant degraded amines corroded both materials more quickly. A more deliberate study is needed to clearly separate the effects of amine concentration, CO_2 loading, and degradation.

Chapter 5. Fe^{2+} Solubility and Siderite Formation in Monoethanolamine and Piperazine

The work in this chapter was submitted as a paper to the proceedings of the 14th international conference on Greenhouse Gas Control Technologies. Significant experimental work in this chapter was performed by Shyam S. Sharma, an undergraduate researcher.

A protective $FeCO_3$ layer is known to sometimes form on carbon steel and can inhibit corrosion. Although the formation of this layer is understood in simple aqueous systems, its behavior in CO_2 capture solutions is not well understood. $FeCO_3$ layer formation is driven by supersaturation, so accurate measurements of equilibrium Fe^{2+} solubility need to be made. The relationship between amine type, degradation level, CO_2 loading, and temperature on Fe^{2+} solubility was measured with the goal of determining at what conditions $FeCO_3$ precipitates out of amines. MEA and PZ solutions with differing CO_2 loadings and degradation levels were placed in agitated, sealed reactors with 0.25 M $FeSO_4$ and Na_2CO_3. Several experiments used air and CO_2 sparged reactors to simulate absorber conditions. Liquid samples were taken from the reactors over time and analyzed for dissolved Fe^{+2}/Fe^{+3} using ICP-OES. After the experiments reached equilibrium, solid samples were taken from the reactors and characterized using powder X-ray diffraction (XRD). 9 m MEA was found to have Fe^{2+} solubility 10X-100X higher than clean 5 m PZ. Degraded PZ showed Fe^{2+} solubility 10X-700X higher than clean PZ. $FeCO_3$ was only found to form in rich clean PZ and rich degraded PZ. Lean MEA and lean PZ (both clean and degraded) formed magnetite while rich MEA formed goethite. Similar to measurements in aqueous systems, iron solubility for both MEA and PZ decreased with increasing temperature. CO_2 loading effects were a little more complicated. In MEA, Fe^{2+}

solubility increased with increasing loading. In PZ, Fe^{2+} solubility decreased with increasing loading.

5.1. INTRODUCTION

The formation of $FeCO_3$ and FeS protective films is well studied in the context of CO_2-H_2O-H_2S systems (Y. Zheng et al., 2016). Formation of $FeCO_3$ depends on supersaturation of Fe^{2+} and CO_3^{2-}, shown in Equation 5-1. The rate of $FeCO_3$ formation, shown in Equation 5-2, has been modelled based on species supersaturation at the metal surface (W. Sun et al., 2008). Although not shown here, mass transfer models to account for transport of species from the bulk solution to the steel surface have been developed (Nešić & Lee, 2003; Nešić, Nordsveen, et al., 2003; Nordsveen et al., 2003; Y. Zheng et al., 2016). Nomenclature used in these equations is given in Table 5-1.

$$SS = \frac{a_{Fe^{2+}} a_{CO_3^{2-}}}{K_{sp}} \tag{5-1}$$

$$R_{FeCO_3} = e^{28.20 - \frac{64.85}{RT}} \frac{S}{V} K_{sp} (SS - 1) \tag{5-2}$$

Table 5-1: Nomenclature for Fe^{2+} solubility

C_{Fe}	"Equilibrium" soluble Fe (mmol/kg)
$a_{Fe^{2+}}$	Activity of Fe^{2+} (mol/L)
$a_{CO_3^{2-}}$	Activity of CO_3^{2-} (mol/L)
K_{sp}	Solubility product constant for $FeCO_3$ (mol^2/L^2)
SS	Supersaturation of $FeCO_3$
R_{FeCO_3}	Precipitation rate of FeCO3 (mol/m^3s)
$\frac{S}{V}$	Surface area to solution volume ratio (1/m)
I	Ionic strength (mol/L)

The accuracy of this model depends on having high quality values of K_{sp}. The K_{sp} values used by previous researchers were measured in aqueous systems of pH 4-6, which have low iron solubilities and thus low K_{sp} values (W. Sun et al., 2009). K_{sp} in these systems has been reported as 1.28×10^{-11} mol^2/L^2 at T = 25 °C and $I \approx 0$, and varies with T_k and I as given below in Equation 5-3 (W. Sun et al., 2009), where T_k is temperature (Kelvin) and I is ionic strength (mol/L). This equation shows that K_{sp} generally decreases with increasing T and increases with increasing *I* at low values of *I*.

$$log(K_{sp}) = -59.3498 - 0.041377T_k - \frac{2.1963}{T_k} + 24.5724\, log(T_k) + 2.518I^{0.5} - 0.657I \quad (5\text{-}3)$$

K_{sp} values measured in simple aqueous systems are not representative of multicomponent, high ionic strength amine solutions used for CO_2 capture. Accurate Fe^{2+} solubility data is crucial to developing a model that allows prediction of the conditions under which $FeCO_3$ will form. Understanding when this $FeCO_3$ layer forms is crucial for understanding which amines and conditions are compatible with carbon steel construction.

5.2. METHODS

A series of bench-scale experiments was conducted to determine Fe^{2+} solubility while varying amine type, degradation level, CO_2 loading, and temperature. Amine solutions (Alfa Aesar) were added to a jacketed, 1 L, glass reactor containing a Teflon stir bar. Next, 0.25 M $FeSO_4$ and 0.25 M Na_2CO_3 from (Fisher Scientific) were added as solids to the reactor. Several experiments used $FeCl_3$ (Fisher Scientific) rather than $FeSO_4$ to investigate Fe^{3+} solubility.

9 m MEA, 5 m clean PZ, and several degraded pilot plant PZ solutions were evaluated at rich and lean loading. Three pilot plant piperazine solutions were evaluated to

study the effect of degradation on Fe^{2+} solubility, they are referred to as Tarong PZ, 8 m SRP PZ, and 5 m SRP PZ. The Tarong PZ is from a pilot plant operated at the Tarong Power station in Queensland, Australia. The plant operated for 1700 hours, and the coal flue gas contained 200 ppm NO, <5 ppm NO_2, and other impurities. The Tarong PZ is used here to represent a heavily degraded PZ. Degradation products in Tarong PZ have been characterized by Cousins (Cousins et al., 2015). The Tarong PZ was diluted for transport to a concentration of 3 m, so this concentration was used for these experiments. A sample of 8 m PZ from the 2011 pilot plant campaign of the Separations Research Program (SRP) at the University of Texas was also evaluated. The "8 m SRP PZ" used in this work was from a 2011 sample taken after 1350 hours of operation. The SRP pilot plant used a synthetic flue gas consisting of CO_2 mixed with air, and the PZ contains an oxidation inhibitor referred to here as Inhibitor A (Paul T. Nielsen et al., 2013). The SRP PZ was later diluted to 5 m and used in two additional pilot plant campaigns (2015, 2017). The 2015 campaign was described by Chen (E. Chen et al., 2017). The SRP PZ sampled after the 2017 pilot plant campaign accumulated a total of 1700 operating hours and is referred to here as "5 m SRP PZ." Although the 5 m SRP PZ has accumulated more operating hours than the 8 m SRP PZ, they primarily differ in PZ concentration, not in degradation level. This is because the synthetic flue gas used at SRP contains no contaminants, and as a result degradation of PZ and accumulation of heat stable salts is very slow. Both the "8 m SRP PZ" and the "5 m SRP PZ" are used to represent a solution with a low to moderate level of degradation.

Fe^{2+} solubility in 9 m MEA and 5 m clean PZ was investigated at 24 °C and 45 °C for both amines, with MEA also being evaluated at ≈ 60 °C. The 8 m SRP PZ experiments were conducted at 32 °C while the 5 m SRP PZ experiments were conducted at ≈ 45 °C

and ≈ 60 °C. The 3 m Tarong PZ experiments were done at 44 °C and 55 °C. All solutions were evaluated at rich and lean loadings at each temperature.

All metals analysis was done by inductively coupled plasma (ICP) optical emission spectroscopy. ICP is used to measure total iron in solution. Much of the discussion in this report assumes that all iron in solution is Fe^{2+} because Fe^{3+} is presumed to be insoluble. In reality, some of the iron in solution may be present as Fe^{3+}. The upper limit of calibration for these experiments is approximately 16.3 mmol/kg and the lower limit is approximately 0.076 mmol/kg. Several experiments report Fe concentrations below this calibration limit. Extrapolation outside these calibration limits is not strictly accurate. However, the instrument calibration is very linear and these results are within the instrument detection limit, so these results are included for the purpose of making qualitative conclusions about the behavior of these solutions.

5.3. RESULTS

In both MEA and clean PZ solutions, Fe^{2+} solubility initially was high before rapidly decreasing to an equilibrium concentration after approximately 100–200 hours (Figure 5-1). For MEA, the highest equilibrium Fe^{2+} was found in a cold rich solution. Moderate equilibrium Fe^{2+} solubility was observed for warm rich and cold lean solutions. The lowest Fe^{2+} solubility was seen in two warm lean experiments.

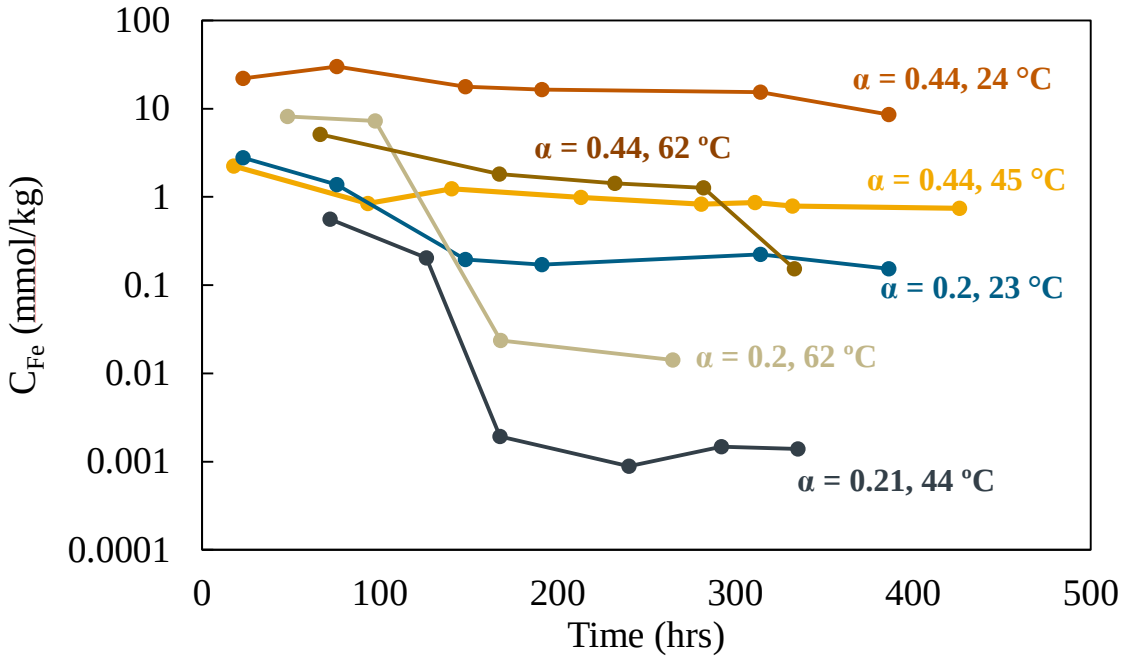

Figure 5-1: Soluble Fe in 9 m MEA with the addition of 0.25 M $FeSO_4$ and Na_2CO_3.

In clean 5 m PZ, most equilibrium Fe^{2+} was at least an order of magnitude lower than in MEA (Figure 5-2). Fe^{2+} solubility did not seem to vary significantly among the temperatures and loadings investigated. However, equilibrium Fe^{2+} was slightly higher at rich loadings for both warm and cold solutions. The two experiments done with clean PZ containing an oxidation inhibitor (referred to as "Inhibitor A") showed exceptionally low Fe^{2+} solubility at both rich and lean loadings. It is possible that the inhibitor (a free radical scavenger) catalysed the oxidation of Fe^{+2} to Fe^{+3}, which has significantly lower solubility than Fe^{2+}.

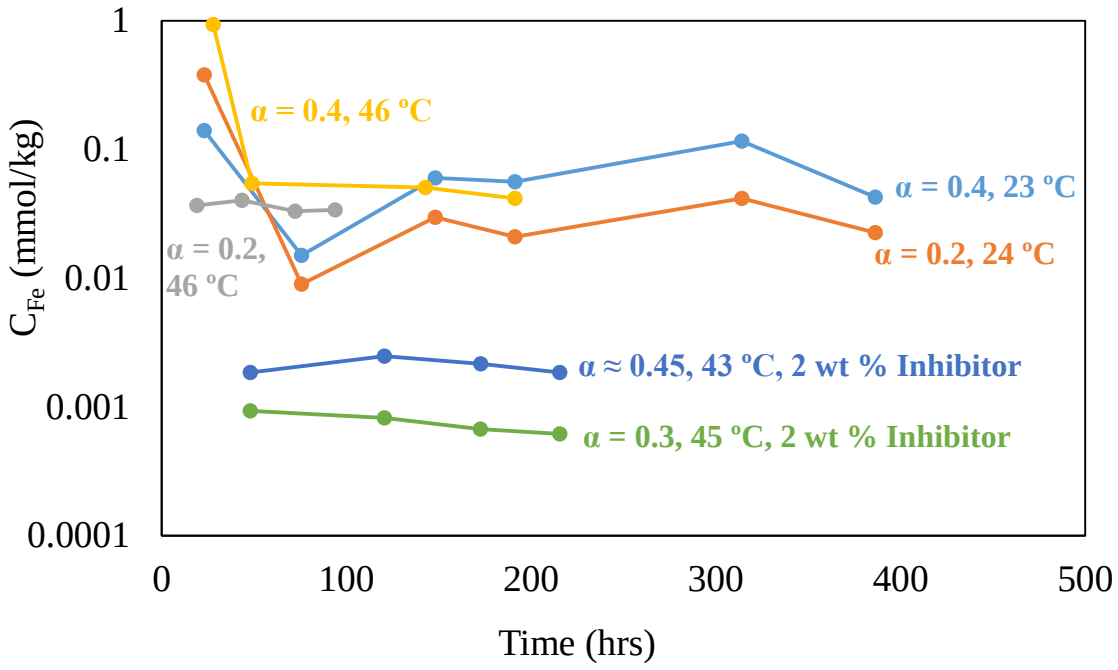

Figure 5-2: Soluble Fe in 5 m clean PZ with the addition of 0.25 M $FeSO_4$ and Na_2CO_3.

The MEA and clean PZ experiments reported in this paper are compared to those done by Fytianos (Fytianos, 2016) at similar conditions, as shown in Figure 5-3. This figure shows rich MEA and PZ Fe^{2+} solubilities with changing temperatures. The MEA and PZ experiments reported in this paper showed the same general trend. As temperature increased, Fe^{2+} solubility in rich MEA and PZ tended to decrease. The magnitude of this temperature effect in MEA was more significant in the current work. The temperature effect for PZ in this work seemed comparable to that for rich loading in Fytianos. Although Fytianos reported the PZ experiment as having a lean loading, it is likely that the loading was higher than α = 0.2 since the reactors were sparged with small amounts of CO_2. Regardless, he found higher Fe^{2+} solubility in PZ than this work. A key difference is that his experiments were shorter (72 hrs), and he did not add Na_2CO_3.

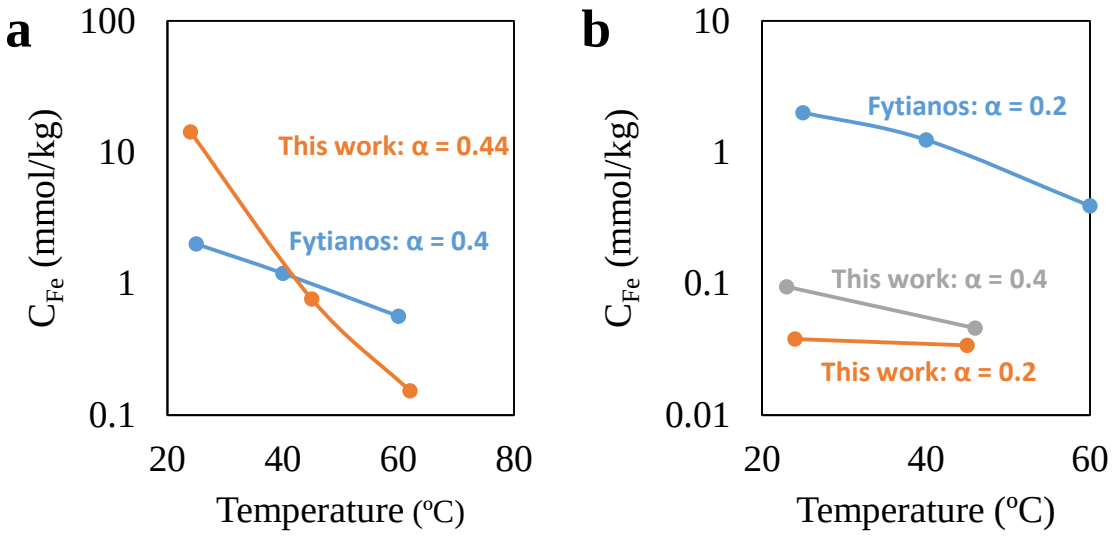

Figure 5-3: a) Rich MEA soluble Fe as a function of temperature. b) Rich PZ soluble Fe as a function of temperature (Fytianos, 2016).

At most conditions in the degraded SRP PZ, Fe^{2+} solubility was 10–100X higher than in clean PZ (Figure 5-4). In all degraded PZ solutions, Fe^{2+} solubility decreased as CO_2 loading increased. The highest equilibrium Fe^{2+} was observed for warm lean 5 m SRP PZ. 8 m SRP PZ showed comparable solubility to similar 5 m SRP solutions. Moderate Fe^{2+} was seen for warm rich 5 m solutions. The two experiments using Fe^{3+} showed very low Fe concentrations in warm solutions with both rich and moderate loadings. This shows that Fe^{3+} is not readily soluble in these solutions, and that Fe^{3+} is not readily converted to the more soluble Fe^{2+} under these conditions. The experiment conducted in the sparged reactor showed low Fe^{2+} solubility when sparged with 10% CO_2, 90% air. Switching the gas feed to 10% CO_2, 90% N_2 did not appreciably increase Fe^{2+} solubility. Experiments in prior work (Voice, 2013), showed that switching from an O_2/CO_2 to an N_2/CO_2 atmosphere contacting 8 m PZ in a cyclic oxidation reactor at 120 °C caused a rapid increase in dissolved metals, presumably due to corrosion of the stainless steel apparatus. The sparged

reactor experiments in this work were performed to evaluate if this rapid increase in dissolved metals were due to different metal solubilities in the different atmospheres. No appreciable increase in equilibrium dissolved iron occurred however. Apparently there is no quick switch in Fe^{2+} solubility with a change in atmosphere from air/CO_2 to N_2/CO_2 in 5 m SRP PZ at 45°C.

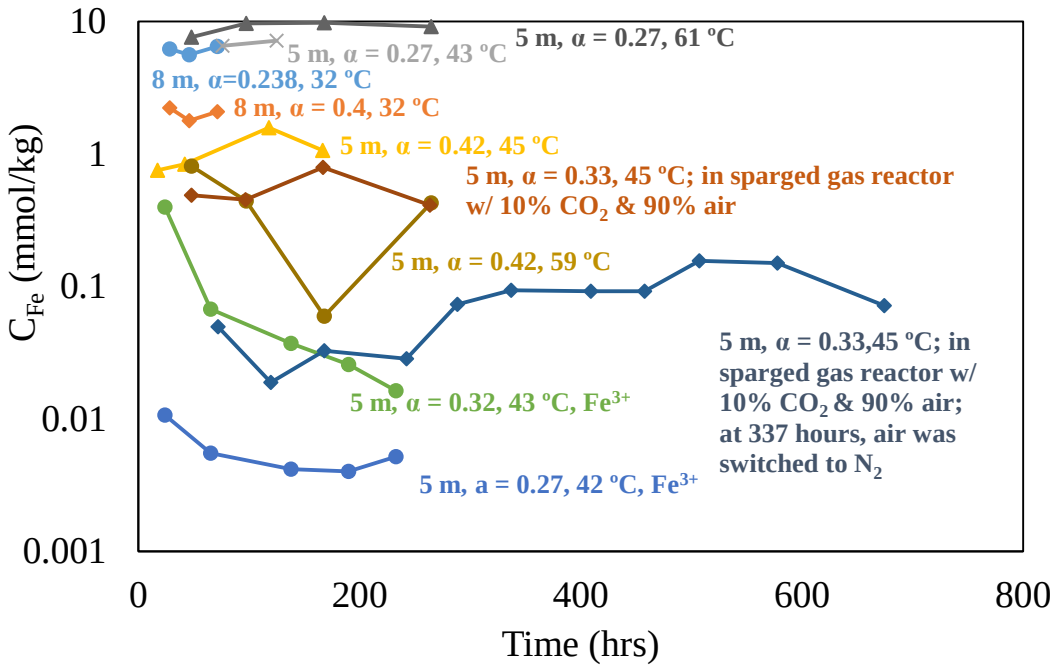

Figure 5-4: Soluble Fe in 5 m degraded SRP PZ with the addition of 0.25 M $FeSO_4$ and 0.25 M Na_2CO_3.

In warm lean 3 m Tarong PZ, Fe^{2+} solubility was several orders of magnitude higher than clean 5 m PZ solutions (Figure 5-5). Warm lean Tarong solutions had equilibrium Fe^{2+} over 100X what was seen in warm solutions with moderate loadings. Tarong solutions with moderate loadings showed a significant temperature dependence, with an experiment at 54 ºC having equilibrium Fe^{2+} approximately 40X higher than an experiment at 44 ºC and similar loading.

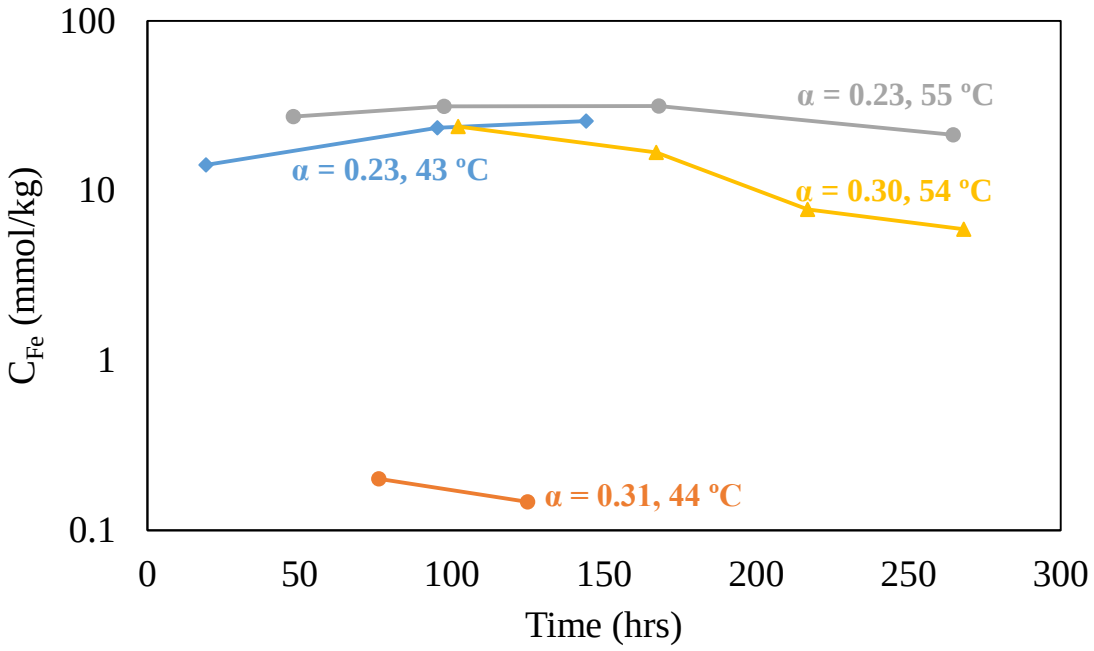

Figure 5-5: Soluble Fe in 3 m degraded Tarong PZ with the addition of 0.25 M $FeSO_4$ and Na_2CO_3.

In Figure 5-6, the equilibrium Fe^{2+} concentration is plotted as a function of temperature and loading for clean MEA and PZ. Rich MEA had a 10–100X higher equilibrium Fe^{2+} than lean or rich PZ at 24 and 45 °C. Fe^{2+} solubility was a very strong function of loading for MEA but not a significant one for clean PZ.

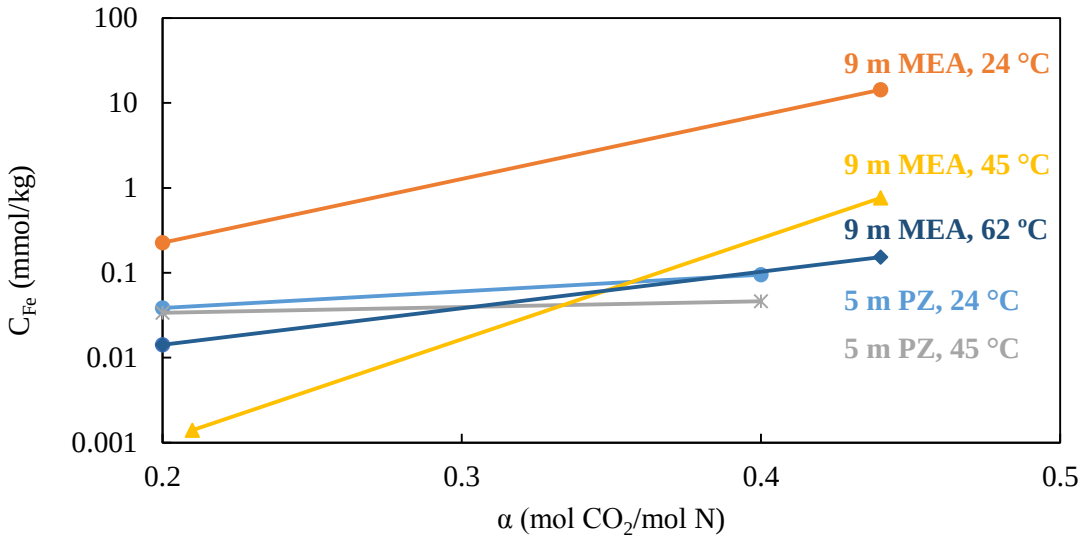

Figure 5-6: Soluble Fe as a function of CO_2 loading for 9 m MEA and 5 m PZ.

In Figure 5-7, the equilibrium Fe^{2+} concentration is plotted as a function of temperature and loading for degraded PZ solutions. Degraded Tarong PZ showed higher equilibrium Fe^{2+} as loading decreased. In SRP PZ, Fe^{2+} solubility appeared to become a stronger function of loading as temperature increased. SRP PZ also showed higher equilibrium Fe^{2+} as loading decreased.

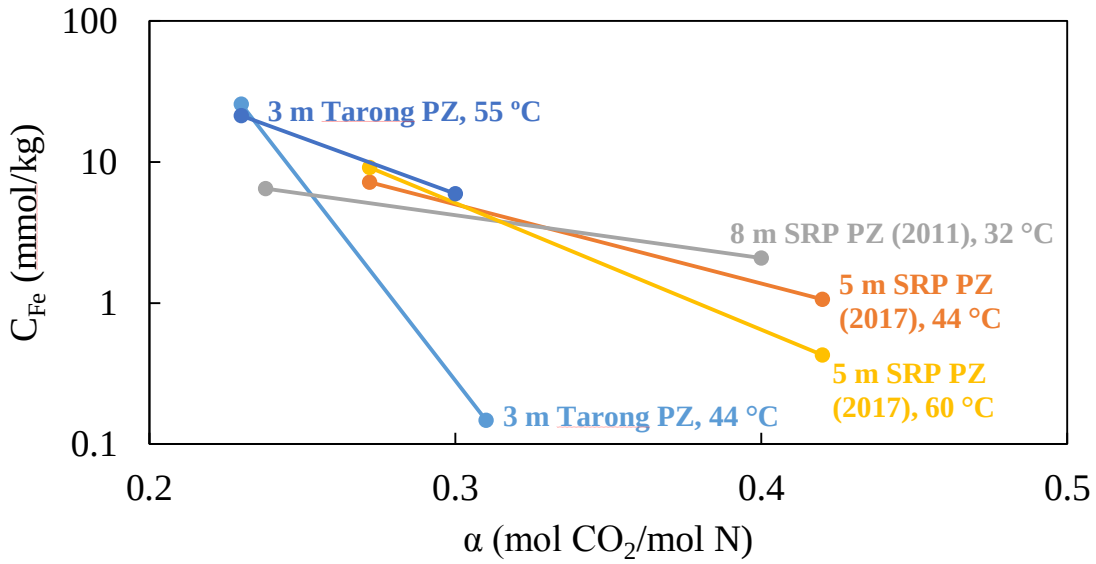

Figure 5-7: Soluble Fe as a function of CO_2 loading for degraded PZ.

The solid phases characterized in these experiments showed that $FeCO_3$ only formed under specific conditions. As seen in Table 5-2 and Table 5-3, $FeCO_3$ (siderite) was only identified in PZ solutions with rich CO_2 loading. Since siderite was found in both rich clean PZ and rich SRP PZ, its formation is independent of amine degradation level. Lean PZ solutions tended to form magnetite, as did lean MEA solutions. The solid sample from a rich MEA experiment that was characterized appeared to be FeO(OH) (goethite). The solid sample analyzed from the 5 m SRP PZ sparged gas reactor experiment with air and CO_2 formed goethite.

Table 5-2: Equilibrium Fe in 9 m MEA and 5 m clean PZ

Amine	CO_2 Loading (α)	T (°C)	Experiment Length (hrs)	C_{Fe} (mmol/kg)	Solid Phase (if identified)
9 m MEA	0.44	45	426	0.765	
9 m MEA	0.44	24	386	14.334	
9 m MEA	0.44	24	166	7.13	Goethite (FeO(OH))
9 m MEA	0.44	62	333	0.153	
9 m MEA	0.2	23	386	0.225	
9 m MEA	0.2	45	335	0.0014	Magnetite (Fe_3O_4)
9 m MEA	0.2	62	265	0.014	Magnetite (Fe_3O_4)
5 m PZ	0.4	46	191	0.046	
5 m PZ	0.4	45	167	0.047	Siderite ($FeCO_3$)
5 m PZ	0.4	23	386	0.095	
5 m PZ	0.2	24	386	0.038	
5 m PZ	0.2	45	94	0.034	

Table 5-3: Equilibrium Fe in degraded Tarong and SRP PZ

Amine	CO_2 Loading (α)	T (°C)	Experiment Length (hrs)	C_{Fe} (mmol/kg)	Solid Phase (if identified)
3 m Tarong	0.23	44	144	25.8	
3 m Tarong	0.23	55	386	21.36	Magnetite (Fe_3O_4)
3 m Tarong	0.31	44	125	0.147	
3 m Tarong	0.30	54	268	5.95	
8 m SRP	0.238	32	75	6.49	
8 m SRP	0.4	32	191	2.08	
5 m SRP	0.42	44	167	1.06	
5 m SRP	0.42	60	265	0.427	Siderite ($FeCO_3$)
5 m SRP	0.27	45	125	7.18	
5 m SRP	0.27	60	265	9.13	Magnetite (Fe_3O_4)
5 m SRP (w/Fe^{3+})	0.32	43	233	0.0163	
5 m SRP (w/Fe^{3+})	0.27	42	233	0.00519	
5 m SRP (in sparged gas reactor w/CO_2 & air)	0.33	45	264	0.412	Goethite (FeO(OH))
5 m SRP (in sparged gas reactor w/CO_2 & air; switched to N_2)	0.33	45	674	0.0717	

5.4. CONCLUSIONS

5.4.1. In loaded amine solutions, Fe^{2+} solubility is a strong negative function of temperature.

Fe^{2+} solubility for both MEA and PZ decreased with increasing temperature at almost all conditions tested. As an example, Fe^{2+} solubility in 9 m MEA (α = 0.44) decreased from 14 mmol/kg to 0.15 mmol/kg when T was increased from 24 °C to 62 °C. One implication of this is that protective $FeCO_3$ films will preferentially form at high temperature conditions due to lower equilibrium solubilities as well as presumably faster kinetics.

5.4.2. Fe^{2+} is significantly more soluble in MEA than clean PZ at rich loadings.

Rich 9 m MEA was found to have Fe^{2+} solubility of 0.77 mmol/kg at rich loading (α = 0.44) and 45 C. At similar conditions, Fe^{2+} solubility in clean 5 m PZ was 0.05 mmol/kg. The same trend is evident at several different temperatures at rich loadings. It is likely that MEA carbamate effectively complexes Fe^{2+}, increasing its solubility. PZ carbamate has a constrained structure, and is likely unable to complex Fe^{2+}. The range of Fe^{2+} solubilities in MEA across all conditions measured was 0.001 to 14 mmol/kg. The range of Fe^{2+} solubilities in clean PZ across all conditions tested was 0.03 to 0.1 mmol/kg.

5.4.3. The effect of CO_2 loading on Fe^{2+} solubility is affected by amine type.

In 9 m MEA, increasing CO_2 loading increases iron solubility dramatically. In clean 5 m PZ, CO_2 loading does not affect Fe^{2+} solubility, which is low (< 0.1 mmol/kg) at all conditions. Presumably, neither MEA nor PZ complex Fe^{2+} effectively. However at high CO_2 loadings, MEA carbamate forms and readily complexes Fe^{2+}. PZ carbamate's constrained structure prevents it from forming stable complexes with Fe^{2+}.

5.4.4. The presence of amine degradation products significantly increased Fe^{2+} solubility in PZ.

Degraded PZ had much higher Fe^{2+} solubility (up to 26 mmol/kg) than clean PZ. Degraded PZ has linear amine degradation products, such as EDA, which likely chelate Fe^{2+}. Apparently, this EDA complex increases Fe^{2+} solubility in PZ at all conditions. The range of Fe^{2+} solubilities in degraded PZ across all conditions tested was 0.1 to 26 mmol/kg.

In degraded PZ, Fe^{2+} solubility decreased with increasing loadings. This is counterintuitive, because presumably EDA carbamate is also an effective complexing agent for Fe^{2+}. The reason for the decrease of Fe^{2+} solubility in degraded PZ at high loadings is not known.

As PZ degrades, its increasing Fe^{2+} solubility might keep Fe^{2+} in solution, preventing formation of $FeCO_3$ films. This explains the observed relationship between PZ degradation and accelerated C1010 corrosion.

5.4.5. In low temperature, agitated solubility experiments, Fe^{2+} is frequently converted to Fe^{3+}, except in PZ at high CO_2 loadings.

The solid phases characterized in these experiments showed that $FeCO_3$ only formed under specific conditions. Siderite ($FeCO_3$) was only identified in PZ solutions with rich CO_2 loading. Since siderite was found in both rich clean PZ and rich SRP PZ, its formation appears to be relatively independent of amine degradation level. Lean PZ solutions tended to form magnetite (Fe_3O_4), as did lean MEA solutions. The solid sample from a rich MEA experiment that was characterized appeared to be FeO(OH) (goethite). A special air and CO_2-sparged experiment with 5 m SRP PZ air and CO_2 also formed goethite. The conversion of Fe^{2+} to Fe^{3+} requires relatively oxidizing conditions. These

experiments suggest that MEA and lean PZ are somewhat more oxidizing than rich PZ solutions.

5.4.6. Fe^{3+} has limited solubility in PZ solutions.

Fe^{3+} has apparent solubility of 0.01 mmol/kg in slightly degraded 5 m PZ solution at 42°C. At comparable conditions, Fe2+ solubility is 7 mmol/kg. This suggests that at a commercial plant, Fe^{3+} may be precipitated out when it is formed. Fe^{3+} is probably formed at oxidizing conditions in the amine absorber.

5.4.7. The strong effects of CO_2 loading and T on Fe^{2+} solubility suggest the equilibrium concentration of Fe^{2+} will change as the solvent moves through a real plant.

One implication of these results is that there will be strong fluctuations in equilibrium Fe^{2+} concentration as solvent moves through a real plant. In degraded PZ for example, Fe^{2+} solubility is apparently highest at low temperatures and lean loadings, so these conditions are least likely to be protected by $FeCO_3$ and may experience corrosion. However an amine stream that is unsaturated at cold, lean conditions may be supersaturated at hot, rich conditions. This means corrosion could occur in the absorber, and those corrosion products are deposited in the stripper. This also means that the observed Fe^{2+} concentration at a plant may not be an equilibrium value, but rather a complicated average value affected by the residence times at unsaturated and supersaturated parts of the process.

Chapter 6. Corrosion in Monoethanolamine and Piperazine during 2017 Pilot Campaigns

The work in this chapter was submitted as a paper to the proceedings of the 14th international conference on Greenhouse Gas Control Technologies.

Corrosion measurements are presented from two 2017 pilot plant campaigns. Corrosion was evaluated at the Separations Research Program (SRP) pilot plant in April 2017. The SRP pilot plant uses air/CO_2 and 5 m piperazine (PZ) with an oxidation inhibitor. Stainless steel (316L) and carbon steel (C1010) were evaluated with electrical resistance corrosion probes and corrosion coupons at two locations in the process. A second pilot plant campaign was conducted in June 2017 at the National Carbon Capture Center (NCCC) with 7 m monoethanolamine (MEA). Stainless steel and carbon steel were evaluated with corrosion coupons at four locations in the process.

This work seeks to replicate the bench-scale corrosion benefits of PZ at the pilot scale and gain insight into how temperature, CO_2 loading, and amine type affect the formation of passivating $FeCO_3$ layers. These two pilot plant campaigns allow the direct comparison between corrosion in MEA and PZ systems. Protective product layers were not seen on carbon steel in 7 m MEA. This is likely because high ferrous solubility in MEA solutions prevents precipitation of ferrous products. This led to unacceptably high carbon steel corrosion at high temperature. Despite the lack of protective ferrous corrosion products, corrosion of carbon steel was slow at absorber conditions, suggesting carbon steel construction is appropriate for at least low temperature equipment in MEA operation.

In 5 m PZ at hot lean conditions protective layers of Fe_3O_4 and $FeCO_3$ were observed, suggesting that ferrous products are either less soluble in PZ than MEA, or that ferric production is slow or minor. These protective films sometimes led to very low corrosion rates at hot, lean conditions. Protective films formed preferentially at higher

temperature in the stripping system, but were absent in the absorber. This counterintuitive result means that carbon steel corrosion can actually be slower at higher temperature. Carbon steel construction is most likely appropriate both for low temperature equipment in the absorber as well as at least some equipment at high temperature.

6.1. SRP 2017 PZ CAMPAIGN MEASUREMENT LOCATIONS

Corrosion was evaluated at the Separations Research Program (SRP) pilot plant in April 2017. The SRP pilot plant uses a synthetic flue gas (air with added CO_2) and 5 m PZ which contains an oxidation inhibitor. The piperazine inventory had been used in several previous pilot plant campaigns (E. Chen et al., 2017). The stripper operated at 150 °C, and the average absorber sump temperature was 30 °C. CO_2 loading varied throughout the campaign, but the average rich loading was $\alpha = 0.33$ and the average lean loading was $\alpha = 0.21$. The gas conditions were varied to simulate both high and low CO2 concentrations, and as a consequence, O2 concentration varied from 17-20 % (Table 6-1). Stainless and carbon steel ER probes and coupons were placed in the pipe containing the hot, lean amine stream leaving the bottom of the amine stripper. In addition, a carbon steel ER probe and stainless and carbon steel coupons were placed in the cold, rich amine stream in the absorber sump.

Table 6-1: Gas conditions during SRP 2017 campaign (Zhang, 2018).

CO_2	vol %	4, 12, 20
O_2	vol %	20, 18, 17
H_2O	vol %	1 to 2
Temperature	° C	30
Gas Rate	acfm	350, 550, 600

A C1010 corrosion probe was mounted in a small 1" bypass line connected to the hot, lean amine pipe leaving the bottom of the advanced flash stripper (AFS) flash tank. A diagram of the SRP pilot plant equipment is given in Figure 6-1. This probe collected corrosion data for 502 hours at the beginning of the campaign until the probe was removed. The C1010 corrosion probe was replaced with a 316L corrosion probe which collected corrosion data for 134 hours during the second half of the campaign. The stripper corrosion probes were connected to a transmitter that continuously logged data throughout the campaign.

Solution potential was measured with an ORP probe in the hot lean bypass line throughout the campaign. The potential stayed between -400 and -600 mV (vs Ag/AgCl) for most of the campaign. Data from the ORP probe is presented in Appendix B.

Absorber corrosion was monitored using a C1010 corrosion probe mounted in the absorber sump. This probe collected corrosion data for 636 hours over the course of the entire campaign. The absorber corrosion probe was not connected to a transmitter for continuous data collection. Instead, a handheld ER probe reader was used throughout the campaign to take periodic corrosion measurements.

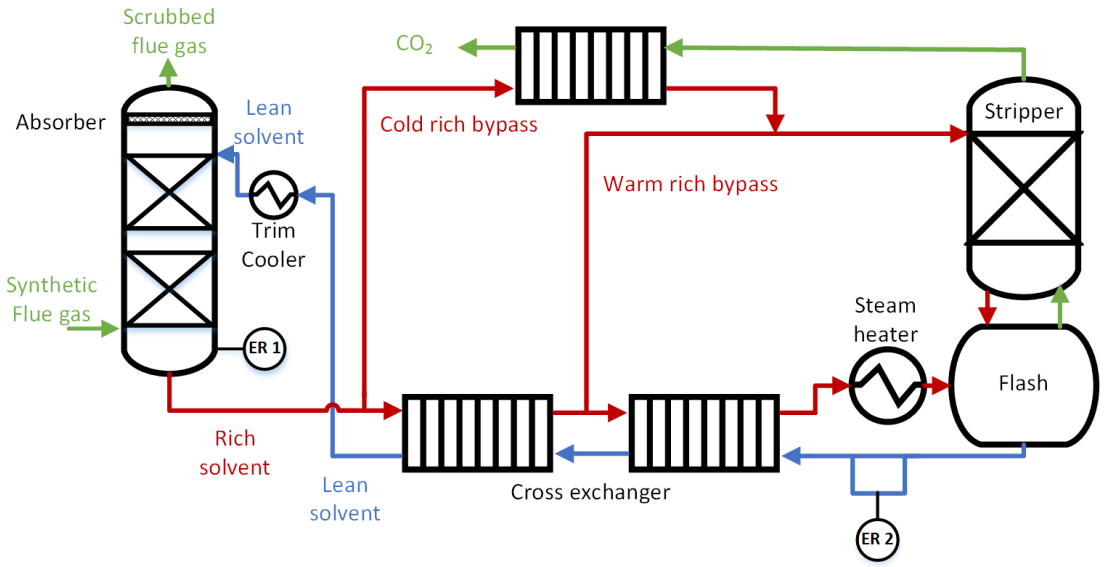

Figure 6-1: Simplified PFD for the SRP pilot plant highlighting location of ER probes

The pilot plant operated continuously during the week, but was shut down over the weekends. During operation, 36 steady state runs were achieved, each about 45 minutes long. For the stripper ER probes, one ER probe signal reading per minute was taken during these runs, and these data averaged to yield an average corrosion probe reading during the run. Plotting the average probe life remaining for each run chronologically gives a corrosion rate over the entire exposure time for the C1010 probe and the 316L probe. The corrosion rates were then determined using the method of least squares. In the absorber, corrosion of the ER probe was measured intermittently with a handheld reader. These intermittent readings were regressed into a corrosion rate with the method of least squares. The corrosion rates reported here assume that no corrosion occurred over the weekends when the plant was not operating.

6.2. NCCC 2017 MEA CAMPAIGN MEASUREMENT LOCATIONS

Corrosion was measured at four locations on the pilot solvent test unit (PSTU) at the National Carbon Capture Center (NCCC) during a campaign using 7 m MEA in June 2017. This unit treated flue gas from a coal fired boiler, and the flue gas conditions in the pilot unit are given in Table 6-2. A simplified PFD for the PSTU is shown in Figure 6-2. Measurements were taken at the absorber midbed (WL2), the absorber sump (WL3), the stripper inlet separator (WL6), and the stripper sump (WL8). The ER probes indicated low corrosion rates at several locations where coupons experienced high corrosion. The data from the ER probes during this campaign were probably unreliable, so it is not discussed further here.

During this campaign, the stripper temperature varied from 110 to 120 °C. The absorber temperature varied from 40–70°C, with a temperature bulge of up to 80 °C for some operating conditions. Lean loading was varied over a range of α = 0.15–0.35. Rich loading was varied over a range of α = 0.4–0.5. The inlet separator temperature varied from 98–112 °C. The plant was shut down on July 10, but coupons were not removed until July 17. The times used for the weight loss corrosion rates (see Table 6-5) assume no corrosion occurred over the 7 days the plant was shut down before the coupons were removed.

Table 6-2: Flue gas composition at NCCC (Zhang et al., 2017).

CO_2	vol %	11.6
O_2	vol %	5.4
N_2	vol %	71.4
H_2O	vol %	11.6
Temperature	° C	48.9
Pressure	Pa	101325
Mass flow rate	lb/hr	4180

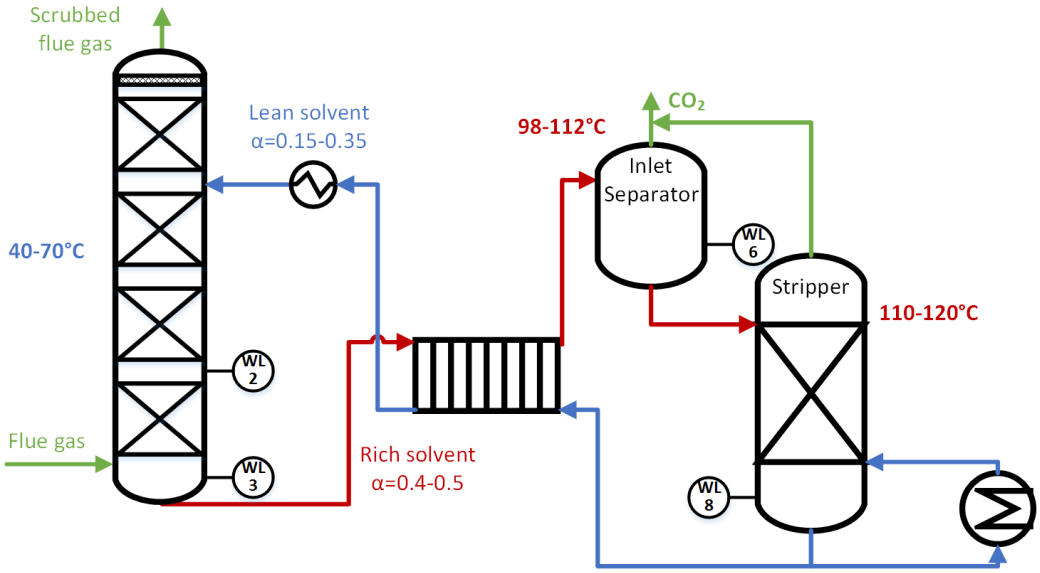

Figure 6-2: Simplified PFD for the NCCC PSTU highlighting location of WL (coupon) probes

6.3. SRP 2017 PZ CAMPAIGN ER PROBE RESULTS

Corrosion of the hot, lean C1010 probe is given in Figure 6-3, showing a corrosion rate of 325 µm/yr during the first half of the campaign. Corrosion of the stripper 316L probe is given in Figure 6-4, which yielded a corrosion rate of 174 µm/yr for the second half of the campaign. Corrosion of the absorber C1010 probe over the entire campaign is given in Figure 6-5, which yielded a corrosion rate of 331 µm/yr. A summary of the corrosion rates and conditions at these locations is given in Table 6-3. These corrosion rates are compared with the corresponding coupon corrosion rates in Section 4.5.

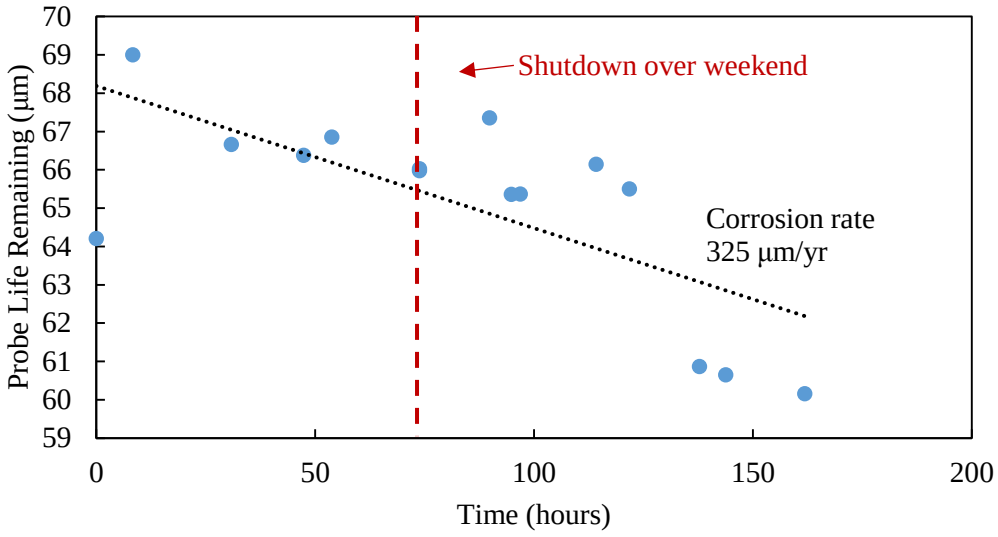

Figure 6-3: Corrosion of carbon steel (C1010) measured with ER probe in SRP stripper corrosion bypass line. Probe life values are averages for each steady state run.

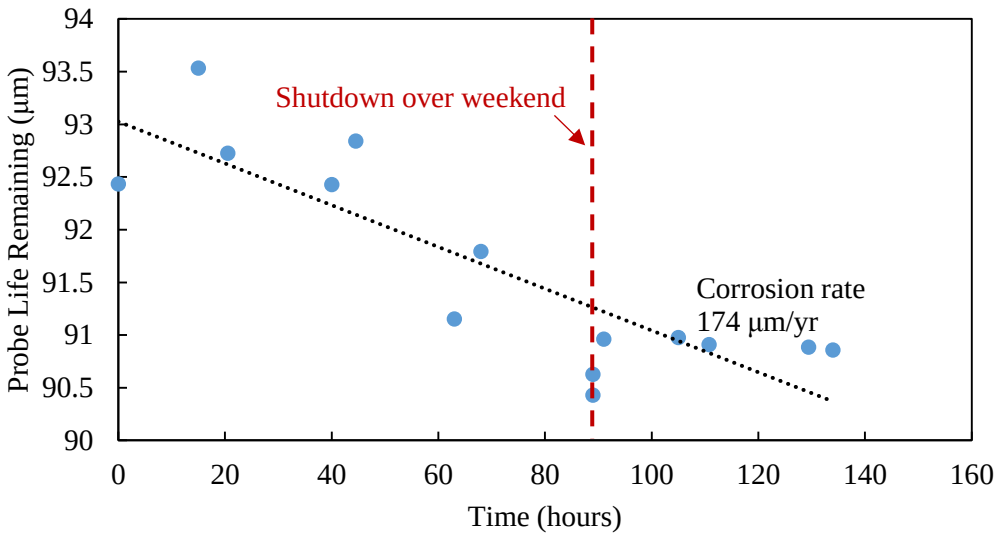

Figure 6-4: Corrosion of stainless steel (316L) measured with ER probe in SRP stripper corrosion bypass line. Probe life values are averages for each steady state run.

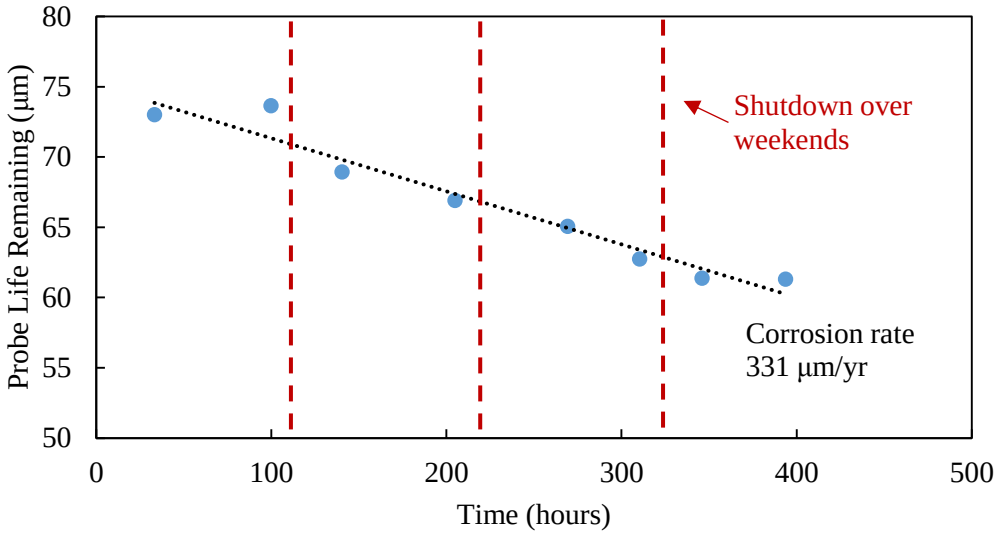

Figure 6-5: Corrosion of carbon steel (C1010) measured with ER probe in SRP absorber sump. Readings are instantaneous values recorded with handheld ER reader.

Table 6-3: Summary of SRP 2017 PZ campaign ER probe corrosion measurement

Location	Alloy	T (°C)	Avg. Loading (mol CO_2/mol C N)	(µm/yr)	Standard error of slope (µm/yr)	Coefficient of determination
Absorber	C1010	30	0.33	331	± 32	0.946
Hot, lean	C1010	150	0.21	325	± 92	0.490
Hot, lean	316L	150	0.21	174	± 31	0.724

These pilot plant results are compared to previously obtained bench-scale corrosion results in Figure 6-6. C1010 performance at bench scale agreed with the pilot-scale results. 316L performance at the bench scale was significantly worse than at the pilot scale. The high 316L corrosion rates at bench scale may be because that work was conducted using a system that did not have gas cycling (i.e., the cyclic absorption and desorption of flue gas). This means the bench-scale conditions may have been more oxygen-depleted and reducing than a representative system. These oxygen-depleted, reducing conditions probably

corrode 316L faster because the conditions are not oxidizing enough to generate the Cr_2O_3 layer that typically passivates stainless steel.

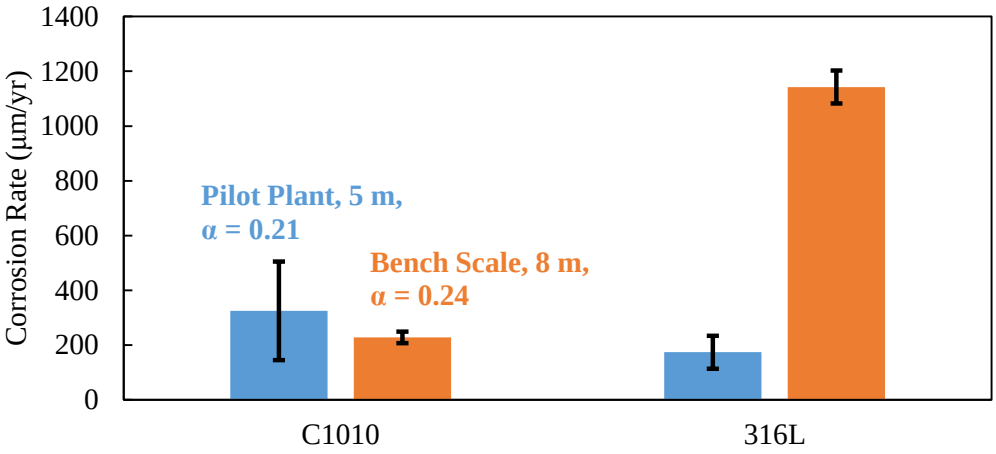

Figure 6-6: Pilot- vs bench-scale SRP PZ, 150° C, 95% confidence intervals shown. 5 m PZ results are from SRP 2017 pilot plant campaign; 8 m PZ results are from a bench-scale experiment using a SRP 2011 pilot plant campaign sample.

6.4. SRP 2017 PZ CAMPAIGN CORROSION COUPON RESULTS

The coupon insertion and removal timeline is illustrated in Figure 6-7. Each coupon mount has space for two coupons, so two coupons were inserted at a time: one 316L and one C1010. Some coupons were inserted at the beginning of water testing the pilot equipment. These coupons were exposed to deionized water at 20–150 °C in the hot, lean section and 20–30°C in the absorber section. Water testing lasted for 340 hours, then piperazine operation began. After 167 hours of steady state piperazine operation, the first set of hot, lean coupons was removed and replaced with a second set of hot, lean coupons. The second set of hot, lean coupons were removed after 152 hours of PZ operation, when the campaign ended. The absorber coupons were also removed at the end of the campaign, having experienced 320 hours of PZ operation. Corrosion rates reported here assume that all corrosion occurred during PZ operation. This assumes no corrosion occurred during the

equipment commissioning phase. This assumption means that the coupons from the absorber and the first batch of hot lean coupons may be a significant overestimation of PZ corrosion.

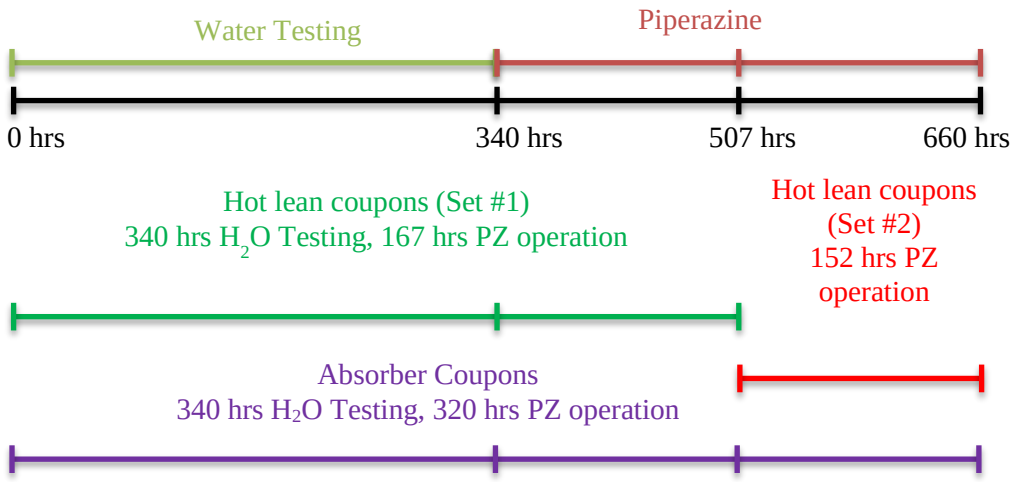

Figure 6-7: Coupon removal timeline for SRP 2017 PZ campaign

Corrosion rates by coupon weight loss are given in Table 6-4. Stainless steel (316L) performed well at all locations, experiencing undetectable corrosion in the absorber and 2.0–9.0 µm/yr of corrosion in the stripper. Carbon steel (C1010) performed well in the absorber, experiencing 312 µm/yr of corrosion. This agrees with the ER probe rate in the absorber (331 µm/yr). Stripper corrosion differed significantly between the first and second sets of C1010 coupons. The first experienced moderate corrosion of 878.2 µm/yr, but the second set performed excellently, only showing 96.4 µm/yr of corrosion. Apparently extended water testing with the first set of coupons caused the formation of alternative corrosion products, which slowed or inhibited the formation of the protective $FeCO_3$ film.

Table 6-4: Weight loss for SRP 2017 PZ campaign coupons

Alloy	Location	Initial Mass (g)	Mass loss (g)	PZ Operation Time (hours)	Corrosion rate (μm/yr)	Mass of Corrosion Product (g)
C1010	absorber sump	10.7566	0.1879	320	312.2	0.0013
C1010	hot lean (batch 1)	10.4823	0.2752	167	878.2	0.0829
C1010	hot lean (batch 2)	9.5602	0.0275	152	96.4	0.0232
316L	absorber sump	10.5709	-0.0001	320	-0.2	0.0008
316L	hot lean (batch 1)	10.5863	0.0006	167	2.0	0.0004
316L	hot lean (batch 2)	10.1300	0.0026	152	9.0	0.0000

Figure 6-8 shows the appearance of the first set of hot, lean coupons immediately after removal and rinsing with deionized water. The 316L coupon is pristine, but the C1010 coupon is covered with a flaky, black and red film. Figure 6-9Ashows the SEM micrograph of the C1010 red product, which is fluffy and porous. This product was identified as FeO(OH) by powder XRD. Figure 6-9B shows the SEM micrograph of the C1010 black product, which is crystalline but patchy. This product was identified as Fe_3O_4 by powder XRD.

Figure 6-8: 316L and C1010 coupons after removal from SRP stripper. Coupons experienced approximately 340 hours of water testing and 167 hours operating at temperature in PZ solution. Average $\alpha = 0.21$. T = 150 °C.

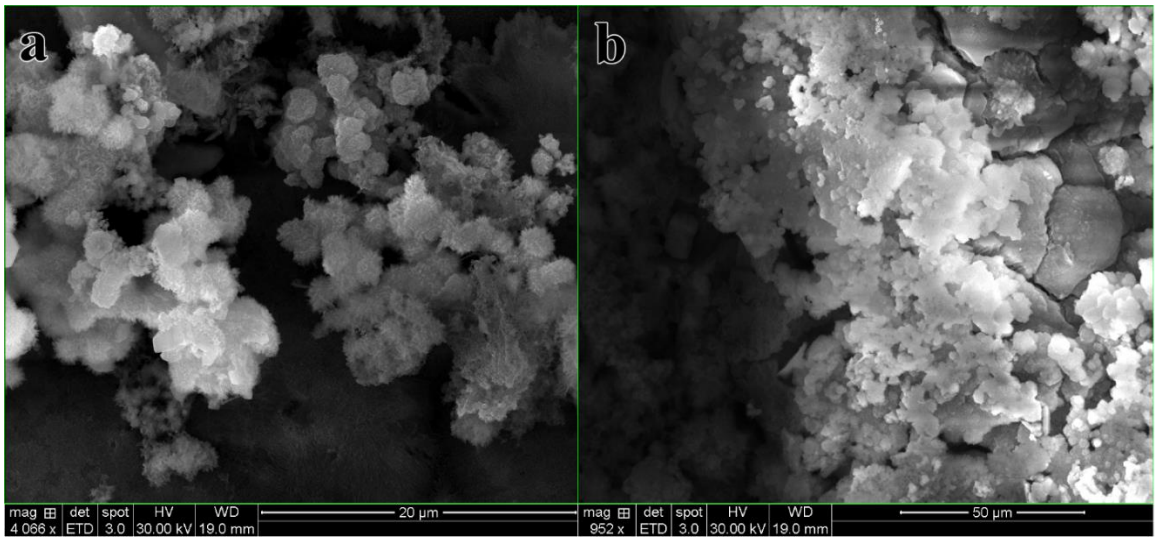

Figure 6-9: (a) SEM micrograph of red product on C1010 coupon after removal from SRP stripper. Identified with powder XRD as FeO(OH). (b) SEM micrograph of black product on C1010 coupon after removal from SRP stripper. Identified with powder XRD as Fe_3O_4. Probe experienced approximately 340 hours of water testing and 167 hours operating at temperature in PZ solution.

Figure 6-10A shows the appearance of the second set of hot, lean coupons immediately after removal and rinsing with deionized water. The 316L coupon is pristine, and the C1010 coupon is covered with a coherent, black layer. Figure 6-10B shows the SEM micrograph of the C1010 black product, which is a regular crystalline layer, with a few pores. This product was identified as $FeCO_3$ by powder XRD.

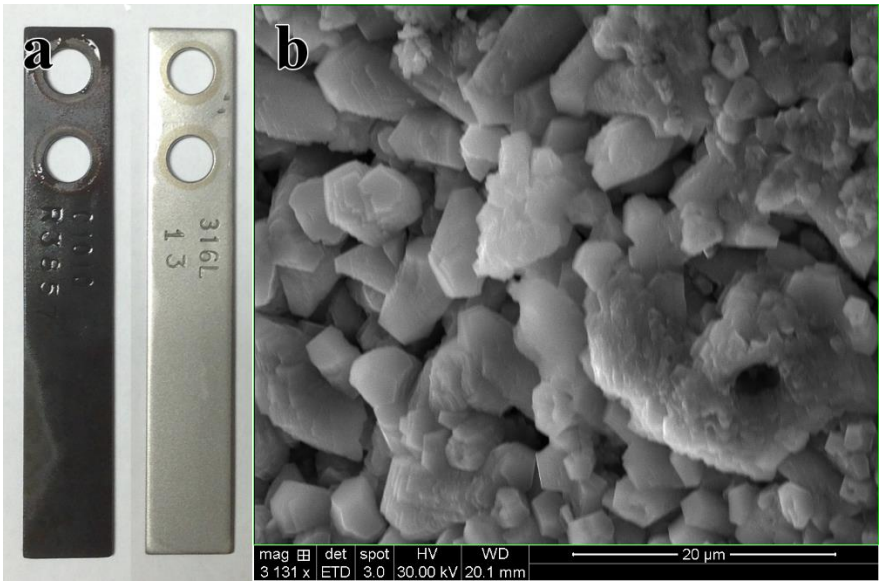

Figure 6-10: (a) 316L and C1010 coupons after removal from SRP stripper. (b) SEM micrograph of black product on C1010 coupon. Identified with powder XRD as $FeCO_3$. Probe experienced 152 hours operating at temperature in PZ solution. Average $\alpha = 0.21$. T = 150 °C

Figure 6-11A shows the appearance of the absorber sump coupons immediately after removal and rinsing with deionized water. The 316L coupon is mostly pristine, but the C1010 coupon is covered with a patchy black film with a few red flakes. Figure 6-11B shows the SEM micrograph of the C1010 black product, which is irregular and patchy with a few small crystalline patches. The black product was identified as Fe by powder XRD, although EDS mapping suggests the large crystal in the center of Figure 6-11B could be $FeCO_3$. The secondary red product was identified as FeO(OH) by powder XRD.

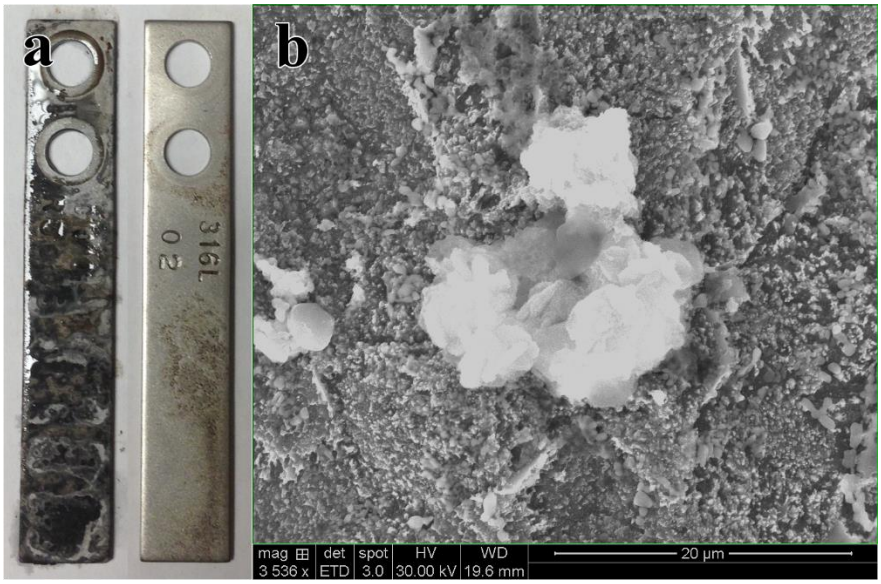

Figure 6-11: (a) 316L and C1010 coupons after removal from SRP absorber. (b) SEM micrograph of black product on C1010 coupon after removal from SRP absorber. Identified by powder XRD as Fe. EDS suggests crystal in SEM micrograph center could be $FeCO_3$. Probe experienced approximately 340 hours of water testing and 320 hours operating at temperature in PZ solution. Average $\alpha = 0.33$.

Figure 6-12 shows powder X-ray diffraction spectra of corrosion products found on coupons from the SRP campaign. Siderite ($FeCO_3$) was only observed in the hot lean stream during batch 2. In general ferrous products (such as siderite) are expected in the stripper, since the absence of dissolved oxygen makes this location relatively reducing. Goethite (FeO(OH)) was observed in the absorber. Ferric products (such as goethite) are expected in the absorber, which is a relatively oxidizing location. The occurrence of Goethite and Magnetite (Fe_3O_4) on the batch 1 hot lean coupon was unexpected, and may be due to extended water testing.

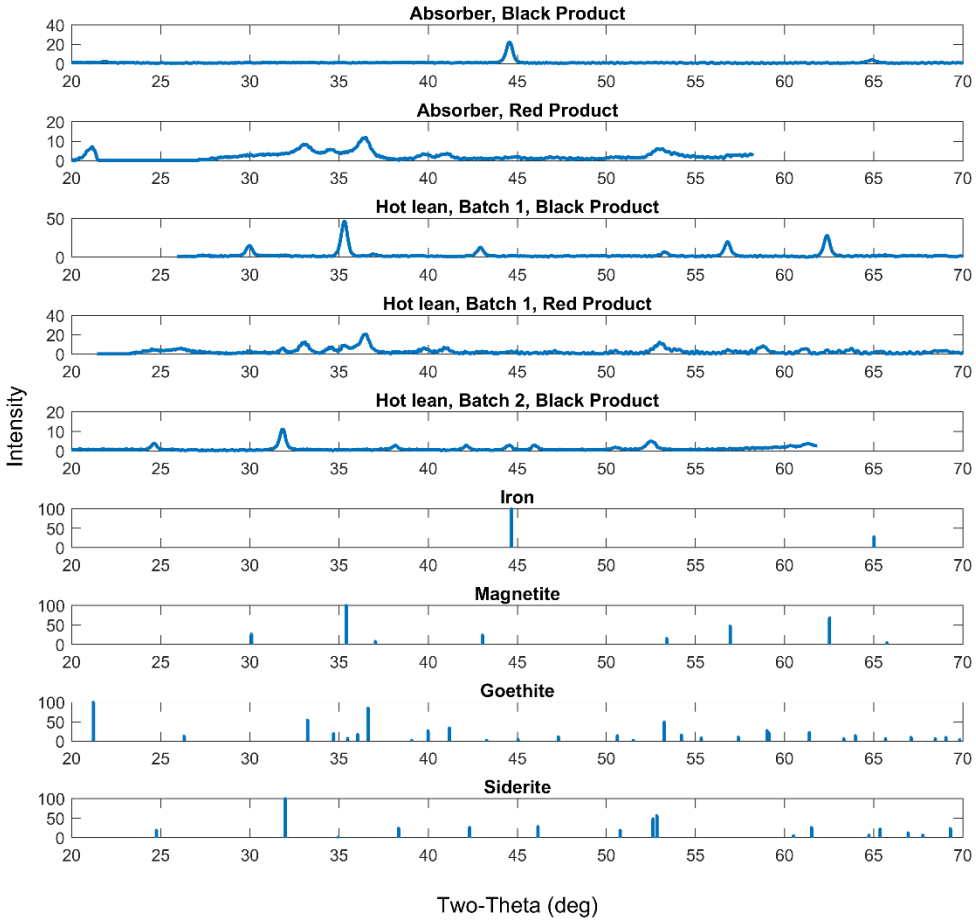

Figure 6-12: Powder X-ray diffraction products observed on C1010 coupons from the SRP PZ campaign. Reference diffraction patterns for Iron, Magnetite, Goethite and Siderite are shown.

6.5. NCCC 2017 MEA CAMPAIGN CORROSION COUPON RESULTS

Corrosion rates by coupon weight loss are given in Table 6-5. Stainless steel (316L) performed well at all locations, experiencing 0–0.3 μm/yr of corrosion in the absorber and 0.2–0.6 μm/yr of corrosion in the stripper. Carbon steel (C1010) performed well in the

absorber, experiencing 1.8–8.9 μm/yr of corrosion, but performed unacceptably in the stripper, experiencing 3586–3959 μm/yr of corrosion.

Table 6-5: Weight loss for NCCC 2017 MEA campaign coupons

Alloy	Location	Initial Mass (g)	Mass loss (g)	Time (hours)	C (μm/yr)	Mass of Corrosion Product (g)
C1010	Inlet Separator	9.6567	4.2075	625	3586.4	0.0393
316L	Inlet Separator	10.6151	0.0003	625	0.2	0.0003
C1010	Stripper Sump	10.5296	4.6222	622	3958.8	0.0105
316L	Stripper Sump	10.4453	0.0007	622	0.6	0.0044
C1010	Absorber Sump	10.3603	0.0104	625	8.9	0.0048
316L	Absorber Sump	10.6149	-0.0001	625	-0.1	0.0003
C1010	Absorber Middle	10.3389	0.0021	625	1.8	0.0015
316L	Absorber Middle	10.5952	0.0003	625	0.3	0.0006

In the NCCC absorber, only minimal corrosion of carbon steel occurred. Carbon steel coupons in the absorber middle showed no evidence of corrosion, so their SEM micrographs are not shown here. Additionally, stainless steel coupons from both absorber locations showed no evidence of corrosion, so their SEM micrographs are not shown here.

In the absorber sump, C1010 formed a patchy red product, shown in Figure 6-13. The steel was mostly bare, but with scattered crystals of corrosion product. A micrograph of the patchy red corrosion product is also shown in Figure 6-13B. This product was analyzed by powder X-ray diffraction as $Fe(OH)_3$.

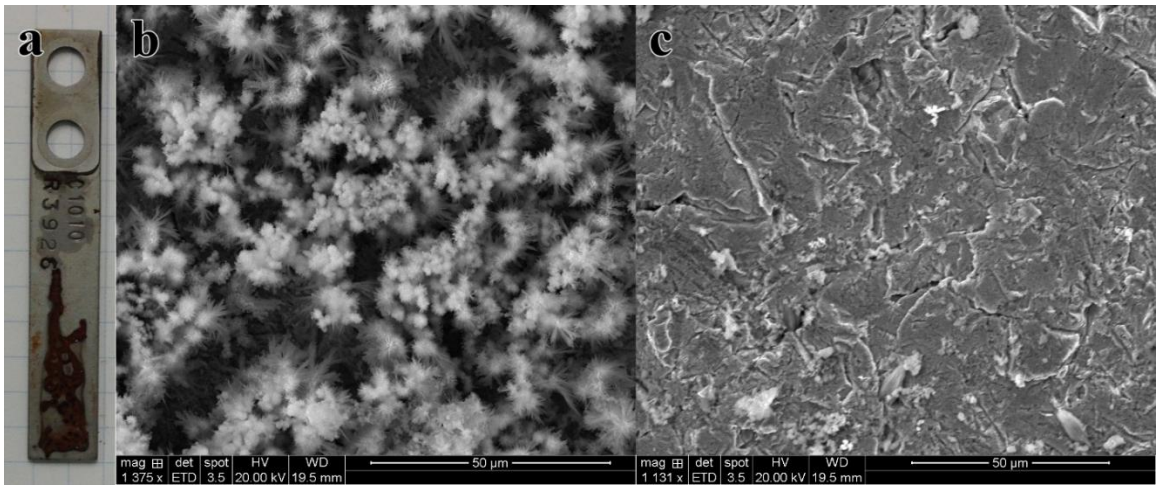

Figure 6-13: (a) C1010 coupon after removal from NCCC absorber sump. (b) SEM micrograph of red product. Identified by powder XRD as $Fe(OH)_3$. (c) SEM micrograph of steel surface without product formation. Probe experienced 625 hours of operation in 7 m MEA.

Stainless steel coupons from the stripper inlet separator showed no evidence of corrosion, so their SEM micrographs are not shown here. Corrosion in the stripper inlet separator was severe for carbon steel. The coupon appearance and SEM micrograph is shown in Figure 6-14. The micrograph shows the coupon surface is about half bare steel and half red product. EDS mapping suggests the surface is bare iron with small clusters of oxide or carbon. Powder X-ray diffraction of this product appears to show a combination of several products, possibly a mixture of Fe_3O_4 and $FeCO_3$.

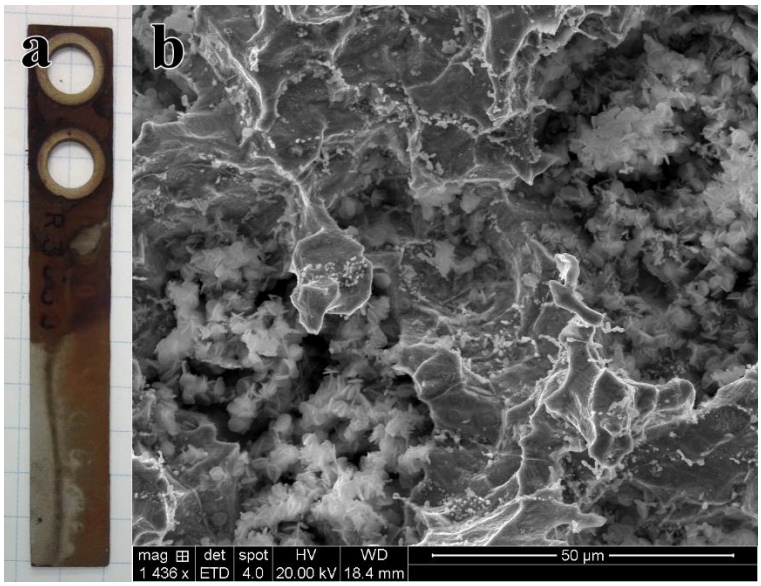

Figure 6-14: (a) C1010 coupon after removal from NCCC stripper inlet separator (ER6) corrosion coupon. (b) SEM micrograph of steel surface. Product identified as a mixture of Fe_3O_4 and $FeCO_3$. Probe experienced 625 hours of operation in 7 m MEA.

Corrosion of stainless steel in the stripper sump was minor. A white film was observed on the coupon surface (Figure 6-15). The micrograph shows a fine, crystalline product. EDS mapping shows the crystals contain manganese, whereas the surface of the bare metal is largely chromium. This product was identified by powder X-ray diffraction as $MnCO_3$. Interestingly, the mass of the corrosion product was significantly less than the weight loss of the coupon (see Table 6-5), suggesting some manganese was deposited from the amine solution onto the coupon.

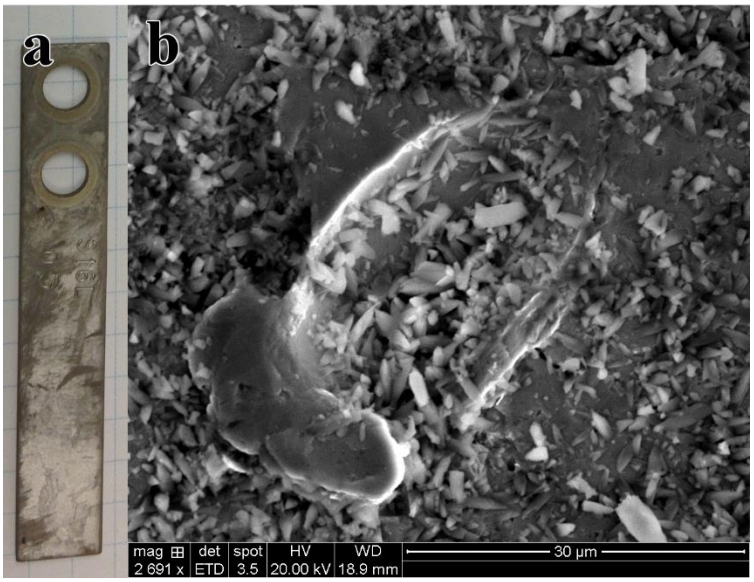

Figure 6-15: (a) 316L coupon after removal from NCCC stripper sump. (b) SEM micrograph of white product. Identified by powder XRD as $MnCO_3$. Probe experienced 622 hours of operation in 7 m MEA.

Corrosion in the stripper sump was severe for carbon steel. The coupon appearance and its SEM micrograph shows the coupon surface is largely bare, pitted steel (Figure 6-16). Small amounts of a red product were observed, identified by powder X-ray diffraction as $Fe(OH)_3$.

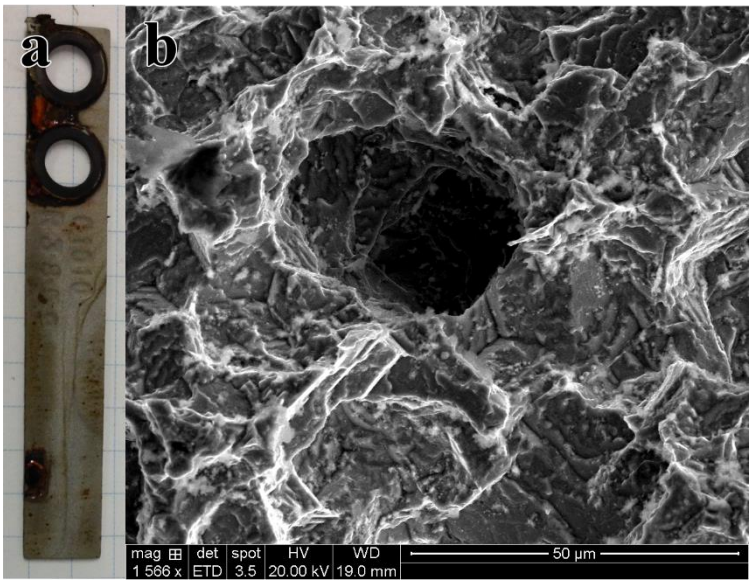

Figure 6-16: (a) C1010 coupon after removal from NCCC stripper sump. (b) SEM micrograph of steel surface. EDS suggests the surface is bare Fe. Probe experienced 622 hours of operation in 7 m MEA.

Figure 6-17 shows powder X-ray diffraction spectra of corrosion products found on coupons from the NCCC MEA campaign. In contrast to PZ campaigns, primarily ferric products were observed, even at high temperature. Ferric hydroxide was observed at several locations, which is not a product observed in PZ campaigns. Rhodochrosite ($MnCO_3$) was observed as a corrosion product on 316L in the stripper sump, which was not observed in other campaigns. Product films were, in general, not productive in the MEA campaign.

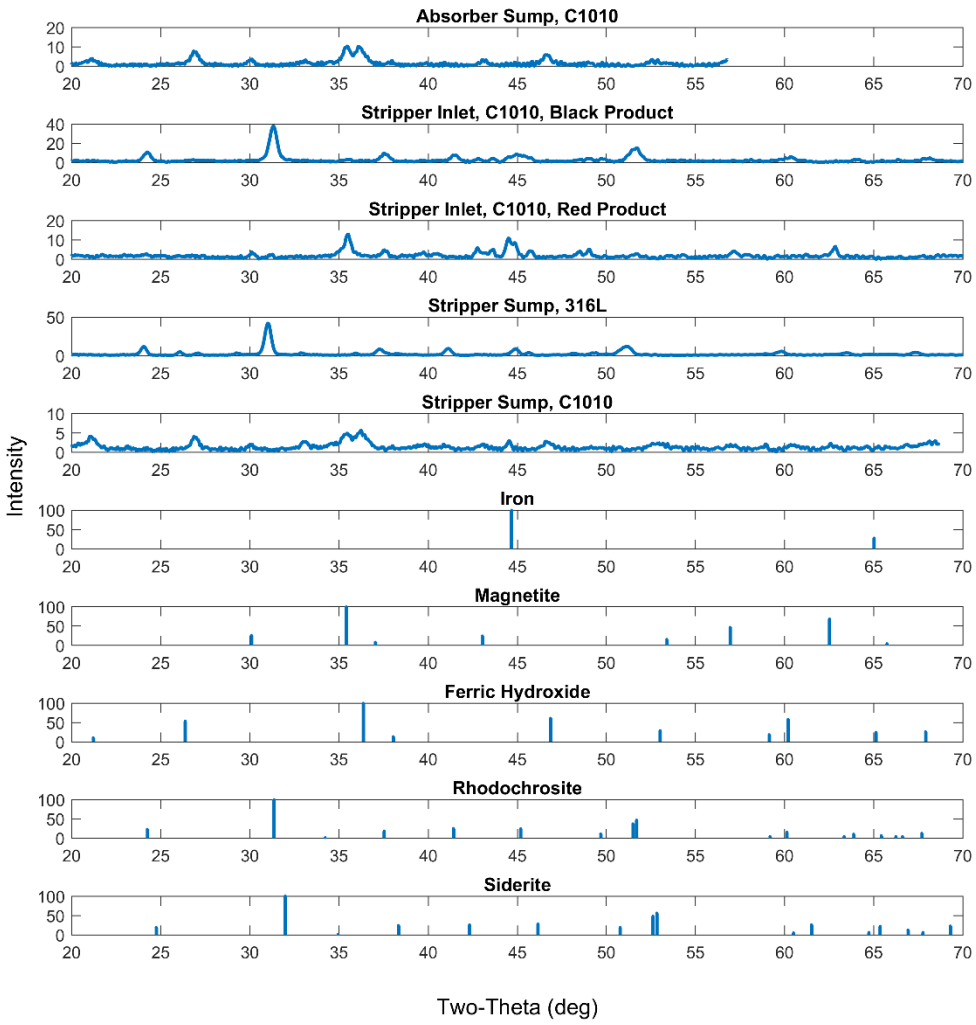

Figure 6-17: Powder X-ray diffraction products observed on coupons from the NCCC MEA campaign. Reference diffraction patterns for Iron, Magnetite, Ferric Hydroxide, Rhodochrosite, and Siderite are shown.

6.6. DISCUSSION

These two pilot plant campaigns, taken together, allow the direct comparison between corrosion in MEA and PZ systems. Protective product layers were not seen on carbon steel in 7 m MEA. Ferric oxide and hydroxide products were formed on carbon

steel in MEA, but few ferrous products were observed. This is likely because high ferrous solubility in MEA solutions prevents precipitation of ferrous products. Alternatively, oxidation of Fe^{2+} to Fe^{3+} by Equation 6-1 could be rapid or thermodynamically favored in MEA, reducing availability of Fe^{2+} to form ferrous corrosion products. Despite the lack of protective ferrous corrosion products, corrosion of carbon steel was slow at absorber conditions, suggesting carbon steel construction is appropriate for at least low temperature equipment in MEA operation.

$$O_2 + 2H_2O + 4Fe^{2+} \leftrightarrow 4Fe^{3+} + 4OH^- \quad (6\text{-}1)$$

In 5 m PZ at hot lean conditions protective layers of Fe_3O_4 and $FeCO_3$ were observed, suggesting that ferrous products are either less soluble in PZ than MEA, or that ferric production by Equation 2-2 is slow or minor. These protective films sometimes led to very low corrosion rates at hot, lean conditions. Protective films formed preferentially at higher temperatures in the stripping system, but were absent in the absorber. This counterintuitive result means that carbon steel corrosion can actually be slower at higher temperatures. Protective product formation was inhibited in the absorber, likely due to higher ferrous solubility at low T, high α, or because the rate of ferrous product formation is kinetically limited. Although protective films were absent, corrosion was still slow in the absorber.

6.7. CONCLUSIONS

6.7.1. $FeCO_3$ formation at 150°C in 5 m PZ protects carbon steel, leading to low corrosion rates.

Corrosion coupons from the 2017 SRP pilot plant campaign show a protective, crystalline layer of $FeCO_3$ forms on C1010 in 5 m PZ at 150 °C and $\alpha = 0.21$.When this layer formed, corrosion performance was good (96.4 μm/yr).

6.7.2. Equipment commissioning with water and steam appears more corrosive to carbon steel than PZ operation.

Commissioning of equipment with water and steam generated a non-protective layer of FeO(OH) and Fe_3O_4 on C1010 in the stripper sump. The C1010 coupon corroded at 878 μm/yr (assumes all corrosion occurred during PZ operation). Significant corrosion of this coupon likely occurred during extended water testing, rather than during PZ operation. . This period of PZ operation apparently was not sufficient to generate a $FeCO_3$ layer on the water-corroded coupon.

6.7.3. Absorber corrosion of carbon steel can be moderate, but this may be due to equipment commissioning rather than exposure to PZ operation.

Primarily non-protective products form on C1010 in 5 m PZ at absorber conditions ($\alpha = 0.33$ and 30 °C). A patchy black layer of Fe with flakes of red FeO(OH) were observed. C1010 experienced 312 μm/yr of corrosion (assumes all corrosion occurred during PZ operation). Significant corrosion of this coupon likely occurred during extended water testing, rather than during PZ operation.

6.7.4. Stainless steel performed well in 5 m PZ both in the absorber and in the hot, lean stream. This may be partially due to the high O_2 content at SRP.

Stainless steel (316L) performed excellently in the absorber (α = 0.33 and 30 °C) corroding at 0 μm/yr. Stainless steel also performed excellently in the hot (150°C), lean (α = 0.21) stream, showing 2.0–9.0 μm/yr of corrosion. Stainless steel is clearly not attacked by either PZ operation or water commissioning at these conditions. This may be due to higher O_2 concentration at in SRP synthetic flue gas (≈18 %) compared to a coal flue gas stream (5.4 %), which may lead to more oxidizing conditions which can support chromium oxide passive film formation on stainless steel.

6.7.5. Carbon steel performs well at 40-70 °C in 7 m MEA, but it is unacceptable at 120 °C.

Carbon steel (C1010) performed well in the absorber (40-70 °C), experiencing 1.8–8.9 μm/yr of corrosion, but performed unacceptably in the stripper (110-120°C), experiencing 3586–3959 μm/yr of corrosion.

6.7.6. Stainless steel performs well in 7 m MEA at both absorber and stripper conditions.

Stainless steel (316L) performed well at all locations, experiencing 0–0.3 μm/yr of corrosion in the absorber (40-70 °C), and 0.2–0.6 μm/yr of corrosion in the stripper (110-120°C).

6.7.7. Corrosion products on carbon steel are largely Ferric (Fe^{3+}) in 7 m MEA service, suggesting more oxidizing conditions than PZ. Protective corrosion product layers were not observed.

In 7 m MEA, $Fe(OH)_3$ was observed on carbon steel coupons in the absorber sump and the stripper sump. This ferric product, particularly at relatively reducing stripper sump conditions, suggests MEA is more oxidizing than PZ. In general corrosion product films

on C1010 in MEA were not thick or tightly adhering. Presumably higher Fe^{2+} solubilities prevent precipitation of protective ferrous films. Alternatively, ferrous product formation is prevented at most conditions because MEA rapidly oxidizes Fe^{2+} to Fe^{3+}.

Chapter 7. Corrosion in Piperazine during 2018 Pilot Campaign

Corrosion in amine units for CO_2 capture has been measured at several pilot plants (Cousins et al., 2013; Flø et al., 2019; Hjelmaas et al., 2017; Khakharia et al., 2015; Kittel et al., 2009; Li et al., 2018; Li et al., 2017). All these studies (except one) investigated MEA, and as a consequence are typically limited to operation at 120 °C. To date there is limited published data on pilot scale corrosion in second generation solvents, like PZ. The following pilot campaign was conducted at the National Carbon Capture Center in Wilsonville, AL. Some details about the pilot plant campaign were published (Gao et al., 2019; G. Rochelle et al., 2019; Selinger, 2018), but detailed corrosion measurements were not published. Ching-Ting Liu assisted with equipment installation and coupon analysis during this pilot campaign.

Corrosion was measured with weight loss coupons and ER probes, but ultimately the coupon weight loss measurements were determined to be more reliable. Coupon surfaces were imaged, showing protective $FeCO_3$ film on carbon steel at many conditions. Significant carbon steel corrosion occurred primarily at high temperature, high velocity locations where increased mass transfer or erosion removed protective films. Stainless steel was found to be occasionally vulnerable at high temperature, which is likely a consequence of the uniquely high operating temperatures used with PZ. The effect of temperature and solution velocity on corrosion of carbon and stainless steel are evaluated, and tentative materials choice recommendations are given for different locations in the PZ process.

7.1. Corrosion Measurement Locations

The National Carbon Capture Center pilot unit captures CO_2 from a 0.6 MWe coal flue gas stream. Flue gas details for the pilot unit are given in Table 7-1. The campaign used 5 m PZ, and ranges of CO_2 loadings during the PZ campaign are given in Table 7-2.

The pilot unit uses a conventional absorber and an advanced stripper configuration called the Advanced Flash Stripper (AFS). Corrosion measurements were made at many locations on the pilot unit to measure corrosion in each unit operation.

Table 7-1: Flue gas composition at NCCC (Zhang et al., 2017).

CO_2	vol %	11.6
O_2	vol %	5.4
N_2	vol %	71.4
H_2O	vol %	11.6
Temperature	° C	48.9
Pressure	Pa	101325
Mass flow rate	lb/hr	4180

Table 7-2: PZ 2018 campaign CO_2 loadings during steady state runs.

	α min (mol CO_2/ mol N)	α max (mol CO_2/ mol N)	α median (mol CO_2/ mol N)
Lean	0.20	0.27	0.23
Rich	0.38	0.42	0.40

In the absorber system, coupon measurements were made at 7 locations and ER probe measurements were made at 2 locations. These locations are illustrated in Figure 7-1 and listed in Table 7-3. Coupons were not inserted at one planned location (WL3), because a nitrogen injection system was installed at that location instead for solvent oxidation control.

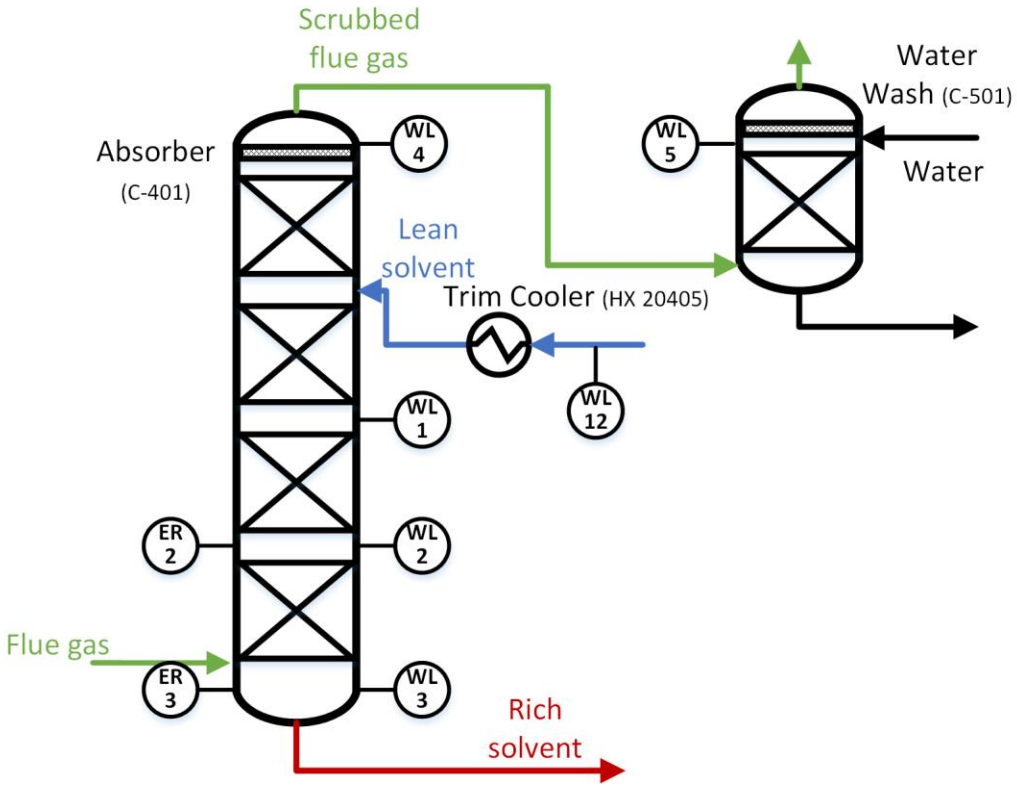

Figure 7-1: Simplified PFD of NCCC absorber system, showing ER and WL locations.

Table 7-3: Description of Absorber ER and WL locations

Tag	Location Description	Instrument Type
WL1	Absorber between beds 2 and 3	Coupon probe
WL2	Absorber between beds 1 and 2	Coupon probe
WL3	Absorber sump (below bed 1)	Coupon Probe
ER2	Absorber between beds 1 and 2	ER Probe & ER coupon adapter
ER3	Absorber sump (below bed 1)	ER probe & ER coupon adapter
WL4	Absorber above mist eliminator	Coupon probe
WL5	Water wash below mist eliminator	Coupon probe
WL12	Cold lean solvent downstream of HX20404 and upstream of HX20405 (trim cooler)	Coupon probe

In the regeneration system, coupon measurements were made at 5 locations, ER probe measurements were made at 4 locations, and ORP measurements were made at 2

locations. These locations are illustrated in Figure 7-2 and listed in Table 4. Coupons were not inserted at one planned location (WL11) because of a broken process isolation valve. The CO_2 and water environment expected at WL11 is well characterized in literature, so repairing this coupon location was not a priority.

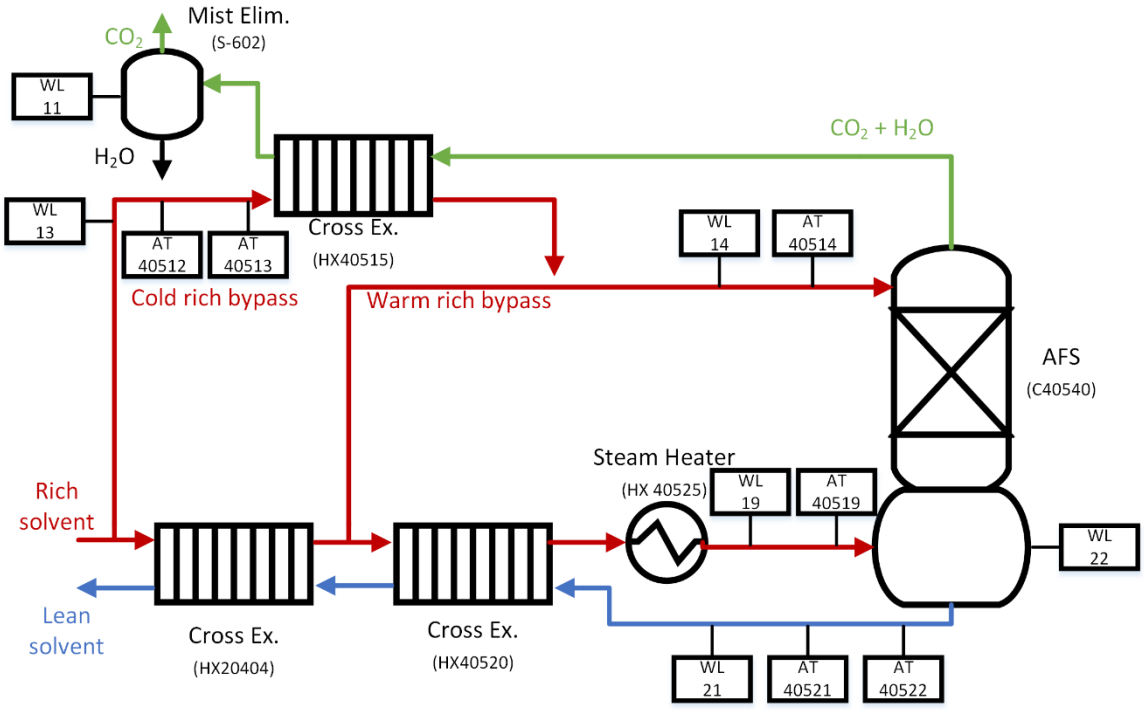

Figure 7-2: Simplified PFD of NCCC regeneration system, showing ER, WL, and ORP locations.

Table 7-4: Description of regeneration system ER and WL locations

Tag	Location Description	Instrument Type
WL11	In mist elimination tank for CO2 stream	Coupon probe
AT40512	Rich solvent to cold rich bypass exchanger	ORP probe
AT40513	Rich solvent to cold rich bypass exchanger	ER probe
WL13	Rich solvent to cold rich bypass exchanger	Coupon probe
AT40519	Rich solvent from steam heater to AFS	ER probe
WL19	Rich solvent from steam heater to AFS	Coupon probe
AT40514	Rich solvent from cold rich bypass exchanger to AFS	ER probe
WL14	Rich solvent from cold rich bypass exchanger to AFS	Coupon probe
AT40521	Lean solvent from AFS to hot cross exchanger	ER probe
AT40522	Lean solvent from AFS to hot cross exchanger	ORP probe
WL21	Lean solvent from AFS to hot cross exchanger	Coupon probe
WL22	Stripper sump	Coupon probe

Superficial fluid velocities and typical operating temperatures are shown in Table 7-5 for several corrosion coupon locations. Velocity has a strong effect on carbon steel corrosion because it removes protective corrosion product films. Velocities were typically under 1 m/s, but were as high as 2.16 m/s at one location during a steady state run. These velocities do not include flashing or two phase flow, and thus underestimate fluid velocity, particularly in the hot rich location, where flashing is expected. In addition, coupon orientation was not controlled in this campaign, and coupons may have been inserted perpendicular rather than parallel to flow. Strip coupons inserted perpendicular to flow obstruct 30-39 % of the pipe's cross sectional area, which is also shown in Table 7-5, compared to parallel insertion, which only obstructs 4-5% of the pipe's cross sectional area. High fluid velocities and turbulence caused by coupons inserted perpendicularly could have contributed to some carbon steel corrosion measurements being not entirely reproducible.

Table 7-5: PZ 2018 campaign superficial fluid velocity during steady state runs and typical operating temperatures.

Location	V min (m/s)	V max (m/s)	V median (m/s)	T (° C)	Pipe Area Blocked Max (%)	Pipe Area Blocked Min (%)
Cold Lean	0.42	0.85	0.50	50	-	-
Cold Rich Bypass	0.03	0.08	0.04	50	30	4
Warm Rich Bypass	0.23	0.66	0.39	116	39	5
Hot Rich	0.65	2.16	0.83	155	39	5
Hot Lean	0.64	1.31	0.77	150	30	4
Absorber Sump	-	-	-	50	-	-
AFS Sump	-	-	-	150	-	-

7.2. COUPON BATCHING SCHEDULE

Coupons were inserted and removed in four chronological batches. This allowed more coupons to be examined, and allowed an investigation of whether corrosion conditions changed over the course of the campaign. An illustration of the coupon batch insertion and removal dates is given in Table 7-6.

Table 7-6: Calendar illustration of coupon batches. The colored sections of each row represent the coupon batches insertion and removal dates. Green sections represent periods of piperazine operation, black sections represent periods when coupons were inserted but the plant was shut down, and the yellow section represents the period of simple stripper operation.

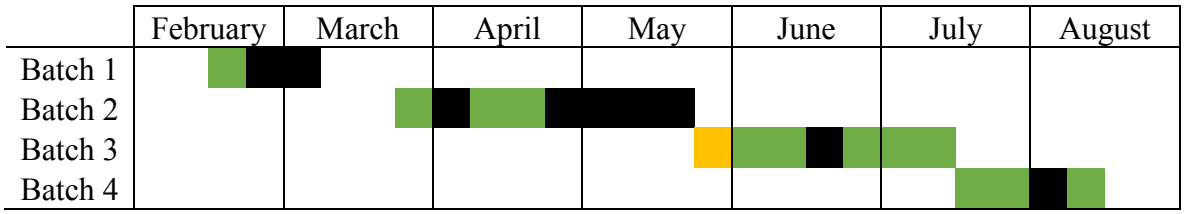

Batch 1 was a period of parametric testing over February 21–28, 2018. The coupons were inserted during equipment water and steam testing, which lasted 47 hours after insertion. The coupons then experienced 66 hours of PZ operation, after which the plant was unexpectedly shut down, drained, and rinsed with water. Water was circulated through the plant for 168 hours. Finally the system was drained again, and the coupons remained in the drained, shut down state for 48 hours before retrieval. The corrosion rates for this period assume that all corrosion ocurred during the 66 hours of PZ operation. Assuming all corrosion happened during this short interval gives the most conservative (ie, the highest) corrosion rates. Given the significant water testing before and after the period of PZ operation, the corrosion rates for this period significantly overestimate PZ corrosion. Batch 1 evaluated carbon steel (C1010) in the AFS locations. Because of the uncertainty of the corrosion rates observed in Batch 1, these rates are excluded when drawing conclusions about PZ performance.

Batch 2 experienced 388 hours of operation on the AFS skid between March 26, 2018 and April 21, 2018. After this period, an unexpected shutdown occurred, and the coupons were left in the shut-down, drained plant for 720 hours before they were retrieved. The corrosion rates reported here assume no corrosion occurred during the shut-down period. Batch 2 evaluated carbon steel (C1010) and stainless steel (316L) in the AFS locations. Several coupon locations on the absorber side (WL1, WL2, WL4, WL5, WL12) were not removed at the end of Batch 2. This set of coupons experienced both Batch 2 and Batch 3 before removal.

At the beginning of Batch 3, there was a 256 hour period of simple stripper operation. This was an equipment configuration that bypassed the AFS skid, instead using a simple stripper for regeneration. This was performed to compare the energy performance of the AFS to the simple stripper, but corrosion was not evaluated in the simple stripper

during this time. Coupons in the absorber equipment experienced corrosion, but AFS coupons were in shut-down, drained lines and experienced no corrosion. After simple stripper operation, Batch 3 experienced 879 hours of operation on the AFS skid between June 3, 2018 and July 17, 2018. The plant was shut down for a 120 hour period during the middle of Batch 3. Test conditions were slightly different during Batch 3 because two strategies were implemented to reduce amine oxidation. Batch 3 evaluated carbon steel (C1010) and stainless steel (304) in the AFS locations.

Batch 4 experienced 363 hours of operation on the AFS skid between July 21, 2018 and August 15, 2018. The plant was shut down for a 200 hour period during the middle of Batch 4. Batch 4 evaluated carbon steel (C1010) and stainless steel (316L) in the AFS locations. Similar to Batch 3, Batch 4 test conditions were slightly different because two strategies were implemented to reduce amine oxidation.

7.3. CORROSION RESULTS

7.3.1. Effect of Temperature and Velocity

There was a clear effect of temperature and fluid velocity on carbon steel corrosion. These effects are illustrated in Figure 7-3. High velocity locations had higher corrosion than low velocity locations regardless of temperature or CO_2 loading. High fluid velocity exacerbated carbon steel corrosion because it removes the protective $FeCO_3$ layer. A strong effect of CO_2 loading was not apparent. The effect of temperature on carbon steel corrosion was apparently weaker than its effect on stainless steel. This weak temperature effect is counterintuitive, but it is driven by several factors:

1. $FeCO_3$ solubility is lower at elevated temperatures, increasing the driving force for precipitation of $FeCO_3$ protective films.
2. Kinetics of $FeCO_3$ formation are faster at higher temperatures.

3. Oxidation of Fe is faster at higher temperatures, but this is irrelevant because the rate of corrosion is limited by $FeCO_3$ formation.

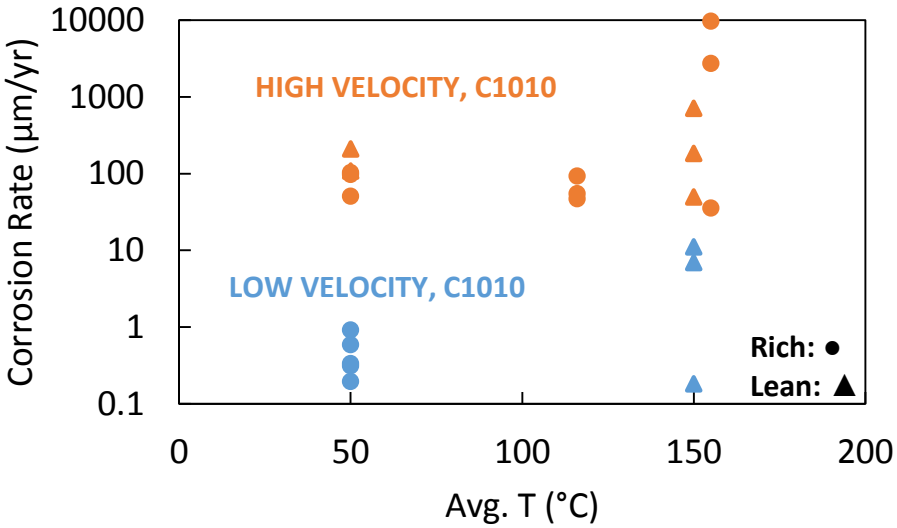

Figure 7-3: Carbon steel corrosion rates from coupon weight loss during 2018 PZ campaign, excluding Batch 1 results. Blue points are low velocity locations (eg. Sumps, vessel sample points), and red points are high velocity locations (eg. Inside pipes). Points that are circles have a rich CO_2 loading, and points that are triangles have a lean CO_2 loading.

There was no clear effect of velocity on stainless steel corrosion, which is illustrated in Figure 7-4. Low velocity locations did not demonstrate notably lower corrosion than high velocity locations. Velocity has no strong effect on stainless corrosion because stainless corrosion is not controlled by the formation of a product layer. Likewise there is a clear

effect of temperature on the corrosion of stainless steel because the more rapid oxidation of the steel at higher temperature is not limited by the formation of a protective film.

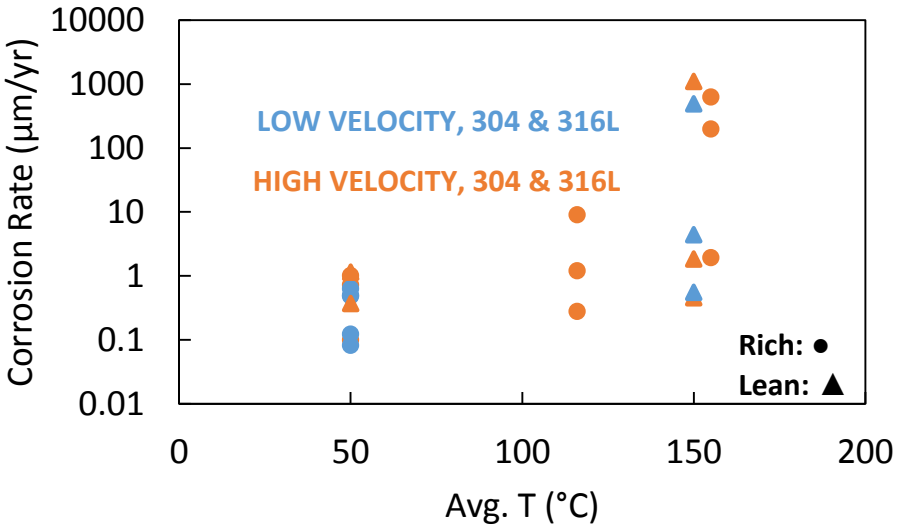

Figure 7-4: Stainless steel (304 and 316L) corrosion rates from coupon weight loss during 2018 PZ campaign. Blue points are low velocity locations (eg. Sumps, vessel sample points), and red points are high velocity locations (eg. Inside pipes). Points that are circles have a rich CO_2 loading, and points that are triangles have a lean CO_2 loading.

Apparent activation energies for coupon corrosion rates are given in Table 7-7. These activation energies were determined using least squares regressions of the weight loss coupon corrosion rates on Arrhenius plots. The limited dataset and the imperfect reproducibility of corrosion measurements at the pilot scale mean there is significant uncertainty in these activation energies. Several different activation energies were determined by isolating parts of the dataset. Notably, activation energy for carbon steel corrosion is higher at rich CO_2 loadings, but velocity had only a small effect on activation energy. The overall activation energy for carbon steel corrosion is 29 kJ/mol. Activation energy for stainless steel corrosion has a similar loading effect, with higher activation

energy at rich CO_2 loadings. Velocity had very little effect on activation energy of stainless steel corrosion. The overall activation energy for stainless steel corrosion was 42 kJ/mol.

Table 7-7: Apparent activation energies for coupon corrosion rates.

Alloy	Loading	Velocity	Apparent Activation Energy (kJ/mol)
C1010	Lean	Combined	-22
C1010	Rich	Combined	60
C1010	Combined	High	14
C1010	Combined	Low	20
C1010	Combined	Combined	29
304 & 316L	Lean	Combined	31
304 & 316L	Rich	Combined	49
304 & 316L	Combined	High	41
304 & 316L	Combined	Low	42
304 & 316L	Combined	Combined	42

The effect of velocity on the corrosion of carbon steel is given in Figure 7-5. This is the same data presented in Figure 7-3, but highlighting the effect of velocity instead of temperature. Clearly velocity has a strong effect on carbon steel corrosion. The highest velocity points on this plot are in the hot rich location, where flashing is expected. These velocities do not include flashing or two phase flow, and thus may underestimate fluid velocity.

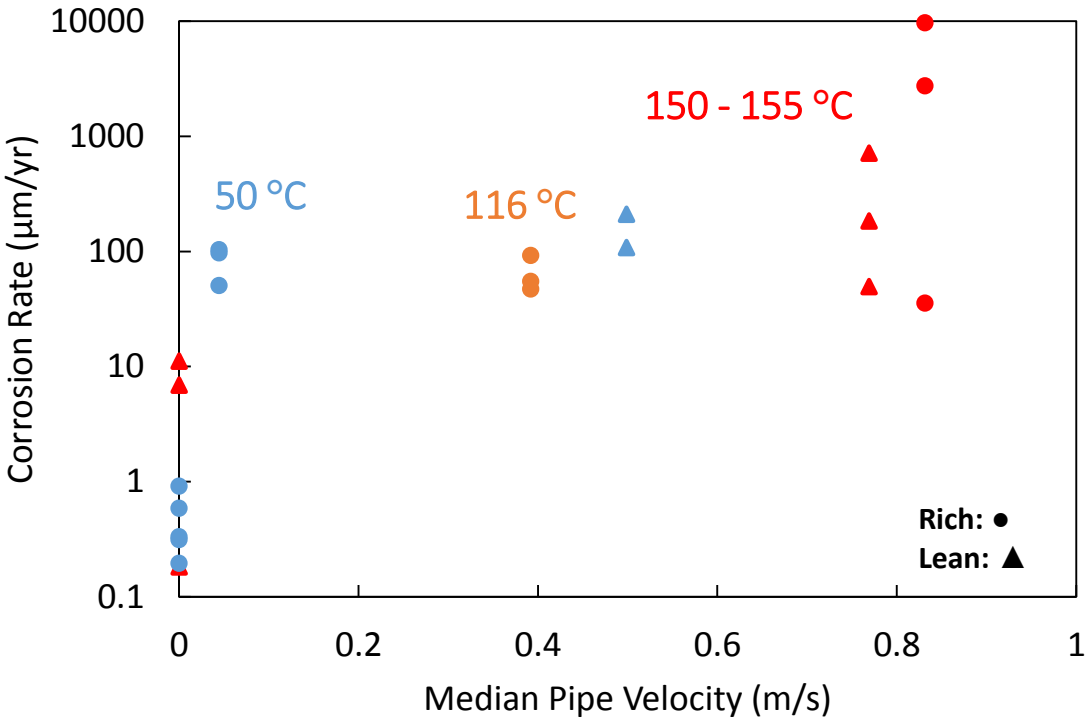

Figure 7-5: Carbon steel corrosion rates from coupon weight loss during 2018 PZ campaign, excluding Batch 1 results. Velocities represent median velocities at that location over all steady state runs throughout the entire campaign. Velocities are assumed to be zero in vessel sumps and midbed sample points. Points that are circles have a rich CO_2 loading, and points that are triangles have a lean CO_2 loading.

The effect of velocity on the corrosion of stainless steel is given in Figure 7-6. This is the same data presented in Figure 7-4, but highlighting the effect of velocity instead of temperature. Apparently velocity has a negligible effect on the corrosion of stainless steel.

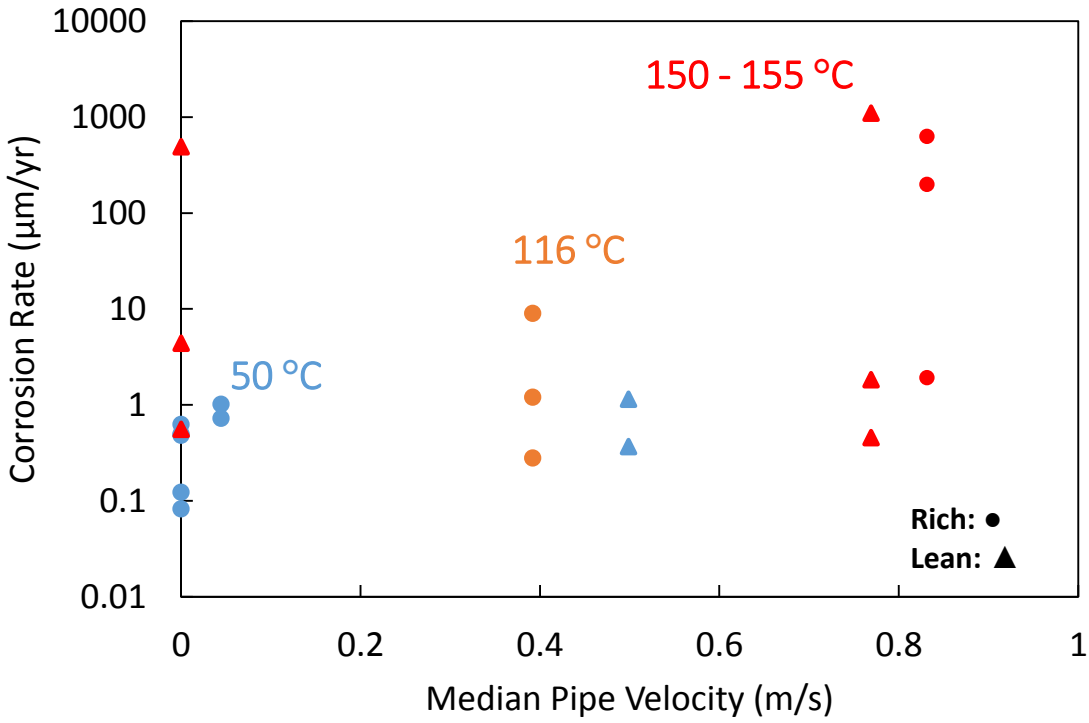

Figure 7-6: Stainless steel (304 and 316L) corrosion rates from coupon weight loss during 2018 PZ campaign. Velocities represent median velocities at that location over all steady state runs throughout the entire campaign. Velocities are assumed to be zero in vessel sumps and midbed sample points. Points that are circles have a rich CO_2 loading, and points that are triangles have a lean CO_2 loading.

7.3.2. Summary of corrosion by location

Performance of both carbon steel (C1010) and stainless steel (some 316L, others 304) were excellent (≈1µm/yr) in the absorber middle and absorber sump. Problems may occur at locations that are not adequately wetted with amine, where carbonic acid attack may occur—for example the absorber top. Non amine-wetted locations were not thoroughly investigated in this report.

In relatively low temperature piping, carbon steel is likely acceptable for some equipment. In the cold lean piping, C1010 corrosion was moderate (108 – 210 µm/yr)

during most batches (2, 3, 4). Performance in the cold rich piping was comparable (50 – 202 μm/yr). Stainless performance (some 304, others 316L) at both cold lean location and the cold rich location was excellent (0 – 1 μm/yr). The moderate performance of C1010 here suggest that it may be acceptable for some equipment at this condition, although the corrosion rates may still be too high for very thin surfaces (ie, heat exchanger surfaces).

At some elevated temperature locations, carbon steel is likely appropriate for some equipment. C1010 performance in the warm rich bypass was good (55 – 158 μm/yr). C1010 also performed well in the AFS sump (7 – 11 μm/yr). The surprising performance of C1010 at elevated temperature is due to the presence of protective siderite and magnetite films. Stainless steel (some 304, others 316L) also typically performs well at these locations (0 – 9 μm/yr). However stainless steel was attacked (489 μm/yr) during Batch 2 in the AFS sump. The occasional vulnerability of stainless steel at this location suggests that carbon steel may be a preferable material of construction for the AFS sump.

At high temperature, high fluid velocity locations, protective films are not adequate to protect carbon steel, and corrosion can be high. Overall performance of C1010 was poor (50 – 711 μm/yr) in the hot lean stream and poor in the hot rich stream (36 – 9621 μm/yr).

At high temperature, high fluid velocity locations, stainless steel is also frequently attacked. In the hot rich location, stainless performance (some 304, others 316L) was poor (1 – 629 μm/yr). In the hot lean stream, stainless (some 304, others 316L) performed well for Batches 3 and 4 (1 – 2 μm/yr), but experienced high corrosion (1095 μm/yr) during Batch 2. Until the occasional vulnerability of stainless steel at these locations is understood, higher alloy steels (ie, duplex stainless) should be investigated.

A simplified diagram showing equipment selection recommendations is shown in Figure 7-7.

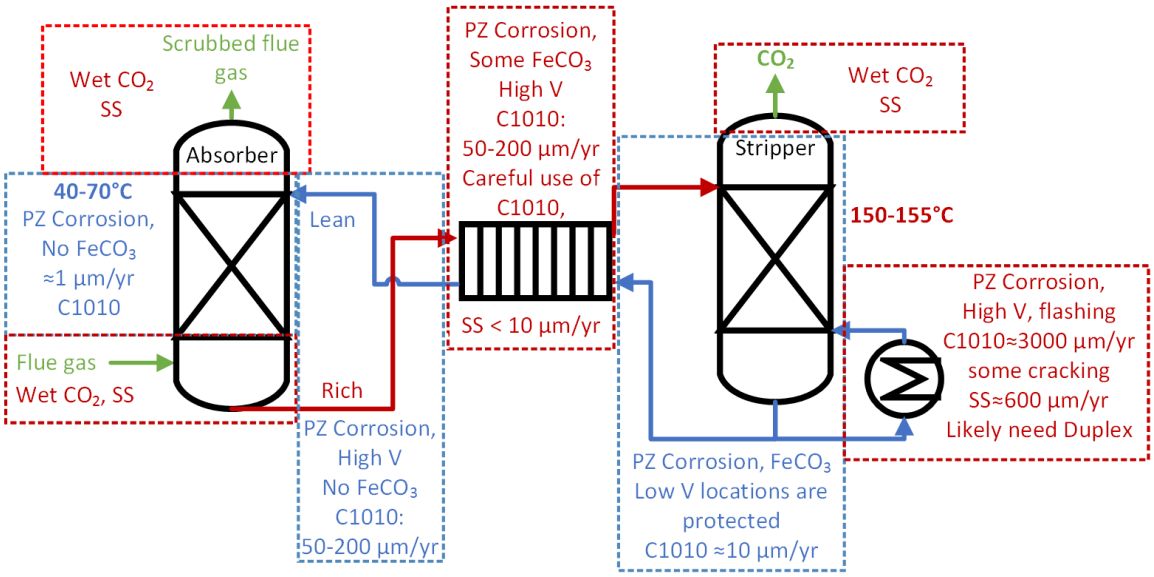

Figure 7-7: Simplified equipment selection diagram, highlighting locations where stainless steel (SS) or carbon steel are appropriate.

7.3.3. Corrosion compared between batches

One hypothesis for this campaign was that corrosion rates would increase over time as the amine solution became more degraded. There was no strong trend of corrosivity increasing over time during the campaign. Corrosion rates of carbon steel by location and batch are shown in Table 7-8, and a similar table for corrosion of stainless steel by location and batch is shown in Table 7-9.

Corrosion was not perfectly reproducible between the batches, and a few unusual results are immediately apparent. Batch 2 was unusually corrosive to stainless steel at high temperatures. Although stainless vulnerability was seen during other batches at the hot rich location, Batch 2 was the only time when the hot lean location and AFS sump experienced stainless attack. In addition, during Batch 2, carbon steel performed well at the hot lean location, which experienced severe attack during Batches 3 and 4. Carbon steel also

performed much worse during Batch 2 in the hot lean location than during Batches 3 and 4.

The poor performance of stainless in Batch 2, combined with its improved performance in Batches 3 and 4 suggest that stainless was pushed from the active region (Batch 2) into the passive region (Batch 3 and 4). This suggests conditions became more oxidizing. Several process changes could be responsible. First, several strategies were tried to reduce solvent oxidative degradation beginning in Batch 3 and continuing through the end of the campaign. A small flowrate of nitrogen (≈1-2 cfm) was injected into the absorber sump in an attempt to strip dissolved oxygen from the rich solvent so it wouldn't be carried over to the stripper. This would have the effect of making the solvent less oxidizing. Nitrogen stripping did not have a large effect on solvent oxidative degradation during the campaign (G. Rochelle et al., 2019). This suggests that the nitrogen stripping method was ineffective in reducing dissolved oxygen. The nitrogen flowrate may have been too small, or the gas/liquid contacting area insufficient to allow proper stripping of dissolved oxygen. The coupon evidence that the solvent actually became more oxidizing is another piece of evidence that dissolved oxygen stripping was ineffective in this campaign. SO_3 was injected into the flue gas to cause amine aerosol formation for 2-4 hours a day for 11 days during Batch 3. This may have had some effect on making the solution more oxidizing, although it is likely that the SO_3 is rapidly converted to H_2SO_4 in the flue gas before contacting the amine. Thus the SO_3 injection is equivalent to adding sulfate, which is likely not strongly oxidizing. The most likely explanation is that degradation products and dissolved Fe^{2+} in solution slowly increased through the campaign and made the solvent more oxidizing. This finally crossed a threshold during Batch 3 that passivated the stainless steel.

Corrosion rates were elevated for Batch 1, this is partially due to the short time period used for the corrosion rate calculations for this batch. In addition, the water testing and water/CO_2 circulation conditions present during Batch 1 are challenging for C1010. Batch 1 is representative of the commissioning phase, when equipment is pressure tested by circulating water and steam. Apparently equipment commissioning can be more corrosive to carbon steel than operation with 5 m PZ. Notably, operation with 5 m PZ in the absorber typically leaves C1010 pristine, but extended water testing caused moderate corrosion. High velocity locations also experienced corrosion (hot lean, hot rich, cold lean).

Table 7-8: Coupon weight loss corrosion rates (μm/yr) of carbon steel (C1010) by batch and location

Location Tag	Location Description	BATCH 1	BATCH 2	BATCH 2 & 3	BATCH 3	BATCH 4
WL4	Absorber top			5		
WL2	Absorber middle			0		
ER2	Absorber middle	181				0
ER3	Absorber sump	135	1		0	1
WL12	Cold lean	603		108		210
WL13	Cold rich bypass	202	97		50	103
WL14	Warm rich bypass	157	55		47	92
WL19	Hot rich	297	36		2729	9621
WL21	Hot lean	481	711		49	184
WL22	AFS Sump	157	7		0	11

Table 7-9: Coupon weight loss corrosion rates (μm/yr) of stainless steel (316L and 304) by batch and location

Location Tag	Location Description	BATCH 2	BATCH 2 & 3	BATCH 3	BATCH 4
WL2	Absorber middle		0		
ER2	Absorber middle				0
ER3	Absorber sump	0		0	1
WL12	Cold lean		0		1
WL13	Cold rich bypass	1		0	1
WL14	Warm rich bypass	9		0	1
WL19	Hot rich	629		198	2
WL21	Hot lean	1095		0	2
WL22	AFS Sump	489		1	4

7.4. CORROSION BY LOCATION

The next sections present detailed corrosion results for each location.

7.4.1. Absorber Middle

Corrosion in the absorber middle (ER2 and WL2) is summarized in Table 7-10. Overall performance of C1010 was good (0.2 – 0.3) during most batches (2, 3, and 4). Stainless performance (some 304, others 316L) was good (0.1 – 0.5 μm/yr). The good performance of C1010 here suggests that it is likely acceptable for equipment at this condition.

SEM micrographs were not made of the Batch 1 C1010 coupon taken from the absorber middle. Powder XRD found a layer of iron on the coupon surface. The high corrosion rate at this location (181.1 μm/yr) is partially due to the short time period used for the corrosion rate calculations for Batch 1. Notice the mass loss for C1010 at this location was more significant during Batch 1 than during the other batches, despite the shorter immersion time. This shows that the water testing and water/CO_2 circulation

conditions present during Batch 1 are challenging for C1010. It is possible that some of the mass lost occurred during the initial water testing period, and that the post-PZ exposure water circulation period was less corrosive.

Figure 7-8 shows the SEM micrographs of coupons that experienced both Batches 2 and 3 in the absorber middle. The 316L surface is mostly clean, and corrosion here is low (0.1 μm/yr). Small imperfections are visible in the SEM micrograph. These imperfections are not pits, but rather are small crystal deposits, which energy-dispersive X-ray spectroscopy suggests are a calcium compound, possibly $CaCO_3$. The SEM micrograph of the C1010 coupon shows a mostly clean surface with small amounts of corrosion product formation. This corrosion product was not identified. Although this coupon lacked a protective product layer, corrosion at this location was low (0.3 μm/yr)

Figure 7-9 shows the SEM micrographs of Batch 4 coupons taken from the absorber middle. The SEM micrograph of the 316L coupon shows a mostly pristine surface, and corrosion here was low (0.5 μm/yr). The SEM micrograph of the C1010 coupon shows a mostly pristine surface, and corrosion at this location was low (0.2 μm/yr).

Table 7-10: Summary of coupon weight loss for ER2 and WL2 (Absorber Middle locations)

Batch	Location	Alloy	Original Mass (g)	Mass Loss (g)	Mass of Film(g)	Operating Time (hrs)	Coupon Type	Corrosion rate (μm/yr)	XRD Products
Batch 2 & 3	WL2	316L	16.1039	0.0002	0.0002	1523	Disc	0.1	None
Batch 4	ER2	316L	10.4931	0.0003	0.0001	363	Strip	0.5	None
Batch 1	ER2	C1010	10.1579	0.0225	0.0077	66	Strip	181.1	Iron
Batch 2 & 3	WL2	C1010	17.4983	0.0008	0.0005	1523	Disc	0.3	None
Batch 4	ER2	C1010	8.8801	0.0001	0.0004	363	Strip	0.2	None

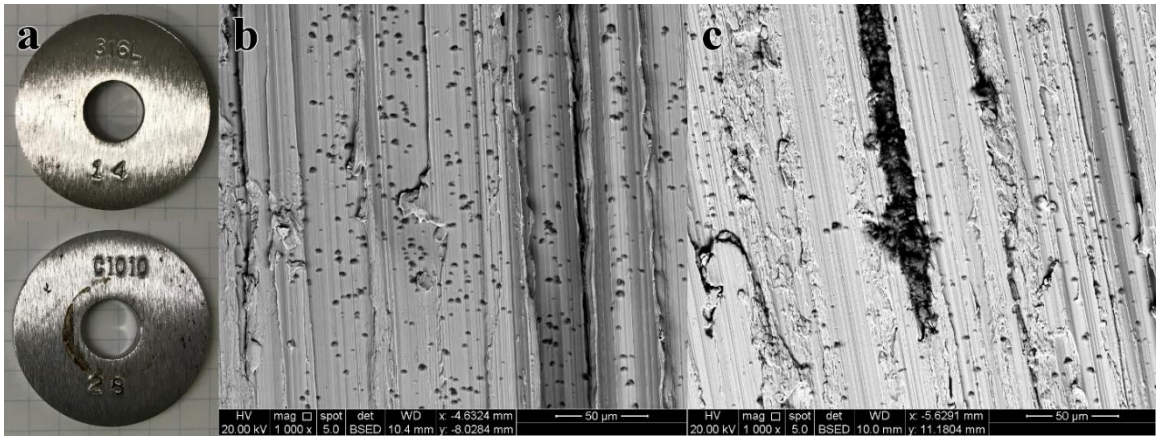

Figure 7-8: (a) 316L and C1010 coupons from Batch 2 and 3 after removal from absorber middle (WL2). (b) SEM micrograph of 316L coupon. The small imperfections are not pits, but rather are small crystal deposits, which energy-dispersive X-ray spectroscopy suggests are a calcium compound, possibly $CaCO_3$. (c) SEM micrograph of C1010, coupon, showing small amounts of an unidentified corrosion product.

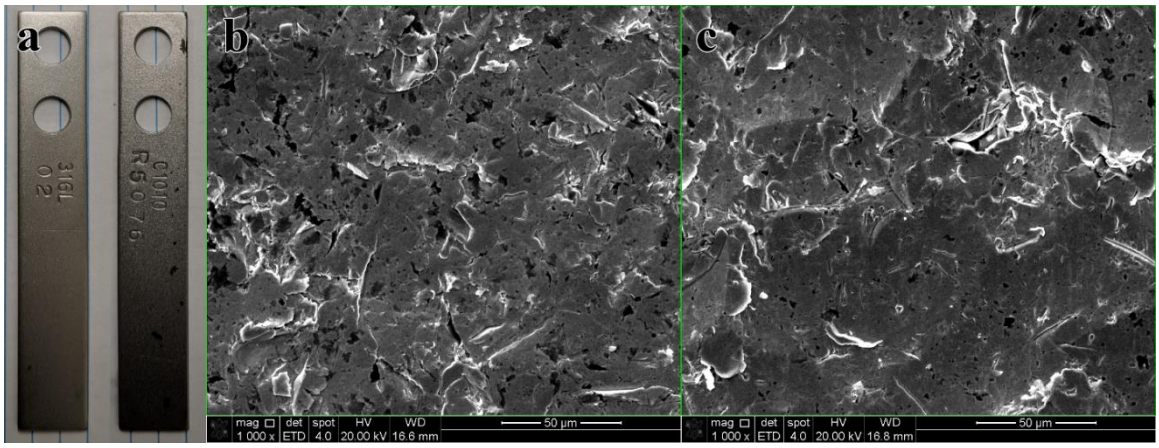

Figure 7-9: (a) 316L and C1010 coupons from Batch 4 after removal from absorber middle (ER2). (b) SEM micrograph of 316L coupon, showing largely pristine coupon surface. (c) SEM micrograph of C1010, coupon, showing largely pristine coupon surface.

7.4.2. Absorber Sump

Corrosion in the absorber sump (ER3) is summarized in Table 7-11Table 7-16. Overall performance of C1010 was good (0.3 – 0.9) during most batches (2, 3, and 4).

Stainless performance (some 304, others 316L) was good (0.1 – 0.6 μm/yr). The good performance of C1010 here suggests that it is likely acceptable for equipment at this condition.

Figure 7-10 shows the SEM micrograph of a Batch 1 C1010 coupon taken from the absorber sump. The SEM micrograph of this coupon shows a patchy crystalline layer. This product was identified as iron by powder XRD. The high corrosion rate at this location (135.3 μm/yr) is partially due to the short time period used for the corrosion rate calculations for Batch 1. Notice the mass loss for C1010 at this location was more significant during Batch 1 than during the other batches, despite the shorter immersion time. This shows that the water testing and water/CO_2 circulation conditions present during Batch 1 are challenging for C1010. It is possible that some of the mass lost occurred during the initial water testing period, and that the post-PZ exposure water circulation period was less corrosive.

Figure 7-11, Figure 7-12, and Figure 7-13 show the coupon images and SEM micrographs of coupons from the absorber sump during Batch 2, Batch 3, and Batch 4, respectively. Corrosion of C1010 during these batches was low (0.3 – 0.9 μm/yr), the SEM micrographs look pristine, and no corrosion products were observed. Corrosion of stainless steel (some 304, others 316L) was low (0.1 – 0.6 μm/yr), the SEM micrographs look pristine, and no corrosion products were observed.

Table 7-11: Summary of coupon weight loss for ER3 (Absorber Sump)

Batch	Alloy	Original Mass (g)	Mass Loss (g)	Mass of Film(g)	Operating Time (hrs)	Coupon Type	Corrosion rate (μm/yr)	XRD Products
Batch 3	304	10.5712	0.0003	0.0001	1135	Strip	0.1	None
Batch 2	316L	10.3752	0.0004	0.0002	388	Strip	0.5	None
Batch 4	316L	10.5040	0.0004	0.0003	363	Strip	0.6	None
Batch 1	C1010	10.3201	0.0168	0.0077	66	Strip	135.3	Iron
Batch 2	C1010	9.9742	0.0007	0.0004	388	Strip	0.9	None
Batch 3	C1010	10.6997	0.0007	0.0003	1135	Strip	0.3	None
Batch 4	C1010	8.8170	0.0004	0.0001	363	Strip	0.6	None

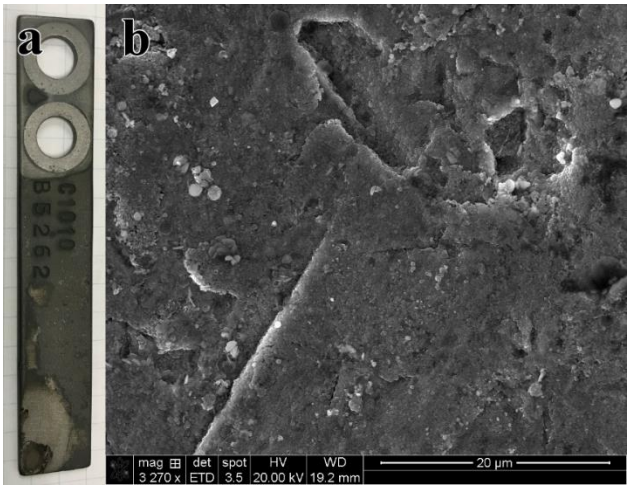

Figure 7-10: (a) C1010 coupon from Batch 1 after removal from absorber sump. (b) SEM micrograph of C1010 coupon, showing black product identified by powder XRD as iron.

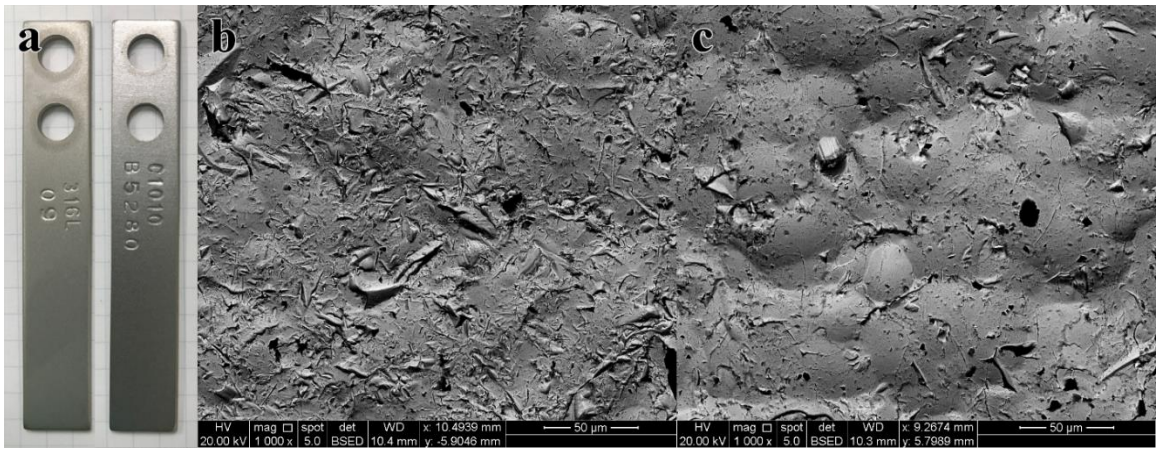

Figure 7-11: (a) 316L and C1010 coupons from Batch 2 after removal from absorber sump. (b) SEM micrograph of 316L coupon, showing largely pristine coupon surface. (c) SEM micrograph of C1010, coupon, showing largely pristine coupon surface.

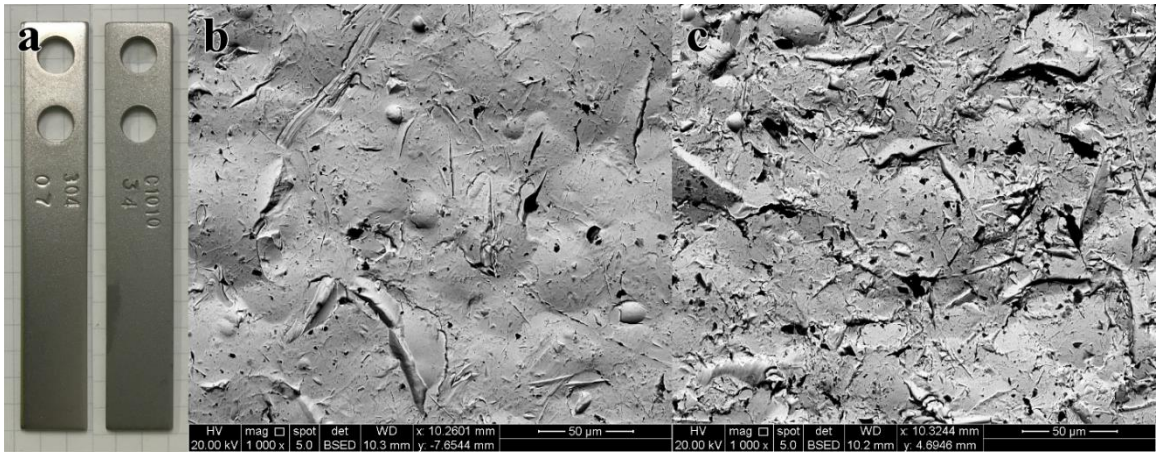

Figure 7-12: (a) 304 and C1010 coupons from Batch 3 after removal from absorber sump. (b) SEM micrograph of 304 coupon, showing largely pristine coupon surface. (c) SEM micrograph of C1010, coupon, showing largely pristine coupon surface.

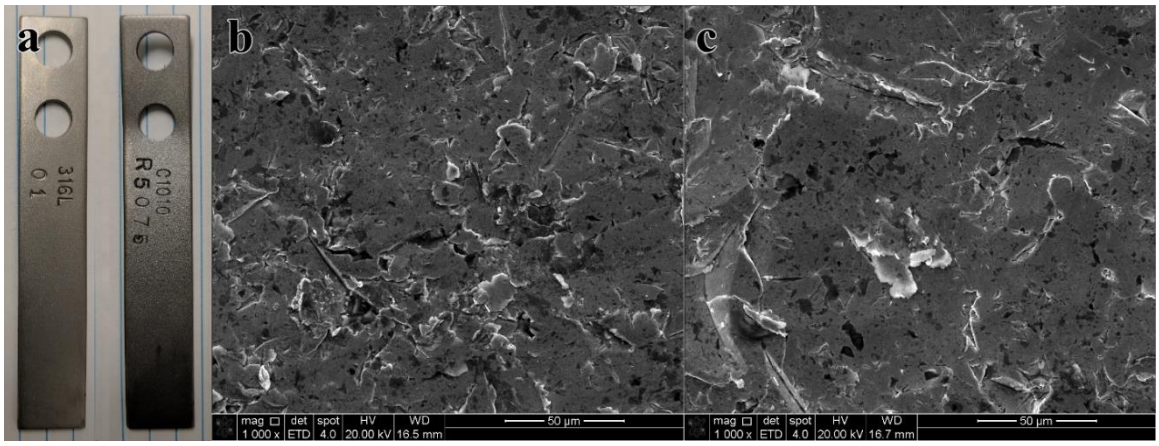

Figure 7-13: (a) 316L and C1010 coupons from Batch 4 after removal from absorber sump. (b) SEM micrograph of 316L coupon, showing largely pristine coupon surface. (c) SEM micrograph of C1010, coupon, showing largely pristine coupon surface.

7.4.3. Absorber Top

Corrosion at the absorber top (WL4) is summarized in Table 7-12. Limited coupons from this location were analyzed, because the largely amine-free water and CO_2 environment is well characterized in literature. Performance of C1010 was good (5.1 µm/yr). Stainless corrosion was not quantified, but appears low. Despite the low corrosion rate measured here, C1010 is typically avoided in amine free water and CO_2 environments because any locations that collect water will reach low pH and experience carbonic acid corrosion.

Figure 7-14 shows the SEM micrographs of coupons that experienced both Batches 2 and 3 in the absorber top. The 316L surface is mostly pristine, and there is no evidence of corrosion, although a weight loss measurement was not performed for this coupon. The SEM micrograph of the C1010 coupon shows a patchy corrosion product film. This product was identified as goethite and magnetite by powder XRD. Although this coupon lacked a protective product layer, corrosion at this location was low (5.1 µm/yr)

Table 7-12: Summary of coupon weight loss for WL4 (Absorber Top)

Batch	Alloy	Original Mass (g)	Mass Loss (g)	Mass of Film(g)	Operating Time (hrs)	Coupon Type	Corrosion rate (μm/yr)	XRD Products
Batch 2 & 3	C1010	17.4892	0.0122	0.0138	1523	Disc	5.1	Goethite, Magnetite

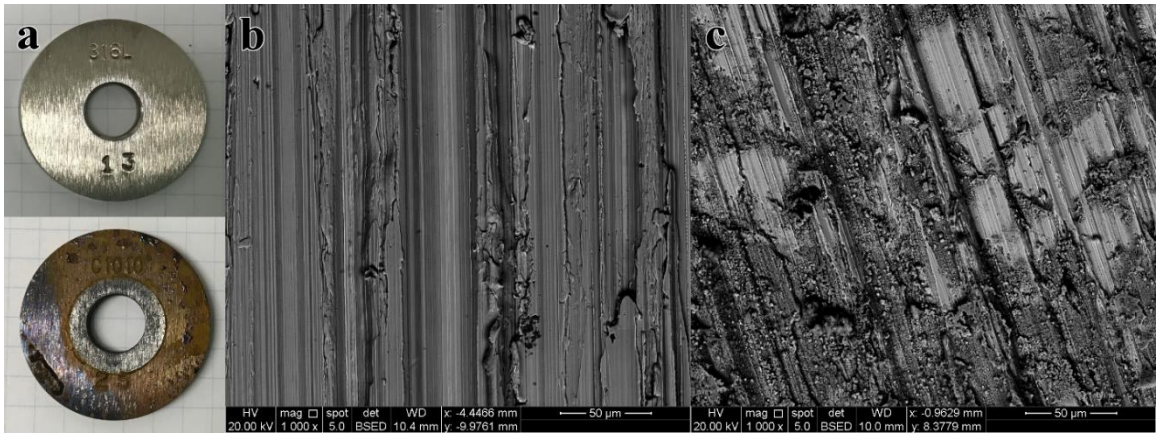

Figure 7-14: (a) 316L and C1010 coupons from Batch 2 and 3 after removal from absorber top. (b) SEM micrograph of 316L coupon, showing largely pristine surface. (c) SEM micrograph of C1010, coupon, showing product identified by powder XRD as a mix of goethite and magnetite.

7.4.4. Cold Lean

Corrosion in the cold lean stream (WL12) is summarized in Table 7-13. Overall performance of C1010 was only moderate (108 – 210 μm/yr) during most batches (2, 3, 4). Stainless performance (some 304, others 316L) was good (0 – 1 μm/yr). The moderate performance of C1010 here suggests that it might be acceptable for some equipment at this condition, although the corrosion rates may still be too high for thin surfaces (ie, heat exchanger surfaces).

Figure 7-15 shows the SEM micrograph of a Batch 1 C1010 coupon taken from the cold lean stream. The SEM micrograph of this coupon shows a rough corrosion product layer. This product was identified as a mix of iron, siderite, and magnetite by powder

XRD. The high corrosion rate at this location (602.9 μm/yr) is partially due to the short time period used for the corrosion rate calculations for Batch 1. It is possible that some of the mass lost occurred during the initial water testing period, and that the post-PZ exposure water circulation period was less corrosive.

Figure 7-16 shows the SEM micrographs of coupons that experienced both Batches 2 and 3 in the cold lean stream. The 316L surface is mostly pristine, and corrosion here is low (0.4 μm/yr). The SEM micrograph of the C1010 coupon shows a porous crystalline layer. This product was identified as iron by powder XRD. Although this coupon lacked a protective product layer, corrosion at this location was moderate (108.2 μm/yr)

Figure 7-17 shows the SEM micrographs of Batch 4 coupons taken from the cold lean stream. The SEM micrograph of the 316L coupon shows a mostly pristine surface, and corrosion here was low (1.1 μm/yr). The SEM micrograph of the C1010 coupon shows a porous crystalline product layer. This product was identified as iron by powder XRD. Although this coupon lacked a protective product layer, corrosion at this location was moderate (210.1 μm/yr).

Table 7-13: Summary of coupon weight loss for WL12 (Cold lean)

Batch	Alloy	Original Mass (g)	Mass Loss (g)	Mass of Film(g)	Operating Time (hrs)	Coupon Type	Corrosion rate (μm/yr)	XRD Products
Batch 2 & 3	316L	16.4105	0.0009	0.0003	1523	Disc	0.4	None
Batch 4	316L	16.4469	0.0007	0.0003	363	Disc	1.1	None
Batch 1	C1010	17.5147	0.0631	0.0326	66	Disc	602.9	Iron, Siderite, Magnetite
Batch 2 & 3	C1010	17.5266	0.2601	0.0108	1523	Disc	108.2	Iron
Batch 4	C1010	17.1705	0.1205	0.0074	363	Disc	210.1	Iron

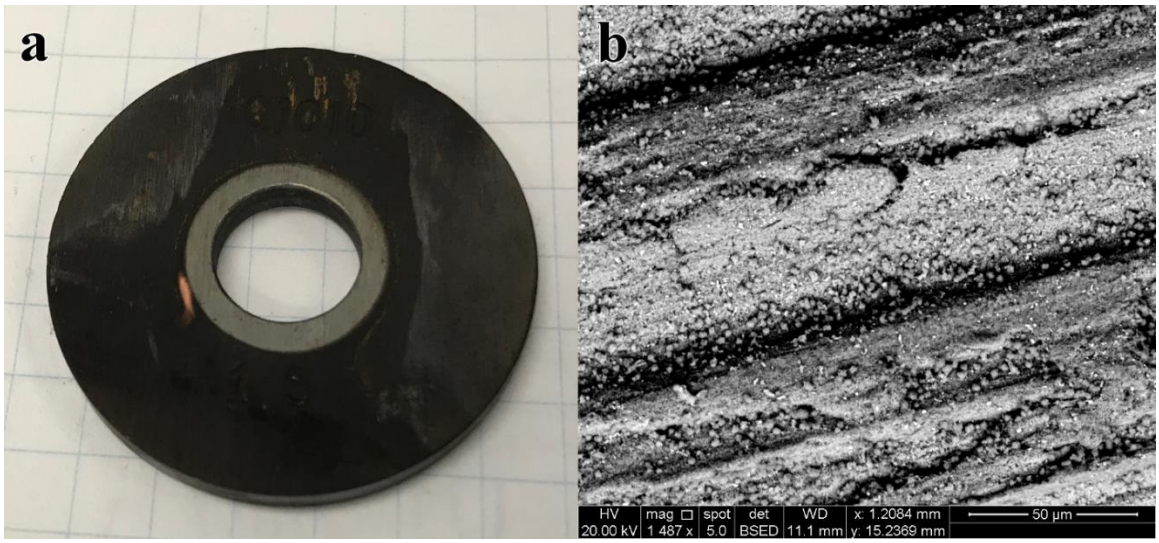

Figure 7-15: (a) C1010 coupon from Batch 1 after removal from cold lean stream. (b) SEM micrograph of C1010, coupon, showing product identified by powder XRD as a mix of iron, siderite, and magnetite.

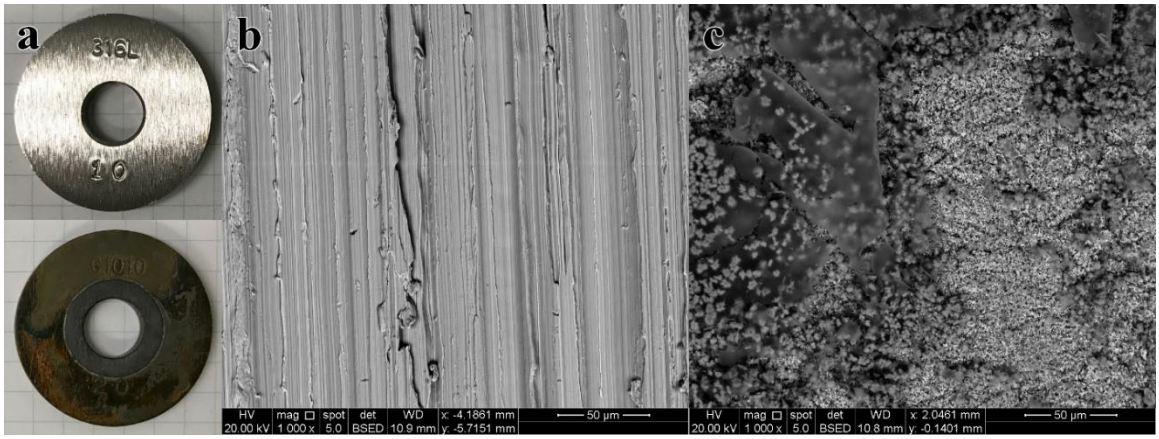

Figure 7-16: (a) 316L and C1010 coupons from Batch 2 and 3 after removal from cold lean stream. (b) SEM micrograph of 316L coupon, showing largely pristine surface. (c) SEM micrograph of C1010, coupon, showing a rough, porous layer identified by powder XRD as iron.

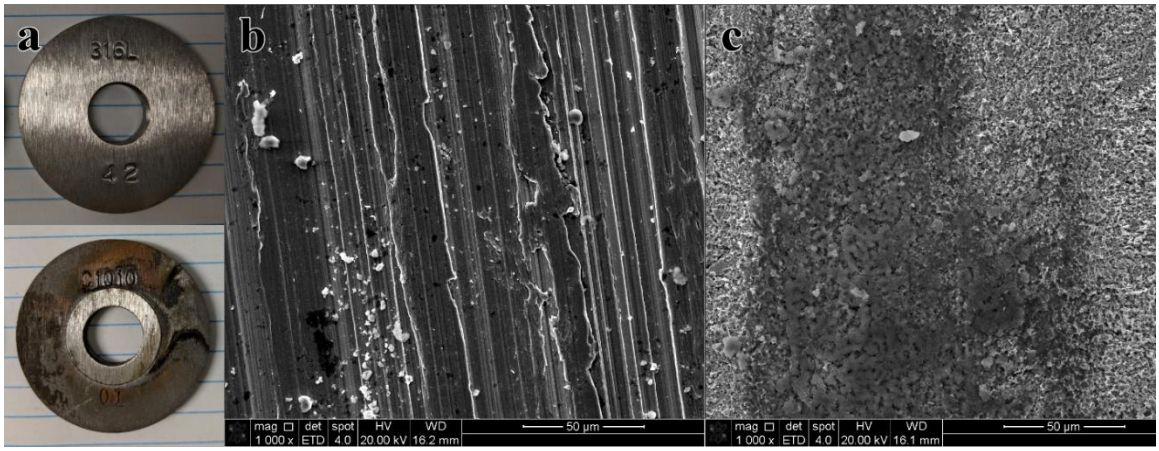

Figure 7-17: (a) 316L and C1010 coupons from Batch 4 after removal from cold lean stream. (b) SEM micrograph of 316L coupon, showing largely pristine surface. (c) SEM micrograph of C1010, coupon, showing a rough, porous layer identified by powder XRD as iron. Can we add the measured corrosion rate to all of the figures?

7.4.5. Cold Rich Bypass

Corrosion in the cold rich bypass (WL13) is summarized in Table 7-14. Overall performance of C1010 was good (50 – 202 µm/yr). Stainless performance (some 304, others 316L) was good (0 – 1 µm/yr). The good performance of C1010 here suggest that it may be acceptable for some equipment at this condition, although the corrosion rates may still be too high for very thin surfaces (ie, heat exchanger surfaces).

Figure 7-18 shows the SEM micrograph of a Batch 1 C1010 coupon taken from the cold rich bypass. The SEM micrograph of this coupon shows a patchy crystalline layer. This product was identified as a mix of iron, siderite, and magnetite by powder XRD. The high corrosion rate at this location (202.2 µm/yr) is partially due to the short time period used for the corrosion rate calculations for Batch 1. It is possible that some of the mass lost occurred during the initial water testing period, and that the post-PZ exposure water circulation period was less corrosive.

Figure 7-19 shows the SEM micrographs of Batch 2 coupons taken from the warm rich bypass. The 316L surface is mostly pristine, and corrosion here is low (0.7 μm/yr). The SEM micrograph of the C1010 coupon shows a somewhat porous crystalline layer. This product was identified as iron by powder XRD. Although this coupon lacked a protective product layer, corrosion at this location was moderate (96.8 μm/yr)

Figure 7-20Figure 7-28 shows the SEM micrographs of Batch 3 coupons taken from the warm rich bypass. The 304 coupon has a mostly pristine appearance and corrosion was low (0.0 μm/yr). The SEM micrograph of the C1010 coupon shows a crystalline product layer. This product was identified as a mix of iron and siderite by powder XRD. This layer was apparently protective, and corrosion at this location was low (50.3 μm/yr).

Figure 7-21 shows the SEM micrographs of Batch 4 coupons taken from the warm rich bypass. The SEM micrograph of the 316L coupon shows a mostly pristine surface, and corrosion here was low (1.0 μm/yr). The SEM micrograph of the C1010 coupon shows a crystalline product layer. This product was identified as a mix of siderite and iron by powder XRD. Corrosion at this location was moderate (103.4 μm/yr).

Table 7-14: Summary of coupon weight loss for WL13 (Cold rich bypass)

Batch	Alloy	Original Mass (g)	Mass Loss (g)	Mass of Film(g)	Operating Time (hrs)	Coupon Type	Corrosion rate (μm/yr)	XRD Products
Batch 3	304	10.5690	0.0000	-0.0001	879	Strip	0.0	None
Batch 2	316L	10.3744	0.0005	0.0001	388	Strip	0.7	None
Batch 4	316L	10.3729	0.0007	0.0003	363	Strip	1.0	None
Batch 1	C1010	9.9648	0.0252	0.0119	66	Strip	202.2	Iron, Siderite, Magnetite
Batch 2	C1010	9.8353	0.0705	0.0453	388	Strip	96.8	Iron
Batch 3	C1010	9.8037	0.0831	0.0319	879	Strip	50.3	Iron, Siderite
Batch 4	C1010	10.7251	0.0705	0.0282	363	Strip	103.4	Siderite, Iron

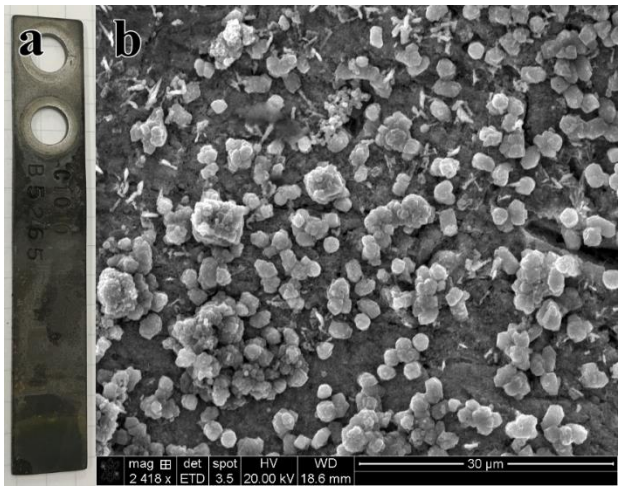

Figure 7-18: (a) C1010 coupon from Batch 1 after removal from cold rich bypass. (b) SEM micrograph of C1010, coupon, showing patchy layer identified by powder XRD as a mix of iron, siderite, and magnetite.

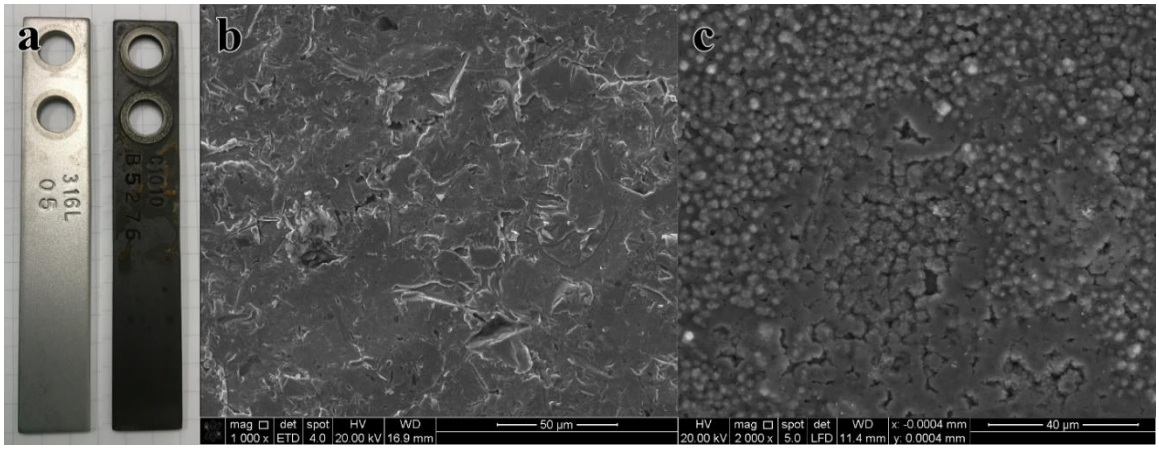

Figure 7-19: (a) 316L and C1010 coupons from Batch 2 after removal from cold rich bypass. (b) SEM micrograph of 316L coupon, showing largely pristine surface. (c) SEM micrograph of C1010, coupon, showing a rough layer identified by powder XRD as iron.

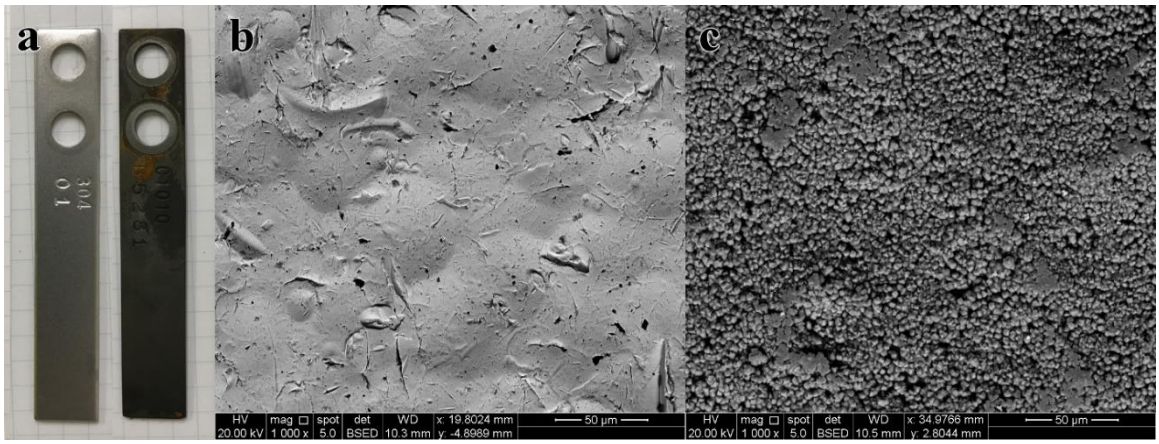

Figure 7-20: (a) 304 and C1010 coupons from Batch 3 after removal from cold rich bypass. (b) SEM micrograph of 304 coupon, showing largely pristine surface. (c) SEM micrograph of C1010, coupon, showing a crystalline layer identified by powder XRD as a mix of iron and siderite.

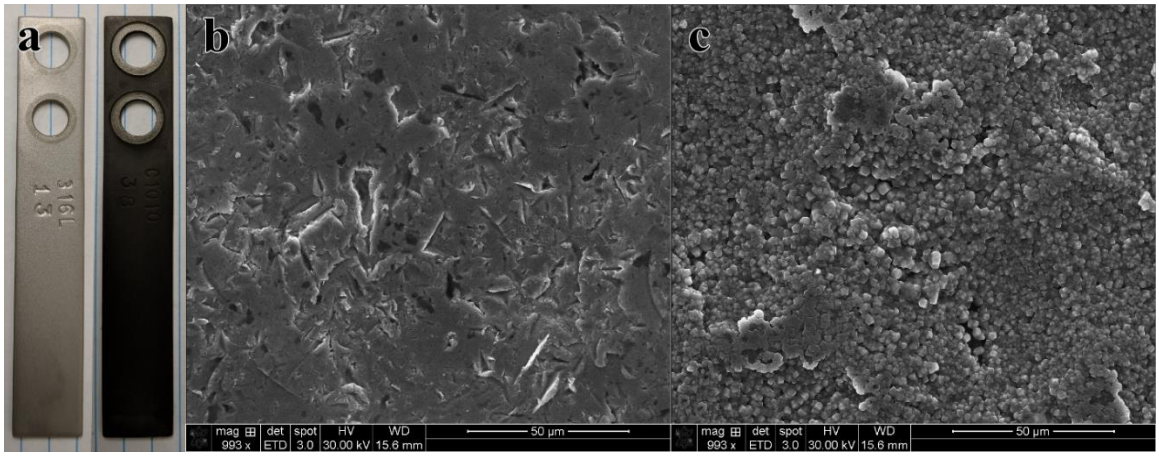

Figure 7-21: (a) 316L and C1010 coupons from Batch 4 after removal from cold rich bypass. (b) SEM micrograph of 316L coupon, showing largely pristine surface. (c) SEM micrograph of C1010, coupon, showing a crystalline layer identified by powder XRD as a mix of siderite and iron.

7.4.6. Warm Rich Bypass

Corrosion in the warm rich bypass (WL14) is summarized in Table 7-15. Overall performance of C1010 was good (55 – 158 µm/yr). Stainless performance (some 304,

others 316L) was good (0 – 9 μm/yr). The good performance of C1010 here suggests that it may be acceptable for some equipment at this condition, although the corrosion rates may still be too high for very thin surfaces (ie, heat exchanger surfaces).

Figure 7-22 shows the SEM micrograph of a Batch 1 C1010 coupon taken from the warm rich bypass. The SEM micrograph of this coupon shows a regular, crystalline layer. This product was identified as a mix of siderite and magnetite by powder XRD. The high corrosion rate at this location (157.5 μm/yr) is partially due to the short time period used for the corrosion rate calculations for Batch 1. It is possible that some of the mass lost occurred during the initial water testing period, and that the post-PZ exposure water circulation period was slightly more protected by the siderite/magnetite layer.

Figure 7-23 shows the SEM micrographs of Batch 2 coupons taken from the warm rich bypass. The 316L surface is slightly etched, but corrosion here is low (9.0 μm/yr). The SEM micrograph of the C1010 coupon shows an irregular crystalline layer. This product was identified as goethite by powder XRD. Despite the irregular product layer, corrosion at this location was low (54.8 μm/yr)

Figure 7-24 shows the SEM micrographs of Batch 3 coupons taken from the warm rich bypass. The 304 coupon has a mostly pristine appearance and corrosion was low (0.3 μm/yr). The SEM micrograph of the C1010 coupon shows an irregular product layer. This product was identified as a mix of siderite and goethite by powder XRD. Despite the irregular product layer, corrosion at this location was low (47.0 μm/yr)

Figure 7-25 shows the SEM micrographs of Batch 4 coupons taken from the warm rich bypass. The SEM micrograph of the 316L coupon shows a mostly pristine surface, and corrosion here was low (1.2 μm/yr). The SEM micrograph of the C1010 coupon shows a patchy, crystalline product layer. This product was identified as a mix of siderite by powder XRD. Corrosion at this location was moderate (92.2 μm/yr)

Table 7-15: Summary of coupon weight loss for WL14 (Warm rich bypass)

Batch	Alloy	Original Mass (g)	Mass Loss (g)	Mass of Film(g)	Operating Time (hrs)	Coupon Type	Corrosion rate (μm/yr)	XRD Products
Batch 3	304	10.6164	0.0005	0.0002	879	Strip	0.3	None
Batch 2	316L	10.3825	0.0066	0.0001	388	Strip	9.0	None
Batch 4	316L	10.3742	0.0008	0.0001	363	Strip	1.2	None
Batch 1	C1010	9.8024	0.0196	0.0171	66	Strip	157.5	Siderite, Magnetite
Batch 2	C1010	10.0250	0.0399	0.0492	388	Strip	54.8	Goethite
Batch 3	C1010	10.2811	0.0776	0.0422	879	Strip	47.0	Siderite, Goethite
Batch 4	C1010	10.7588	0.0629	0.0347	363	Strip	92.2	Siderite

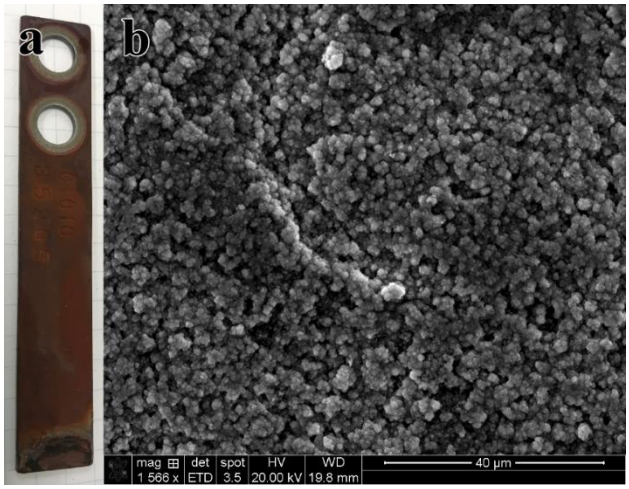

Figure 7-22: (a) C1010 coupon from Batch 1 after removal from warm rich bypass. (b) SEM micrograph of C1010, coupon, showing crystalline layer identified by powder XRD as a mix of siderite and magnetite.

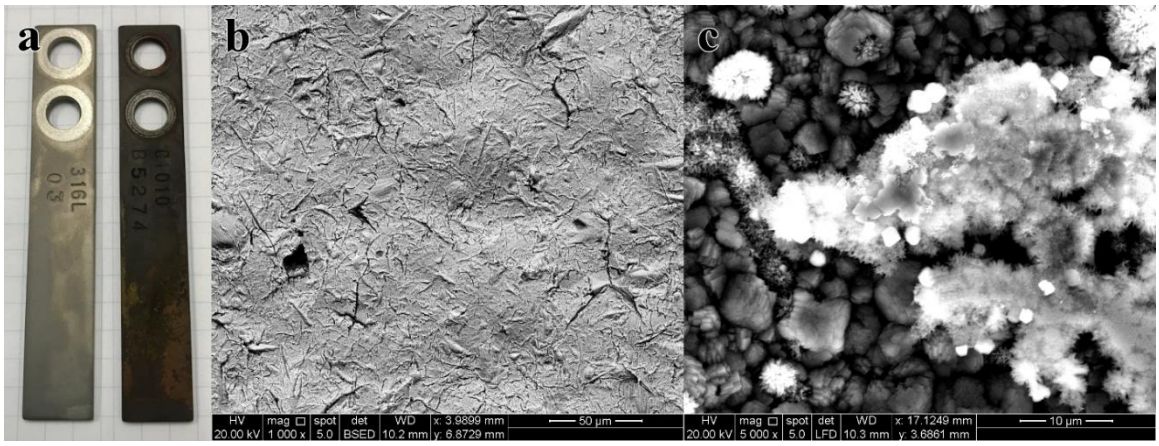

Figure 7-23: (a) 316L and C1010 coupons from Batch 2 after removal from warm rich bypass. (b) SEM micrograph of 316L coupon, showing slightly etched surface. (c) SEM micrograph of C1010, coupon, showing a layer identified by powder XRD as goethite.

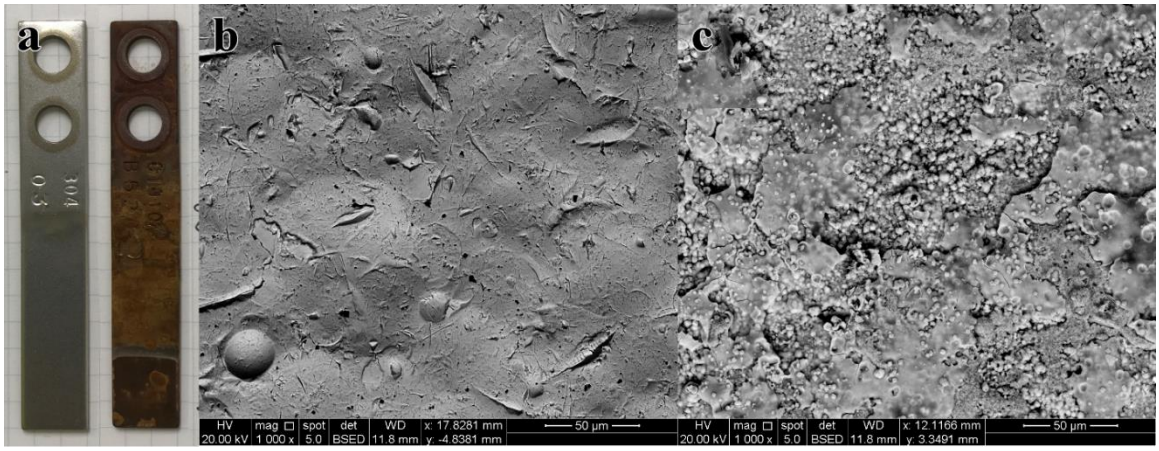

Figure 7-24: (a) 304 and C1010 coupons from Batch 3 after removal from warm rich bypass. (b) SEM micrograph of 304 coupon, showing largely pristine surface. (c) SEM micrograph of C1010, coupon, showing a layer identified by powder XRD as siderite and goethite.

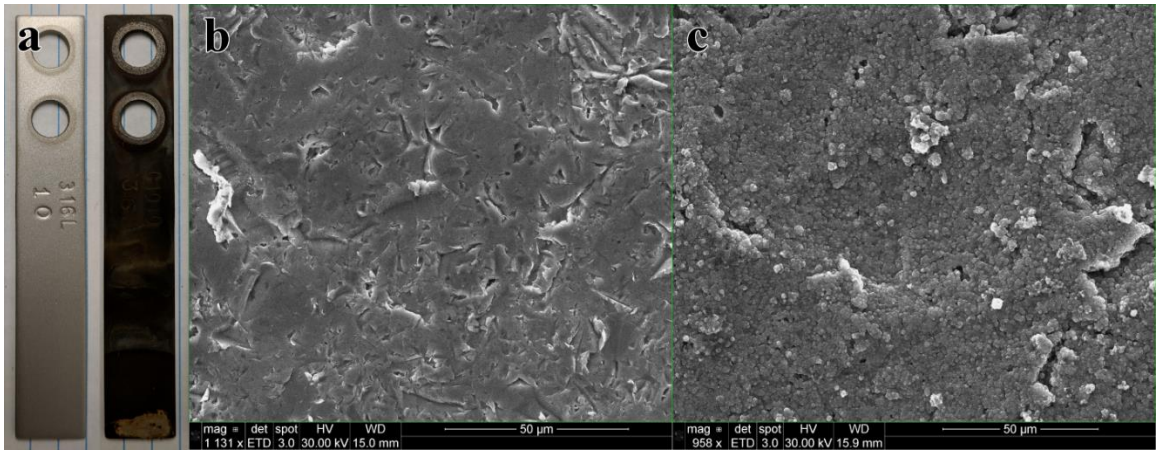

Figure 7-25: (a) 316L and C1010 coupons from Batch 4 after removal from warm rich bypass. (b) SEM micrograph of 316L coupon, showing largely pristine surface. (c) SEM micrograph of C1010, coupon, showing a layer identified by powder XRD as siderite.

7.4.7. Hot rich

Corrosion in the hot rich stream (WL19) is summarized in Table 7-16. Overall performance of C1010 was unnacceptable (36 – 9621 µm/yr). In Batch 4, a C1010 coupon cracked, suggesting that environmentally induced cracking may occur at this condition. Stainless performance (some 304, others 316L) was poor (1 – 629 µm/yr). Until the occasional vulnerability of stainless steel at this location is understood, higher alloy steels (ie, duplex stainless) should be investigated for use at this location.

Figure 7-26 shows the SEM micrograph of a Batch 1 C1010 coupon taken from the hot rich stream. The SEM micrograph of this coupon shows a regular, crystalline layer. This product was identified as a mix of siderite and magnetite by powder XRD. The high corrosion rate at this location (297.0 µm/yr) is partially due to the short time period used for the corrosion rate calculations for Batch 1. It is possible that some of the mass lost occurred during the initial water testing period, and that the post-PZ exposure water circulation period was slightly more protected by the siderite/magnetite layer.

Figure 7-27 shows the SEM micrographs of Batch 2 coupons taken from the hot rich stream. The 316L surface is etched and bare, consistent with the high corrosion rate (628.6 μm/yr) observed here. The austenitic grain boundaries are clearly visible in the etched 316L steel (Figure 7-27-B). The SEM micrograph of the C1010 coupon shows a regular, crystalline layer. This product was identified as a mixture of $FeCO_3$ and Fe_3O_4 by powder XRD. The low corrosion rate at this location (35.5 μm/yr) shows that this layer was protective.

Figure 7-28 shows the SEM micrographs of Batch 3 coupons taken from the hot rich stream. The 304 coupon has a yellow, corroded appearance, and corrosion was high (198.4 μm/yr). An SEM micrograph of the 304 coupon shows an etched surface with clearly visible austenitic grain boundaries. Any corrosion product present was too thin to be scraped off and identified by powder XRD. The SEM micrograph of the C1010 coupon shows a coat of very large pyramidal crystals. This product was identified as $FeCO_3$ and Fe by powder XRD. The high corrosion rate at this location (2728.9 μm/yr) shows that this layer was not protective.

Figure 7-29 shows the SEM micrographs of Batch 4 coupons taken from the hot rich stream. The 316L coupon has a slightly discolored appearance, but corrosion was low (1.9 μm/yr). The SEM micrograph of the 316L coupon shows a mostly pristine surface. The C1010 coupon at this location cracked and the majority of the coupon was lost. The high corrosion rate reported here (9620.6 μm/yr) is high because the mass loss here includes the mass of the missing coupon fragment. The remaining coupon fragment has a sharp fracture plane, suggesting some type of environmentally induced cracking. The SEM micrograph of the remaining C1010 coupon fragment shows a somewhat porous crystalline layer. This product was identified as Siderite and iron by powder XRD.

Table 7-16: Summary of coupon weight loss for WL19 (Hot rich)

Batch	Alloy	Original Mass (g)	Mass Loss (g)	Mass of Film(g)	Operating Time (hrs)	Coupon Type	Corrosion rate (μm/yr)	XRD Products
Batch 3	304	10.5667	0.3329	0.0017	879	Strip	198.4	None
Batch 2	316L	10.3982	0.4646	0.0014	388	Strip	628.6	None
Batch 4	316L	10.3867	0.0013	0.0011	363	Strip	1.9	None
Batch 1	C1010	10.1688	0.0370	0.0446	66	Strip	297.0	Siderite, Magnetite
Batch 2	C1010	10.3255	0.0259	0.0279	388	Strip	35.5	Siderite, Magnetite
Batch 3	C1010	9.7064	4.5039	0.0148	879	Strip	2728.9	Siderite, Iron
Batch 4	C1010	10.7431	6.5638	0.0201	363	Strip	9620.6	Siderite, Iron

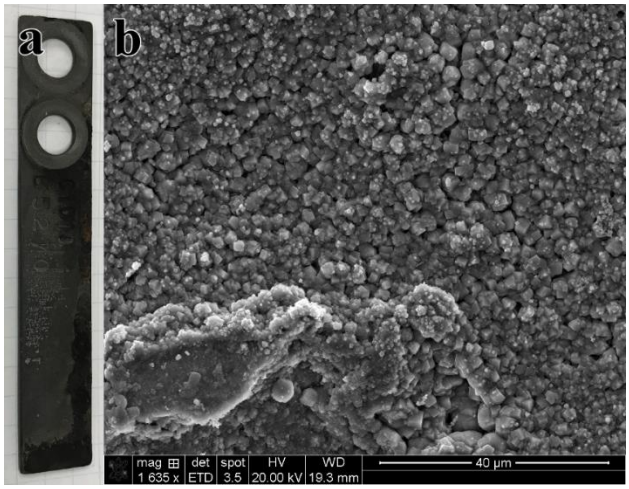

Figure 7-26: (a) C1010 coupon from Batch 1 after removal from hot rich stream. (b) SEM micrograph of C1010, coupon, showing crystalline layer identified by powder XRD as a mix of siderite and magnetite.

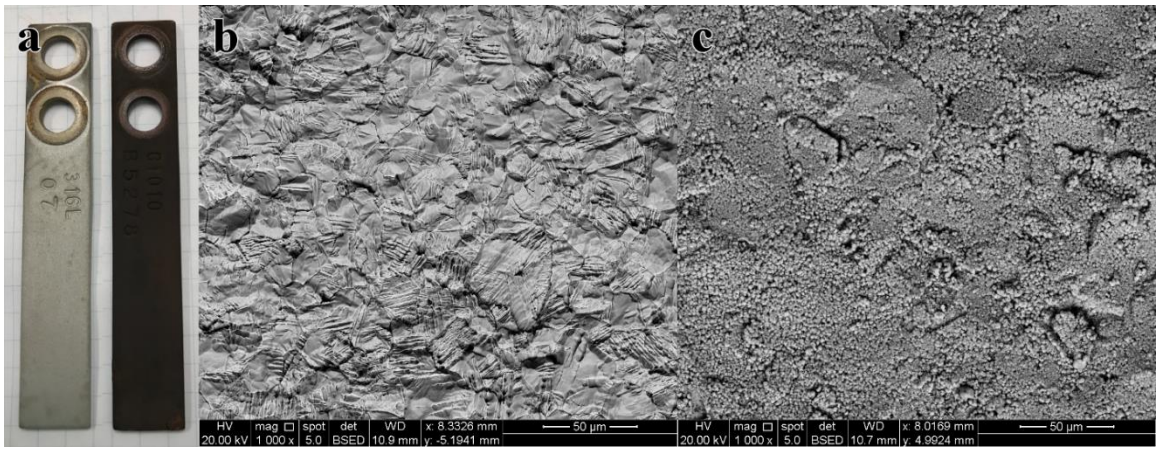

Figure 7-27: (a) 316L and C1010 coupons from Batch 2 after removal from hot rich stream. (b) SEM micrograph of 316L coupon, showing etched surface. (c) SEM micrograph of C1010, coupon, showing black product identified by powder XRD as a mix of siderite and magnetite.

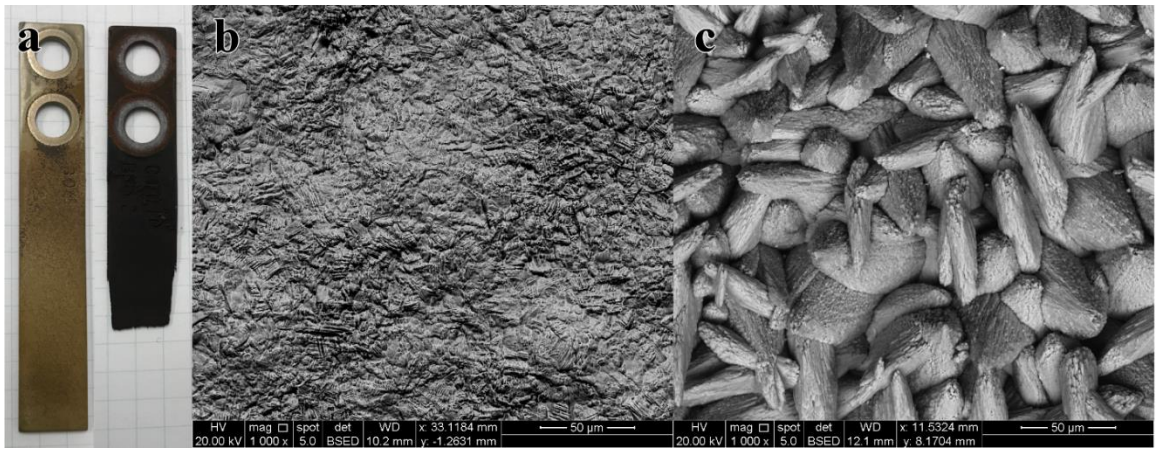

Figure 7-28: (a) 304 and C1010 coupons from Batch 3 after removal from hot rich stream. (b) SEM micrograph of 304 coupon, showing its etched surface. (c) SEM micrograph of C1010 coupon, showing black product identified by powder XRD as siderite and iron.

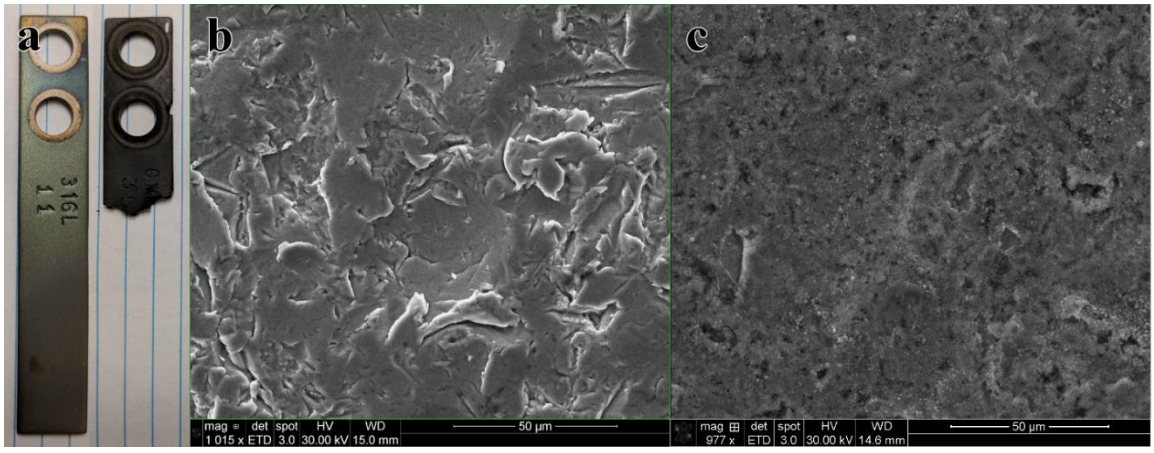

Figure 7-29: (a) 316L and C1010 coupons from Batch 4 after removal from hot rich stream. (b) SEM micrograph of 316L coupon, showing its largely pristine surface. (c) SEM micrograph of C1010 coupon, showing somewhat porous black product identified by powder XRD as siderite and iron.

7.4.8. Hot lean

Corrosion in the hot lean stream (WL21) is summarized in Table 7-17. Overall performance of C1010 was poor (50 – 711 µm/yr). Stainless performance (some 304, others 316L) was good for Batches 3 and 4 (1 – 2 µm/yr). Stainless (316L) experienced high corrosion (1095 µm/yr) during Batch 2. The vulnerability of C1010 at this location indicates that it should not be used here until the difference between the low corrosion batch and vulnerable batches is understood. Stainless steel is also sometimes vulnerable and at other times performs well. Until the occasional vulnerability of stainless steel at this location is understood, higher alloy steels (ie, duplex stainless) should be investigated for use at this location.

Figure 7-30 shows the SEM micrograph of a Batch 1 C1010 coupon taken from the hot lean stream. The SEM micrograph of this coupon shows a regular, crystalline layer. This product was identified as a mix of siderite and magnetite by powder XRD. The high corrosion rate at this location (481.3 µm/yr) is partially due to the short time period used

for the corrosion rate calculations for Batch 1. It is possible that some of the mass lost occurred during the initial water testing period, and that the post-PZ exposure water circulation period was slightly more protected by the siderite/magnetite layer.

Figure 7-31 shows the SEM micrographs of Batch 2 coupons taken from the hot lean stream. The 316L surface is etched and bare, consistent with the high corrosion rate (1094.7 μm/yr) observed here. The austenitic grain boundaries are clearly visible in the etched 316L steel (Figure 7-31-B). The C1010 surface shows a coat of very large pyramidal crystals which was identified by powder XRD as $FeCO_3$. Apparently this $FeCO_3$ layer was not protective, because high corrosion was observed here (711.4 μm/yr).

Figure 7-32 shows the SEM micrographs of Batch 3 coupons taken from the hot lean stream. The 304 coupon a clean surface, and corrosion here was low (0.5 μm/yr). The SEM micrograph of the C1010 coupon shows a crystalline layer with two different morphologies. Figure 7-32-C shows an interface between one morphology, which is regular and crystalline, and the second morphology which is jagged and has large pyramidal crystals. This product was identified as a mixture of siderite and iron by powder XRD. The low corrosion rate at this location (49.5 μm/yr) shows that this layer was protective.

Figure 7-33 shows the SEM micrographs of Batch 4 coupons taken from the hot lean stream. The 316L surface is almost pristine, and corrosion here was low (1.8 μm/yr). The C1010 surface shows somewhat porous, crystalline layer which was identified by powder XRD as a mix of siderite and magnetite. Apparently this $FeCO_3$ layer was not protective, because moderate corrosion was observed here (183.3 μm/yr).

Table 7-17: Summary of coupon weight loss for WL21 (Hot lean)

Batch	Alloy	Original Mass (g)	Mass Loss (g)	Mass of Film(g)	Operating Time (hrs)	Coupon Type	Corrosion rate (μm/yr)	XRD Products
Batch 3	304	10.6129	0.0008	0.0000	879	Strip	0.5	None
Batch 2	316L	10.3775	0.8091	0.0002	388	Strip	1094.7	None
Batch 4	316L	10.3820	0.0013	0.0001	363	Strip	1.8	None
Batch 1	C1010	10.2730	0.0599	0.0517	66	Strip	481.3	Siderite, Magnetite
Batch 2	C1010	9.6961	0.5186	0.0349	388	Strip	711.4	Siderite
Batch 3	C1010	9.8722	0.0816	0.0180	879	Strip	49.5	Siderite, Iron
Batch 4	C1010	10.7270	0.1254	0.0471	363	Strip	183.8	Siderite, Magnetite

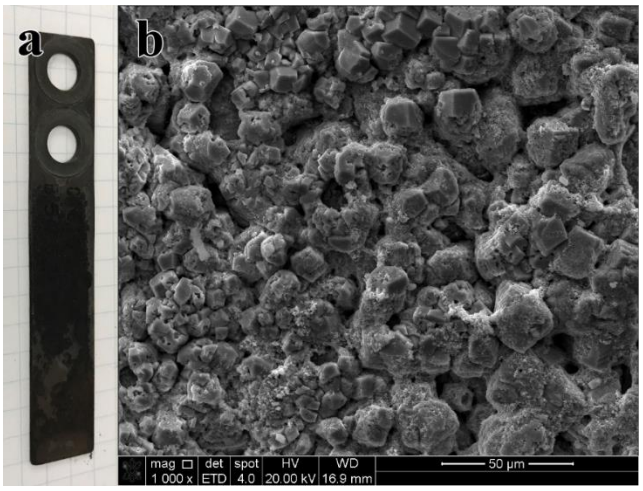

Figure 7-30: (a) C1010 coupon from Batch 1 after removal from hot lean stream. (b) SEM micrograph of C1010, coupon, showing crystalline layer identified by powder XRD as siderite.

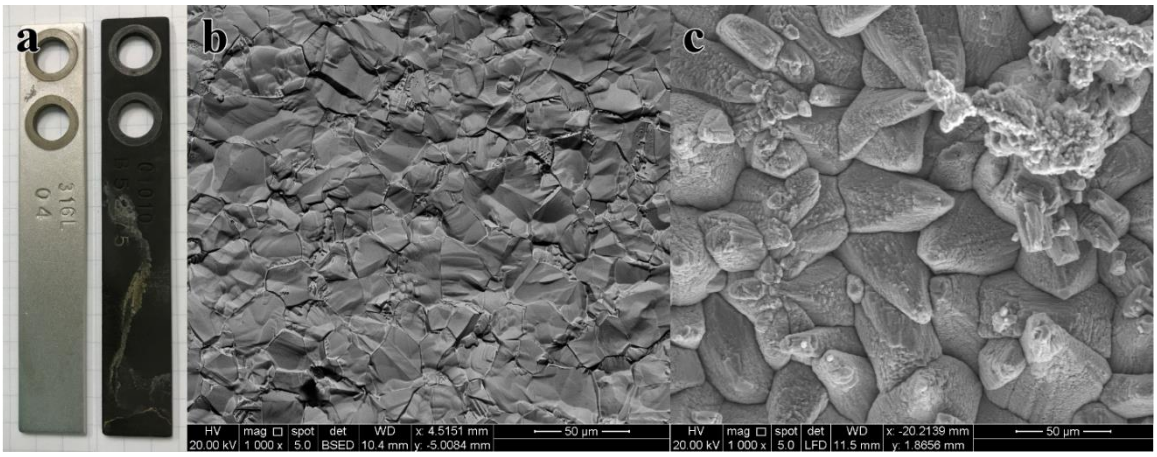

Figure 7-31: (a) 316L and C1010 coupons from Batch 2 after removal from hot lean stream. (b) SEM micrograph of 316L coupon, showing etched surface. (c) SEM micrograph of C1010 coupon, showing black product identified by powder XRD as siderite.

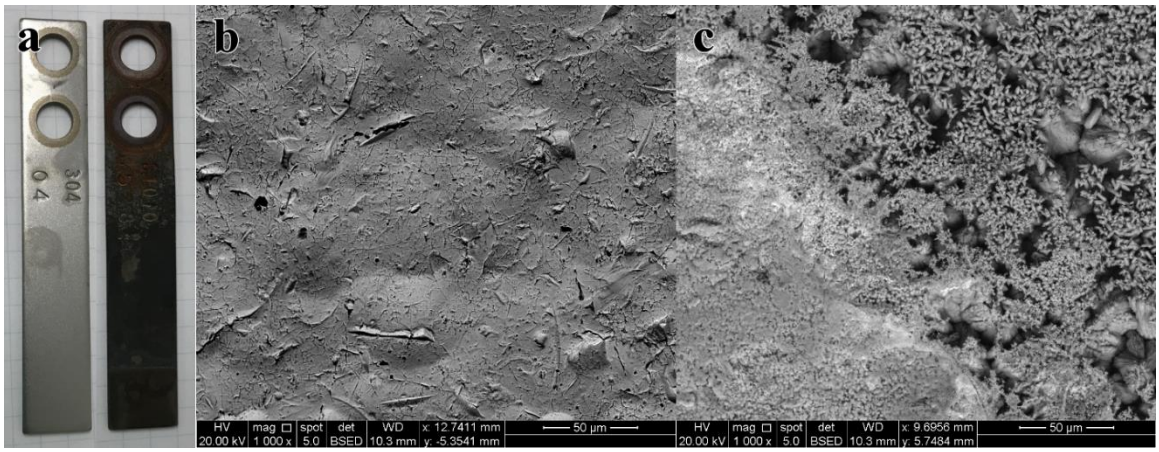

Figure 7-32: (a) 304 and C1010 coupons from Batch 3 after removal from hot lean stream. (b) SEM micrograph of 304 coupon, showing its relatively clean surface. (c) SEM micrograph of C1010 coupon, showing black product identified by XRD as siderite and iron.

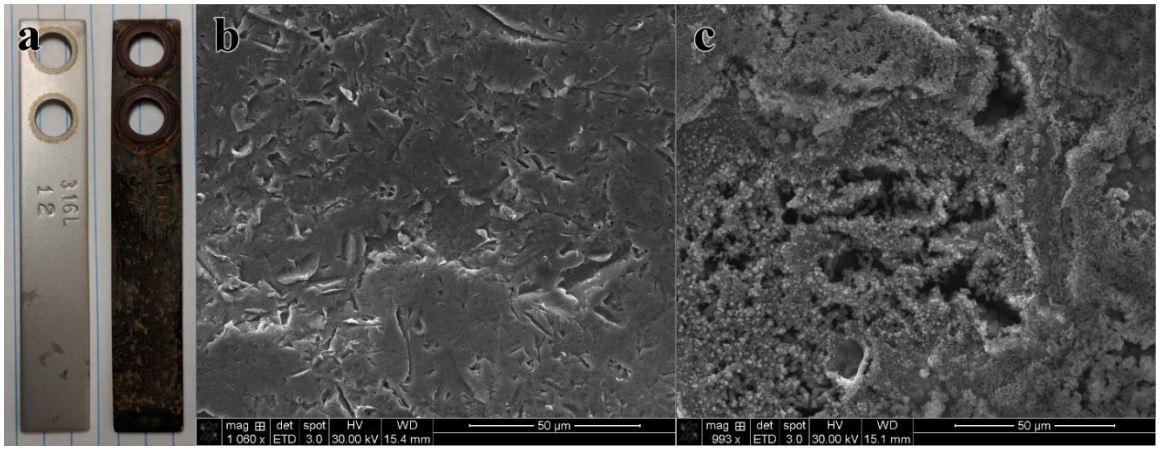

Figure 7-33: (a) 316L and C1010 coupons from Batch 4 after removal from hot lean stream. (b) SEM micrograph of 316L coupon, showing its relatively clean surface. (c) SEM micrograph of C1010 coupon, showing black product identified by XRD as siderite and magnetite.

7.4.9. AFS Sump

Corrosion in the AFS sump (WL22) is summarized in Table 7-18. Overall performance of C1010 was good (7 – 11 µm/yr) for Batches 2, 3, and 4. Performance of C1010 was moderate during Batch 1 (157 µm/yr), which was probably due to the coupons being exposed during water testing. Stainless performance (some 304, others 316L) was good for Batches 3 and 4 (1 – 4 µm/yr). Stainless (316L) experienced high corrosion (489 µm/yr) during Batch 2. The occasional vulnerability of stainless steel at this location suggests that carbon steel may be a preferable material of construction for the AFS sump, as long as coupons do not undergo extensive water testing.

Figure 7-34 shows the SEM micrograph of a Batch 1 C1010 coupon taken from the AFS sump. The SEM micrograph of this coupon shows a regular, crystalline layer. This product was identified as a mix of siderite and magnetite by powder XRD. The moderate corrosion rate at this location (156.9 µm/yr) is partially due to the short time period used for the corrosion rate calculations for Batch 1. The siderite layer at this location appears

crystalline, but it was not fully protective. Notice the mass loss for C1010 at this location was more significant than during the other batches, despite the shorter immersion time. This shows that the water testing and water/CO_2 circulation conditions present during Batch 1 are challenging for C1010. It is possible that most of the mass lost occurred during the initial water testing period, and that the post-PZ exposure water circulation period was protected by the siderite/magnetite layer. Magnetite was only detected at this location in Batch 1, which suggests that water/CO_2 circulation converts the PZ-promoted siderite layer to magnetite.

Figure 7-35 shows the SEM micrographs of Batch 2 coupons taken from the AFS sump. The 316L coupon is covered with a flakey, non-protective layer of rosette crystals. This was the only coupon where a thick corrosion product film was detected on stainless steel. Powder XRD identified this layer as siderite. The high corrosion rate (488.8 μm/yr) shows that this layer was not protective. The SEM micrograph of the C1010 coupon shows a regular, crystalline layer. This product was identified as $FeCO_3$ by powder XRD. The low corrosion rate at this location (6.9 μm/yr) shows that this layer was protective.

Figure 7-36 shows the SEM micrographs of Batch 3 coupons taken from the AFS sump. The 304 coupon had nearly pristine appearance, and corrosion was very low (0.6 μm/yr). The SEM micrograph of the C1010 coupon shows a regular, crystalline layer. This product was identified as $FeCO_3$ by powder XRD. The low corrosion rate at this location (6.9 μm/yr) shows that this layer was protective.

Figure 7-37 shows the SEM micrographs of Batch 4 coupons taken from the AFS sump. The 316L coupon looks slightly etched, but and corrosion was very low (4.4 μm/yr). The SEM micrograph of the C1010 coupon shows a regular, crystalline layer. This product was identified as a mix of iron and siderite by powder XRD. The low corrosion rate at this location (11.1 μm/yr) shows that this layer was protective.

Table 7-18: Summary of coupon weight loss for WL22 (AFS Sump)

Batch	Alloy	Original Mass (g)	Mass Loss (g)	Mass of Film(g)	Operating Time (hrs)	Coupon Type	Corrosion rate (μm/yr)	XRD Products
Batch 3	304	10.6139	0.0009	0.0001	879	Strip	0.6	None
Batch 2	316L	10.3765	0.3613	0.0601	388	Strip	488.8	Siderite
Batch 4	316L	10.3723	0.0030	0.0005	363	Strip	4.4	None
Batch 1	C1010	10.3627	0.0195	0.0283	66	Strip	156.9	Siderite, Magnetite
Batch 2	C1010	10.2149	0.0050	0.0081	388	Strip	6.9	Siderite
Batch 3	C1010	9.8405	0.0003	0.0069	879	Strip	0.2	Siderite, Iron
Batch 4	C1010	10.7219	0.0076	0.0109	363	Strip	11.1	Iron, Siderite

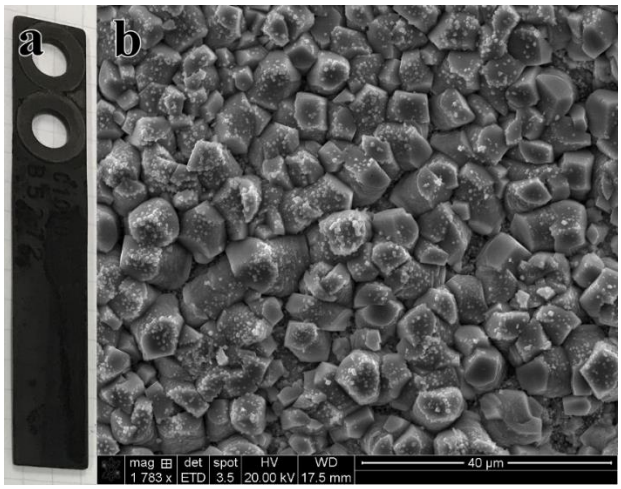

Figure 7-34: (a) C1010 coupon from Batch 1 after removal from AFS sump. (b) SEM micrograph of C1010, coupon, showing crystalline layer identified by powder XRD as siderite and magnetite.

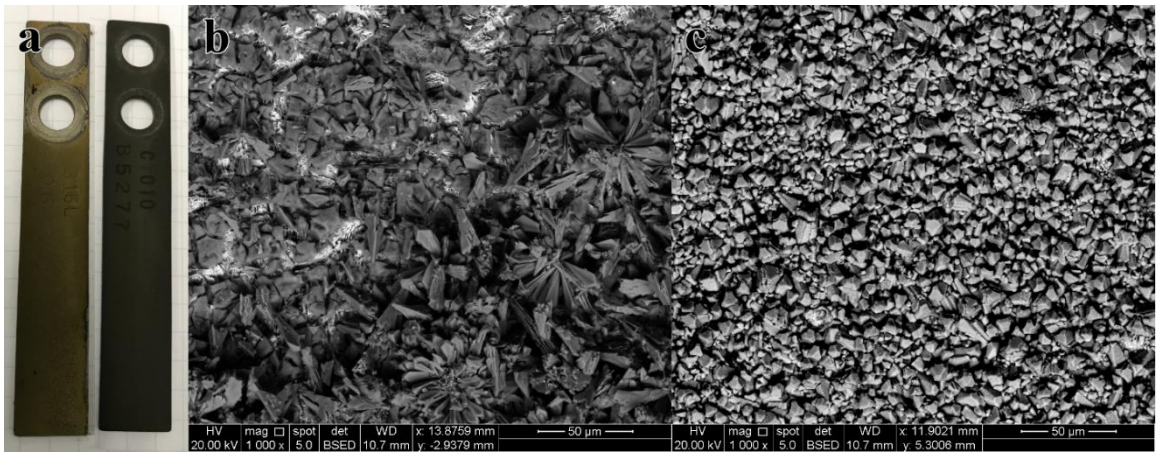

Figure 7-35: (a) 316L and C1010 coupons from Batch 2 after removal from AFS sump. (b) SEM micrograph of 316L coupon, showing yellow product identified by powder XRD as siderite. (c) SEM micrograph of C1010 coupon, showing black product identified by powder XRD as siderite.

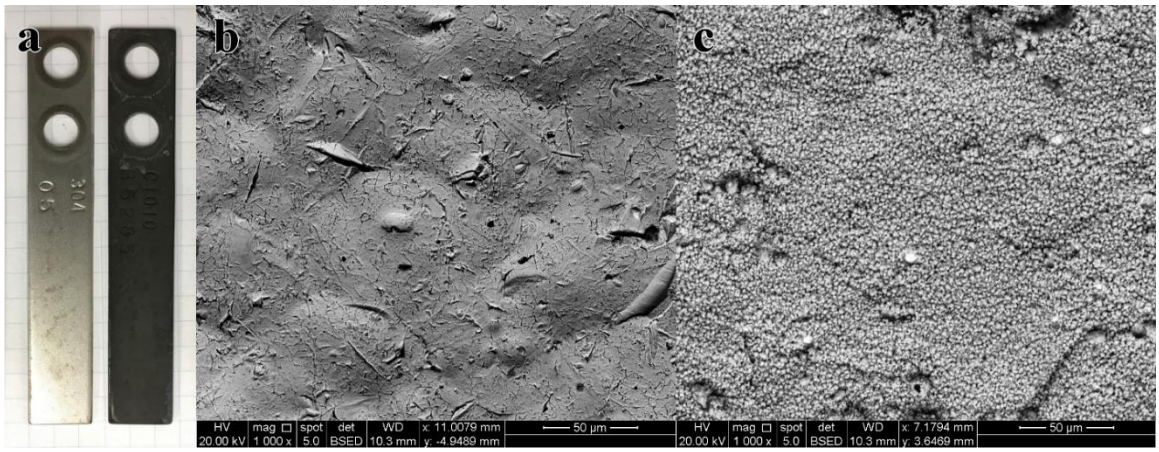

Figure 7-36: (a) 304 and C1010 coupons from Batch 3 after removal from AFS sump. (b) SEM micrograph of 304 coupon, showing its relatively clean surface. (c) SEM micrograph of C1010 coupon, showing black product identified by XRD as siderite and iron.

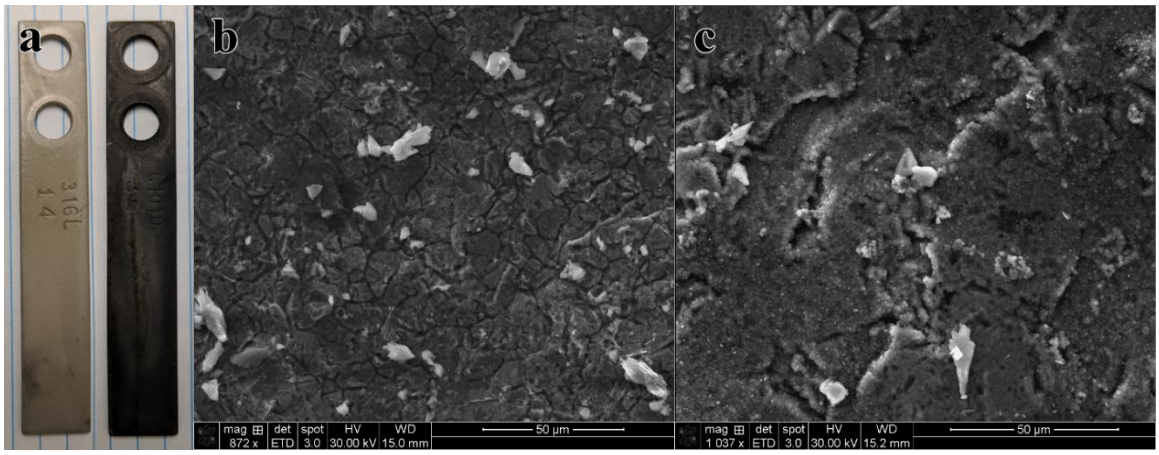

Figure 7-37:(a) 316L and C1010 coupons from Batch 4 after removal from AFS sump. (b) SEM micrograph of 316L coupon, showing slightly etched surface. (c) SEM micrograph of C1010 coupon, showing black product identified by powder XRD as a mix of iron and siderite.

7.5. POWDER X-RAY DIFFRACTION OF CORROSION PRODUCTS.

Figure 7-38, Figure 7-39, Figure 7-40, and Figure 7-41 shows the X-ray spectra of corrosion products from Batches 1, 2, 3, and 4 respectively. In general, ferric (Fe^{3+}) products (magnetite, goethite) are observed at absorber locations, which are expected to be more oxidizing. Ferrous (Fe^{2+}) products (siderite) are typically observed at higher temperatures, which are expected to be slightly more reducing due to the absence of dissolved oxygen.

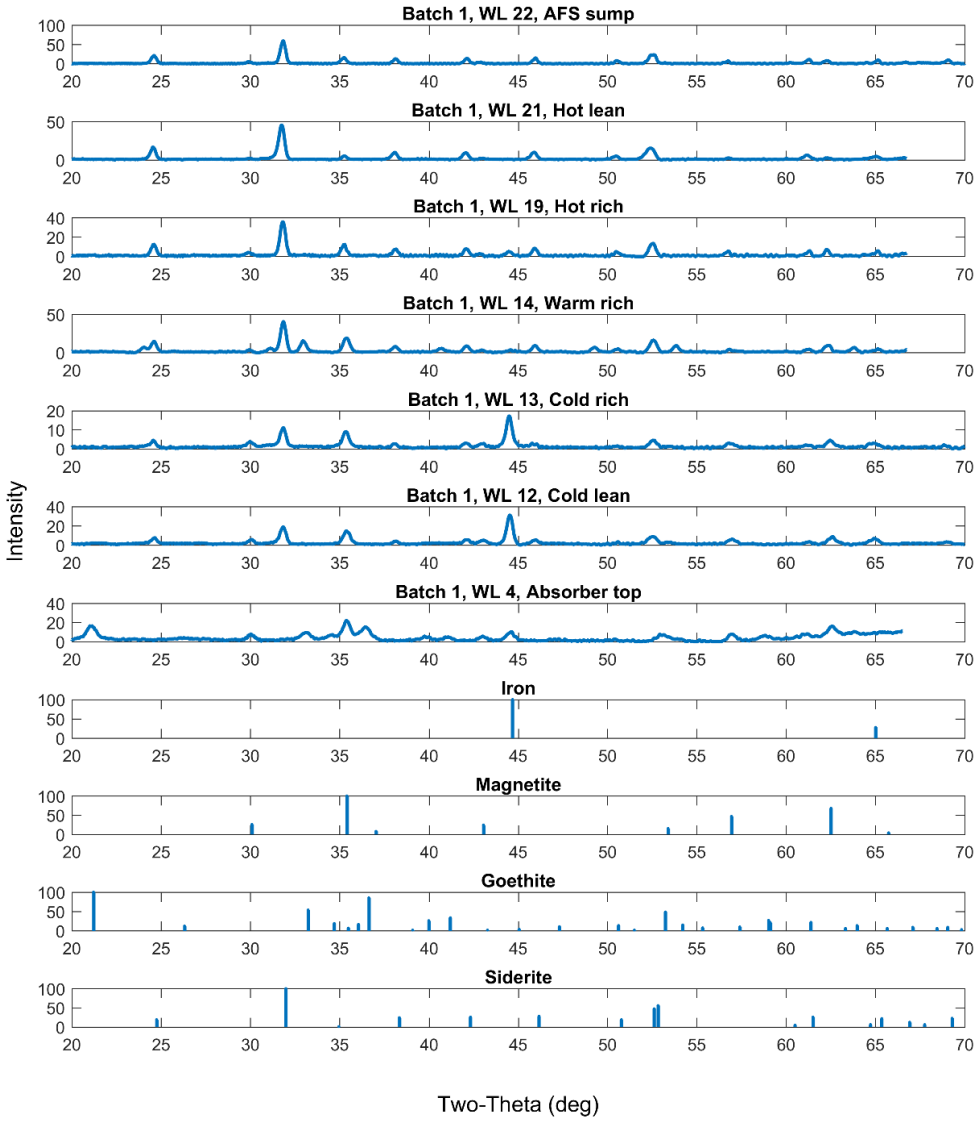

Figure 7-38: Powder X-ray diffraction products observed on C1010 coupons from Batch 1. Reference diffraction patterns for Iron, Magnetite, Goethite and Siderite are shown.

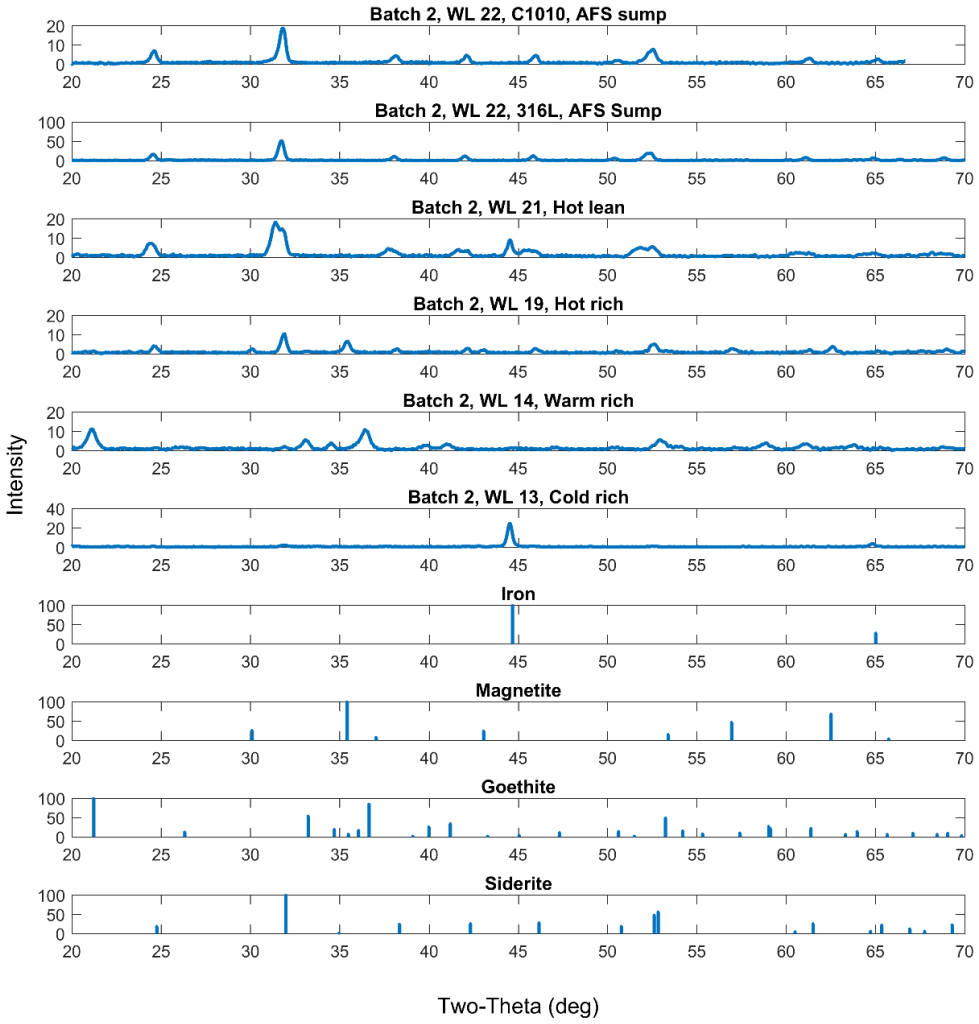

Figure 7-39: Powder X-ray diffraction products observed on coupons from Batch 2. All coupons are C1010 except one from WL22. Reference diffraction patterns for Iron, Magnetite, Goethite and Siderite are shown.

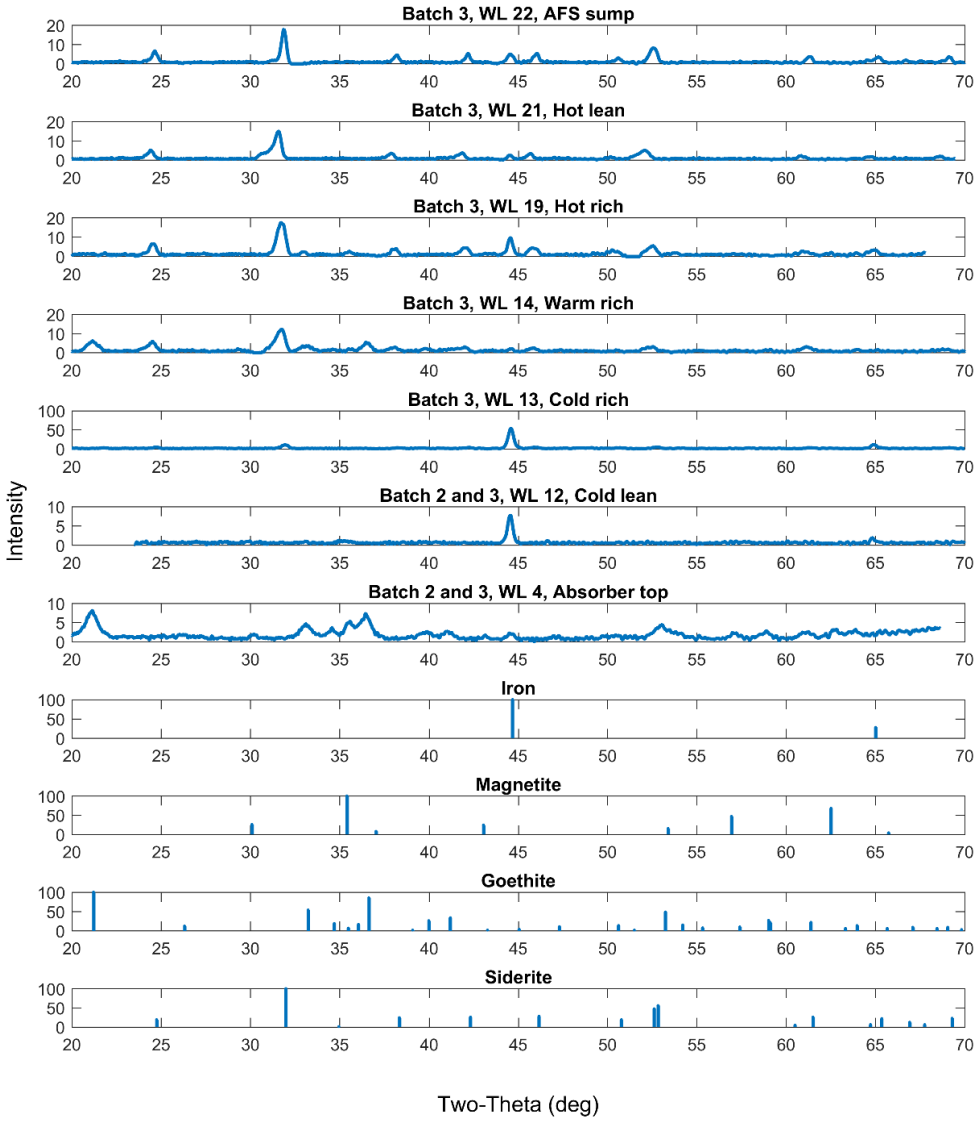

Figure 7-40: Powder X-ray diffraction products observed on C1010 coupons from Batch 3. Coupons from WL12 and WL4 experienced corrosion during Batch 2 and Batch 3. Reference diffraction patterns for Iron, Magnetite, Goethite and Siderite are shown.

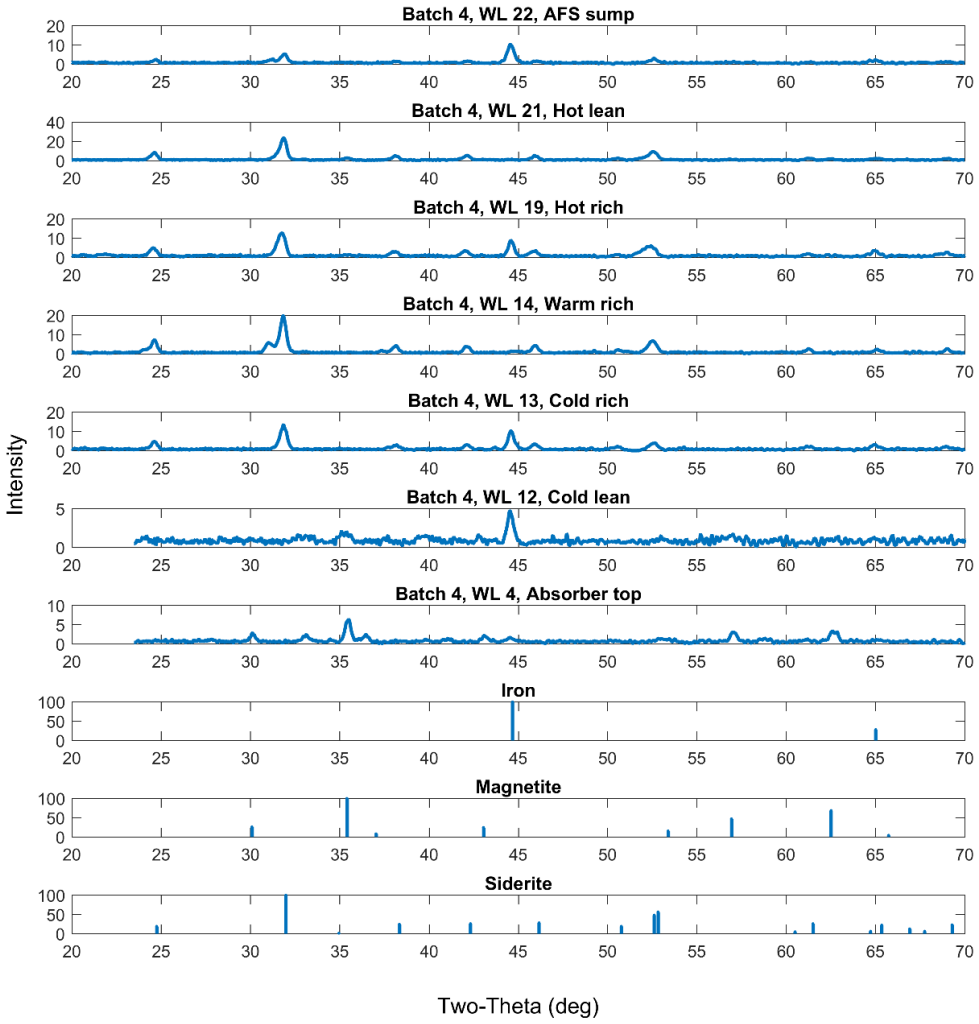

Figure 7-41: Powder X-ray diffraction products observed on C1010 coupons from Batch 4. Reference diffraction patterns for Iron, Magnetite, and Siderite are shown.

7.6. ER Probe Corrosion Measurement

Overall ER probe corrosion measurements were disappointing. In most cases, ER probes underpredicted corrosion rates, although there were several instances where ER probes significantly overpredicted corrosion. The systematic underprediction of carbon

steel corrosion rates could be because corrosion product films altered the electrical resistance measurement. Stainless steel measurements could have been impacted by periodic cleaning of the probes with concentrated HCl, which is not recommended for use with stainless (ASTM, 2017) due to pitting (Jones, 1996).

ER readings were continuous, but daily averages are used for corrosion rate determination to reduce instrument noise. Daily readings were plotted versus operating hours, then the method of least squares was used to determine a corrosion rate over the operating period. Using operating hours assumes that no probe corrosion occurred during shutdowns.

Table 7-19 gives a summary of corrosion rates measured by carbon steel ER probes by batch and location. The table highlights the difference between ER probe corrosion rates and comparable coupon corrosion rates. Several ER corrosion rates are negative, which appears to be due several temperature fluctuations in Batch 4, which caused erratic ER results. This reveals apparently inadequate temperature compensation in the ER instrument. Figure 7-47 is a good example of the shift in instrument reading with temperature. There is significant disagreement between ER probe corrosion rates and coupon corrosion rates. Notably ER probes reported higher significantly higher corrosion of C1010 at the warm rich bypass in Batch 2. The ER probes reported significantly lower corrosion of C1010 at the warm rich bypass and the hot lean stream during Batch 4.

Table 7-19: Coupon weight loss (WL) corrosion rates (μm/yr) compared to ER corrosion rates (μm/yr) of carbon steel (C1010) by batch and location

Location Tag	Location Description	Batch 1 WL	Batch 2 WL	Batch 2 ER	Batch 2 & 3 WL	Batch 3 WL	Batch 3 ER	Batch 4 WL	Batch 4 ER
WL4	Absorber top				5				
WL2	Absorber middle				0				
ER2	Absorber middle	181						0	**-2.3**
ER3	Absorber sump	135	1			0	**-0.4**	1	**3.9**
WL12	Cold lean	603			108			210	
WL13	Cold rich bypass	202	97	**55**		50	**-4.9**	103	
WL14	Warm rich bypass	157	55	**404**		47		92	**-33.3**
WL19	Hot rich	297	36			2729		9621	
WL21	Hot lean	481	711			49		184	**24.3**
WL22	AFS Sump	157	7			0		11	

Table 7-20 gives a summary of corrosion rates measured by stainless steel ER probes by batch and location. The table highlights the difference between the ER probe corrosion rates and comparable coupon corrosion rates. The table includes some 316L corrosion rates and some 304 corrosion rates. There is disagreement between corrosion measured at ER probes and coupons. The most notable difference is in the hot rich location during Batch 3, where the 304 coupon corroded at 198 μm/yr and the 316L ER probe corroded at 4 μm/yr. ER probes during batch 4 reported a slightly negative corrosion rate, which appears to be related to a temperature change at the end of that batch and inadequate temperature compensation of the ER instruments.

Table 7-20: Coupon weight loss (WL) corrosion rates (μm/yr) compared to ER corrosion rates (μm/yr) of stainless steel (316L and 304) by batch and location

		Batch 2	Batch 2 & 3	Batch 3		Batch 4	
Location Tag	**Location Description**	WL	WL	WL	**ER**	WL	**ER**
WL2	Absorber middle		0				
ER2	Absorber middle					0	
ER3	Absorber sump	0		0		1	
WL12	Cold lean		0			1	
WL13	Cold rich bypass	1		0		1	**-34**
WL14	Warm rich bypass	9		0	**16**	1	
WL19	Hot rich	629		198	**4**	2	**-18**
WL21	Hot lean	1095		0	**20**	2	
WL22	AFS Sump	489		1		4	

Table 7-21 gives a comparison of ER probe corrosion rates and coupon corrosion rates. It shows that ER probes typically under predict corrosion rates by a significant amount. Notably, there were also four instances in which ER probes over predicted corrosion.

Table 7-21: Comparison of ER and coupon corrosion rates.

Location	Batch	ER Alloy	Coupon Alloy	ER Corrosion Rate (μm/yr)	Coupon Corrosion Rate (μm/yr)	ER Error (μm/yr)	ER Percent Error
40513	Batch 2	C1010	C1010	55	96.8	-41	-43
40514	Batch 2	C1010	C1010	404	54.8	349	637
ER3	Batch 3	C1010	C1010	-0.4	0.3	-1	-217
40513	Batch 3	C1010	C1010	-5	50.3	-55	-110
40514	Batch 3	304	304	16	0.3	16	5796
40519	Batch 3	316L	304	4.4	198.4	-194	-98
40521	Batch 3	316L	304	20	0.5	20	4355
ER2	Batch 4	C1010	C1010	-2.3	0.2	-2	-1268
ER3	Batch 4	C1010	C1010	3.9	0.6	3	565
40513	Batch 4	316L	316L	-34	1.0	-35	-3493
40514	Batch 4	C1010	C1010	-33	92.2	-126	-136
40519	Batch 4	304	316L	-18	1.9	-19	-1010
40521	Batch 4 Period 1	C1010	C1010	24	183.8	-159	-87
40521	Batch 4 Period 2	C1010	C1010	51	183.8	-133	-72

Table 7-22 gives detailed information about the ER probe corrosion rate determinations. Corrosion rates were determined based on the method of least squares, and regression parameters are shown.

Table 7-22: Summary Table of ER Probe corrosion rate regression parameters.

Location	Batch	Alloy	Slope	Intercept	Error Slope	Error intercept	R2	Corrosion Rate (µm/yr)	Corrosion Rate error (µm/yr)
40513	Batch 2	C1010	-6.E-03	78	3.E-03	0.5	0.30	55	25
40514	Batch 2	C1010	-5.E-02	67	1.E-02	2	0.54	404	113
ER3	Batch 3	C1010	4.E-05	78	1.E-04	0.1	0.005	-0.4	1
40513	Batch 3	C1010	6.E-04	77	2.E-04	0.1	0.21	-5	2
40514	Batch 3	304	-2.E-03	240	8.E-04	0.4	0.20	16	7
40519	Batch 3	316L	-5.E-04	78	2.E-04	0.1	0.28	4.4	1
40521	Batch 3	316L	-2.E-03	80	7.E-04	0.4	0.36	20	6
ER2	Batch 4	C1010	3.E-04	101	2.E-04	0.0	0.13	-2.3	2
ER3	Batch 4	C1010	-4.E-04	61	6.E-04	0.1	0.05	3.9	5
40513	Batch 4	316L	4.E-03	77	4.E-03	0.7	0.09	-34	33
40514	Batch 4	C1010	4.E-03	37	3.E-03	0.5	0.15	-33	23
40519	Batch 4	304	2.E-03	240	1.E-03	0.2	0.27	-18	9
40521	Batch 4 Period 1	C1010	-3.E-03	100	5.E-03	1	0.06	24	44
40521	Batch 4 Period 2	C1010	-6.E-03	64	6.E-03	2	0.18	51	54

7.7. ER PROBE CORROSION BY LOCATION

The following sections explain corrosion at ER instruments at each location.

7.7.1. Absorber middle and sump

Overall corrosion rates of C1010 in the absorber were below 5 µm/yr for all ER probes and coupons. The rates between ER probes and coupons at this location differ slightly, but are largely consistent.

Figure 7-42 shows corrosion of C1010 in the absorber middle during Batch 4. The ER probe reported -2 µm/yr and the coupon in the same location corroded at 0 µm/yr. Figure 7-43 shows corrosion of C1010 in the absorber sump during Batch 3, where the ER probe reported -0.4 µm/yr and the corresponding coupon corroded at 0 µm/yr. Figure 7-44 shows corrosion of C1010 in the absorber sump during Batch 4, where the ER probe reported 4 µm/yr, and the corresponding coupon corroded at 1 µm/yr.

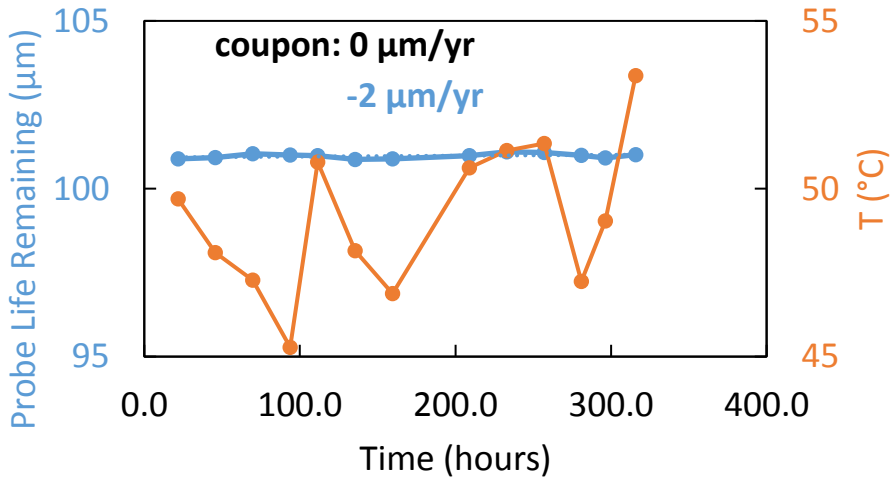

Figure 7-42: Corrosion of carbon steel (C1010) at absorber middle (ER2) ER Probe during Batch 4.

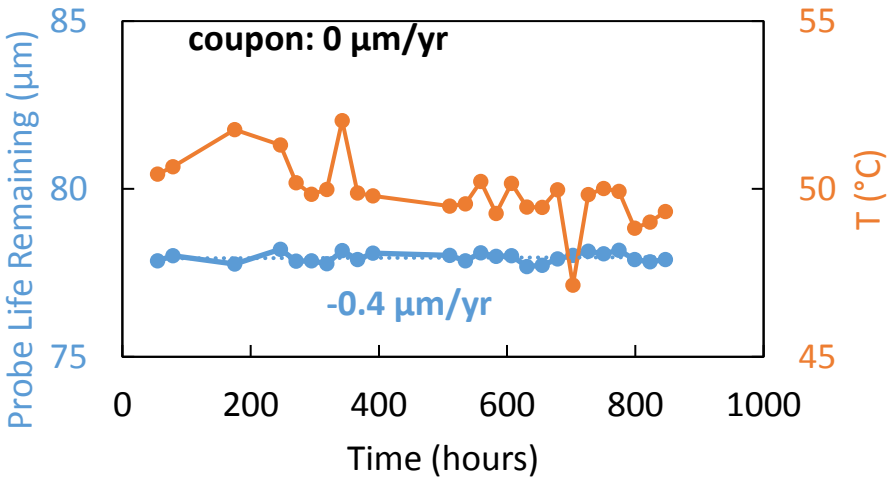

Figure 7-43: Corrosion of carbon steel (C1010) at absorber sump (ER3) ER Probe during Batch 3.

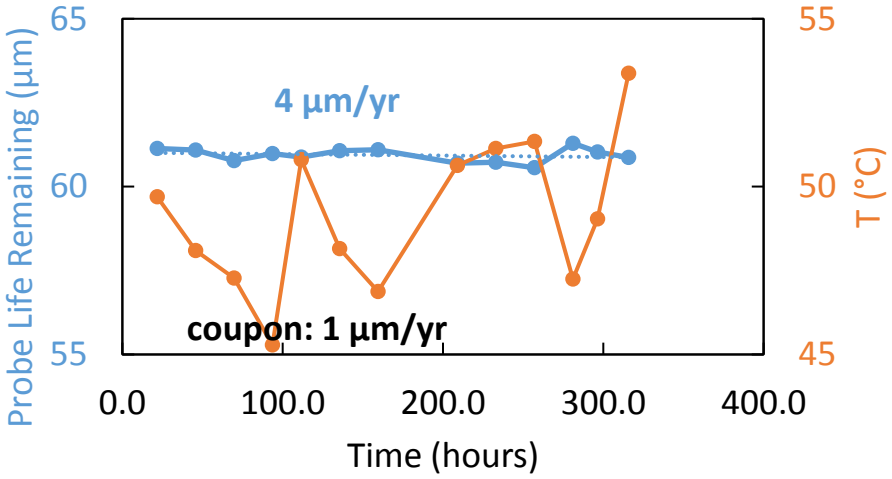

Figure 7-44: Corrosion of carbon steel (C1010) at absorber sump (ER3) ER Probe during Batch 4.

7.7.2. Cold rich bypass

Figure 7-45 shows corrosion of C1010 in the cold rich bypass during Batch 2, where the ER probe reported corrosion of 55 µm/yr and the corresponding coupon corroded at 97

µm/yr. Figure 7-46 shows corrosion of C1010 in the cold rich bypass during Batch 3, where the ER probe reported corrosion of -5 µm/yr, and the corresponding coupon corroded at 50 µm/yr. Figure 7-47 shows corrosion of 316L in the cold rich bypass during Batch 4, where the ER probe reported corrosion of -34 µm/yr, but the coupon corroded at 1 µm/yr.

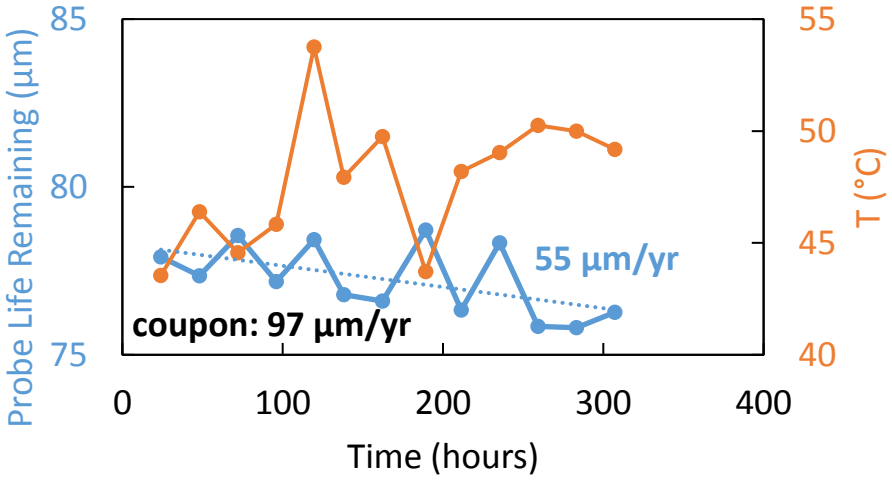

Figure 7-45: Corrosion of carbon steel (C1010) at cold rich bypass (40513) ER Probe during Batch 2.

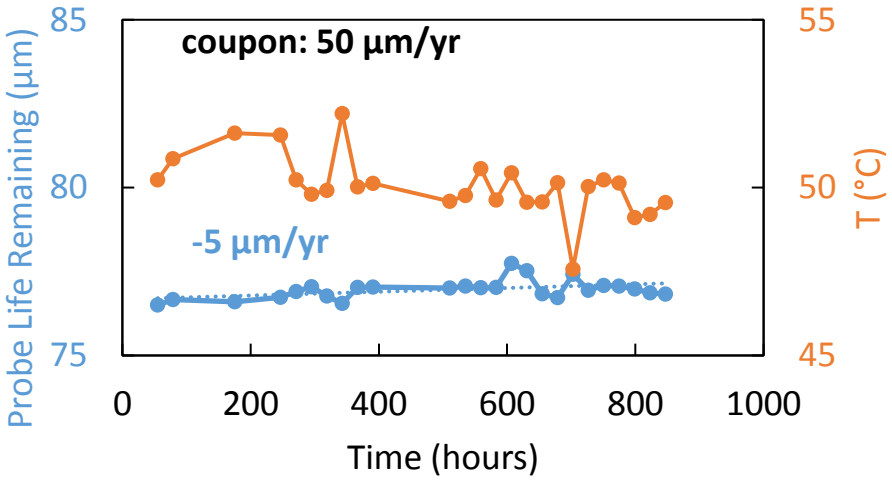

Figure 7-46: Corrosion of carbon steel (C1010) at cold rich bypass (40513) ER Probe during Batch 3.

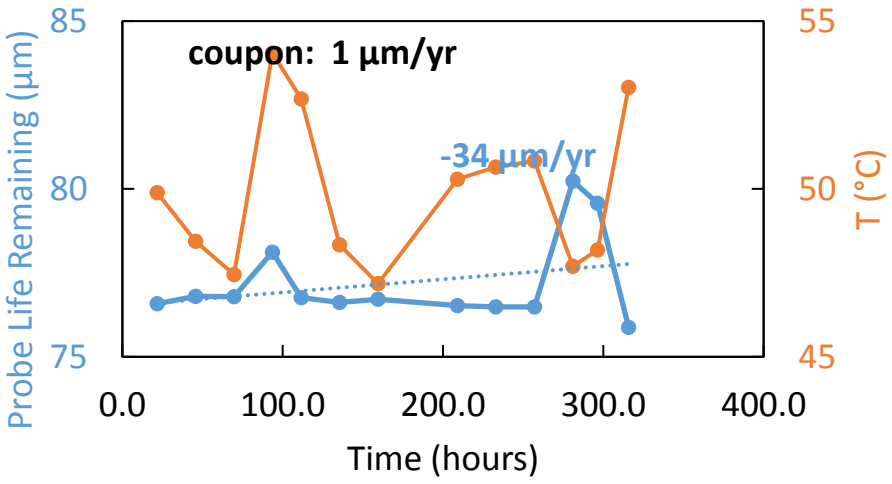

Figure 7-47: Corrosion of stainless steel (316L) at cold rich bypass (40513) ER Probe during Batch 4.

7.7.3. Warm rich bypass

Figure 7-48 shows ER corrosion of C1010 in the warm rich bypass during Batch 2, where the ER probe reported corrosion of 404 µm/yr, and the corresponding coupon corroded at 55 µm/yr. Figure 7-49 shows ER corrosion of 304 in the warm rich bypass during Batch 3, where the ER probe reported corrosion of 16 µm/yr, and the corresponding coupon corroded at 0.3 µm/yr. Figure 7-50 shows ER probe corrosion of C1010 in the warm rich bypass during Batch 4, where the ER probe reported corrosion of -33 µm/yr, and the coupon corroded at 92 µm/yr.

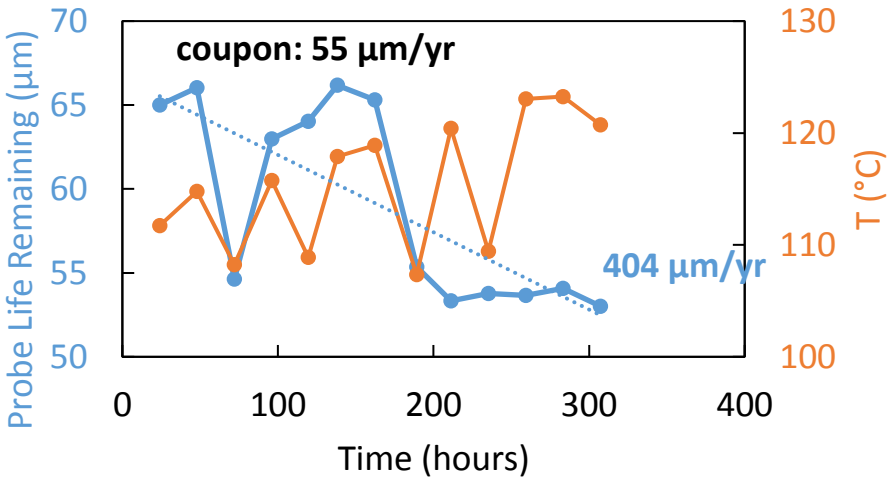

Figure 7-48: Corrosion of carbon steel (C1010) at warm rich bypass (40514) ER Probe during Batch 2.

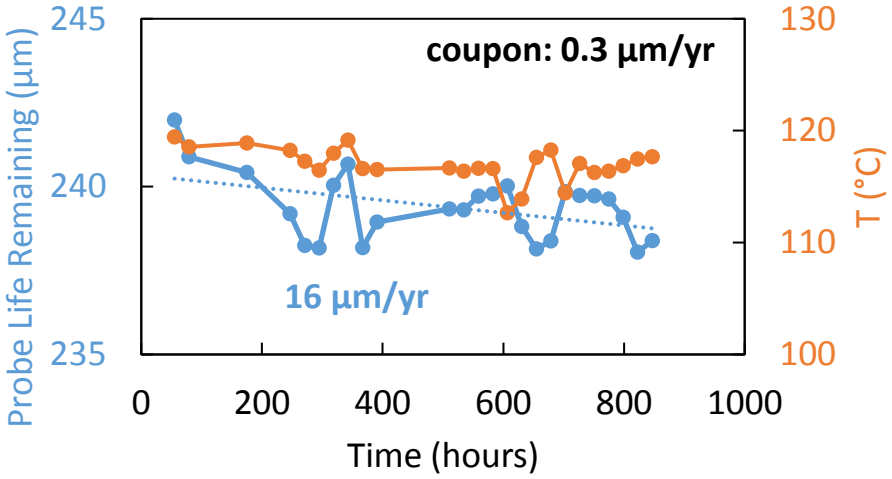

Figure 7-49: Corrosion of stainless steel (304) at warm rich bypass (40514) ER Probe during Batch 3.

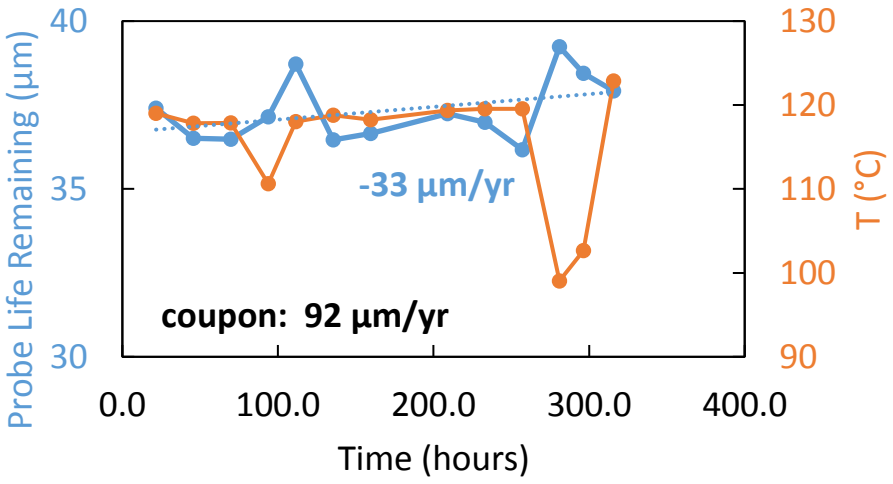

Figure 7-50: Corrosion of carbon steel (C1010) at warm rich bypass (40514) ER Probe during Batch 4.

7.7.4. Hot Rich

Figure 7-51 shows corrosion of 316L in the hot rich stream during Batch 3, where the ER probe corroded at 4 µm/yr. There was no 316L coupon in the hot rich stream during this batch, but there was a 304 coupon, which corroded at 198 µm/yr. Figure 7-52 shows corrosion of 304 in the hot rich stream during Batch 4, where the ER probe reported corrosion of -18 µm/yr. There was no 304 coupon in the hot rich stream during this batch, but there was a 316L coupon, which corroded at 1.9 µm/yr.

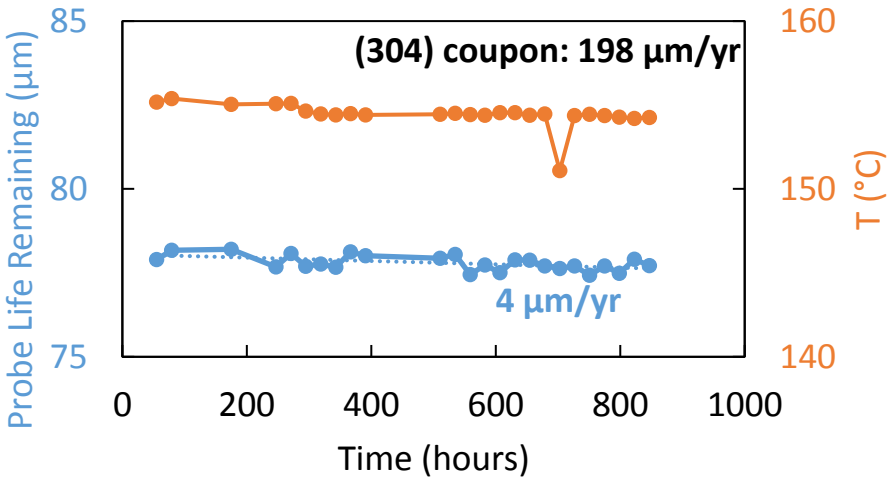

Figure 7-51: Corrosion of stainless steel (316L) at hot rich stream (40519) ER Probe during Batch 3.

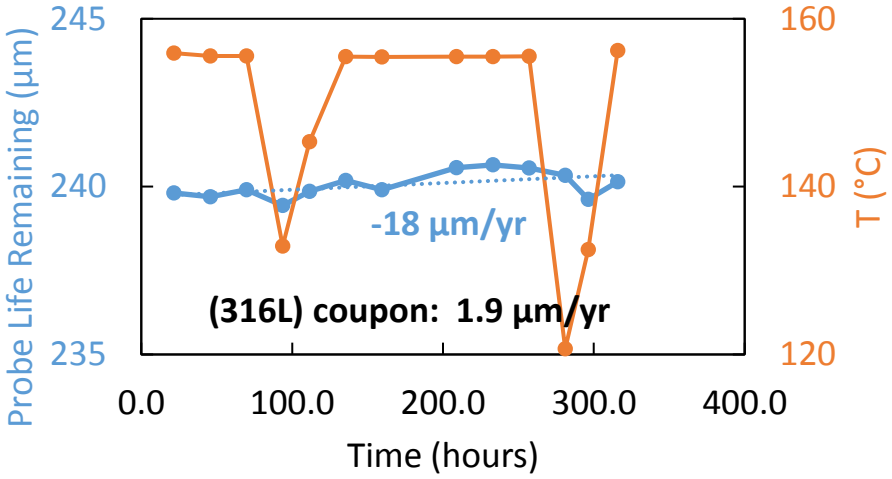

Figure 7-52: Corrosion of stainless steel (304) at hot rich stream (40519) ER Probe during Batch 4.

7.7.5. Hot Lean

Figure 7-53 shows ER probe corrosion of 316L in the hot lean stream during Batch 3, where the ER probe reported corrosion of 20 µm/yr. There was no 316L coupon in the

hot lean stream during this batch, but there was a 304 coupon, which corroded at 0.5 µm/yr. Figure 7-54 shows ER probe corrosion of C1010 in the hot lean stream during Batch 4. There was a discontinuity in corrosion measurement during this batch, where probe life suddenly decreased sharply. This discontinuity was not included when regressing the corrosion rate. During the first period of Batch 4, the ER probe reported corrosion of 24 µm/yr . After the discontinuity, the ER probe reported corrosion of 51 µm/yr. The corresponding Batch 4 coupon corroded at 184 µm/yr.

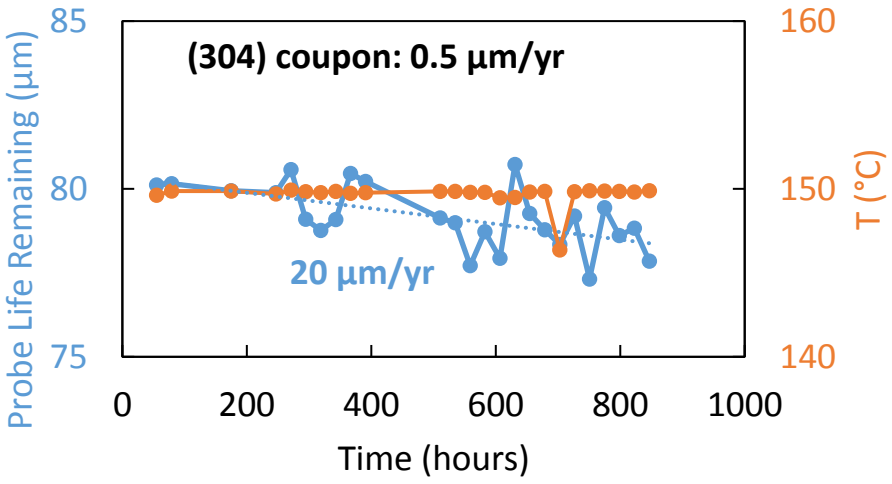

Figure 7-53: Corrosion of stainless steel (316L) at hot lean stream (40521) ER Probe during Batch 3.

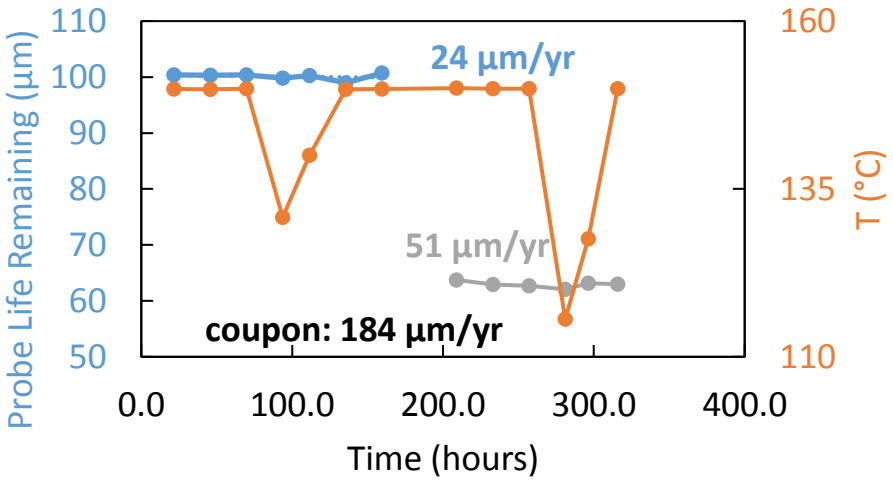

Figure 7-54: Corrosion of carbon steel (C1010) at hot lean stream (40521) ER Probe during Batch 4.

7.8. CONCLUSIONS

7.8.1. Carbon steel performs well in 5 m PZ at lean and rich loadings, at 116 – 150 °C, when fluid velocities are low. This good performance is due to the formation of a protective $FeCO_3$ film.

Carbon steel (C1010) in 5 m PZ is frequently protected by a crystalline siderite ($FeCO_3$) layer at 116 - 150 ºC. Siderite is observed at both lean ($\alpha = 0.23$) and rich ($\alpha = 0.4$) CO_2 loadings at these temperatures. At 116°C and rich loading, corrosion varied from 47 - 92 µm/yr. At 150°C and lean loadings, corrosion ranged from 0 - 11 µm/yr. These measurements were in vessels or low velocity pipes (≈0.39 m/s).

7.8.2. At 150 – 155 °C, at lean and rich loadings, when fluid velocity is moderate or high (> 0.8 m/s), $FeCO_3$ films are sometimes not protective to carbon steel, leading to high corrosion in 5 m PZ.

At high temperature (150-155 °C), high fluid velocity locations (≈ 0.8 m/s, not accounting for two phase flow), protective films are sometimes not adequate to protect carbon steel in 5 m PZ, and corrosion can be high (up to 2800 µm/yr). High fluid velocity

increases mechanical erosion of $FeCO_3$ films and also increases transport of Fe^{2+} to the bulk solution. During several batches, $FeCO_3$ was somewhat protective (<200 μm/yr) at these conditions. The non-reproducibility at these conditions could be due to poor control of coupon insertion orientation. This would have the effect of obstructing flow and increasing local fluid velocity and turbulence around the coupon significantly.

7.8.3. Limited evidence suggests environmentally induced cracking of carbon steel can occur in 5 m PZ at 155 °C at high fluid velocity.

One C1010 coupon cracked and was lost in the hot (155 °C) rich stream (typically 0.4 mol CO_2/ mol N), leading to an exceptionally high corrosion rate (9700 μm/yr). This suggests that environmentally induced cracking may be an issue for carbon at high temperatures in PZ. Environmentally induced cracking was not thoroughly investigated in this work.

7.8.4. At 50 °C, carbon steel performs well in 5 m PZ, despite not forming protective $FeCO_3$ layers.

Carbon steel performed excellently at PZ wetted locations in the absorber (≈50 °C, α = 0.4), frequently showing no corrosion products and negligible corrosion (1 μm/yr).

Rich (α = 0.4) and lean (α = 0.23) locations at higher flow rates (0.04 – 0.77 m/s) primarily showed a rough, porous iron layer. Presumably higher solubility of Fe^{2+} at low temperatures prevents formation of siderite layers. These locations experienced low to moderate corrosion (50 – 210 μm/yr).

7.8.5. At 150 – 155 °C, stainless steel sometimes experiences high corrosion in 5 m PZ.

At high temperature (150-155 °C) locations, stainless steel is also sometimes attacked in 5 m PZ and shows high corrosion (up to 1100 μm/yr). Attack of stainless

occurred at high and low fluid velocities, and lean and rich loadings. Both 316L and 304 experienced high corrosion. During some batches, stainless performed excellently at these locations. It is not clear why stainless was attacked during some batches, but not others at similar conditions. Vulnerability of stainless steel could be due to the uniquely high operating temperature of PZ compared to other amines, which typically operate at 120 °C. Until the occasional vulnerability of stainless steel at these locations is understood, higher alloy steels (ie, duplex stainless) should be investigated.

7.8.6. At 50 – 116 °C, stainless steel performs well in 5 m PZ.

In the absorber and 50 – 116 °C piping, stainless steel (304 and 316L) performed excellently (0 – 9 μm/yr). CO_2 loading and fluid velocity did not appear to have a strong effect on stainless performance at these conditions.

7.8.7. Fe^{3+} products are observed at rich conditions, which are relatively oxidizing, but Fe^{2+} is observed at lean conditions, which are reducing. The cyclic oxidation and reduction of Fe^{3+} likely plays a role in high temperature oxidation of PZ.

At warm or hot rich conditions, the corrosion products on carbon steel include oxidized species, but not at lean conditions, suggesting that dissolved Fe^{3+} is depleted in the stripper sump by reaction with piperazine. Magnetite (Fe_3O_4) or goethite (Fe(O)OH) are often observed in addition to siderite at warm (116 °C) and hot rich (155 °C) locations. Presumably, these ferric species are generated in the absorber, which is relatively oxidizing due to O_2 in the flue gas. The absence of ferric products in the stripper sump suggests that ferric is reduced back to ferrous at the high temperature, anoxic conditions of the stripper. Presumably this reduction is accompanied by an oxidation of an amine, degrading it. This Fe^{3+} to Fe^{2+} reduction is probably the cyclic oxidizer hypothesized by other researchers to play a significant role in PZ oxidation (Paul Thomas Nielsen, 2018).

7.8.8. Equipment commissioning with water and steam appears more corrosive to carbon steel than PZ operation.

There is evidence that the commissioning phase, when equipment is pressure tested by circulating water and steam, is more corrosive to carbon steel than operation with 5 m PZ. Notably, operation with 5 m PZ in the absorber typically leaves C1010 pristine, but extended water testing caused moderate corrosion. High velocity locations also experienced corrosion (hot lean, hot rich, cold lean). If carbon steel is used, care should be taken to avoid extended equipment water testing. CO_2 circulation should be avoided during equipment commissioning with water.

Chapter 8. Conclusions

This work yielded four conclusions that shed light on the effect of amine structure and several process variables on corrosion in PCCC systems. Section 8.1 describes what conditions promote protective $FeCO_3$ films on carbon steel. Section 8.2 describes conditions that can sometimes lead to attack of stainless steel at high T. Section 8.3 gives evidence that the conversion of ferric to ferrous plays a key role in high temperature corrosion. Finally Section 8.4 develops a relationship between amine structure, iron solubility, and corrosion.

8.1. CARBON STEEL OFTEN PERFORMS WELL IN 5 MOLAL PZ DUE TO THE FORMATION OF A PASSIVATING $FeCO_3$ LAYER. THIS LAYER IS PROMOTED AT HIGH T, HIGH CO_2 LOADING, LOW SOLUTION VELOCITY, AND IN AMINES WITH LOW Fe^{2+} SOLUBILITY.

When protective $FeCO_3$ layers form, the corrosion rate of carbon steel in amine solutions can be very low. The formation of $FeCO_3$ layers is controlled by local supersaturation of Fe^{2+} and CO_3^{2-} near the metal surface. Higher intrinsic Fe^{2+} solubility in MEA explains its lack of $FeCO_3$ formation. High fluid velocities reduce local supersaturation of Fe^{2+} and CO_3^{2-} and can lead to limited $FeCO_3$ formation and high corrosion rates. $FeCO_3$ formation is favored at high temperatures because Fe^{2+} solubility decreases at high T and because kinetics of $FeCO_3$ formation are likely faster at higher T. These reasons also mean that $FeCO_3$ is not observed at low T conditions. Despite the lack of $FeCO_3$ formation, carbon steel performs well at low T due to slower kinetics of metal oxidation. Limited evidence of environmentally induced cracking of carbon steel was observed at high T in 5 m PZ. Finally, $FeCO_3$ films do not form on carbon steel in the absence of amine and CO_2, so care must be taken when water testing carbon steel equipment.

This conclusion is supported by the following experimental observations:

- **Carbon steel performs well at 40-70 °C in 7 m MEA, but it is unacceptable at 120 °C.**

With 7 m MEA carbon steel (C1010) performed well in the absorber (40-70 °C), experiencing 1.8–8.9 μm/yr of corrosion, but performed unacceptably in the stripper (110-120°C), experiencing 3600–4000 μm/yr of corrosion.

- **The strong effects of CO_2 loading and T on Fe^{2+} solubility suggest the equilibrium concentration of Fe^{2+} will change as the solvent moves through a real plant.**

One implication of bench-scale Fe^{2+} solubility experiments is that there will be strong fluctuations in equilibrium Fe^{2+} concentration as solvent moves through a real plant. In degraded PZ for example, Fe^{2+} solubility is apparently highest at low temperature and lean loading, so these conditions are least likely to be protected by $FeCO_3$ and may experience corrosion. However an amine stream that is unsaturated at cold, lean conditions may be supersaturated at hot, rich conditions. This means corrosion could occur in the absorber, and those corrosion products are deposited in the stripper. This also means that the observed Fe^{2+} concentration at a plant may not be an equilibrium value, but rather a complicated average value affected by the residence times at unsaturated and supersaturated parts of the process.

- **Carbon steel experiences low corrosion at high temperature in PZ solution.**

In a set of bench-scale experiments from 100°C to 160°C, at lean loading ($\alpha \approx 0.23$), even in very degraded solutions of PZ, C1010 performance was good to moderate (< 400 μm/yr), and showed no strong increase with temperature. Counterintuitively, at higher

loading of α = 0.3 carbon steel performed better (<100 μm/yr). Higher loading likely promotes the formation of a $FeCO_3$ layer.

- **At 50 °C, carbon steel performs well in 5 m PZ, despite not forming protective $FeCO_3$ layers.**

Carbon steel performed well at PZ wetted locations in the absorber (≈50 °C, α = 0.4), frequently showing no corrosion products and negligible corrosion (1 μm/yr).

Rich (α = 0.4) and lean (α = 0.23) locations at higher flow rate (0.04 – 0.77 m/s) primarily showed a rough, porous iron layer. Presumably higher solubility of Fe^{2+} at low temperature prevents formation of siderite layers. These locations experienced low to moderate corrosion (50 – 210 μm/yr).

- **Carbon steel performs well in 5 m PZ at lean and rich loading, at 116 – 150 °C, when fluid velocity is low. This good performance is due to the formation of a protective $FeCO_3$ film.**

Carbon steel (C1010) in 5 m PZ is frequently protected by a crystalline siderite ($FeCO_3$) layer at 116 - 150 ºC. Siderite is observed at both lean (α = 0.23) and rich (α = 0.4) CO_2 loading at these temperatures. At 116°C and rich loading, corrosion varied from 47 - 92 μm/yr. At 150°C and lean loading, corrosion ranged from 0 - 11 μm/yr. These measurements were in vessels or low velocity pipes (≈0.39 m/s).

Corrosion coupons from the 2017 SRP pilot plant campaign show a protective, crystalline layer of $FeCO_3$ forms on C1010 in 5 m PZ at 150 °C and α = 0.21. When this layer formed, corrosion performance was good (96.4 μm/yr).

- **At 150 – 155 °C, at lean and rich loading, when fluid velocity is moderate or high (> 0.8 m/s), $FeCO_3$ films are sometimes not protective to carbon steel, leading to high corrosion in 5 m PZ.**

At high temperature (150-155 °C), high fluid velocity locations (≈ 0.8 m/s, not accounting for two phase flow), protective films are sometimes not adequate to protect carbon steel in 5 m PZ, and corrosion can be high (up to 2800 μm/yr). High fluid velocity increases transport of Fe^{2+} to the bulk solution and may cause mechanical erosion of $FeCO_3$ films. During several batches, $FeCO_3$ was somewhat protective (<200 μm/yr) at these conditions. The non-reproducibility at these conditions could be due to poor control of coupon insertion orientation. This would have the effect of obstructing flow and increasing local fluid velocity and turbulence around the coupon significantly.

- **Limited evidence suggests environmentally induced cracking of carbon steel can occur in 5 m PZ at 155 °C at high fluid velocity.**

One C1010 coupon cracked and was lost in the hot (155 °C) rich stream (typically $\alpha = 0.4$), leading to an exceptionally high corrosion rate (9700 μm/yr). This suggests that environmentally induced cracking may be an issue for carbon at high temperatures in PZ. Environmentally induced cracking was not thoroughly investigated in this work.

- **Equipment commissioning with water and steam appears more corrosive to carbon steel than PZ operation.**

There is evidence that the commissioning phase, when equipment is pressure tested by circulating water and steam, is more corrosive to carbon steel than operation with 5 m PZ. Notably, operation with 5 m PZ in the absorber typically leaves C1010 pristine, but extended water testing caused moderate corrosion. High velocity locations also experienced corrosion (hot lean, hot rich, cold lean). If carbon steel is used, care should be

taken to avoid extended equipment water testing. CO_2 circulation should be avoided during equipment commissioning with water.

8.2. DEPASSIVATION AND HIGH CORROSION OF STAINLESS STEEL CAN OCCUR IN AMINE SOLUTIONS AT HIGH TEMPERATURE. DEPASSIVATION OF STAINLESS IS PROMOTED BY HIGHER T (150 °C) WHEN CONDITIONS ARE RELATIVELY ANOXIC AND REDUCING.

Stainless steel (316L) appears to be very close to the active/passive transition in amine solutions at high T in PCCC conditions.

Bench-scale screening suggests that MEA and PZ solutions can attack stainless at anoxic, high T conditions. Very anoxic conditions at the bench scale cause corrosion in PZ especially above 120 °C. Attack of stainless in MEA was also observed at 120 °C in anoxic conditions, but higher temperatures were not evaluated with MEA. This behavior has not been well reported in MEA since operation for MEA units is limited to 120 °C by thermal degradation of the solvent. PCCC pilot plants contain oxygen, and thus stainless performance is better than in the anoxic bench-scale experiments. Stainless performs well at 120 °C in MEA in pilot plants. Stainless performed well up to 116 °C in PZ at pilot plants at all times.

At high temperatures (150°C) in pilot plants, stainless steel in PZ is sometimes attacked, but is passivated at other times. Performance of stainless steel in PZ at pilot plants suggests that it can be pushed into and out of the active state by small process changes. One hypothesis is that stainless steel performs better when flue gas O_2 concentration is higher. High flue gas O_2 means that oxidizing species (dissolved O_2, Fe^{3+}) are carried over to the stripper. These oxidizing species increase the solution potential and push stainless into the passive state. In a pilot plant with 17 – 20% O_2 in the flue gas, stainless was passive in 5 m PZ at 150 °C (<9 μm/yr). In a pilot plant with 5.4 % O_2 in the flue gas, stainless

performance was initially very poor (500 – 1100 μm/yr) at high T (150-155 °C), suggesting it was in the active state.

However this hypothesis does not explain all observed behavior of stainless in PZ. Later in the low O_2 flue gas campaign, stainless performance at high T improved (5-200 μm/yr). Several process changes in the second half of the campaign could be responsible, including increasing degradation products and iron in solution, stripping of dissolved O_2 from rich solvent, and injection of SO_3 into the flue gas to study aerosol. Whatever the cause, it is clear that small process changes made the solution overall more oxidizing, leading to stainless passivation. The tentative conclusion from this work is that stainless may experience lower corrosion at high T when the solvent is more oxidizing. However, until the occasional vulnerability of stainless steel is better understood, higher alloy steels (ie, duplex stainless) should be investigated for use at these locations.

This conclusion is supported by the following experimental observations:

- **Stainless steel performs well in 7 m MEA at both absorber and stripper conditions.**

Stainless steel (316L) performed well in a pilot plant campaign at all locations, experiencing 0–0.3 μm/yr of corrosion in the absorber (40-70 °C), and 0.2–0.6 μm/yr of corrosion in the stripper (110-120°C).

- **At 50 – 116 °C, stainless steel performs well in 5 m PZ.**

During a pilot plant campaign, in the absorber and 50 – 116 °C piping, stainless steel (304 and 316L) performed well (0 – 9 μm/yr). CO_2 loading and fluid velocity did not appear to have a strong effect on stainless performance at these conditions.

- **Stainless steel sometimes experiences attack in PZ and MEA at high temperature, anoxic conditions.**

In bench-scale experiments, several solutions of slightly degraded PZ, at lean loadings ($\alpha \approx 0.23$), 316L experienced corrosion with a strong temperature effect, with good performance at 120 °C (<150 μm/yr), but poor performance (>1000 μm/yr) at 149 °C and higher. Notably, attack of stainless was not observed in completely clean PZ at similar conditions. At higher loading of $\alpha = 0.3$, stainless steel showed excellent corrosion performance (<100 μm/yr). It is not clear why stainless steel performed well at higher CO_2 loading. Attack of 316L was also seen in 9 m MEA (500 μm/yr at 120 °C, $\alpha = 0.42$), although higher temperature were not evaluated. These stainless corrosion rates may be higher than in a real plant, because the reducing environment of the corrosion loop is particularly challenging for 316L.

- **Stainless steel performed well in 5 m PZ both in the absorber and in the hot, lean stream. This may be partially due to the high O_2 content at SRP.**

Stainless steel (316L) performed excellently in the absorber ($\alpha = 0.33$ and 30 °C) corroding at 0 μm/yr. Stainless steel also performed excellently in the hot (150°C), lean ($\alpha = 0.21$) stream, showing 2.0–9.0 μm/yr of corrosion. Stainless steel is clearly not attacked by either PZ operation or water commissioning at these conditions. This may be due to higher O_2 concentration at in SRP synthetic flue gas (17-20 %) compared to a coal flue gas stream (5.4 %), which may lead to more oxidizing conditions which can support chromium oxide passive film formation on stainless steel.

- **At 150 – 155 °C, stainless steel sometimes experiences high corrosion in 5 m PZ.**

At high temperature (150-155 °C), stainless steel is also sometimes attacked in 5 m PZ and shows high corrosion (up to 1100 μm/yr). Attack of stainless occurred at high and

low fluid velocity, and lean and rich loading. Both 316L and 304 experienced high corrosion. During some batches, stainless performed well at these locations. It is not clear why stainless was attacked during some batches, but not others at similar conditions. Vulnerability of stainless steel could be due to the uniquely high operating temperature of PZ compared to other amines, which typically operate at 120 °C. Until the occasional vulnerability of stainless steel at these locations is understood, higher alloy steels (ie, duplex stainless) should be investigated.

8.3. FERRIC PRODUCTS ARE GENERATED IN THE ABSORBER, THEN REDUCED AT HIGH TEMPERATURE, ANOXIC CONDITIONS. THIS REDUCTION REACTION INCREASES THE OXIDATION OF STEEL AND AMINE.

Other researchers have determined that amine oxidation at high temperatures proceeds through the carryover of oxidizers from the absorber to the stripper, even in the absence of dissolved O_2. The conversion of Fe^{3+} to Fe^{2+} has been suggested as a likely culprit (Paul Thomas Nielsen, 2018). Observation of corrosion products supports this theory. Ferric products are frequently found in the rich amine stream in PZ pilot plants, but only ferrous products are observed in the stripper, after dissolved O_2 has been stripped out or reacted away. Presumably, the conversion of Fe^{3+} to Fe^{2+} is a very favorable reduction reaction in the absence of O_2. In this way, carried-over ferric likely is responsible for oxidation of amine and corrosion at high temperature. Thus lowering Fe^{2+} concentration in amine solutions could be a key way to limit amine oxidation and corrosion. Alternatively, increasing Fe^{2+} concentration would increase the generation of Fe^{3+} and make the solution more oxidizing. This could be used to increase the solution potential at high T, possibly pushing stainless into the passive region in PZ.

Ferrous products were not observed in MEA at pilot plants. The prevalence of ferric in MEA suggests MEA is more oxidizing, or perhaps ferric is strongly complexed and stabilized in MEA.

This conclusion is supported by the following experimental observations:

- **In low temperature, agitated solubility experiments, Fe^{2+} is frequently converted to Fe^{3+}, except in PZ at high CO_2 loadings.**

The solid phases characterized in these experiments showed that $FeCO_3$ only formed under specific conditions. Siderite ($FeCO_3$) was only identified in PZ solutions with rich CO_2 loading. Since siderite was found in both rich clean PZ and rich degraded PZ, its formation appears to be relatively independent of amine degradation level. Lean PZ solutions tended to form magnetite (Fe_3O_4), as did lean MEA solutions. The solid sample from a rich MEA experiment that was characterized appeared to be goethite (FeO(OH)). An air and CO_2-sparged experiment with 5 m SRP PZ air and CO_2 also formed goethite. The conversion of Fe^{2+} to Fe^{3+} requires relatively oxidizing conditions. These experiments suggest that MEA and lean PZ are somewhat more oxidizing than rich PZ solutions.

- **Corrosion products on carbon steel are largely Ferric (Fe^{3+}) in 7 m MEA, suggesting more oxidizing conditions than PZ. Protective corrosion product layers were not observed.**

In 7 m MEA, $Fe(OH)_3$ was observed on carbon steel coupons in the absorber sump and the stripper sump. This ferric product, particularly at relatively reducing stripper sump conditions, suggests MEA is more oxidizing than PZ. Corrosion product films on C1010 in MEA were not thick or tightly adhering. Presumably higher Fe^{2+} solubilities prevent precipitation of protective ferrous films. Alternatively, ferrous product formation is prevented at most conditions because MEA conditions rapidly oxidize Fe^{2+} to Fe^{3+}.

- **Fe^{3+} products are observed at rich conditions, which are relatively oxidizing, but Fe^{2+} is observed at lean conditions, which are reducing. The cyclic oxidation and reduction of Fe^{3+} likely plays a role in high temperature oxidation of PZ.**

At warm or hot rich conditions, the corrosion products on carbon steel include oxidized species, but not at lean conditions, suggesting that dissolved Fe^{3+} is depleted in the stripper sump by reaction with piperazine. Magnetite (Fe_3O_4) or goethite (Fe(O)OH) are often observed in addition to siderite at warm (116 °C) and hot rich (155 °C) locations. Presumably, these ferric species are generated in the absorber, which is relatively oxidizing due to O_2 in the flue gas. The absence of ferric products in the stripper sump suggests that ferric is reduced back to ferrous at the high temperature, anoxic conditions of the stripper. Presumably this reduction is accompanied by an oxidation of an amine, degrading it. This Fe^{3+} to Fe^{2+} reduction is probably the cyclic oxidizer hypothesized by other researchers to play a significant role in PZ oxidation (Paul Thomas Nielsen, 2018).

8.4. CERTAIN AMINES AND AMINE DEGRADATION PRODUCTS HAVE HIGH IRON SOLUBILITY. THESE AMINES LIKELY COMPLEX IRON AND STABILIZE IT IN SOLUTION, ACCELERATING CORROSION.

Ethylamines were found to be more corrosive than their propylamine counterparts. It was also found that MEA had higher Fe^{2+} solubility than clean PZ at rich CO_2 loadings. Ethylamines are likely the correct chain length to form stable iron complexes with iron in solution. Longer amines, and particularly sterically hindered amines like PZ, are less likely to form such stable complexes with iron. This iron complexation hypothesis explains why $FeCO_3$ films are not observed in MEA solutions, but they are observed in PZ solutions. Effective Fe complexation in MEA increases solubility and prevents $FeCO_3$ formation.

One of these high iron solubility ethylamines is ethylenediamine (EDA), which is a key degradation product in PZ solutions. As PZ solutions degrade, increasing EDA increases stabilization and solubility of Fe in solution. Eventually, iron solubility is

elevated enough to reduce formation of $FeCO_3$ films, which accelerates corrosion. This hypothesis explains the correlation between PZ degradation and increased corrosion.

This conclusion is supported by the following experimental observations:

- **Ethylamines, such as, MEA and EDA, are more corrosive than their propylamine counterparts, EDA and PDA. The ethyl- backbone amines likely form more stable coordination complexes with oxidized iron, increasing corrosion.**

MEA, 3-amino-1-propanol (MPA), ethylenediamine (EDA), and 1,3-diaminopropane (PDA) were evaluated to determine a relationship between amine chain length and corrosion. MEA was significantly more corrosive to C1010 and 316L than MPA in both thermal cylinders and the corrosion loop. The results are less complete for EDA/PDA, but PDA appears to be less corrosive than EDA to 316L in thermal cylinders. One hypothesis is that ethylamine carbamates form very stable octahedral complexes with iron. The same complex cannot be formed with the longer propylamine carbamates as it is too long and labile to easily form an octahedral complex

- **Fe^{2+} is significantly more soluble in MEA than clean PZ at rich loading.**

Rich 9 m MEA was found to have Fe^{2+} solubility of 0.77 mmol/kg at rich loading (α = 0.44) and 45 C. At similar conditions, Fe^{2+} solubility in clean 5 m PZ was 0.05 mmol/kg. The same trend is evident at several different temperatures at rich loadings. It is likely that MEA carbamate effectively complexes Fe^{2+}, increasing its solubility. PZ carbamate has a constrained structure, and is likely unable to complex Fe^{2+}. The range of Fe^{2+} solubilities in MEA across all conditions measured was 0.001 to 14 mmol/kg. The range of Fe^{2+} solubilities in clean PZ across all conditions tested was 0.03 to 0.1 mmol/kg.

- **The effect of CO_2 loading on Fe^{2+} solubility is affected by amine type.**

In 9 m MEA, increasing CO_2 loading increases iron solubility dramatically. In clean 5 m PZ, CO_2 loading does not affect Fe^{2+} solubility, which is low (< 0.1 mmol/kg) at all conditions. Presumably, neither MEA nor PZ complex Fe^{2+} effectively. However at high CO_2 loadings, MEA carbamate forms and readily complexes Fe^{2+}. PZ carbamate's constrained structure prevents it from forming stable complexes with Fe^{2+}.

- **PZ degradation apparently accelerates corrosion of carbon and stainless steel.**

In anoxic, bench-scale experiments, PZ degradation apparently increased corrosion of both C1010 and 316L. Completely fresh PZ solutions were often non-corrosive to both C1010 and 316L. Pilot plant degraded amines corroded both materials more quickly. A more deliberate study is needed to clearly separate the effects of amine concentration, CO_2 loading, and degradation.

- **The presence of amine degradation products significantly increased Fe^{2+} solubility in PZ.**

Degraded PZ had much higher Fe^{2+} solubility (up to 26 mmol/kg) than clean PZ. Degraded PZ has linear amine degradation products, such as EDA, which likely chelate Fe^{2+}. Apparently, this EDA complex increases Fe^{2+} solubility in PZ at all conditions. The range of Fe^{2+} solubilities in degraded PZ across all conditions tested was 0.1 to 26 mmol/kg.

In degraded PZ, Fe^{2+} solubility decreased with increasing loading. This is counterintuitive, because presumably EDA carbamate is also an effective complexing agent for Fe^{2+}. The reason for the decrease of Fe^{2+} solubility in degraded PZ at high loadings is not known.

As PZ degrades, its increasing Fe^{2+} solubility might keep Fe^{2+} in solution, preventing formation of $FeCO_3$ films. This explains the observed relationship between PZ degradation and accelerated C1010 corrosion.

APPENDICES

Appendix A. Operating Procedures

A.1. Corrosion Loop Procedure and Safety Analysis

JOB SAFETY ANALYSIS		DATE 5/15/15	☒NEW ☐REVISED
Operation of Corrosion Loop Apparatus			☐LABORATORY ☐PILOT PLANT
DEVELOPMENT TEAM	POSITION/TITLE	DEVELOPMENT TEAM	POSITION/TITLE
Kent Fischer	Graduate Researcher		
REQUIRED AND/OR RECOMMENDED PERSONAL PROTECTIVE EQUIPMENT			
☒SAFETY GLASSES ☒LAB COAT ☒NITRILE GLOVES	☐FRC ☐HARD HAT ☐HEARING PROTECTION ☐FACE SHIELD	☐AIR PURIFYING RESPIRATOR ☐LEATHER GLOVES	☐OTHER

JOB STEPS	POTENTIAL HAZARDS	CRITICAL ACTIONS
1. Pressure test apparatus with compressed air line to ensure no leaks.	• If a leak is present, when the loop is filled with amine, the amine could be released.	• Open ball valve to compressed air line. Allow apparatus to fill until 100psig is reached. Shut ball valve and wait to see if pressure decreases over time. If pressure decreases, there is a leak in the system. • Depressurize by **very slowly** opening the top ball valve.
2. Ensure ball valves are closed. Remove the ORP probe and fill the corrosion loop with liquid to be tested.	• Do not overfill the loop. • DO NOT PUT RICH AMINE IN THE LOOP FOR HIGH T EXPERIMENTS	• The loop has a liquid volume of 1070 mL, do not add more than this. • The Loop has a pressure relief disk (PRD) that will burst at 200 PSIG at room temperature. The disk ruptures at 176 PSIG at 160 °C. You must ensure that the amine solution is lean, because rich solutions will have a total pressure at elevated temperatures that will rupture the disk.
3. Reinsert the ORP probe.	• Potential site of leak.	• Make sure to reapply Teflon tape to the ORP threaded fitting and to tighten the ORP probe thoroughly.
4. Fasten Swagelok plugs onto ball valves to prevent apparatus being accidentally opened.	• Accidental ball valve open during operation.	• If ball valves are accidentally opened, the user will be sprayed with high temperature amine and CO_2. Make sure both ball valves

		are capped with the appropriate Swagelok plugs.
5. Plug in PID controller and set desired temperature.		
6. Watch apparatus pressure while heating to avoid overpressure.	• Loop overpressure and PRD rupture.	• It is possible that your solution has a higher vapor pressure than you anticipated. Watch the apparatus carefully as the temperature increases. Pressure should rise slowly with temperature and never exceed 150 PSIG. • If pressure is not rising with temperature, the pressure gauge has probably failed. Unplug the apparatus and abort run. • If pressure exceeds 150 PSIG, immediately unplug the apparatus and abort run.
7. Run Data acquisition software and observe.		Once target temperature is reached and pressure is no longer increasing, the apparatus no longer needs to be watched as closely. Check back while it runs to ensure nothing goes wrong.
8. Once run is complete, set PID to zero to stop heating. Allow apparatus to cool to room temperature. This may take several hours.	• Accidental release of pressure	• DO NOT OPEN BALL VALVES WHILE SYSTEM IS HOT.
9. Once system is at room temperature (verify by touching steel pipe to see that it is cool), you may unfasten Swagelok plug on TOP ball valve. Slowly open the TOP ball valve to release pressure from headspace.	• Accidental release of pressure • ONLY OPEN THE TOP BALL VALVE. • ONLY OPEN BALL VALVE IF SYSTEM IS AT ROOM TEMPERATURE.	• Make sure to only open the top ball valve in the system (the one near the pressure gauge). If you open the bottom ball valve, you will be sprayed with amine. • Slowly open the top ball valve, allowing any excess pressure to vent.
10. Once system pressure has been vented, you may unscrew the Swagelok plug from the bottom ball valve and then open it to drain out the amine.	• Amine spill	• Make sure to have a tubing connected to the ball valve to collect amine in an appropriate waste container.

11. Close the bottom ball valve and fill the system with water to rinse out residual amine. Open bottom ball valve to drain.	• Water spill	• Make sure to have a tubing connected to the ball valve to collect rinse water in an appropriate waste container.

A.2. ER PROBE INSERTION PROCEDURE

STANDARD OPERATING PROCEDURE	DATE: 13 February 2018	REVISION # **2**

Insertion and removal of ER probes during plant operation at NCCC

DEVELOPMENT TEAM	POSITION/TITLE
Kent Fischer	Graduate Researcher

REQUIRED PERSONAL PROTECTIVE EQUIPMENT

☒SAFETY GLASSES ☐LAB COAT ☒NITRILE GLOVES	☐FRC ☒HARD HAT ☐HEARING PROTECTION ☐FACE SHIELD	☐AIR PURIFYING RESPIRATOR ☐LEATHER GLOVES	☐ OTHER

EQUIPMENT LIST

Model ER4000 retractable ER probe from Metal Samples Company
3/8” drive torque wrench capable of torqueing to 20 ft·lb
1” crowfoot wrench adapter for a 3/8” drive ratchet
3/8” wrench
(Quantity=2) 1” wrench
1-13/16” wrench
14” pipe wrench
(Quantity=2) 7/8” wrench
Nickel anti-seize lubricant
Hydrostatic Pressure Testing Pump

BACKGROUND INFORMATION

1. This model ER probe can be inserted and removed under pressure. The probe is rated for use up to 500°F and 1500 PSI. However, this removal procedure should only be used for system pressures equal or less than 150 PSI. Insertion or removal above this pressure requires a special tool.

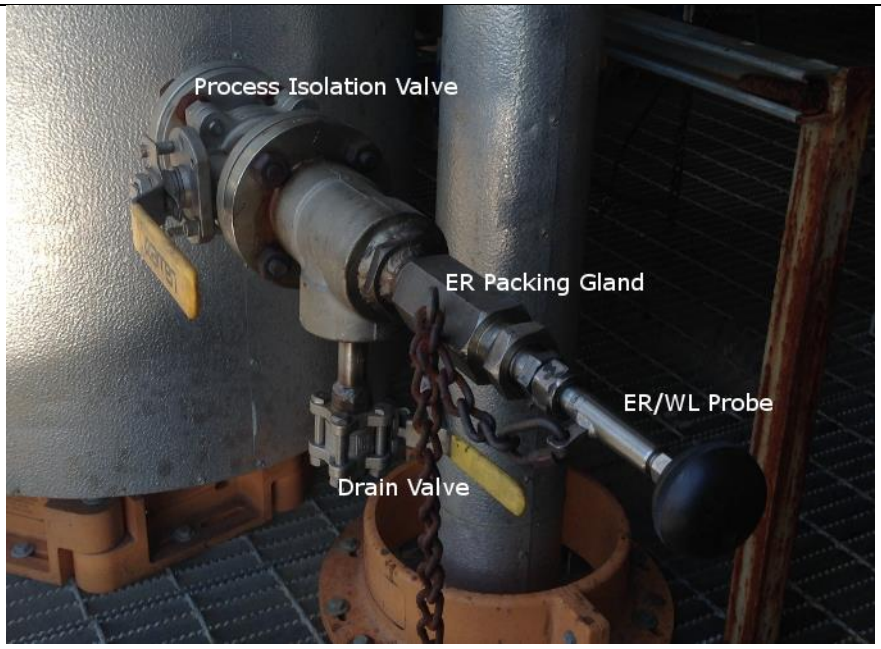

2. The ER Probe is a long retractable rod that is inserted through a compression fitting (called the ER packing gland). The ER packing gland attaches to a 1" male NPT pipe nipple. A 1" full port ball valve isolates the ER probe from the process flow. A drain ball valve is also affixed to the male NPT pipe nipple to allow pressure to be drained for ER probe removal.

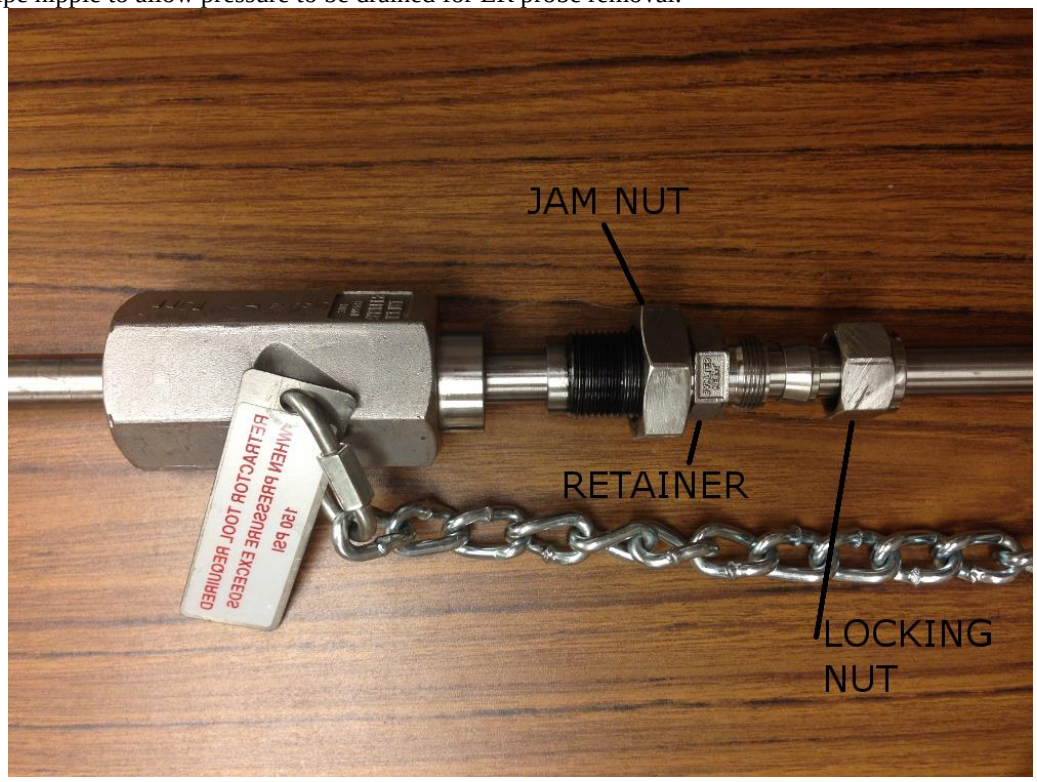

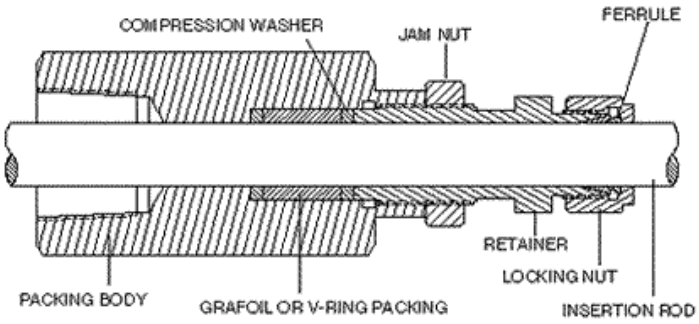

3. The ER packing gland consists of a packing body, a jam nut, a retainer, and a locking nut. The compression fitting seal is formed by the tightening of the retainer into the packing body, which compresses a Teflon fitting inside the packing body. The jam nut is a secondary fitting that prevent the retainer from being loosened by vibration. The locking nut is another secondary fitting that prevents the insertion rod from being slowly pushed out by the process pressure.

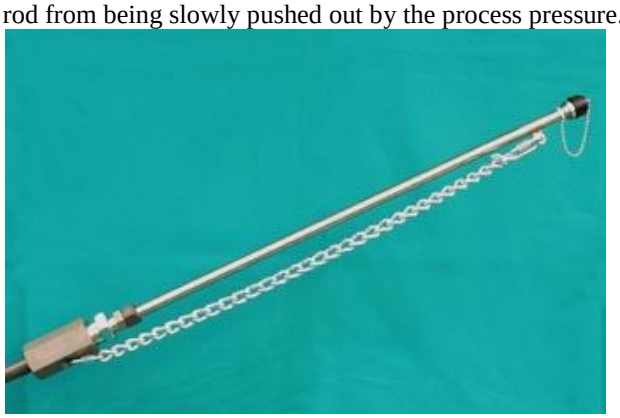

4. A safety chain is used to prevent the insertion rod from being pushed out slowly by the process pressure. The safety chain also prevents against accidental injury due to a blowout. A blowout may occur during retraction if retraction is performed improperly.

INSERTION PROCEDURE

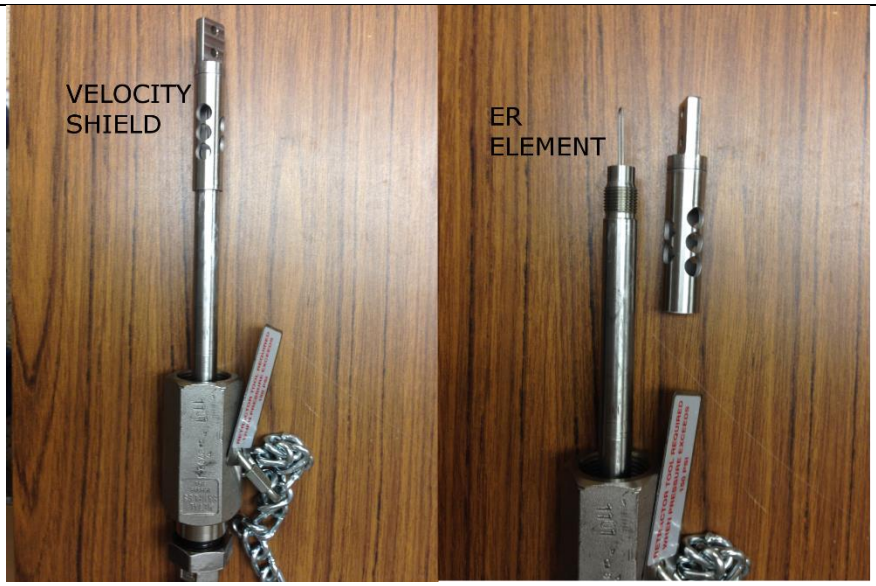

1. When the ER probe is new, it is shipped in a protective plastic wrap. Remove this wrap. In addition, the ER probe element is covered with a piece of paper that prevents corrosion during shipping. To remove this paper, you must first carefully unscrew the velocity shield that protects the ER element. Once the velocity shield is removed, carefully remove the protective paper around the ER element. Replace the velocity shield. The velocity shield is an additional protection against probe blowout, so it should always be used.
2. Fully unscrew the locking nut. Pull the locking nut and the ferrule away from the retainer. Fully unscrew the jam nut. Unscrew the retainer until the insertion rod can slide freely back and forth. Fully retract the insertion rod.
3. Before mounting the ER probe, check that the process isolation valve is closed. Ensure that the 1" male NPT nipple is wrapped with Teflon tape to ensure the NPT fitting seals properly. Ensure Using the 1-13/16" wrench, tighten the ER packing body onto the 1" male NPT nipple where the ER probe will be mounted.
4. The ER probe should still be fully retracted. Use the torque wrench to tighten the retainer to 20 ft·lb of torque. Tighten the jam nut, but do not tighten the locking nut. The locking nut must remain loose to allow insertion.
5. Attach the hydrostatic pressure testing pump to the drain valve. Open the drain valve, but make sure the process isolation valve is still closed. Use the pressure testing pump to raise the pressure inside the mounting hardware to 120 psig. Ensure that the fitting holds the pressure for 10 minutes without leaking.
6. Ensure the safety chain is attached to both the ER probe and the ER packing gland.
7. Release the pressure in the fitting using the drain valve on the hydrostatic pressure testing pump. Detach the pump and close the drain valve.
8. With the help of a plant operator or an NCCC engineer, open the process isolation valve. Grab the ER probe body and push it into the packing gland. The rod should slowly slide in, through the

compression fitting. Because the compression fitting is tight, this may require some force. Twisting the probe can help.
9. Once the probe is fully inserted, tighten the locking nut to prevent the rod from sliding back out.
10. The safety chain should now have some slack in it. Refasten the chain to take in the slack.

Appendix B. ORP Measurement in Piperazine during Pilot Campaigns

Pilot ORP measurements were made at SRP during the 2017 PZ campaign. The ORP probe was calibrated with Light's solution prior to insertion, then was exposed to 340 hours of water testing, then 300 hours of piperazine operation. During operation of the pilot plant, 36 steady state runs were achieved, each about 45 minutes long. One ORP reading per minute was taken during these runs, and these data averaged to yield an average ORP reading during the run. These average ORP readings during a steady state run are plotted chronologically for the pilot campaign in Figure B-1. Times reported here are operating hours with PZ. A dramatic decrease in ORP at 250 hours likely represents probe failure at that point, rather than a real process change. These pilot ORP measurements can be directly compared to ORP measurement in the corrosion loop (Table 4-1). Surprisingly, these ORP values are not dramatically different than in the corrosion loop. This was unexpected, because the loop has no gas cycling, so it is expected to be oxygen-depleted and reducing compared to the pilot plant. These ORP readings at the bench and pilot scale need to be reproduced to ensure they are reliable.

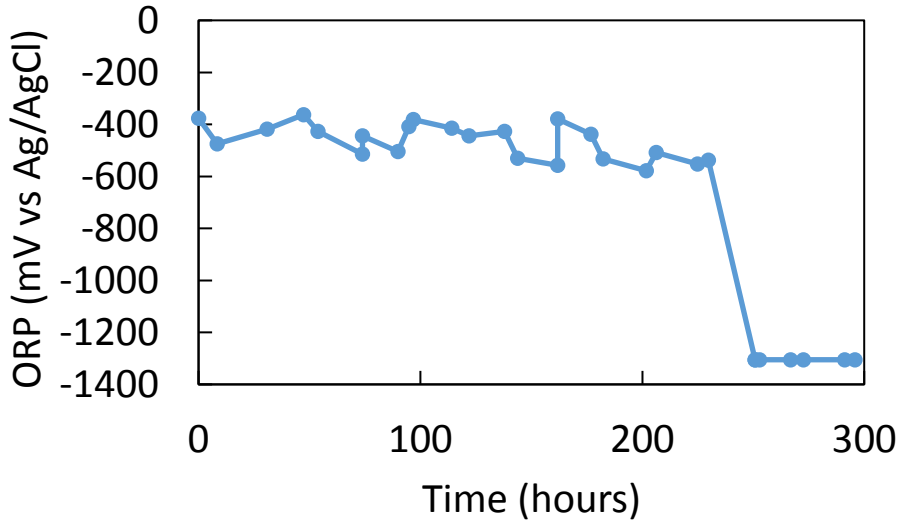

Figure B-1: ORP measurement in hot lean stream during 2017 SRP PZ campaign.

Pilot ORP measurements at NCCC during the 2018 PZ are not entirely reliable. The ORP probes were installed several months before pilot operation began, and the probes may have dried out and become damaged. In addition, the probe mounting hardware was not designed to allow retraction and recalibration of the probes. So, the probes calibration and reading may have shifted significantly over the course of the campaign. Finally, the probe transmitter range was set from -1500 mV to +1500 mV based on bench-scale experience. It appears the probes drifted to oxidizing values outside this range during measurement. Any reading at or outside these artificial bounds should be considered innacurrate. Probe readings reported here are daily averages of ORP readings taken every minute. Times reported here represent operating hours with PZ. However, probe readings largely stayed inside these bounds during Batch 2, which, although innaccurate, may be a useful. It appears during Batch 2 that the cold rich location was significantly more oxidizing (1200 to 1500 mV) than the hot lean location (400 to 600 mV). However, there

is an abrupt decrease in the hot, lean ORP during the second half of Batch 2 (to -600 mV). See Figure B-2 and Figure B-3. This abrupt decrease may be a real change in conditions, or it may just be erratic behavior due to probe failure. ORP behavior was largely erratic during Batch 3 (Figure B-4 and Figure B-5) and Batch 4 (Figure B-6 and Figure B-7), suggesting the probes had failed.

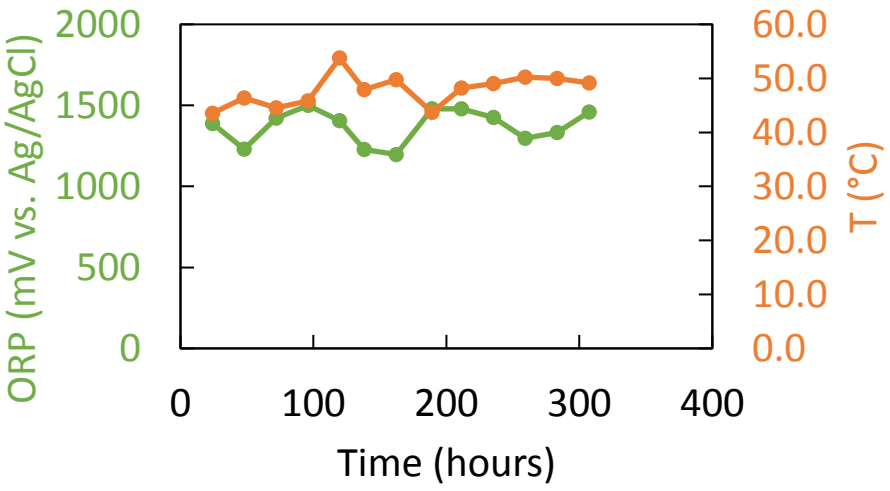

Figure B-2: ORP measurement in cold rich bypass (AT40512) during Batch 2 of 2018 NCCC PZ campaign

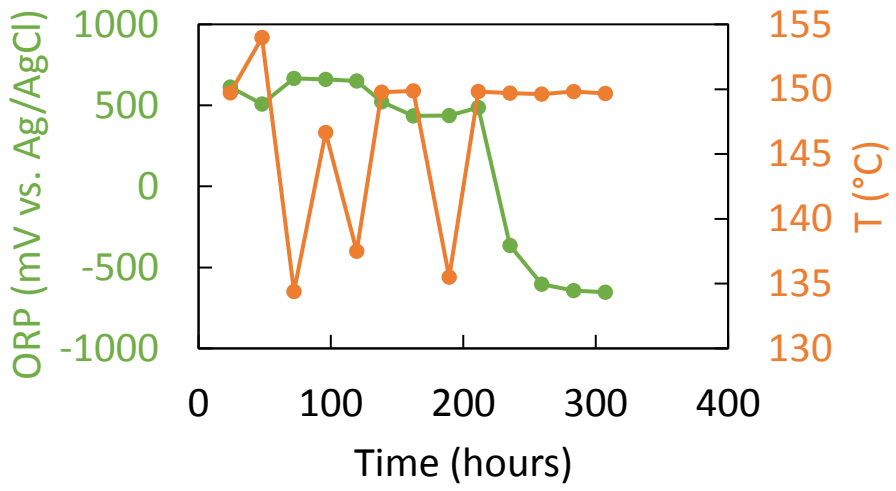

Figure B-3: ORP measurement in hot lean stream (AT40522) during Batch 2 of 2018 NCCC PZ campaign

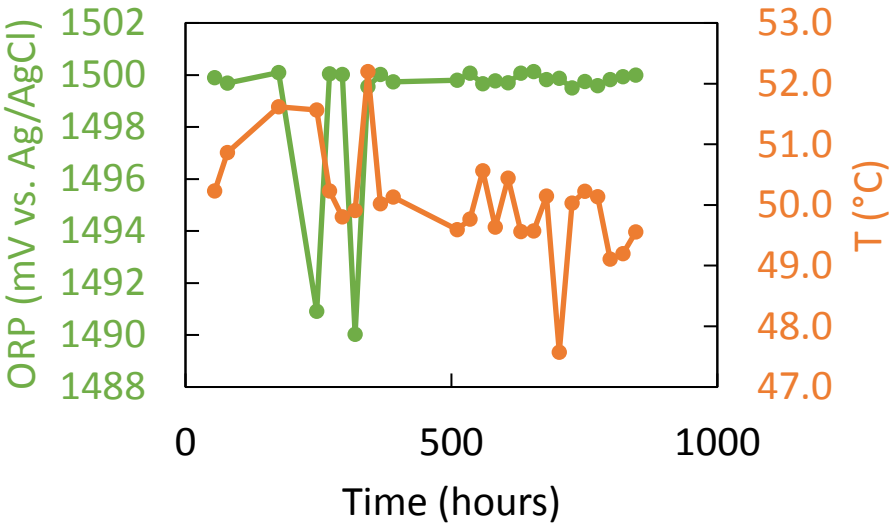

Figure B-4: ORP measurement in cold rich bypass (AT40512) during Batch 3 of 2018 NCCC PZ campaign

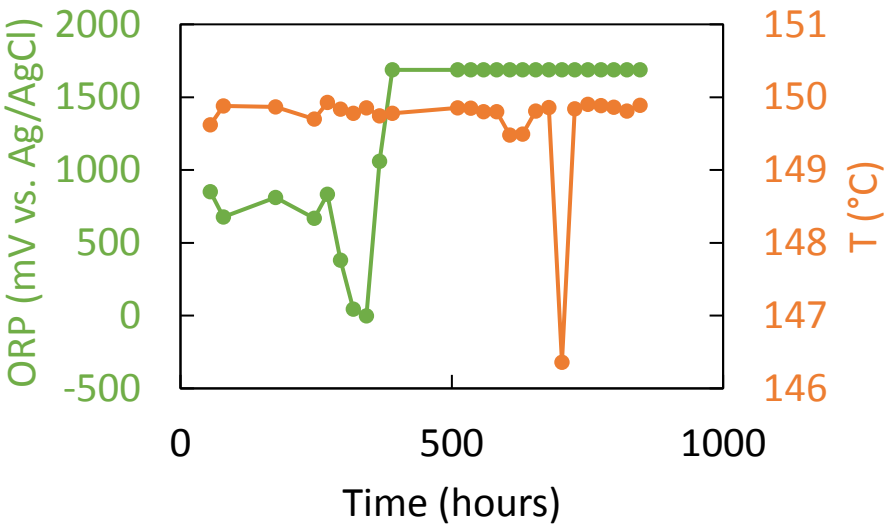

Figure B-5: ORP measurement in hot lean stream (AT40522) during Batch 3 of 2018 NCCC PZ campaign

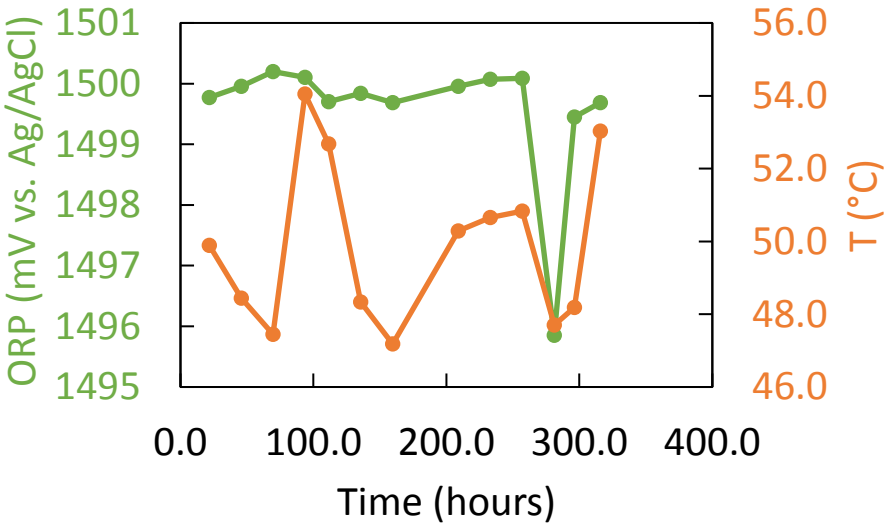

Figure B-6: ORP measurement in cold rich bypass (AT40512) during Batch 4 of 2018 NCCC PZ campaign

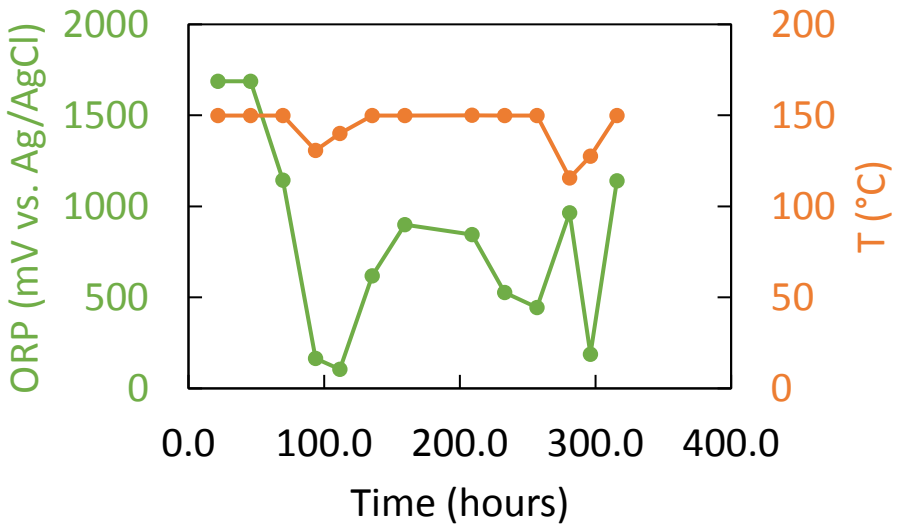

Figure B-7: ORP measurement in hot lean stream (AT40522) during Batch 4 of 2018 NCCC PZ campaign

References

API. (2003). Avoiding environmental cracking in amine units. In (Vol. RP945): American Petroleum Institute.

Arrhenius, S. (1896). XXXI. On the influence of carbonic acid in the air upon the temperature of the ground. *The London, Edinburgh, and Dublin Philosophical Magazine and Journal of Science, 41*(251), 237-276.

ASTM. (2017). Standard Practice for Preparing, Cleaning, and Evaluating Corrosion Test Specimens. In *G1-03(2017)e1*. West Conshohocken, PA: ASTM International.

Au-Yeung, S. C. F., Denes, G., Greedan, J. E., Eaton, D. R., & Birchall, T. (1984). A novel synthetic route to "iron trihydroxide, Fe(OH)3": characterization and magnetic properties. *Inorganic Chemistry, 23*(11), 1513-1517. doi:10.1021/ic00179a009

Bauccio, M. (1993). *ASM metals reference book* (3rd ed.). Materials Park, OH: ASM international.

Beaudry, M. R. (2017). *Aerosol Measurement and Mitigation in CO2 Capture by Amine Scrubbing*. (Ph.D. Dissertation), The University of Texas at Austin,

Beverskog, B., & Puigdomenech, I. (1996). Revised pourbaix diagrams for iron at 25–300 °C. *Corrosion Science, 38*(12), 2121-2135. doi:10.1016/S0010-938X(96)00067-4

Beverskog, B., & Puigdomenech, I. (1997a). Revised pourbaix diagrams for chromium at 25–300 °C. *Corrosion Science, 39*(1), 43-57. doi:10.1016/S0010-938X(97)89244-X

Beverskog, B., & Puigdomenech, I. (1997b). Revised Pourbaix diagrams for nickel at 25–300 °C. *Corrosion Science, 39*(5), 969-980. doi:10.1016/S0010-938X(97)00002-4

Booras, G. S., & Smelser, S. C. (1991). An engineering and economic evaluation of CO2 removal from fossil-fuel-fired power plants. *Energy, 16*(11), 1295-1305. doi:10.1016/0360-5442(91)90003-5

Boot-Handford, M. E., Abanades, J. C., Anthony, E. J., Blunt, M. J., Brandani, S., Mac Dowell, N., . . . Fennell, P. S. (2014). Carbon capture and storage update. *Energy & Environmental Science, 7*(1), 130-189. doi:10.1039/C3EE42350F

Bottoms, R. R. (1930). Process for separating acidic gases. In: Google Patents.

Brouwer, A. S., van den Broek, M., Seebregts, A., & Faaij, A. (2014). Impacts of large-scale Intermittent Renewable Energy Sources on electricity systems, and how these can be modeled. *Renewable and Sustainable Energy Reviews, 33*, 443-466. doi:10.1016/j.rser.2014.01.076

Bui, M., Adjiman, C. S., Bardow, A., Anthony, E. J., Boston, A., Brown, S., . . . Mac Dowell, N. (2018). Carbon capture and storage (CCS): the way forward. *Energy & Environmental Science, 11*(5), 1062-1176. doi:10.1039/C7EE02342A

Bui, M., Gunawan, I., Verheyen, V., Feron, P., Meuleman, E., & Adeloju, S. (2014). Dynamic modelling and optimisation of flexible operation in post-combustion CO2 capture plants—A review. *Computers & Chemical Engineering, 61*, 245-265. doi:10.1016/j.compchemeng.2013.11.015

Campbell, K. L. S., Zhao, Y., Hall, J. J., & Williams, D. R. (2016). The effect of CO2-loaded amine solvents on the corrosion of a carbon steel stripper. *International Journal of Greenhouse Gas Control, 47*, 376-385. doi:10.1016/j.ijggc.2016.02.011

Campbell, M. (2014). Technology Innovation & Advancements for Shell Cansolv CO2 capture solvents. *Energy Procedia, 63*, 801-807. doi:10.1016/j.egypro.2014.11.090

Chen, E., Zhang, Y., Lin, Y., Nielsen, P., & Rochelle, G. (2017). Review of Recent Pilot Plant Activities with Concentrated Piperazine. *Energy Procedia, 114*, 1110-1127. doi:10.1016/j.egypro.2017.03.1266

Chen, L., Li, F., Zhang, Y., Bentley, C. L., Horne, M., Bond, A. M., & Zhang, J. (2017). Electrochemical Reduction of Carbon Dioxide in a Monoethanolamine Capture Medium. *ChemSusChem, 10*(20), 4109-4118. doi:10.1002/cssc.201701075

Clack, C. T. M., Qvist, S. A., Apt, J., Bazilian, M., Brandt, A. R., Caldeira, K., . . . Whitacre, J. F. (2017). Evaluation of a proposal for reliable low-cost grid power with 100% wind, water, and solar. *Proceedings of the National Academy of Sciences, 114*(26), 6722-6727. doi:10.1073/pnas.1610381114

Cousins, A., Cottrell, A., Lawson, A., Huang, S., & Feron, P. H. M. (2012). Model verification and evaluation of the rich-split process modification at an Australian-based post combustion CO2 capture pilot plant. *Greenhouse Gases: Science and Technology, 2*(5), 329-345. doi:10.1002/ghg.1295

Cousins, A., Ilyushechkin, A., Pearson, P., Cottrell, A., Huang, S., & Feron, P. H. M. (2013). Corrosion coupon evaluation under pilot-scale CO2 capture conditions at an Australian coal-fired power station. *Greenhouse Gases: Science & Technology, 3*(3), 169-184. doi:10.1002/ghg.1341

Cousins, A., Nielsen, P. T., Huang, S., Rowland, R., Edwards, B., Cottrell, A., . . . Feron, P. H. M. (2015). Pilot-scale evaluation of concentrated piperazine for CO2 capture at an Australian coal-fired power station: Nitrosamine measurements. *International Journal of Greenhouse Gas Control, 37*, 256-263. doi:10.1016/j.ijggc.2015.03.007

Davis, J. (2009). *Thermal Degradation of Aqueous Amines Used for Carbon Dioxide Capture.* (Ph.D. Dissertation), The University of Texas at Austin,

DIPPR. (2019). DIPPR 801 Database. from Design Institute for Physical Property Data, https://dippr.aiche.org

DOE. (2017). WA Parish Project, Office of Fossil Energy, US Department of Energy (DOE). Retrieved from www.energy.gov/fe/petra-nova-wa-parish-project

DuPart, M., Bacon, T., & Edwards, D. (1993). Understanding corrosion in alkanolamine gas treating plants. *Hydrocarbon Processing, 72*(5), 89-94.

Edenhofer, O., Pichs-Madruga, R., Sokona, Y., Farahani, E., Kadner, S., Seyboth, K., . . . Minx, J. (2014). *Climate Change 2014: Mitigation of Climate Change. Contribution of Working Group III to the Fifth Assessment Report of the Intergovernmental Panel on Climate Change*: Cambridge University Press.

EPA. (2018). *Inventory of US Greenhouse Gas Emissions and Sinks: 1990–2016*. (430-R-18-003).

Etheridge, D., Steele, L., Langenfelds, R., & Francey, R. (1996). Natural and anthropogenic changes in atmospheric CO2 over the last 1000 years from air in Antarctic ice and firn. *Journal of Geophysical Research, 101*(D2), 4115-4128.

Field, C., Barros, V., Dokken, D., Mastrandrea, M., Mach, K., Bilir, T., . . . Genova, R. (2014). *Climate change 2014: impacts, adaptation, and vulnerability-Part A: global and sectoral aspects-Contribution of working group II to the fifth assessment report of the Intergovernmental Panel on Climate Change*: Cambridge University Press.

Fine, N. A. (2015). *Nitrosamine Management in Aqueous Amines for Post-Combustion Carbon Capture.* (Ph.D. Dissertation), The University of Texas at Austin,

Fischer, K. B., Daga, A., Hatchell, D., & Rochelle, G. T. (2017). MEA and Piperazine Corrosion of Carbon Steel and Stainless Steel. *Energy Procedia, 114*, 1751-1764. doi:10.1016/j.egypro.2017.03.1303

Flø, N. E., Faramarzi, L., Iversen, F., Kleppe, E. R., Graver, B., Bryntesen, H. N., & Johnsen, K. (2019). Assessment of material selection for the CO2 absorption process with aqueous MEA solution based on results from corrosion monitoring at Technology Centre Mongstad. *International Journal of Greenhouse Gas Control, 84*, 91-110. doi:10.1016/j.ijggc.2019.02.004

Fontana, M. G. (1986). *Corrosion Engineering* (3rd ed.): McGraw-Hill.

Frailie, P. T. I. (2014). *Modeling of Carbon Dioxide Absorption/Stripping by Aqueous Methyldiethanolamine/Piperazine.* (Ph.D. Dissertation), The University of Texas at Austin,

Freeman, S. A. (2011). *Thermal Degradation and Oxidation of Aqueous Piperazine for Carbon Dioxide Capture.* (Ph.D. Dissertation), The University of Texas at Austin,

Fytianos, G. (2016). (Ph.D. Dissertation), Norwegian University of Science and Technology,

Fytianos, G., Grimstvedt, A., Knuutila, H., & Svendsen, H. F. (2014). Effect of MEA's Degradation Products on Corrosion at CO2 Capture Plants. *Energy Procedia, 63*, 1869-1875. doi:10.1016/j.egypro.2014.11.195

Fytianos, G., Ucar, S., Grimstvedt, A., Hyldbakk, A., Svendsen, H. F., & Knuutila, H. K. (2016). Corrosion and degradation in MEA based post-combustion CO2 capture. *International Journal of Greenhouse Gas Control, 46*, 48-56. doi:10.1016/j.ijggc.2015.12.028

Gao, T., Selinger, J. L., & Rochelle, G. T. (2019). Demonstration of 99% CO2 removal from coal flue gas by amine scrubbing. *International Journal of Greenhouse Gas Control, 83*, 236-244. doi:10.1016/j.ijggc.2019.02.013

Gunasekaran, P., Veawab, A., & Aroonwilas, A. (2013). Corrosivity of Single and Blended Amines in CO2 Capture Process. *Energy Procedia, 37*, 2094-2099. doi:10.1016/j.egypro.2013.06.088

Harrison, R. (1975). Goethite from Hindlow, Derbyshire. *Bulletin of the Geological Survey of Great Britain, 52*.

Hatchell, D., Liu, H., Namjoshi, O. A., & Rochelle, G. T. (2015). *Thermal Degradation and Corrosion of Amines for CO2 Capture.* (Honors Thesis), The University of Texas at Austin,

Hatchell, D., Namjoshi, O., Fischer, K., & Rochelle, G. T. (2014). Thermal Degradation of Linear Amines for CO2 Capture. *Energy Procedia, 63*, 1558-1568. doi:10.1016/j.egypro.2014.11.165

Heuberger, C. F., Staffell, I., Shah, N., & Dowell, N. M. (2017). A systems approach to quantifying the value of power generation and energy storage technologies in future electricity networks. *Computers & Chemical Engineering, 107*, 247-256. doi:10.1016/j.compchemeng.2017.05.012

Hjelmaas, S., Storheim, E., Flø, N. E., Thorjussen, E. S., Morken, A. K., Faramarzi, L., . . . Hamborg, E. S. (2017). Results from MEA Amine Plant Corrosion Processes at the CO2 Technology Centre Mongstad. *Energy Procedia, 114*, 1166-1178. doi:10.1016/j.egypro.2017.03.1280

IAEA. (2018). *Nuclear Power Reactors in the World*. Vienna: International Atomic Energy Agency.

Ibanez, J. G., Choi, C. S., & Becker, R. S. (1987). Aqueous Redox Transition Metal Complexes for Electrochemical Applications as a Function of pH. *Journal of The Electrochemical Society, 134*(12), 3083-3089. doi:10.1149/1.2100344

ICDD. (2018). PDF-4+ 2019 Database. from International Centre for Diffraction Data

Imbrie, J., Boyle, E. A., Clemens, S. C., Duffy, A., Howard, W. R., Kukla, G., . . . Toggweiler, J. R. (1992). On the Structure and Origin of Major Glaciation Cycles 1. Linear Responses to Milankovitch Forcing. *7*(6), 701-738. doi:doi:10.1029/92PA02253

Jacobson, M. Z., Delucchi, M. A., Cameron, M. A., & Frew, B. A. (2015). Low-cost solution to the grid reliability problem with 100% penetration of intermittent wind, water, and solar for all purposes. *Proceedings of the National Academy of Sciences*, 201510028. doi:10.1073/pnas.1510028112

Jacobson, M. Z., Delucchi, M. A., Cameron, M. A., & Frew, B. A. (2017). The United States can keep the grid stable at low cost with 100% clean, renewable energy in all sectors despite inaccurate claims. *Proceedings of the National Academy of Sciences, 114*(26), E5021-E5023. doi:10.1073/pnas.1708069114

Janssens-Maenhout, G., Crippa, M., Guizzardi, D., Muntean, M., Schaaf, E., Dentener, F., . . . Olivier, J. (2017). EDGAR v4.3.2 Global Atlas of the three major Greenhouse Gas Emissions for the period 1970–2012 (Publication no. 10.2904/JRC_DATASET_EDGAR). Retrieved 12/30/2018

Jones, D. A. (1996). *Principles and prevention of corrosion* (2nd ed.). Upper Saddle River, NJ: Prentice-Hall.

Kayafas, I. (1980). Technical Note: Corrosion Product Removal From Steel Fracture Surfaces for Metallographic Examination. *CORROSION, 36*(8), 443-445. doi:10.5006/0010-9312-36.8.443

Keeling, R. F. K., Charles D. (2017). Atmospheric Monthly In Situ CO2 Data - Mauna Loa Observatory, Hawaii. *In Scripps CO2 Program Data*. doi:10.6075/J08W3BHW

Khakharia, P., Mertens, J., Huizinga, A., De Vroey, S., Sanchez Fernandez, E., Srinivasan, S., . . . Goetheer, E. (2015). Online Corrosion Monitoring in a Postcombustion CO2 Capture Pilot Plant and its Relation to Solvent Degradation and Ammonia Emissions. *Industrial & Engineering Chemistry Research, 54*(19), 5336-5344. doi:10.1021/acs.iecr.5b00729

Kittel, J., Idem, R., Gelowitz, D., Tontiwachwuthikul, P., Parrain, G., & Bonneau, A. (2009). Corrosion in MEA units for CO2 capture: Pilot plant studies. *Energy Procedia, 1*(1), 791-797. doi:10.1016/j.egypro.2009.01.105

Kohl, A. L., & Nielsen, R. (1997). *Gas purification*: Elsevier.

Kump, L. R., Brantley, S. L., & Arthur, M. A. (2000). Chemical Weathering, Atmospheric CO2, and Climate. *28*(1), 611-667. doi:10.1146/annurev.earth.28.1.611

Le Quéré, C., Andrew, R. M., Friedlingstein, P., Sitch, S., Pongratz, J., Manning, A. C., . . . Zhu, D. (2018). Global Carbon Budget 2017. *Earth Syst. Sci. Data, 10*(1), 405-448. doi:10.5194/essd-10-405-2018

Li, W., Landon, J., Irvin, B., Thompson, J., Nikolic, H., & Liu, K. (2018). *A Corrosion Inhibition Study of Carbon Steel in a 0.7 MWe Pilot CO2 Capture Process*. Paper presented at the CORROSION 2018, Phoenix, Arizona, USA.

Li, W., Landon, J., Irvin, B., Zheng, L., Ruh, K., Kong, L., . . . Liu, K. (2017). Use of Carbon Steel for Construction of Post-combustion CO2 Capture Facilities: A Pilot-Scale Corrosion Study. *Industrial & Engineering Chemistry Research, 56*(16), 4792-4803. doi:10.1021/acs.iecr.7b00697

Lin, Y.-J., & Rochelle, G. T. (2016). Approaching a reversible stripping process for CO2 capture. *Chemical Engineering Journal, 283*, 1033-1043. doi:10.1016/j.cej.2015.08.086

Liu, H., Hatchell, D., Namjoshi, O. A., & Rochelle, G. (2015). *Oxidative degradation of amine solvents for CO2 capture.* (Honors Thesis), The University of Texas at Austin,

Liu, H., Namjoshi, O. A., & Rochelle, G. T. (2014). Oxidative Degradation of Amine Solvents for CO2 Capture. *Energy Procedia, 63*, 1546-1557. doi:10.1016/j.egypro.2014.11.164

Lovering, J. R., Yip, A., & Nordhaus, T. (2016). Historical construction costs of global nuclear power reactors. *Energy Policy, 91*, 371-382. doi:10.1016/j.enpol.2016.01.011

Lüthi, D., Le Floch, M., Bereiter, B., Blunier, T., Barnola, J.-M., Siegenthaler, U., . . . Stocker, T. F. (2008). High-resolution carbon dioxide concentration record 650,000–800,000 years before present. *Nature, 453*, 379. doi:10.1038/nature06949

MacDonald, A. E., Clack, C. T. M., Alexander, A., Dunbar, A., Wilczak, J., & Xie, Y. (2016). Future cost-competitive electricity systems and their impact on US CO2 emissions. *Nature Climate Change, 6*, 526. doi:10.1038/nclimate2921

MacDowell, N., Florin, N., Buchard, A., Hallett, J., Galindo, A., Jackson, G., . . . Fennell, P. (2010). An overview of CO2 capture technologies. *Energy & Environmental Science, 3*(11), 1645-1669. doi:10.1039/C004106H

McHenry, H., Purtscher, P., & Shives, T. (1987). Observations of hydrogen damage in a failed pressure vessel. *Corrosion Science, 27*(10-11), 1041-1057.
Metal Samples Company. (2019). Model RT4000. Retrieved from www.alspi.com/rt4000.htm
Metz, B., Davidson, O., De Coninck, H., Loos, M., & Meyer, L. (2005). *IPCC, 2005: IPCC special report on carbon dioxide capture and storage. Prepared by Working Group III of the Intergovernmental Panel on Climate Change* (Vol. 442). Cambridge, United Kingdom: Cambridge University Press.
NACE. (2013). Preparation, Installation, Analysis, and Interpretation of Corrosion Coupons in Oilfiled Operations. In *SP0775-2013*. Houston, TX: NACE International.
Namjoshi, O. A. (2015). *Thermal Degradation of PZ-Promoted Tertiary Amines for CO2 Capture.* (Ph.D. Dissertation), The University of Texas at Austin,
NBS. (1955). Standard X-ray diffraction powder patterns. In *Circular 539* (Vol. 4): National Bureau of Standards.
NBS. (1967). Standard X-ray diffraction powder patterns. In *Monograph 25* (Vol. 5): National Bureau of Standards.
NBS. (1978). Standard X-ray diffraction powder patterns. In *Monograph 25* (Vol. 15): National Bureau of Standards.
Nešić, S., & Lee, K.-L. J. (2003). A Mechanistic Model for Carbon Dioxide Corrosion of Mild Steel in the Presence of Protective Iron Carbonate Films—Part 3: Film Growth Model. *59*(7), 616-628. doi:10.5006/1.3277592
Nešić, S., Nordsveen, M., Nyborg, R., & Stangeland, A. (2003). A Mechanistic Model for Carbon Dioxide Corrosion of Mild Steel in the Presence of Protective Iron Carbonate Films—Part 2: A Numerical Experiment. *CORROSION, 59*(6), 489-497. doi:10.5006/1.3277579
Nielsen, P. T. (2018). *Oxidation of Piperazine in Post-Combustion Carbon Capture.* (Ph.D. Dissertation), The University of Texas at Austin,
Nielsen, P. T., Li, L., & Rochelle, G. T. (2013). Piperazine Degradation in Pilot Plants. *Energy Procedia, 37*, 1912-1923. doi:10.1016/j.egypro.2013.06.072
Nordsveen, M., Nešić, S., Nyborg, R., & Stangeland, A. (2003). A Mechanistic Model for Carbon Dioxide Corrosion of Mild Steel in the Presence of Protective Iron Carbonate Films—Part 1: Theory and Verification. *59*(5), 443-456. doi:10.5006/1.3277576
Pacala, S., & Socolow, R. (2004). Stabilization Wedges: Solving the Climate Problem for the Next 50 Years with Current Technologies. *Science, 305*(5686), 968-972. doi:10.1126/science.1100103
Pachauri, R. K., Allen, M. R., Barros, V. R., Broome, J., Cramer, W., Christ, R., . . . Dasgupta, P. (2015). *Climate change 2014: synthesis report. Contribution of Working Groups I, II and III to the fifth assessment report of the Intergovernmental Panel on Climate Change*: Cambridge University Press.
Parson, E. A., & Keith, D. W. (1998). Fossil Fuels Without CO₂ Emissions. *Science, 282*(5391), 1053-1054. doi:10.1126/science.282.5391.1053

Petit, J. R., Jouzel, J., Raynaud, D., Barkov, N. I., Barnola, J. M., Basile, I., . . . Stievenard, M. (1999). Climate and atmospheric history of the past 420,000 years from the Vostok ice core, Antarctica. *Nature, 399*, 429. doi:10.1038/20859

Pourbaix, M. (1974). Atlas of electrochemical equilibria in aqueous solution. *NACE, 307*.

Raja, K. S., & Jones, D. A. (2006). Effects of dissolved oxygen on passive behavior of stainless alloys. *Corrosion Science, 48*(7), 1623-1638. doi:10.1016/j.corsci.2005.05.048

Ramezan, M., Skone, T. J., Nsakala, N., & Liljedahl, G. N. (2007). *Carbon Dioxide Capture from Existing Coal-Fired Power Plants*. (DOE/NETL-401/110907).

Richert, J., Bagdasarian, A., & Shargay, C. (1989). Extent of stress corrosion cracking in amine plants revealed by survey. *Oil Gas J.;(United States), 87*(23).

Rochelle, G., Liu, C., Chen, E., Selinger, J., Fischer, K., Akinpelumi, K., . . . Wu, Y. (2019). Pilot plant demonstration of piperazine with the advanced flash stripper. *International Journal of Greenhouse Gas Control*.

Rochelle, G. T. (2009). Amine Scrubbing for CO2 Capture. *Science, 325*(5948), 1652-1654. doi:10.1126/science.1176731

Rubin, E. S., Davison, J. E., & Herzog, H. J. (2015). The cost of CO2 capture and storage. *International Journal of Greenhouse Gas Control, 40*, 378-400. doi:10.1016/j.ijggc.2015.05.018

Sartori, G., & Savage, D. W. (1983). Sterically hindered amines for carbon dioxide removal from gases. *Industrial & Engineering Chemistry Fundamentals, 22*(2), 239-249. doi:10.1021/i100010a016

Selinger, J. (2018). *Pilot Plant Modeling of Advanced Flash Stripper with Piperazine.* (M.S.E. Thesis), The University of Texas at Austin,

Sexton, A. J. (2008). *Amine Oxidation in CO2 Capture Processes.* (Ph.D. Dissertation), The University of Texas at tAustin,

Shrier, A. L., & Danckwerts, P. V. (1969). Carbon Dioxide Absorption into Amine-Promoted Potash Solutions. *Industrial & Engineering Chemistry Fundamentals, 8*(3), 415-423. doi:10.1021/i160031a009

Singh, A., & Stéphenne, K. (2014). Shell Cansolv CO2 capture technology: Achievement from First Commercial Plant. *Energy Procedia, 63*, 1678-1685. doi:10.1016/j.egypro.2014.11.177

Smith, J., Van ness, H., & Abbott, M. (2005). *Introduction to Chemical Engineering Thermodynamics* (7th ed.).

Soosaiprakasam, I. R., & Veawab, A. (2008). Corrosion and polarization behavior of carbon steel in MEA-based CO2 capture process. *International Journal of Greenhouse Gas Control, 2*(4), 553-562. doi:10.1016/j.ijggc.2008.02.009

Sreekanth, N., & Phani, K. L. (2014). Selective reduction of CO2 to formate through bicarbonate reduction on metal electrodes: new insights gained from SG/TC mode of SECM. *Chemical Communications, 50*(76), 11143-11146.

Sun, W., & Nešić, S. (2008). Kinetics of Corrosion Layer Formation: Part 1—Iron Carbonate Layers in Carbon Dioxide Corrosion. *CORROSION, 64*(4), 334-346. doi:10.5006/1.3278477

Sun, W., Nešić, S., & Woollam, R. C. (2009). The effect of temperature and ionic strength on iron carbonate (FeCO3) solubility limit. *Corrosion Science, 51*(6), 1273-1276. doi:10.1016/j.corsci.2009.03.009

Sun, Y., Remias, J. E., Neathery, J. K., & Liu, K. (2011). Electrochemical study of corrosion behaviour of carbon steel A106 and stainless steel 304 in aqueous monoethanolamine. *Corrosion Engineering, Science & Technology, 46*(6), 724-731. doi:10.1179/1743278210Y.0000000001

Sutcliffe, J. M., Fessler, R. R., Boyd, W. K., & Parkins, R. N. (1972). Stress Corrosion Cracking of Carbon Steel in Carbonate Solutions. *CORROSION, 28*(8), 313-320. doi:10.5006/0010-9312-28.8.313

Szulczewski, M. L., MacMinn, C. W., Herzog, H. J., & Juanes, R. (2012). Lifetime of carbon capture and storage as a climate-change mitigation technology. *109*(14), 5185-5189. doi:10.1073/pnas.1115347109 %J Proceedings of the National Academy of Sciences

Tanupabrungsun, T., Young, D., Brown, B., & Nešic, S. (2012). *Construction And Verification of Pourbaix Diagrams For CO2 Corrosion of Mild Steel Valid Up to 250°C*. Paper presented at the CORROSION 2012, Salt Lake City, Utah.

Tsuda, T., Takeda, M., & Hosoya, K. (2010). *Effect Of Iron Carbonate On The Corrosivity Of Amine Solutions In CO2 Removal Units*. Paper presented at the CORROSION 2010, San Antonio, Texas.

Turton, R., Bailie, R. C., Whiting, W. B., & Shaeiwitz, J. A. (2008). *Analysis, synthesis and design of chemical processes*: Pearson Education.

Tyndall, J. (1859). *On the transmission of heat of different qualities through gases of different kinds.* Paper presented at the Proceedings of the Royal Institution.

Veawab, A., & Aroonwilas, A. (2002). Identification of oxidizing agents in aqueous amine–CO2 systems using a mechanistic corrosion model. *Corrosion Science, 44*(5), 967-987. doi:10.1016/S0010-938X(01)00125-1

Veawab, A., Tontiwachwuthikul, P., & Chakma, A. (1999). Corrosion Behavior of Carbon Steel in the CO2 Absorption Process Using Aqueous Amine Solutions. *Industrial & Engineering Chemistry Research, 38*(10), 3917-3924. doi:10.1021/ie9901630

Voice, A. K. (2013). *Amine Oxidation in Carbon Dioxide Capture by Aqueous Scrubbing.* (Ph.D. Dissertation), The University of Texas at Austin,

Wang, P., Tian, J., Cheng, X., Liu, C., & Xu, J. (2004). Major Pleistocene stages in a carbon perspective: The South China Sea record and its global comparison. *19*(4). doi:10.1029/2003PA000991

Wiley, D. E., Ho, M. T., & Donde, L. (2011). Technical and economic opportunities for flexible CO2 capture at Australian black coal fired power plants. *Energy Procedia, 4*, 1893-1900.

Xiang, Y., Choi, Y.-S., Yang, Y., & Nešić, S. (2014). Corrosion of Carbon Steel in MDEA-Based CO2 Capture Plants Under Regenerator Conditions: Effects of O2 and Heat-Stable Salts. *CORROSION, 71*(1), 30-37. doi:10.5006/1354

Xiang, Y., Yan, M., Choi, Y.-S., Young, D., & Nesic, S. (2014). Time-dependent electrochemical behavior of carbon steel in MEA-based CO2 capture process.

International Journal of Greenhouse Gas Control, 30, 125-132. doi:10.1016/j.ijggc.2014.09.003

Yu, L. C. Y., Sedransk Campbell, K. L., & Williams, D. R. (2016). Using carbon steel in the stripper and reboiler for post-Combustion CO2 capture with aqueous amine blends. *International Journal of Greenhouse Gas Control, 51*, 380-393. doi:10.1016/j.ijggc.2016.04.031

Zhang, Y. (2018). *Absorber and Aerosol Modeling in Amine Scrubbing for Carbon Capture.* (Ph.D. Dissertation), The University of Texas at Austin,

Zhang, Y., Kang, J.-L., Fulk, S., & Rochelle, G. (2017). Modeling Amine Aerosol Growth at Realistic Pilot Plant Conditions. *Energy Procedia, 114*, 1045-1060. doi:10.1016/j.egypro.2017.03.1251

Zheng, L., Landon, J., Matin, N. S., Li, Z., Qi, G., & Liu, K. (2014). Corrosion Behavior of Carbon Steel in Piperazine Solutions for Post-Combustion CO2 Capture. *ECS Transactions*(20), 81-95.

Zheng, L., Landon, J., Matin, N. S., Thomas, G. A., & Liu, K. (2016). Corrosion mitigation via a pH stabilization method in monoethanolamine-based solutions for post-combustion CO2 capture. *Corrosion Science, 106*, 281-292. doi:10.1016/j.corsci.2016.02.013

Zheng, L., Landon, J., Zou, W., & Liu, K. (2014). Corrosion Benefits of Piperazine As an Alternative CO2 Capture Solvent. *Industrial & Engineering Chemistry Research, 53*(29), 11740-11746. doi:10.1021/ie501346z

Zheng, L., Matin, N. S., Landon, J., Thomas, G. A., & Liu, K. (2016). CO2 loading-dependent corrosion of carbon steel and formation of corrosion products in anoxic 30wt.% monoethanolamine-based solutions. *Corrosion Science, 102*, 44-54. doi:10.1016/j.corsci.2015.09.015

Zheng, Y., Ning, J., Brown, B., & Nešić, S. (2016). Advancement in Predictive Modeling of Mild Steel Corrosion in CO2- and H2S-Containing Environments. *CORROSION, 72*(5), 679-691. doi:10.5006/1667

Vita

Kent Billington Fischer grew up in San Angelo, TX. He attended Southern Methodist University and received a B.S. in Chemistry. While there, he spent several influential summers synthesizing organometallic compounds in Dr. Michael Lattman's lab. Shortly after receiving his B.S., he joined the Rochelle group at the University of Texas at Austin. Upon graduation, Kent will begin employment with REXtac, LLC in Odessa, TX.

Permanent email: kent.b.fischer@gmail.com

This dissertation was typed by Kent Fischer.